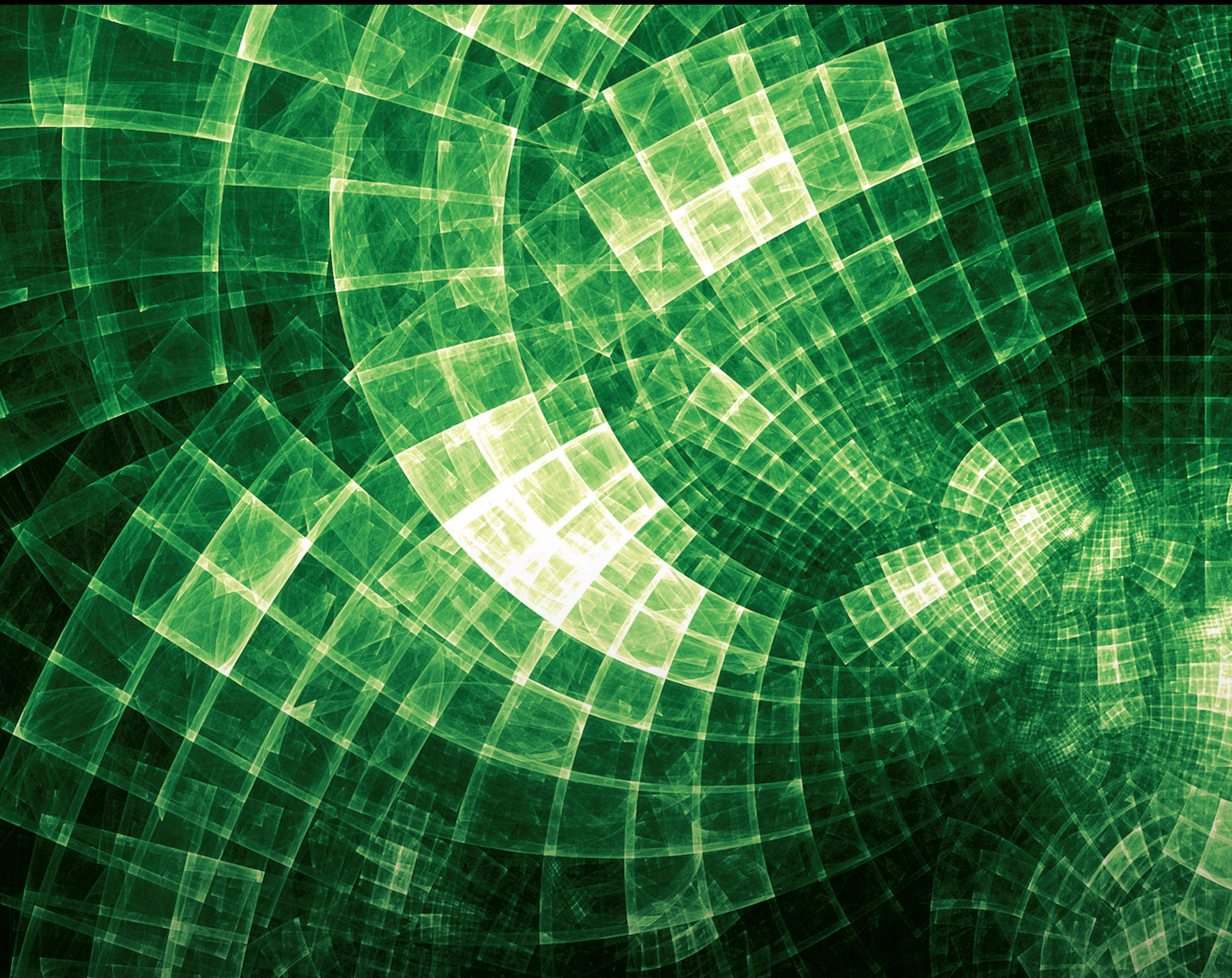# Advances in Barycentric Interpolation Methods and their Applications

Lead Guest Editor: Zhaoqing Wang
Guest Editors: Jin Li, Qingli Zhao, and Long Yuan

Advances in Barycentric Interpolation Methods and their Applications

Advances in Barycentric Interpolation Methods and their Applications

Lead Guest Editor: Zhaoqing Wang
Guest Editors: Jin Li, Qingli Zhao, and Long Yuan

Contents

Nontrivial Solutions for the $2n^{\text{th}}$ Lidstone Boundary Value Problem
Yaohong Li, Jiafa Xu (ID), and Yongli Zan
Review Article (9 pages), Article ID 8811201, Volume 2020 (2020)

Research Article

Linear Barycentric Rational Method for Solving Schrodinger Equation

Peichen Zhao ⓘ[1] **and Yongling Cheng** ⓘ[2]

[1]*School of Mathematics and Statistics, Heze University, Heze 274015, China*
[2]*College of Science, North China University of Science and Technology, Tangshan 063210, China*

Correspondence should be addressed to Yongling Cheng; chengyongling1129@163.com

A linear barycentric rational collocation method (LBRCM) for solving Schrodinger equation (SDE) is proposed. According to the barycentric interpolation method (BIM) of rational polynomial and Chebyshev polynomial, the matrix form of the collocation method (CM) that is easy to program is obtained. The convergence rate of the LBRCM for solving the Schrodinger equation is proved from the convergence rate of linear barycentric rational interpolation. Finally, a numerical example verifies the correctness of the theoretical analysis.

1. Introduction

Schrodinger equation (SDE) is widely used in atomic physics, nuclear physics and solid physics, quantum mechanics, and so on. SDE is only applicable to nonrelativistic particles with low velocity, and there is no description of particle spin. In this paper, we are concerned with solving the numerical solution of the SDE:

$$ih\frac{\partial \varphi(x,t)}{\partial t} = -\frac{h^2}{2m}\frac{\partial^2 \varphi(x,t)}{\partial x^2} + V(x,t)\varphi(x,t) + f(x,t),$$

$$\tag{1}$$

$$\varphi(x,0) = g_1(x), \varphi(x,t) = g_2(x), x \in (a,b), \tag{2}$$

$$\varphi(a,t) = h_1(t), \varphi(b,t) = h_2(t), \quad 0 < t < T, \tag{3}$$

where h is reduced Planck constant and m denotes quality. In [1], the fractional Schrodinger–Choquard equation with blow-up criteria and instability of normalized standing waves is studied. In [2], the finite-difference time-domain (FDTD) method is studied to solve SDE. In [3], nonlinear magnetic Schrodinger–Poisson type equation is studied. In [4], high-order multiscale discontinuous Galerkin method

for one-dimensional stationary SDEs with oscillating solutions is presented. In [5], sixth-order nonlinear SDE is concerned by factorization formula and an analytical method. In [6], nonlinear SDEs are solved by the iterative method. In [7], the two-dimensional Klein–Gordon SDEs are solved by linear compact alternating direction implicit (CADI) scheme.

For getting the equidistant node of the barycentric formula, Floater [8–10] has proposed a reasonable interpolation method; in particular, equidistant distribution nodes and the quasi-equidistant nodes have high numerical stability and accuracy of interpolation [11, 12]. In [13, 14], the linear barycentric rational collocation method (LBRCM) have been used to solve the integro-differential equation. Wang et al. [15–17] have expanded the application fields of the collocation method (CM), such as initial value problems, plane elasticity problems, and nonlinear problems. LBRCM for solving heat conduction equation and biharmonic equation are studied in [18, 19].

In this paper, a LBRCM for solving SDE is proposed. According to the barycentric interpolation method (BIM) of rational polynomial and Chebyshev polynomial, the matrix form of the collocation method that is easy to program is obtained. The convergence rate of the LBRC method for

solving the telegraph equation is proved from the convergence rate of linear barycentric rational interpolation (LBRI). Finally, a numerical example verifies the correctness of the theoretical analysis.

The remaining of this paper is planned as follows. Section 2 presents the differentiation matrices, CM for SDE, and the matrix form of CM. In Section 3, the convergence rate is proved. Finally, a numerical example verifies the theoretical analysis.

2. Differentiation Matrices of SDE

We partition the interval $[a, b]$ and $[0, T]$ into $a = x_0 < x_1 < \cdots < x_m = b$ and $0 = t_0 < t_1 < \cdots < t_n = T$ with $h_i = x_i - x_{i-1}$, $i = 0, 1, \ldots, m$, and $\tau_j = t_j - t_{j-1}$, $j = 0, 1, \ldots, n$, for the uniform partition with $h = (b-a)/m$ and $\tau = T/n$. For $\Omega = [a, b] \times [0, T]$ with (x_i, t_j), $i = 0, 1, \ldots, m$ and $j = 0, 1, \ldots, n$ will be the uniform partition.

Consider the barycentric interpolation function (BIF) as

$$\varphi(x_i, t) = \varphi(x_i), \quad i = 0, 1, \ldots, m, \tag{4}$$

and its barycentric interpolation approximation is

$$\varphi(x, t) = \sum_{i=0}^{m} \sum_{j=0}^{n} r_i(x) r_j(t) \varphi_{ij}, \tag{5}$$

where

$$r_i(x) = \frac{w_i / (x - x_i)}{\sum_{k=0}^{n} w_k / (x - x_k)}, \tag{6}$$

$$w_i = \sum_{k_1 \in J_i} (-1)^{i - d_1} \prod_{h_1 = k_1, h_1 \neq i}^{k_1 + d_1} \frac{1}{|x_i - x_{h_1}|},$$

where $J_i = \{k_1 \in I_m : i - d_1 \leq k_1 \leq i\}$, $I_m = \{0., \ldots, m - d_1\}$, and

$$r_j(t) = \frac{w_j / (t - t_j)}{\sum_{k=0}^{n} w_k / (t - t_k)}, w_j = \sum_{k_2 \in J_j} (-1)^{j - d_2} \prod_{h_2 = k_2, h_2 \neq j}^{k_2 + d_2} \frac{1}{|t_j - t_{h_2}|}, \tag{7}$$

where $J_j = \{k_2 \in I_n : j - d_2 \leq k_2 \leq j\}$, $I_n = \{0. \cdots, n - d_2\}$ is the basis function, and φ_{ij} is the value at point $\varphi(x_i, t_j)$. Combining equations (1) and (5), we obtain

$$i\left(I_m \otimes D^{(1)}\right) \begin{bmatrix} \varphi_0 \\ \vdots \\ \varphi_m \end{bmatrix} + \left(C^{(2)} \otimes I_n\right) \begin{bmatrix} \varphi_0 \\ \vdots \\ \varphi_m \end{bmatrix} - I_n \begin{bmatrix} \varphi_0 \\ \vdots \\ \varphi_m \end{bmatrix} = \begin{bmatrix} f_0 \\ \vdots \\ f_m \end{bmatrix}, \tag{8}$$

and then, we have

$$\left[iI_m \otimes D^{(1)} + \left(C^{(2)} \otimes I_n\right) - I_m \otimes I_n\right] \Phi = F, \tag{9}$$

and

$$L\Phi = F, \tag{10}$$

where

$$L = iI_m \otimes D^{(1)} + \left(C^{(2)} \otimes I_n\right) - I_m \otimes I_n, \tag{11}$$

and

$$D_{ij}^{(1)} = \begin{cases} \dfrac{w_j / w_i}{t_i - t_j}, & i \neq j, \\[3mm] -\sum_{k \neq i} D_{ik}^{(1)}, & i = j, \end{cases} \tag{12}$$

and

$$C_{ij}^{(1)} = \begin{cases} \dfrac{w_j / w_i}{x_i - x_j}, & i \neq j, \\[3mm] -\sum_{k \neq i} C_{ik}^{(1)}, & i = j, \end{cases} \tag{13}$$

$$C_{ij}^{(2)} = \begin{cases} 2C_{ij}^{(1)}\left(D_{ii}^{(1)} - \dfrac{1}{x_i - x_j}\right), & i \neq j, \\[3mm] -\sum_{k \neq i} C_{ik}^{(2)}, & i = j, \end{cases}$$

and $\otimes$ is Kronecher product of matrix. In the following, we define the Kronecher product of matrix $A = (a_{ij})_{m \times n}$ and $B = (b_{ij})_{k \times l}$ as

$$A \otimes B = \left(a_{ij} B\right)_{m \cdot k \times n \cdot l}, \tag{14}$$

where

$$a_{ij} B = \begin{bmatrix} a_{ij} b_{11} & a_{ij} b_{12} & \cdots & a_{ij} b_{1l} \\ a_{ij} b_{21} & a_{ij} b_{22} & \cdots & a_{ij} b_{2l} \\ \vdots & \vdots & \vdots & \vdots \\ a_{ij} b_{k1} & a_{ij} b_{k2} & \cdots & a_{ij} b_{kl} \end{bmatrix}. \tag{15}$$

3. Convergence Rate and Error Analysis

The barycentric rational interpolants of function (BRIF) $\phi(x)$ with $r(x)$ and its error convergence rate is

$$e(x) := \varphi(x) - r_n(x) = (x - x_i) \cdots \\ \cdot (x - x_{i+d}) \varphi[x_i, x_{i+1}, \ldots x_{i+d}, x], \tag{16}$$

and

$$e(x) = \frac{\sum_{i=0}^{n-d} \lambda_i(x)(\varphi(x) - r_n(x))}{\sum_{i=0}^{n-d} \lambda_i(x)} = \frac{A(x)}{B(x)} = O(h^{d+1}), \tag{17}$$

where

$$A(x) := \sum_{i=0}^{n-d} (-1)^i \varphi[x_i, x_{i+1}, \ldots x_{i+d}, x], \qquad (18)$$

and

$$B(x) = \sum_{i=0}^{n-d} \lambda_i(x), \qquad (19)$$

where

$$\lambda_i(x) = \frac{(-1)^i}{(x - x_i) \cdots (x - x_{i+d})}. \qquad (20)$$

The following Lemma was proved by Jean-Pau Berrut in [11].

Lemma 1 (see [11]), *For $e(x)$ defined in (16), we have*

$$\begin{cases} |e(x)| \le Ch^{d+1}, & \varphi \in C^{d+2}[a, b], \\ |e'(x)| \le Ch^{d}, & \varphi \in C^{d+3}[a, b], \\ |e''(x)| \le Ch^{d-1}, & \varphi \in C^{d+4}[a, b], d \ge 1. \end{cases} \qquad (21)$$

For the BRIF $\varphi(x, t)$ with $r(x, t)$, we can get the barycentric rational interpolation (BRI):

$$r_n(x, t) = \frac{\sum_{i=0}^{m} \sum_{j=0}^{n} w_{ij} / [(x - x_i)(t - t_j)] \varphi_{ij}}{\sum_{i=0}^{m} \sum_{j=0}^{n} w_{ij} / (x - x_i)(t - t_j)}, \qquad (22)$$

where

$$w_{ij} = \sum_{k_1 \in J_i} \sum_{k_2 \in J_j} (-1)^{i - d_1 + j - d_2} \prod_{h_1 = k_1, h_1 \neq i}^{k_1 + d_1} \frac{1}{|x_i - x_{h_1}|} \prod_{h_2 = k_2, h_2 \neq j}^{k_2 + d_2} \frac{1}{|t_j - t_{h_2}|}, \qquad (23)$$

and $J_i = \{k_1 \in I_m : i - d_1 \le k_1 \le i\}, I_m = \{0. \ldots, m - d_1\},$

$$J_j = \{k_2 \in I_n : j - d_2 \le k_2 \le j\}, I_n = \{0. \ldots, n - d_2\}. \qquad (24)$$

By the error term of Newton–Cotes rule for two-dimensional function, we have

$$e(x, t) := \varphi(x, t) - r(x, t) = \varphi(x, t) - r_n(x, t)$$
$$= (x - x_i) \cdots (x - x_{i+d_1}) \varphi[x_i, x_{i+1}, \cdots x_{i+d_1}, x]$$
$$+ (t - t_j) \cdots (t - t_{j+d_2}) \varphi[t_j, t_{j+1}, \cdots t_{j+d_2}, t]. \qquad (25)$$

The following theorem has been proved in reference by Li in [18].

Theorem 1. *For $e(x, t)$ defined in (25) and $\varphi(x, t) \in C^{d_1+2}[a, b] \times C^{d_2+2}[0, T]$, we have*

$$|e(x, t)| \le C(h^{d_1+1} + \tau^{d_2+1}). \qquad (26)$$

Corollary 1. *For $e(x, t)$ defined in (25),*

$$\begin{cases} |e_x(x, t)| \le C(h^{d_1} + \tau^{d_2+1}), & \varphi(x, t) \in C^{d_1+3}[a, b] \times C^{d_2+2}[0, T], \\ |e_t(x, t)| \le C(h^{d_1+1} + \tau^{d_2}), & \varphi(x, t) \in C^{d_1+2}[a, b] \times C^{d_2+3}[0, T], \\ |e_{xx}(x, t)| \le C(h^{d_1-1} + \tau^{d_2+1}), & \varphi(x, t) \in C^{d_1+4}[a, b] \times C^{d_2+2}[0, T], \quad d_1 \ge 1. \end{cases} \qquad (27)$$

This corollary can be obtained similarly as Theorem 1, where we omit it.

Let $\varphi(x, t)$ be the solution of (1) and $\varphi(x_m, t_n)$ be the numerical solution; then, we have

$$D\varphi(x_m, t_n) = f(x, t), \qquad (28)$$

and

$$\lim_{m, n \longrightarrow \infty} D\varphi(x_m, t_n) = f(x, t). \qquad (29)$$

According to the above lemma, the following theorem can be proved.

Theorem 2. *Let $\varphi(x_m, t_n): D\varphi(x_m, t_n) = f(x, t)$ and $f(x) \in C[a, b]$; we have*

$$|\varphi(x, t) - \varphi(x_m, t_n)| \le C(h^{d_1-1} + \tau^{d_2}). \qquad (30)$$

Proof. As

TABLE 1: Convergence rate of equidistant nodes with different $d_1 = 7$ and $t = 2$.

n	$d_2 = 2$		$d_2 = 3$		$d_2 = 4$		$d_2 = 5$	
8×8	$6.1237e-01$		$8.7824e-01$		$7.4433e-01$		$1.1222e+00$	
16×16	$1.7534e-01$	1.8042	$1.0471e-01$	3.0682	$3.0341e-02$	4.6166	$4.9307e-02$	4.5084
32×32	$3.3624e-02$	2.3826	$6.6239e-03$	3.9826	$2.3415e-03$	3.6957	$7.0714e-04$	6.1236
64×64	$6.0006e-03$	2.4863	$4.5724e-04$	3.8567	$1.1369e-04$	4.3643	$1.0298e-05$	6.1016

TABLE 2: Convergence rate of equidistant nodes with different $d_2 = 7$ and $t = 2$.

n	$d_1 = 2$		$d_1 = 3$		$d_1 = 4$		$d_1 = 5$	
8×8	1.6771		1.6716		1.6795		1.6782	
16×16	$1.5313e-02$	6.7751	$1.6007e-02$	6.7064	$1.6217e-02$	6.6944	$1.6091e-02$	6.7045
32×32	$1.4665e-03$	3.3843	$7.1109e-05$	7.8144	$8.4703e-05$	7.5809	$7.2416e-05$	7.7957
64×64	$1.8040e-04$	3.0231	$2.9783e-06$	4.5775	$6.9138e-07$	6.9368	$2.4334e-07$	8.2172

TABLE 3: Convergence rate of quasi-equidistant nodes with different $d_1 = 7$ and $t = 2$.

n	$d_2 = 2$		$d_2 = 3$		$d_2 = 4$		$d_2 = 5$	
8×8	$5.1334e-01$		$3.7631e-01$		$1.1156e-01$		$1.2259e-01$	
16×16	$2.8133e-02$	4.1896	$1.1572e-02$	5.0232	$4.8063e-03$	4.5368	$2.5873e-03$	5.5663
32×32	$2.8913e-03$	3.2825	$5.4800e-04$	4.4003	$1.4573e-04$	5.0435	$2.1084e-05$	6.9392
64×64	$3.2935e-04$	3.1340	$3.0820e-05$	4.1523	$4.1594e-06$	5.1308	$2.5797e-07$	6.3528

TABLE 4: Convergence rate of quasi-equidistant nodes with different $d_2 = 7$ and $t = 2$.

n	$d_1 = 2$		$d_1 = 3$		$d_1 = 4$		$d_1 = 5$	
8×8	$2.8707e-01$		$2.8566e-01$		$2.8297e-01$		$2.8323e-01$	
16×16	$1.0263e-02$	4.8059	$5.7980e-04$	8.9445	$5.0888e-04$	9.1191	$5.0644e-04$	9.1274
32×32	$6.1791e-04$	4.0539	$2.9283e-06$	7.6293	$1.1254e-06$	8.8207	$1.0428e-06$	8.9237
64×64	$7.9511e-05$	2.9582	$1.3835e-06$	1.0817	$1.4398e-06$	—	$4.3847e-06$	—
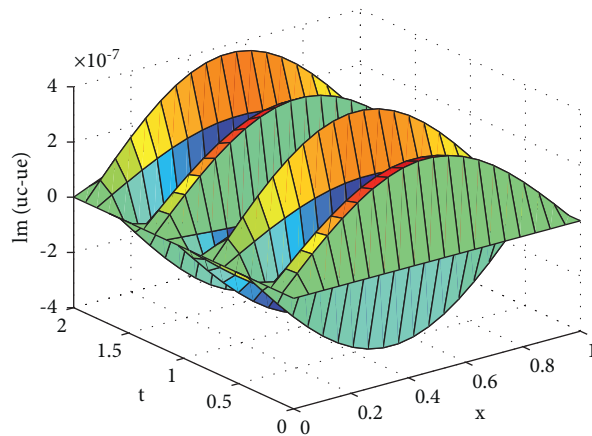
FIGURE 1: Error estimate of equidistant nodes with $t = 2$, $m = n = 19$, and $d_1 = d_2 = 8$.

$$
\begin{aligned}
D\varphi(x,t) &- D\varphi(x_m, t_n) \\
&= i\varphi_t(x,t) - \varphi(x,t) + i\varphi_{xx}(x,t) - [i\varphi_t(x_m, t_n) - \varphi(x_m, t_n) + i\varphi_{xx}(x_m, t_n)] \\
&= i[\varphi_t(x,t) - \varphi_t(x_m, t_n)] + [-\varphi(x,t) + \varphi(x_m, t_n)] + i[\varphi_{xx}(x,t) - \varphi_{xx}(x_m, t_n)] \\
&:= iR_1(x,t) + R_2(x,t) + iR_3(x,t),
\end{aligned}
\tag{31}
$$
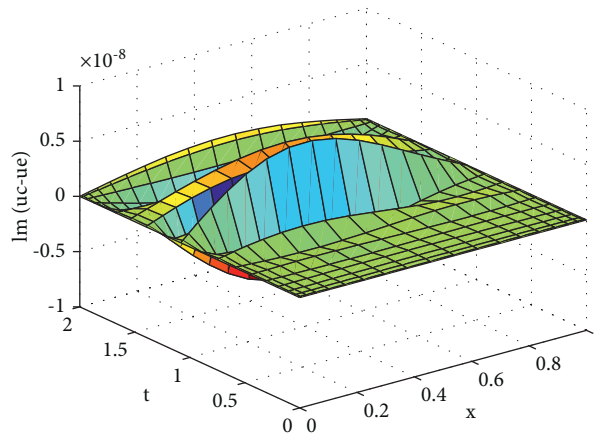
FIGURE 2: Error estimate of quasi-equidistant nodes with $t = 2$, $m = n = 19$, and $d_1 = d_2 = 8$.

TABLE 5: Convergence rate of equidistant nodes with different $d_1 = 7$ and $t = 1$.

n	$d_2 = 2$		$d_2 = 3$		$d_2 = 4$		$d_2 = 5$	
8×8	$1.7995e - 03$		$4.6557e - 04$		$1.5050e - 04$		$1.4417e - 04$	
16×16	$5.5795e - 04$	1.6894	$6.5769e - 05$	2.8235	$1.1394e - 05$	3.7235	$1.5421e - 06$	6.5467
32×32	$1.1570e - 04$	2.2698	$5.2988e - 06$	3.6337	$4.9129e - 07$	4.5355	$2.8309e - 08$	5.7675
64×64	$2.1482e - 05$	2.4291	$4.7396e - 07$	3.4828	$2.3083e - 08$	4.4117	$5.7039e - 10$	5.6332

TABLE 6: Convergence rate of equidistant nodes with different $d_2 = 7$ and $t = 1$.

n	$d_1 = 2$		$d_1 = 3$		$d_1 = 4$		$d_1 = 5$	
8×8	$1.6168e - 03$		$5.1505e - 04$		$1.7042e - 04$		$9.0483e - 05$	
16×16	$1.9952e - 04$	3.0185	$2.1403e - 05$	4.5888	$8.2906e - 06$	4.3615	$1.2726e - 06$	6.1518
32×32	$2.5369e - 05$	2.9754	$1.2042e - 06$	4.1516	$2.4768e - 07$	5.0649	$1.4595e - 08$	6.4461
64×64	$3.4030e - 06$	2.8982	$7.6096e - 08$	3.9842	$8.0774e - 09$	4.9384	$3.4093e - 10$	5.4198

TABLE 7: Convergence rate of quasi-equidistant nodes with different $d_1 = 7$ and $t = 1$.

n	$d_2 = 2$		$d_2 = 3$		$d_2 = 4$		$d_2 = 5$	
8×8	$2.1572e - 03$		$2.1324e - 04$		$2.9588e - 05$		$1.1861e - 05$	
16×16	$1.7804e - 04$	3.5989	$6.5585e - 06$	5.0230	$9.5692e - 07$	4.9505	$7.8014e - 08$	7.2482
32×32	$1.2864e - 05$	3.7907	$4.1551e - 07$	3.9804	$3.2481e - 08$	4.8807	$1.0198e - 09$	6.2574
64×64	$1.3676e - 06$	3.2336	$2.2121e - 08$	4.2314	$8.0913e - 09$	2.0051	$2.4516e - 08$	-

TABLE 8: Convergence rate of quasi-equidistant nodes with different $d_2 = 7$ and $t = 1$.

n	$d_1 = 2$		$d_1 = 3$		$d_1 = 4$		$d_1 = 5$	
8×8	$2.1937e - 03$		$5.6367e - 04$		$7.8737e - 05$		$6.3534e - 06$	
16×16	$1.6769e - 04$	3.7094	$3.6712e - 06$	7.2625	$5.9101e - 07$	7.0577	$8.7629e - 08$	6.1800
32×32	$1.4478e - 05$	3.5339	$1.2449e - 07$	4.8821	$1.2882e - -08$	5.5198	$4.5441e - 10$	7.5913
64×64	$7.0525e - 06$	1.0376	$6.1937e - 07$	—	$2.2631e - 07$	—	$1.0710e - 06$	—

we have

$$R_1(x,t) = \varphi_t(x,t) - \varphi_t(x_m, t_n),$$
$$R_2(x,t) = \varphi(x,t) - \varphi(x_m, t_n), \tag{32}$$
$$R_3(x,t) = \varphi_{xx}(x,t) - \varphi_{xx}(x_m, t_n).$$

As, for $R_3(x,t)$, we have

$$R_3(x,t) = \varphi_{xx}(x,t) - \varphi_{xx}(x_m, t_n)$$

$$= \varphi_{xx}(x,t) - \varphi_{xx}(x_m, t) + \varphi_{xx}(x_m, t) - \varphi_{xx}(x_m, t_n)$$

$$= \frac{\sum_{i=0}^{m-d_1} (-1)^i \varphi_{xx}[x_i, x_{i+1}, \ldots, x_{i+d_1}, x, t]}{\sum_{i=0}^{m-d_1} \lambda_i(x)}$$

$$+ \frac{\sum_{j=0}^{n-d_2} (-1)^j \varphi_{xx}[t_j, t_{j+1}, \ldots, t_{j+d_2}, x_m, t]}{\sum_{j=0}^{n-d_2} \lambda_j(t)}$$

$$= e_{xx}(x, t_n) + e_{xx}(x_m, t_n). \tag{33}$$

By the corollary, we obtain

$$|R_3(x,t)| \leq |e_{xx}(x, t_n) + e_{xx}(x_m, t_n)| \leq C(h^{d_1+1} + \tau^{d_2+1}). \tag{34}$$

Similarly, for $R_2(x,t)$ and $R_1(x,t)$, we have

$$R_1(x,t) = \varphi_t(x,t) - \varphi_t(x_m, t_n) = e_t(x, t_n) - e_t(x_m, t_n), \tag{35}$$

$$|R_1(x,t)| \leq |e_t(x, t_n) + e_t(x_m, t_n)| \leq C(h^{d_1+1} + \tau^{d_2}), \tag{36}$$

and

$$R_2(x,t) = \beta|\varphi(x,t) - \varphi(x_m, t_n)| \leq C(h^{d_1+1} + \tau^{d_2+1}). \tag{37}$$

Combining the identity equations (31), (34), (36), and (37), the conclusion of theorem is obtained.

4. Numerical Examples

Example 1. The SDE $a = 0, b = 1, t = 2,$ and

$$f(x,t) = 0, \tag{38}$$

under condition $g_1(x) = \sqrt{2}\sin(\pi x)$; the analysis solution is

$$\varphi(x,t) = \sqrt{2}e^{-i\pi^2 t/2}\sin(\pi x). \tag{39}$$

Tables 1 and 2 show the errors of the LBRCM for equidistant nodes of space variables and time variables.

Tables 3 and 4 show the errors of the LBRCM for quasi-equidistant nodes of space variables and time variables.

Example 2. The SDE $a = 0, b = 1, t = 1,$ and

$$f(x,t) = (x^2 - 2)e^{i\pi^2 t/4}\cos\left(\frac{\pi x}{2}\right) + 2\pi\sin\left(\frac{\pi x}{2}\right), \tag{40}$$

under condition $g_1(x) = x^2\cos(\pi x/2)$; the analysis solution is

$$\varphi(x,t) = e^{-t}\sin x. \tag{41}$$

In Figures 1 and 2, the error estimate of equidistant and quasi-equidistant nodes with $t = 2, m = n = 19,$ and $d_1 = d_2 = 8$ is presented. It can be seen from Figure 2 that the barycentric rational interpolation collocation method has higher accuracy in both quasi-equidistant and equidistant nodes conditions.

Tables 5 and 6 show the errors of the LBRCM for equidistant nodes of space variables and time variables.

Tables 7 and 8 show the errors of the LBRCM for quasi-equidistant nodes of space variables and time variables.

5. Conclusion

In this paper, the LBRCM have been constructed to solve SDE, while the time variable and space variable are obtained at the same time. Numerical solution confirms the theorem analysis.

Data Availability

The data that support the findings of this study are available from the corresponding author upon reasonable request.

Conflicts of Interest

The authors declare that they have no conflicts of interest.

Authors' Contributions

This manuscript was written by Peicheng Zhao and Yongling Cheng. Some checks of grammar were given by Yongling Cheng.

Acknowledgments

References

[1] B. H. Feng, R. P. Chen, and J. Y. Liu, "Blow-up criteria and instability of normalized standing waves for the fractional Schrdinger-Choquard equation," *Advances in Nonlinear Analysis*, vol. 10, no. 1, pp. 331–330, 2021.

[2] P. Declee, A. V. Londersele, and H. Rogier, "Nonuniform and higher-order FDTD methods for the schrdinger equation," *Journal of Computational and Applied Mathematics*, vol. 381, no. 1, Article ID 113023, 2021.

[3] Y. L. Liu, X. Li, and J. Chao, "Multiplicity of concentrating solutions for a class of magnetic Schrdinger-Poisson type equation," *Advances in Nonlinear Analysis*, vol. 10, no. 1, pp. 131–151, 2021.

[4] B. Dong and W. Wang, "High-order multiscale discontinuous Galerkin methods for the one-dimensional stationary Schrdinger equation," *Journal of Computational and Applied Mathematics*, vol. 380, no. 15, Article ID 112962, 2020.

[5] C. C. Liu, H. M. Wang, and Z. S. Feng, "Global solution for a sixth-order nonlinear Schrodinger equation," *Journal of Mathematical Analysis and Applications*, vol. 490, no. 2, Article ID 124327, 2020.

[6] C.-S. Liu, "A positivity preserving iterative method for finding the ground states of saturable nonlinear schrödinger equations," *Journal of Scientific Computing*, vol. 84, no. 3, 2020.

[7] J. Chen and F. Chen, "Maximum norm error estimates of a linear CADI method for the Klein-Gordon-Schrödinger equations," *Computers and Mathematics with Applications*, vol. 80, no. 5, pp. 1327–1342, 2020.

[8] M. S. Floater and K. Hormann, "Barycentric rational interpolation with no poles and high rates of approximation," *Numerische Mathematik*, vol. 107, no. 2, pp. 315–331, 2007.

[9] G. Klein and J.-P. Berrut, "Linear rational finite differences from derivatives of barycentric rational interpolants," *SIAM Journal on Numerical Analysis*, vol. 50, no. 2, pp. 643–656, 2012.

[10] G. Klein and J.-P. Berrut, "Linear rational finite differences from derivatives of barycentric rational interpolants," *BIT Numerical Mathematics*, vol. 52, no. 2, pp. 407–424, 2012.

[11] J.-P. Berrut, M. S. Floater, and G. Klein, "Convergence rates of derivatives of a family of barycentric rational interpolants," *Applied Numerical Mathematics*, vol. 61, no. 9, pp. 989–1000, 2011.

[12] J.-P. Berrut, S. A. Hosseini, and G. Klein, "The linear barycentric rational quadrature method for Volterra integral equations," *SIAM Journal on Scientific Computing*, vol. 36, no. 1, pp. A105–A123, 2014.

[13] J. Li and Y. L. Cheng, "Linear barycentric rational collocation method for solving second-order Volterra integro-differential equation," *Computational and Applied Mathematics*, vol. 39, no. 2, pp. 1–9, 2020.

[14] J. Li and Y. L. Cheng, "Numerical solution of Volterra integro-differential equations with linear barycentric rational method," *International Journal of Algorithms, Computing and Mathematics*, vol. 6, 2020.

[15] Z. Q. Wang and S. P. Li, *Barycentric Interpolation Collocation Method for Nonlinear Problems*, National Defense Industry Press, Beijing, China, 2015.

[16] Z. Q. Wang, Z. K. Xu, and J. Li, "Mixed barycentric interpolation collocation method of displacement-pressure for incompressible plane elastic problems," *Chinese Journal of Applied Mechanics*, vol. 35, no. 3, pp. 631–637, 2018.

[17] Z. Q. Wang, L. Zhang, and Z. K. Xu, "Barycentric interpolation collocation method based on mixed displacement-stress formulation for solving plane elastic problems," *Chinese Journal of Applied Mechanics*, vol. 35, no. 2, pp. 304–309, 2018.

[18] J. Li and Y. L. Cheng, "Linear barycentric rational collocation method for solving heat conduction equation," *Numerical Methods for Partial Differential Equations*, vol. 37, Article ID 22539, 2020.

[19] J. Li and Y. L. Cheng, "Barycentric rational method for solving biharmonic equation by depression of order," *Numerical Methods for Partial Differential Equations*, vol. 1C15, Article ID 22638, 2020.

Research Article

Barycentric Rational Collocation Method for the Incompressible Forchheimer Flow in Porous Media

Qingli Zhao [ID] **and Yongling Cheng**

School of Science, Shandong Jianzhu University, Jinan, Shandong 250101, China

Correspondence should be addressed to Qingli Zhao; zhaoqingliabc@163.com

Barycentric rational collocation method is introduced to solve the Forchheimer law modeling incompressible fluids in porous media. The unknown velocity and pressure are approximated by the barycentric rational function. The main advantages of this method are high precision and efficiency. At the same time, the algorithm and program can be expanded to other problems. The numerical stability can be guaranteed. The matrix form of the collocation method is obtained from the discrete numerical schemes. Numerical analysis and error estimates for velocity and pressure are established. Numerical experiments are carried out to validate the convergence rates and show the efficiency.

1. Introduction

Darcy flow in porous media is of great interest in many science and engineering fields such as oil recovery and groundwater pollution contamination. Darcy's law,

$$\frac{\mu}{k}u(x) = -\frac{d\widehat{p}(x)}{dx} + \rho g(x), \quad x \in (a, b), \tag{1}$$

mainly describes the linear relationship between Darcy velocity u and derivative of pressure $\widehat{p}$. Here, symbols μ, k, ρ, and $g(x)$ represent the viscosity coefficient, permeability, the density of the fluids, and the gravitational term, respectively. This model is widely used and suitable for low velocity, small porosity, and permeability fluids [1–4].

If the porosity is nonuniform and velocity is higher, a second-order term is needed to be added, the non-Darcy relationship has been researched by Forchheimer [1]. For example, the high-speed Forchheimer flow of single-phase incompressible fluid in porous medium is presented as follows:

$$\frac{\mu}{k}u(x) + \beta\rho|u(x)|u(x) = -\frac{d\widehat{p}(x)}{dx} + \rho g(x), \quad x \in (a, b). \tag{2}$$

Note that when Forchheimer number $\beta = 0$, nonlinear model (2) degenerates to linear Darcy's law (1).

Model (2) is also called Darcy–Forchheimer law [5–10]. In [6], a block-centered finite difference method has been introduced to solve the Darcy–Forchheimer law. Discrete numerical scheme and error estimates were given. Mixed finite element method (MFEM) for equation (2) was studied in [7, 8]. Using this method, velocity and pressure can be approximated simultaneously. Two-grid and multigrid block-centered finite difference method (FDM) for the Darcy–Forchheimer flow in porous media was researched in [10, 11], respectively. This method can improve the efficiency of dealing with nonlinear problems. The barycentric formula is obtained by the Lagrange interpolation formula [12–16] and has been used to solve Volterra equation and Volterra integro-differential equation [12, 17, 18]. Floater and Hormann [19] have proposed a rational interpolation scheme which has higher accuracy on equidistant and special distributed nodes. Wang et al. [20–22] successfully applied the barycentric rational collocation method (BRCM) to solve initial value problem, boundary value problem, plane elasticity problem, and some nonlinear problems. These research studies extended the application fields of

barycentric rational collocation method. In recent papers, Li et al. [23–27] have used the barycentric rational collocation method to solve heat conduction equation, biharmonic problem, and second-order Volterra integro-differential equation.

In this paper, barycentric rational collocation method is introduced to solve the incompressible Forchheimer flow. We demonstrate that barycentric rational collocation method is highly accurate for both velocity and pressure. $O(h^d)$ error estimates for velocity and pressure are given. Numerical experiments [28–32] are carried out to show the convergence rates. The paper is organized as follows. In Section 2, notations and barycentric formula are given. In Section 3, convergence analysis of barycentric rational collocation method for Forchheimer law and error estimates of velocity and pressure are presented. In Section 4, numerical examples are carried out to verify the convergence rates and show the efficiency. Throughout this paper, C denotes a positive constant independent of h.

2. Notations and Barycentric Rational Algorithm

The partition of interval $\Omega = [a, b]$ is as follows:

$$a = x_0 < x_1 < \cdots < x_{n-1} < x_n = b. \tag{3}$$

Define

$$\begin{aligned} \Omega_i &= [x_{i-1}, x_i], \quad 1 \leq i \leq n, \\ h_i &= x_i - x_{i-1}, \quad 1 \leq i \leq n, \\ h &= \max_{1 \leq i \leq n} h_i. \end{aligned} \tag{4}$$

For the function $u(x)$, the interpolation function $r(x)$ $(d = 0, 1, \ldots, n)$ is given as

$$r(x) = \frac{\sum_{i=0}^{n-d} \lambda_i(x) p_i(x)}{\sum_{i=0}^{n-d} \lambda_i(x)}. \tag{5}$$

Symbol $p_i(x)$ denotes the d-order interpolation polynomial such that $p_i(x_k) = u(x_k)$ for $k = i, i+1, \ldots, i+d$,

$$p_i(x) = \sum_{k=i}^{i+d} \prod_{j=i, j \neq k}^{i+d} \frac{x - x_j}{x_k - x_j} u_k, \tag{6}$$

where $u_k = u(x_k)$ and $\lambda_i(x)$ is a blending function

$$\lambda_i(x) = \frac{(-1)^i}{(x - x_i) \ldots (x - x_{i+d})}. \tag{7}$$

For the numerator term in (5), we deduce that

$$\sum_{i=0}^{n-d} \lambda_i(x) p_i(x) = \sum_{i=0}^{n-d} (-1)^i \sum_{k=i}^{i+d} \prod_{i,j \neq k}^{i+d} \frac{1}{x_k - x_j} u_k = \sum_{k=0}^{n} \frac{\omega_k}{x - x_k} u_k. \tag{8}$$

Here,

$$\omega_k = \sum_{i \in J_k} \prod_{j=i, j \neq k}^{i+d} \frac{1}{x_k - x_j}, \tag{9}$$

and $J_k = \{i \in I; k - d \leq i \leq k\}, I = \{0, 1, \ldots, n - d\}$.

Note that

$$\sum_{k=i}^{i+d} \prod_{j=i, j \neq k}^{i+d} \frac{x - x_j}{x_k - x_j} = 1, \tag{10}$$

and for the denominator term in (5),

$$\sum_{i=0}^{n-d} \lambda_i(x) = \sum_{k=0}^{n} \frac{\omega_k}{x - x_k}. \tag{11}$$

Through further deduction, we get

$$r(x) = \frac{\sum_{j=0}^{n} (\omega_j / x - x_j) u_j}{\sum_{j=0}^{n} \omega_j / x - x_j} = \sum_{j=0}^{n} r_j(x) u_j. \tag{12}$$

Here, ω_k is described as (9). The basis function $r_j(x)$ of barycentric rational interpolation is

$$r_j(x) = \frac{\omega_j / x - x_j}{\sum_{j=0}^{n} \omega_j / x - x_j}, \quad j = 0, 1, \ldots, n. \tag{13}$$

Then, we get the derivative formula at node x_i as

$$u^{(m)}(x_i) := u_i^{(m)} = \frac{d^m u(x_i)}{dx^m} = \sum_{j=0}^{n} r_j^{(m)}(x_i) u_j = \sum_{j=0}^{n} D_{ij}^{(m)} u_j, \quad m = 0, 1, 2, \ldots. \tag{14}$$

Its matrix formulation can be given as

$$\mathbf{u}^{(m)} = \mathbf{D}^{(m)} \mathbf{u}, \tag{15}$$

where

$$\begin{aligned} \mathbf{u}^{(m)} &= \left[u_0^{(m)}, u_1^{(m)}, \ldots, u_n^{(m)} \right], \\ D_{ij}^{(m)} &= r_j^{(m)}(x_i). \end{aligned} \tag{16}$$

The derivative formulation of the basis function $r_j(x)$ at node x_i is

$$r'_j(x_i) = \frac{\omega_j/\omega_i}{x_i - x_j}, \quad j \neq i, \tag{17}$$

$$r'_i(x_i) = -\sum_{j \neq i} r'_j(x_i). \tag{18}$$

According to induction (14)–(18), we obtain the recurrence formula of $D_{ij}^{(m)}$ as

$$\begin{cases} D_{ij}^{(m)} = m\left(D_{ii}^{(m-1)} D_{ij}^{(1)} - \dfrac{D_{ij}^{(m-1)}}{x_i - x_j} \right), & i \neq j, \\[2mm] D_{ii}^{(m)} = \sum_{j \neq i} D_{ij}^{(m)}. \end{cases} \tag{19}$$

3. Convergence Rates and Error Estimates

Define the error between $u(x)$ and barycentric rational interpolation function $r(x)$ as

$$e(x) = u(x) - r(x). \tag{20}$$

According to rational interpolation error theory, we know

$$e(x) = (x - x_i) \ldots (x - x_{i+d}) u[x_i, x_{i+1}, \ldots, x_{i+d}, x]. \tag{21}$$

Combing (21) with (5), we see

$$e(x) = \frac{\sum_{i=0}^{n-d} \lambda_i(x)(u(x) - p_i(x))}{\sum_{i=0}^{n-d} \lambda_i(x)} = \frac{A(x)}{B(x)}, \tag{22}$$

where

$$A(x) = \sum_{i=0}^{n-d} (-1)^i u[x_i, x_{i+1}, \ldots, x_{i+d}, x], B(x) = \sum_{i=0}^{n-d} \lambda_i(x). \tag{23}$$

Define the error norm of $e(x)$ as

$$|e(x)| = \max_{a \leq x \leq b} |e(x)|. \tag{24}$$

The following lemma has been proved in [12].

Lemma 1 (see [12]). *For the error $e(x)$ defined as (20), we have*

$$\begin{cases} |e(x)| \leq Ch^{d+1}, & u \in C^{d+2}[a,b], \\ |e_x(x)| \leq Ch^d, & u \in C^{d+3}[a,b]. \end{cases} \tag{25}$$

Now, we deal with the barycentric rational collocation schemes for the following Forchheimer equations:

$$\begin{cases} \mathscr{D}\widehat{p} := \dfrac{d\widehat{p}(x)}{dx} = -\dfrac{\mu}{k} u(x) - \beta\rho|u(x)|u(x) + \rho g(x), & x \in (a,b], \\[3mm] \mathscr{D}u := \dfrac{du(x)}{dx} = f(x), & x \in (a,b], \\[3mm] u(0) = u_0, \\[2mm] \widehat{p}(0) = \widehat{p}_0. \end{cases} \tag{26}$$

For the second equation of (26), the approximate formula is

$$\sum_{j=0}^{n} r'_j(x) u_j = f(x). \tag{27}$$

Taking $x = x_i$ in (27), the numerical scheme is

$$\sum_{j=0}^{n} r'_j(x_i) u_j = f(x_i), \quad i = 0, 1, \ldots, n. \tag{28}$$

For the first equation of (26), the approximate formula is as follows:

$$\sum_{j=0}^{n} r'_j(x)\widehat{p}_j = -\frac{\mu}{k} u(x) - \beta\rho|u(x)|u(x) + \rho g(x). \tag{29}$$

Then, the calculation scheme is

$$\sum_{j=0}^{n} r'_j(x_i)\widehat{p}_j = -\frac{\mu}{k} u_i - \beta\rho|u_i|u_i + \rho g(x_i), \quad i = 0, 1, \ldots, n. \tag{30}$$

Note that, in practical calculation, first step, we approximate the second equation of (26) and then the first equation of (26).

Let $u(x_n)$ denote the numerical solution of $u(x)$, then we have

$$\begin{aligned} \mathscr{D}u(x_n) &= f(x), \\ \lim_{n \to \infty} \mathscr{D}u(x_n) &= f(x). \end{aligned} \tag{31}$$

Based on the above states, the next theorem gives the error analysis of Darcy velocity.

Theorem 1. *Let $u(x_n)$: $\mathscr{D}u(x_n) = f(x)$ and $f(x) \in C[a,b]$. If $u(x) \in C^{d+3}[a,b]$, then we have*

$$|u(x) - u(x_n)| \leq Ch^d. \tag{32}$$

Proof. For the second equation of (26), using the notation of differential matrix, the discrete form of the collocation method is

$$L_1 \mathbf{u} = \mathbf{D}^{(1)} \mathbf{u} = \mathbf{f}, \tag{33}$$

where

$$L_1 = \begin{bmatrix} D_{00}^{(1)} & \cdots & D_{0n}^{(1)} \\ \vdots & \cdots & \vdots \\ D_{n0}^{(1)} & \cdots & D_{nn}^{(1)} \end{bmatrix},$$

$$\mathbf{u} = (u_0, u_1, \cdot, u_n)^T,$$ $$\qquad (34)$$

$$\mathbf{f} = (f_0, f_1, \cdot, f_n)^T.$$

$$\mathcal{D}u(x) - \mathcal{D}u(x_n) = u_x(x) - u_x(x_n) = \frac{\sum_{j=0}^{n-d} (-1)^j u_x [x_j, x_{j+1}, \ldots, x_{j+d}, x]}{\sum_{j=0}^{n-d} \lambda_j(x)} = e_x(x) = O(h^d). \qquad (35)$$

The proof of this theorem is completed.

Let $\widehat{p}(x_n)$ denote the numerical solution of $\widehat{p}(x)$, then we have

$$\mathcal{D}\widehat{p}(x_n) = -\frac{\mu}{k} u(x) - \beta\rho |u(x)| u(x) + \rho g(x),$$ $$\qquad (36)$$

$$\lim_{m \to \infty} \mathcal{D}\widehat{p}(x_n) = -\frac{\mu}{k} u(x) - \beta\rho |u(x)| u(x) + \rho g(x).$$

The following theorem presents the error analysis of pressure $\widehat{p}$.

Theorem 2. *Let* $\widehat{p}(x_n)$: $\mathcal{D}\widehat{p}(x_n) = -(\mu/k)u(x) - \beta\rho |u(x)| u(x) + \rho g(x)$ *and* $f(x) \in C[a, b]$. *If* $\widehat{p}(x) \in C^{d+3}[a, b]$ *and* $u(x) \in C^{d+3}[a, b]$, *then we have*

$$|\widehat{p}(x) - \widehat{p}(x_n)| \le Ch^d. \qquad (37)$$

Proof. For the first equation of (26), the discrete numerical scheme is

Furthermore, we have

$$L_2 \widehat{\mathbf{p}} = \mathbf{D}^{(1)} \widehat{\mathbf{p}} = \mathbf{b}, \qquad (38)$$

where

$$L_2 = \begin{bmatrix} D_{00}^{(1)} & \cdots & D_{0n}^{(1)} \\ \vdots & \cdots & \vdots \\ D_{n0}^{(1)} & \cdots & D_{nn}^{(1)} \end{bmatrix},$$

$$\widehat{\mathbf{p}} = (\widehat{p}_0, \widehat{p}_1, \ldots, \widehat{p}_n)^T,$$ $$\qquad (39)$$

$$\mathbf{b} = (b_0, b_1, \ldots, b_n)^T,$$

$$b_j = -\frac{\mu}{k} u_j - \beta\rho |u_j| u_j + \rho g(x_j), \quad 0 \le j \le n.$$

Furthermore, we see

$$\mathcal{D}\widehat{p}(x) - \mathcal{D}\widehat{p}(x_n) = -\frac{\mu}{k} (u(x) - u(x_n)) - \beta\rho (|u(x)|u(x) - |u(x_n)|u(x_n)) = E_1 + E_2. \qquad (40)$$

As E_1, note that μ and k are positive constants, we have

$$|E_1| = \left| -\frac{\mu}{k} (u(x) - u(x_n)) \right| \le C |u(x) - u(x_n)| = O((h^d) \qquad (41)$$

Similarly, for E_2, according to the monotonicity of the nonlinear term, we know

$$|E_2| = \left| -\beta\rho (|u(x)|u(x) - |u(x_n)|u(x_n)) \right| \le C |u(x) - u(x_n)| = O(h^d). \qquad (42)$$

Combing (40)–(42), the proof is finished.

Remark 1. In the above proof of Theorem 2, coefficients μ, k, β, and ρ are supposed to be positive constants. If they are functions that depend on variable x and bounded, the proof is similar.

4. Numerical Experiments

In this section, we carry out some numerical experiments using barycentric rational collocation method to solve the Forchheimer equations.

TABLE 1: Errors of velocity u with $n = 20$ for Example 1.

d	$e_1(u)$	$e_{r1}(u)$	$e_2(u)$	$e_{r2}(u)$
1	$2.1667e - 03$	$1.0834e - 03$	$6.0702e - 03$	$3.0351e - 03$
2	$9.6414e - 05$	$4.8207e - 05$	$2.7904e - 04$	$1.3952e - 04$
3	$9.6877e - 06$	$4.8438e - 06$	$3.1901e - 05$	$1.5951e - 05$
4	$6.4868e - 07$	$3.2434e - 07$	$2.2867e - 06$	$1.1433e - 06$
5	$1.0361e - 07$	$5.1806e - 08$	$3.7468e - 07$	$1.8734e - 07$
6	$8.9755e - 09$	$4.4877e - 09$	$3.3227e - 08$	$1.6614e - 08$
7	$1.3998e - 09$	$6.9989e - 10$	$5.2848e - 09$	$2.6424e - 09$
8	$1.5167e - 10$	$7.5836e - 11$	$5.8167e - 10$	$2.9083e - 10$
9	$2.0588e - 11$	$1.0294e - 11$	$7.9930e - 11$	$3.9965e - 11$
10	$4.6402e - 12$	$2.3201e - 12$	$1.8986e - 11$	$9.4929e - 12$
11	$1.6687e - 12$	$8.3433e - 13$	$6.4924e - 12$	$3.2462e - 12$

Example 1. Consider the following incompressible Forchheimer model with $\Omega = [0, 1]$:

$$
\begin{cases}
u(x) + \dfrac{3}{10}|u(x)|u(x) = -\dfrac{d\widehat{p}(x)}{dx} + g(x), & x \in \Omega, \\[2mm]
\dfrac{du(x)}{dx} = \pi \cos(\pi x), & x \in \Omega, \\[2mm]
u(0) = 0, \\[2mm]
\widehat{p}(0) = 0.
\end{cases}
\tag{43}
$$

The analysis solution is chosen to be

$$
\begin{aligned}
u(x) &= 2\sin(\pi x), \\
\widehat{p}(x) &= x^2 - x^{13}.
\end{aligned}
\tag{44}
$$

Gravitational term $g(x)$ is determined according to the first equation of (43). Define absolute error and relative error as

$$
\begin{aligned}
e_1(u) &= |u(x) - u(x_n)|, \\[1mm]
e_{r1}(u) &= \frac{|u(x) - u(x_n)|}{|u(x)|}, \\[1mm]
e_2(u) &= \|u(x) - u(x_n)\|_2, \\[1mm]
e_{r2}(u) &= \frac{\|u(x) - u(x_n)\|_2}{\|u(x)\|_2}, \\[1mm]
e_1(\widehat{p}) &= |\widehat{p}(x) - \widehat{p}(x_n)|, \\[1mm]
e_{r1}(\widehat{p}) &= \frac{|\widehat{p}(x) - \widehat{p}(x_n)|}{|u(x)|}, \\[1mm]
e_2(\widehat{p}) &= \|\widehat{p}(x) - \widehat{p}(x_n)\|_2, \\[1mm]
e_{r2}(\widehat{p}) &= \frac{\|\widehat{p}(x) - \widehat{p}(x_n)_2\|}{\|\widehat{p}(x)\|_2}.
\end{aligned}
\tag{45}
$$

TABLE 2: Errors of pressure $\widehat{p}$ with $n = 20$ for Example 1.

d	$e_1(\widehat{p})$	$e_{r1}(\widehat{p})$	$e_2(\widehat{p})$	$e_{r2}(\widehat{p})$
1	$1.5603e - 01$	$2.5935e - 01$	$6.0581e - 01$	$1.0070e + 00$
2	$5.5500e - 02$	$9.2256e - 02$	$2.2664e - 01$	$3.7673e - 01$
3	$2.0024e - 02$	$3.3284e - 02$	$8.3781e - 02$	$1.3926e - 01$
4	$7.0633e - 03$	$1.1741e - 02$	$3.0018e - 02$	$4.9897e - 02$
5	$2.3541e - 03$	$3.9130e - 03$	$1.0104e - 02$	$1.6796e - 02$
6	$7.3023e - 04$	$1.2138e - 03$	$3.1559e - 03$	$5.2458e - 03$
7	$2.0459e - 04$	$3.4008e - 04$	$8.8865e - 04$	$1.4772e - 03$
8	$5.1300e - 05$	$8.5273e - 05$	$2.2367e - 04$	$3.7180e - 04$
9	$1.0396e - 05$	$1.7281e - 05$	$4.5468e - 05$	$7.5580e - 05$
10	$2.0073e - 06$	$3.3367e - 06$	$8.7996e - 06$	$1.4627e - 05$
11	$1.3584e - 07$	$2.2580e - 07$	$5.9683e - 07$	$9.9209e - 07$

Numerical results are listed in Tables 1–4 . The corresponding approximate figures between analysis solution and numerical solution can be seen in Figures 1 and 2. We test the barycentric rational with the uniform nodes for the direct methods. Tables 3 and 4 show that the convergence rates of velocity and pressure are $O(h^d)$ with $d = 1, 2, 3, 4$. The theoretical convergence rate $O(h^d)$ is reflected.

Example 2. Consider the following incompressible Forchheimer flow:

$$
\begin{cases}
u(x) + \dfrac{1}{5}|u(x)|u(x) = -\dfrac{d\widehat{p}(x)}{dx} + g(x), & x \in \Omega = [0, 1], \\[2mm]
\dfrac{du(x)}{dx} = e^x[\sin(8\pi x) + 8\pi \cos(8\pi x)], & x \in \Omega = [0, 1], \\[2mm]
u(0) = 0, \\[2mm]
\widehat{p}(0) = 0.
\end{cases}
\tag{46}
$$

The analytical solution is set to be

$$
\begin{aligned}
u(x) &= e^x \sin(8\pi x), \\
\widehat{p}(x) &= (2x + \cos(7\pi x))\ln(x + 1).
\end{aligned}
\tag{47}
$$

Gravitational term $g(x)$ is determined according to the analytical solution. Numerical results are listed in

TABLE 3: Errors of velocity u and convergence rates for Example 1.

h	$d = 1$	Rate	$d = 2$	Rate	$d = 3$	Rate	$d = 4$	Rate
1/20	$2.1667e - 03$	—	$9.6414e - 05$	—	$9.6877e - 06$	–	$6.4868e - 07$	—
1/40	$4.7993e - 04$	2.17	$9.7770e - 06$	3.30	$4.9514e - 07$	4.29	$1.2656e - 08$	5.68
1/80	$1.0884e - 04$	2.14	$1.0429e - 06$	3.23	$2.5616e - 08$	4.27	$2.8257e - 10$	5.49
1/160	$2.5226e - 05$	2.11	$1.1568e - 07$	3.17	$1.3571e - 09$	4.24	$6.7115e - 12$	5.40
1/320	$5.9548e - 06$	2.08	$1.3223e - 08$	3.13	$7.3897e - 11$	4.20	$1.7519e - 13$	5.26

TABLE 4: Errors of pressure $\hat{p}$ and convergence rates for Example 1.

h	$d = 1$	Rate	$d = 2$	Rate	$d = 3$	Rate	$d = 4$	Rate
1/20	$1.5603e - 01$	—	$5.5500e - 02$	—	$2.0024e - 02$	—	$7.0633e - 03$	—
1/40	$5.3988e - 02$	1.53	$1.0784e - 02$	2.36	$2.1501e - 03$	3.22	$4.1075e - 04$	4.10
1/80	$1.8789e - 02$	1.52	$1.9925e - 03$	2.44	$2.0891e - 04$	3.36	$2.0755e - 05$	4.31
1/160	$6.5786e - 03$	1.51	$3.5968e - 04$	2.47	$1.9340e - 05$	3.43	$9.7970e - 07$	4.40
1/320	$2.3128e - 03$	1.51	$6.4217e - 05$	2.49	$1.7487e - 06$	3.47	$4.4727e - 08$	4.45
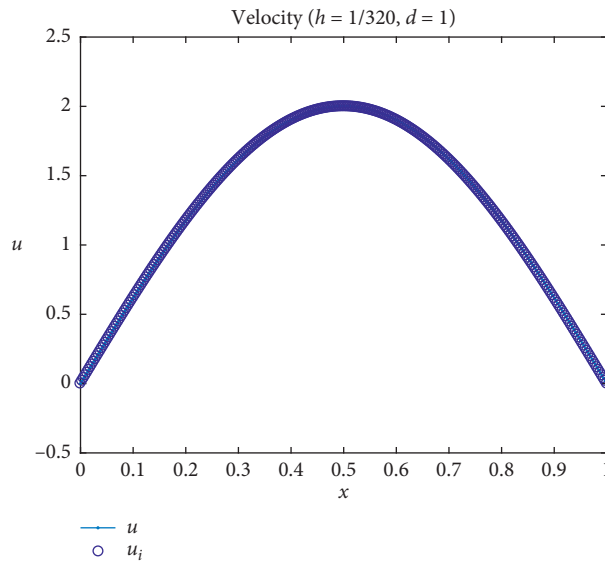
FIGURE 1: Solution of fluid velocity u for Example 1 ($d = 1, h = 1/320$).
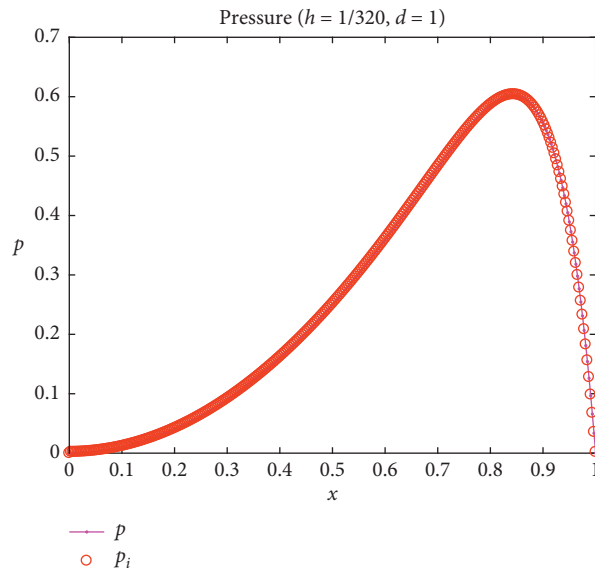
FIGURE 2: Solution of pressure $\hat{p}$ for Example 1 ($d = 1, h = 1/320$).

Table 5: Errors of velocity u and convergence rates for Example 2.

h	$d = 1$	Rate	$d = 2$	Rate	$d = 3$	Rate	$d = 4$	Rate
1/20	$1.2945e + 00$	—	$4.7246e - 01$	—	$1.7784e+00$	—	$1.6443e + 00$	—
1/40	$4.1691e - 01$	1.63	$1.5098e - 01$	1.65	$1.6003e - 01$	3.47	$7.8148e - 03$	7.71
1/80	$1.4368e - 01$	1.54	$3.2078e - 02$	2.23	$1.2557e - 02$	3.67	$1.4539e - 03$	2.43
1/160	$5.0438e - 02$	1.51	$6.0933e - 03$	2.40	$1.0066e - 03$	3.64	$9.8861e - 05$	3.89
1/320	$1.7802e - 02$	1.50	$1.1117e - 03$	2.45	$8.3782e - 05$	3.59	$5.0523e - 06$	4.29
1/640	$6.2931e - 03$	1.50	$1.9941e - 04$	2.48	$7.1647e - 06$	3.55	$2.3727e - 07$	4.41
1/1280	$2.2254e - 03$	1.50	$3.5495e - 05$	2.49	$6.2243e - 07$	3.52	$1.0781e - 08$	4.46

Table 6: Errors of pressure $\widehat{p}$ and convergence rates for Example 2.

h	$d = 1$	Rate	$d = 2$	Rate	$d = 3$	Rate	$d = 4$	Rate
1/20	$1.4816e + 00$	—	$8.3941e - 01$	—	$2.6370e + 00$	—	$2.1833e + 00$	—
1/40	$4.6193e - 01$	1.68	$2.3137e - 01$	1.86	$2.0731e - 01$	3.67	$1.0082e - 02$	7.76
1/80	$1.5886e - 01$	1.54	$4.7049e - 02$	2.40	$1.5931e - 02$	3.70	$2.3613e - 03$	2.09
1/160	$5.5677e - 02$	1.51	$8.7653e - 03$	2.42	$1.2503e - 03$	3.67	$1.4833e - 04$	3.99
1/320	$1.9639e - 02$	1.50	$1.5856e - 03$	2.47	$1.0288e - 04$	3.60	$7.4072e - 06$	4.32
1/640	$6.9404e - 03$	1.50	$2.8326e - 04$	2.48	$8.7430e - 06$	3.56	$3.4459e - 07$	4.43
1/1280	$2.4540e - 03$	1.50	$5.0319e - 05$	2.49	$7.5707e - 07$	3.53	$1.5589e - 08$	4.47
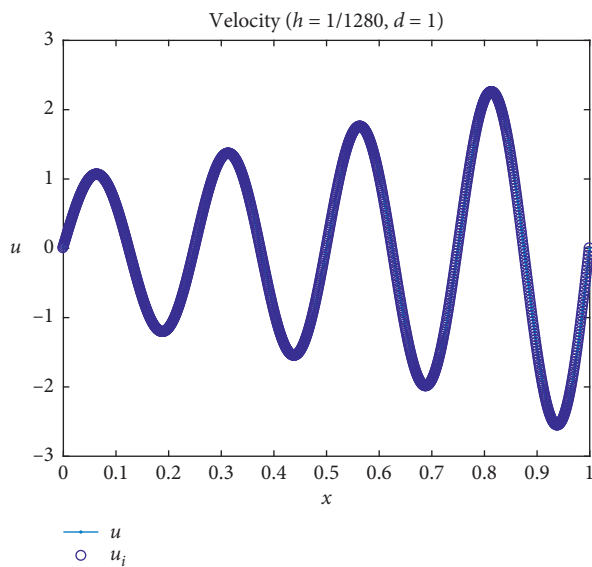
Figure 3: Solution of velocity u for Example 2 ($d = 1, h = 1/1280$).
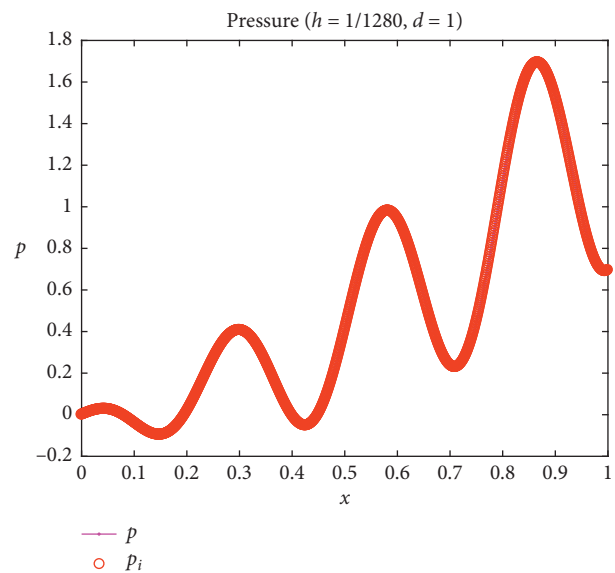
Figure 4: Solution of pressure $\widehat{p}$ for Example 2 ($d = 1, h = 1/1280$).

Tables 5 and 6. The corresponding approximate results between analysis solution and numerical solution can be seen in Figures 3 and 4. We test the barycentric rational with the uniform nodes for the direct methods. Tables 5 and 6 show that the convergence rates are $O(h^d)$ with $d = 1, 2, 3, 4$.

Remark 2. Numerical experiments using the barycentric rational collocation method (BRCM) for the Forchhimer equations show the consistency of the convergence rates with the theoretical analysis. The main advantages of this BRCM are high precision and efficiency. The algorithm and program can be expanded to similar initial value problem and boundary value problem. It can effectively avoid the oscillation of other interpolation collocation methods. The

numerical stability is guaranteed. We demonstrate that the proposed numerical scheme is $O(h^d)$ accurate for both Darcy velocity and pressure. In practical simulation, if the parameter d is further increased, we can get more accurate results. In the future, we will research higher-dimensional Forchheimer law and compressible fluids Forchheimer problems.

Data Availability

No data were used to support this study.

Conflicts of Interest

The authors declare that they have no conflicts of interest.

Acknowledgments

References

[1] K. Aziz and A. Settari, *Petroleum Reservoir Simulation*, Applied Science Publishers LTD, London, UK, 1979.

[2] S. Whitaker, "Flow in porous media I: a theoretical derivation of Darcy's law," *Transport in Porous Media*, vol. 1, no. 1, pp. 3–25, 1986.

[3] D. Ruth and H. Ma, "On the derivation of the Forchheimer equation by means of the averaging theorem," *Transport in Porous Media*, vol. 7, no. 3, pp. 255–264, 1992.

[4] L. T. Hoang, A. Ibragimov, and T. T. Kieu, "One-dimensional two-phase generalized Forchheimer flows of incompressible fluids," *Journal of Mathematical Analysis and Applications*, vol. 401, no. 2, pp. 921–938, 2013.

[5] V. Girault and M. F. Wheeler, "Numerical discretization of a Darcy-Forchheimer model," *Numerische Mathematik*, vol. 110, no. 2, pp. 161–198, 2008.

[6] H. Rui and H. Pan, "A block-centered finite difference method for the Darcy--Forchheimer model," *SIAM Journal on Numerical Analysis*, vol. 50, no. 5, pp. 2612–2631, 2012.

[7] H. Pan and H. Rui, "A mixed element method for Darcy-Forchheimer incompressible miscible displacement problem," *Computer Methods in Applied Mechanics and Engineering*, vol. 264, pp. 1–11, 2013.

[8] H. Pan and H. Rui, "Mixed element method for two-dimensional Darcy-forchheimer model," *Journal of Scientific Computing*, vol. 52, no. 3, pp. 563–587, 2012.

[9] Q. Zhao, H. Rui, and W. Liu, "Cell-centered finite difference method for the one-dimensional forchheimer laws," *Bulletin of the Malaysian Mathematical Sciences Society*, vol. 40, no. 2, pp. 545–564, 2017.

[10] H. Rui and W. Liu, "A two-grid block-centered finite difference method for Darcy--Forchheimer flow in porous media," *SIAM Journal on Numerical Analysis*, vol. 53, no. 4, pp. 1941–1962, 2015.

[11] J. Huang, L. Chen, and H. Rui, "Multigrid methods for a mixed finite element method of the Darcy-Forchheimer model," *Journal of Scientific Computing*, vol. 74, no. 1, pp. 396–411, 2018.

[12] J.-P. Berrut, M. S. Floater, and G. Klein, "Convergence rates of derivatives of a family of barycentric rational interpolants," *Applied Numerical Mathematics*, vol. 61, no. 9, pp. 989–1000, 2011.

[13] J.-P. Berrut and G. Klein, "Recent advances in linear barycentric rational interpolation," *Journal of Computational and Applied Mathematics*, vol. 259, pp. 95–107, 2014.

[14] J. P. Berrut, S. A. Hosseini, and G. Klein, "The linear barycentric rational quadrature method for Volterra integral equations," *Journal. SIAM Journal on Scientific Computing*, vol. 36, pp. 105–123, 2014.

[15] N. R. Bayramov and J. K. Kraus, "On the stable solution of transient convection-diffusion equations," *Journal of Computational and Applied Mathematics*, vol. 280, pp. 275–293, 2015.

[16] E. Cirillo and K. Hormann, "On the Lebesgue constant of barycentric rational Hermite interpolants at equidistant nodes," *Journal of Computational and Applied Mathematics*, vol. 349, pp. 292–301, 2019.

[17] A. Abdi, J. P. Berrut, and S. A. Hosseini, "The linear barycentric rational method for a class of delay Volterra integro-differential equations," *Journal of Scientific Computing*, vol. 75, no. 3, pp. 1757–1775, 2018.

[18] A. Abdi and S. A. Hossseint, "The barycentric rational difference-quadrature scheme for systems of volterra integro-differential equations," *SIAM Journal on Scientific Computing*, vol. 40, pp. A1936–A1960, 2019.

[19] M. S. Floater and K. Hormann, "Barycentric rational interpolation with no poles and high rates of approximation," *Numerische Mathematik*, vol. 107, no. 2, pp. 315–331, 2007.

[20] Z. Wang and S. Li, *Barycentric Interpolation Collocation Method for Nonlinear Problems*, National Defense Industry Press, Beijing, China, 2015.

[21] Z. Wang, Z. Xu, and J. Li, "Mixed barycentric interpolation collocation method of displacement-pressure for incompressible plane elastic problems," *Chinese Journal of Mechanical Engineering*, vol. 35, pp. 195–201, 2018.

[22] Z. Wang, L. Zhang, Z. Xu, and J. Li, "Barycentric interpolation collocation method based on mixed displacement-stress formulation for solving plane elastic problems," *Chinese Journal of Mechanical Engineering*, vol. 35, pp. 304–309, 2018.

[23] J. Li and Y. Cheng, "Linear barycentric rational collocation method for solving second-order Volterra integro-differential equation," *Journal of Computational and Applied Mathematics*, vol. 39, 2020.

[24] J. Li and Y. Cheng, "Barycentric rational method for solving biharmonic equation by depression of order," *Numerical Methods for Partial Differential Equations*, vol. 37, 2021.

[25] J. Li and Y. Cheng, "Linear barycentric rational collocation method for solving heat conduction equation," *Numerical Methods for Partial Differential Equations*, vol. 37, no. 1, pp. 533–545, 2021.

[26] Q. Ge and X. P. Zhang, "Numerical solution for third-order two-point boundary value problems with the barycentric rational interpolation collocation method," *Journal of Mathematics*, vol. 2021, Article ID 6698615, 6 pages, 2021.

[27] J. Li and Y. Sang, "Linear barycentric rational collocation method for beam force vibration equation," *Shock and Vibration*, vol. 2021, Article ID 5584274, 11 pages, 2021.

[28] M. M. Peiravi, J. Alinejad, D. D. Ganji, and S. Maddah, "Numerical study of fins arrangement and nanofluids effects on three-dimensional natural convection in the cubical enclosure," *Challenges in Nano and Micro Scale Science and Technology*, vol. 7, pp. 97–112, 2019.

[29] M. M. Peiravi and J. Alinejad, "Hybrid conduction, convection and radiation heat transfer simulation in a channel with rectangular cylinder," *Journal of Thermal Analysis and Calorimetry*, vol. 140, no. 6, pp. 2733–2747, 2020.

[30] J. Alinejad and M. M. Peiravi, "Numerical analysis of secondary droplets characteristics due to drop impacting on 3D cylinders considering dynamic contact angle," *Meccanica*, vol. 55, pp. 1975–2002, 2020.

[31] M. M. Peiravi, J. Alinejad, D. D. Ganji, and S. Maddah, "Numerical analysis of secondary droplets characteristics due to drop impacting on 3D cylinders considering dynamic contact angle," *International Journal of Numerical Methods*, vol. 30, pp. 2583–2605, 2020.

[32] M. Oru, "Application of a Collocation Method Based on Linear Barycentric Interpolation for Solving 2D and 3D Klein-Gordon-Schrodinger (KGS) Equations Numerically," *Engineering Computations*, vol. 38, 2020.

Research Article

Optimal Design of Intracranial Hematoma Puncture Drainage Tube Based on Adaptive Bifurcation Algorithm

Jincai Chang,[1,2] Liyan Jia [ID],[1] Fei Yu [ID],[1] Xinghui Hao [ID],[1] Ze Lu,[1] and Zhuoyang Li [ID][3]

[1]*College of Science, North China University of Science and Technology, Tangshan, Hebei 063210, China*
[2]*Hebei Key Laboratory of Data Science and Application, Tangshan, Hebei 063210, China*
[3]*College of Clinical Medicine, North China University of Science and Technology, Tangshan, Hebei 063210, China*

Correspondence should be addressed to Liyan Jia; jialiyan0915@163.com

Aiming at the puncture and drainage of clinical intracranial hematoma, we proposed an adaptive bifurcation algorithm based on the hematoma point cloud and optimized the design of the drainage tube. Firstly, based on the CT data of intracranial hematoma patients, a three-dimensional hematoma model was established, the point cloud on the surface of the hematoma was extracted and simplified, and the location of the main drainage tube was located by using the long-axis extraction algorithm. Secondly, the Eight Diagrams algorithm was used to identify the internal point cloud of hematoma, and the positions of multiple absorption points were determined by the K-means clustering algorithm. The locations of the bifurcation points of the main drainage tubes were calculated by the numerical method, and the telescopic lengths and directions of multiple subdrainage tubes were obtained. Finally, connect the main tube and the subtube, design an adaptive bifurcation drainage tube model, and apply it to intracranial hematoma puncture and drainage surgery. The algorithm can accurately determine the puncture point, puncture path, number, and location of subdrainage tubes according to the geometric characteristics of hematoma, achieve a uniform and accurate dose adjustment and drainage of intracranial hematoma, and accelerate the dissolution and drainage speed. The application of an adaptive bifurcation drainage tube can significantly reduce the risk of intracerebral hemorrhage, intracranial infection, and other complications, which has certain guiding significance and application value in clinical practice.

1. Introduction

At present, craniotomy is often used clinically to remove intracranial hematoma in patients. Patients with hematoma have a long anterior and posterior diameter, which is difficult to expose during the operation, requires a larger bone window, and repeatedly stretches the cortex. The operation is more difficult and the hematoma removal rate is low. The patient has a poor prognosis [1]. In recent years, minimally invasive hematoma removal by hematoma puncture and drainage can reduce the surgical incision, facilitate timely removal of hematoma, quickly improve intracranial pressure, do a good job in the prevention, control, and treatment of secondary brain injury, and relieve the damage of hematoma tissue to nerve cells [2]. Neuronavigation hematoma puncture technology can quickly and accurately

remove an intracranial hematoma, intraoperative puncture direction, puncture point, and puncture depth can be controlled, and the drainage tube can be easily and accurately placed into the hematoma cavity, avoiding the blindness of traditional puncture [3]. It is an important means for clinical treatment of cerebral hemorrhage and improvement of prognosis. However, the small hole at the end of the traditional drainage tube is embedded in the wall of the main tube, and the diffusion rate is low and slow, thus prolongs the operation time and increases the operation risk. Moreover, uniform administration and drainage in different directions could not be realized according to the shape of hematoma. Therefore, this paper optimized the design of the traditional drainage tube.

At present, the minimally invasive surgery for the elimination of intracranial hematoma in clinical practice

uses the traditional drug drainage tube. The total length of the main canal is 14 cm, and the diameter is 0.2 cm. The end of the main canal is closed, among which 1 cm and 1.5 cm away from the end are provided with a hole with a diameter of 1 mm, respectively, these two small holes are symmetrically distributed on both sides of the main channel, as shown in Figure 1.

The small hole at the end of the traditional drainage tube is embedded in the wall of the main tube so that the outer surface of the main tube is fully smooth, thus reducing the friction between the drainage tube and intracranial tissue during the operation and ensuring that the drainage tube can reach the center of the hematoma as quickly, safely, and accurately as possible.

The hemolytic agent can produce the interdiffusion reaction with the hematoma. The hemolytic agent drained by the traditional drainage tube is mainly concentrated in the small hole of the main tube, and the blood concentration in the hematoma is also diffused in the direction of the orifice. As a result, the interdiffusion efficiency of hemolytic agent and hematoma is low and the speed is slow, thus prolongs the operation time and increases the operation risk [4].

Cui proposed a multifunctional drainage tube for intracerebral hematoma with multiple subtubes, which could achieve telescopic subtubes in the common duct and 360° rotation of drug delivery in the common duct, so as to achieve the purpose of multipoint and multidirectional uniform drug delivery and drainage [5]. Pan L proposed an improved adaptive weighted particle swarm optimization point cloud search algorithm to improve the efficiency and accuracy of puncture point identification and applied it to extract the optimal external axis, thus providing the optimal path for hematoma drainage tubes [6]. Zhu puts forward visual analysis of flow and diffusion of hemolytic agents and hematomas, using COMSOL more physical software to simulate the hemolysis agent bifurcate drainage tube in the streamline distribution and hemolysis agent in the diffusion behavior of hematoma [4]. Based on previous studies in our team, the drainage tube was optimized, and the adaptive bifurcation drainage tube was customized according to the geometric characteristics of different intracranial hematomas.

In this paper, an optimization model for the traditional drainage tube was proposed. Based on the long-axis extraction algorithm, the main position was determined, and the clustering points were found according to the K-means clustering analysis to accurately locate the position of the subdrainage tube. The optimized adaptive bifurcation drainage tube can achieve uniform and accurate administration and drainage of hematoma in different directions, reduce blood residue, achieve the purpose of maximum drainage, accelerate the dissolution and drainage of hematoma, and improve the safety of surgery. Three-dimensional real-time software simulation technology is used to reconstruct anatomical sites, such as hematoma, blood vessels, skull, and nerve tract. Clinicians can use the adaptive bifurcated drainage tube designed in this paper to conduct preoperative simulation, avoid important parts of the brain, and achieve accurate puncture of hematoma, thus reducing the risk and time of treatment [7–9].

2. Optimal Design of Main Drainage Tube Based on Long-Axis Extraction Algorithm

2.1. Simplify the Surface Structure of Hematoma. In this paper, CT data of intracranial hematoma patients were extracted and preprocessed to achieve 3D reconstruction, and point cloud datasets were extracted. Due to the complexity of the shape of hematoma, the number of point clouds, the location of scattered and discontinuous, and the difficulty of calculation, and the surface hierarchy of hematoma are simplified. The hematoma data were obtained from Tangshan Gongren Hospital, as shown in Figures 2 and 3.

This paper uses decimation of triangle meshes algorithm, with valuation grid on local topology and geometry properties of lattice; the lattice can be divided into simple types; thus, it can be divided into interior and boundary of two types. The judgment of lattice deletion is based on $d < X$, X is given to allow the deviation value, the interior point d is the distance between candidate points to the average plane, and the boundary point d is a candidate to second neighbor points of attachment. Finally, the neighborhood of the deleted grid points is repartitioned by the method of the optimal split plane, and the time complexity is linear [10].

By changing the smoothness of the surface of the hematoma, the surface structure of the hematoma is simplified, and the overall structure of the space remains unchanged. The surface point cloud data is reduced, the algorithm is regular and fast, and the effect of fidelity and detail preservation is good. The simplified hematoma model before and after is shown in Figures 4 and 5.

2.2. Puncture Points Were Extracted Using the Optimized Long-Axis Extraction Algorithm. By studying the long-axis problem of complex geometry, it can be reduced to the farthest point pair problem of the point cloud model [11], that is, the line segment with the longest Euclidean distance between any point pair. By using the long-axis extraction algorithm, the distance function of discrete model is maximized to solve the furthest point pair problem. The distance function of the geometric point cloud model is established to maximize the maximum-minimum distance (max-min) and maximum-average distance (max-avg) between any point pairs. Assume that the given point cloud is set $V = \{v_1, v_2, \ldots, v_n\}$ (nonnegative N points), the distance between each point pair is the edge weight, and each edge weight is nonnegative. The edge weight of any point with respect to $\{v_i, v_j, v_k\} (i \neq j \neq k)$ is called $w(v_i, v_j, v_k)$. The goal of the discrete problem is to locate p points ($p \leq n$) among n points in the point cloud to maximize the function of the distance between point pairs [12].

MAX-MIN points' dispersion (MMPD): for the nonnegative distance $w(v_i, v_j, v_k)$ from any point in set $V = \{v_1, v_2, \ldots, v_N\}$ to v_i, v_j, v_k, there exists subset $P = \{v_{i1}, v_{i2}, v_{i3}\}$ ($P \subset V$) and an integer $p (2 \leq p \leq n)$ so that $|P| = p$ can obtain the distance function:

$$f(P) = \min_{x,y,z \in p} \{w(x, y, z)\}. \tag{1}$$
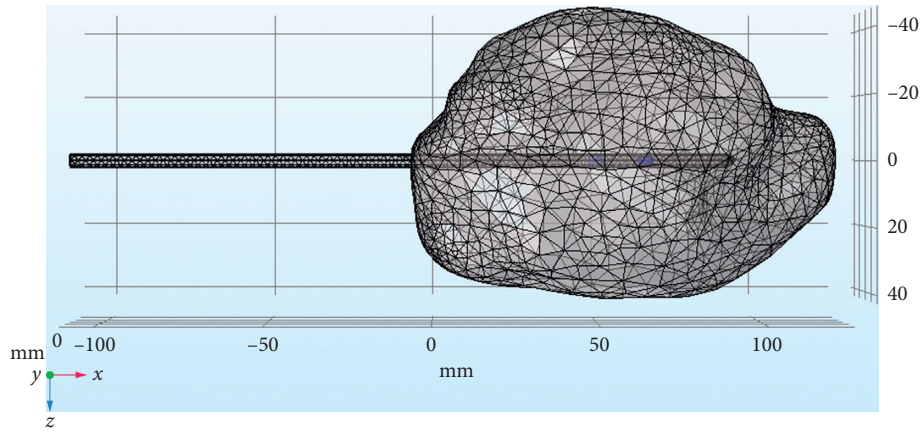
Figure 1: Schematic diagram of traditional drainage tube.
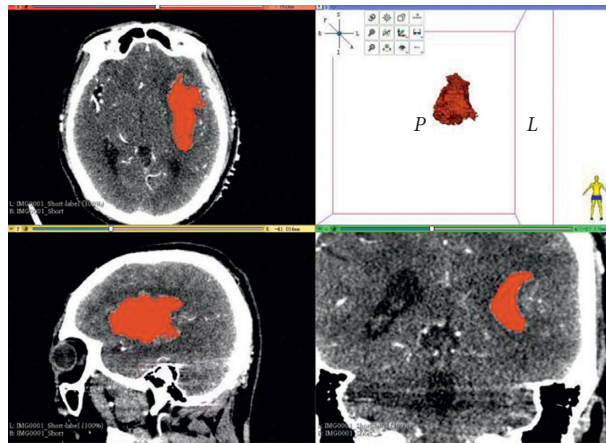
Figure 2: Three-dimensional image of intracranial hematoma.
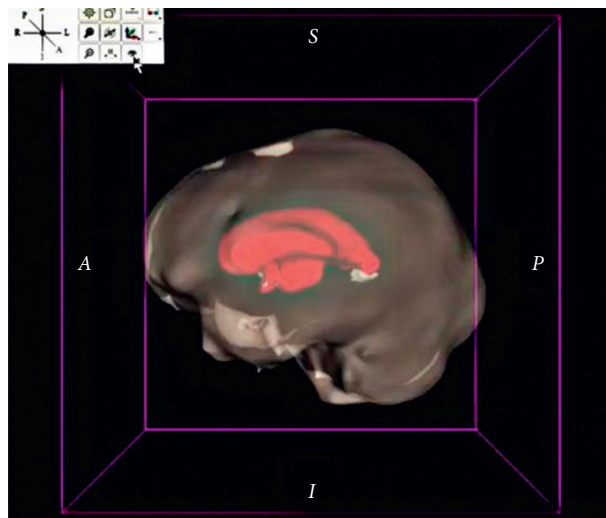
Figure 3: Schematic diagram of intracranial hematoma extraction.
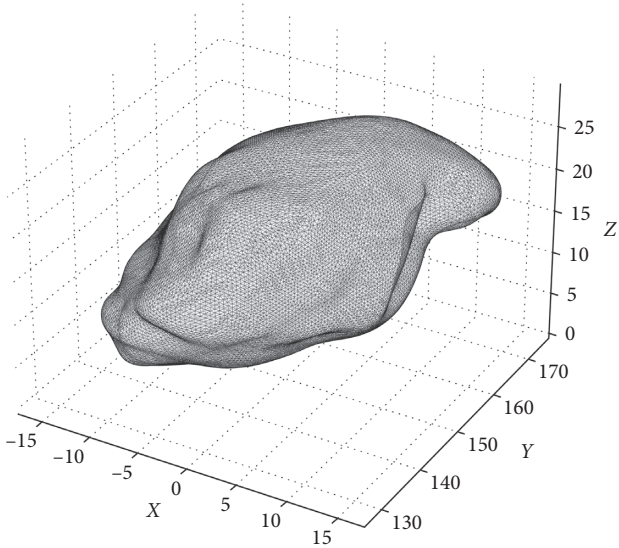
FIGURE 4: Before simplification hematoma model.
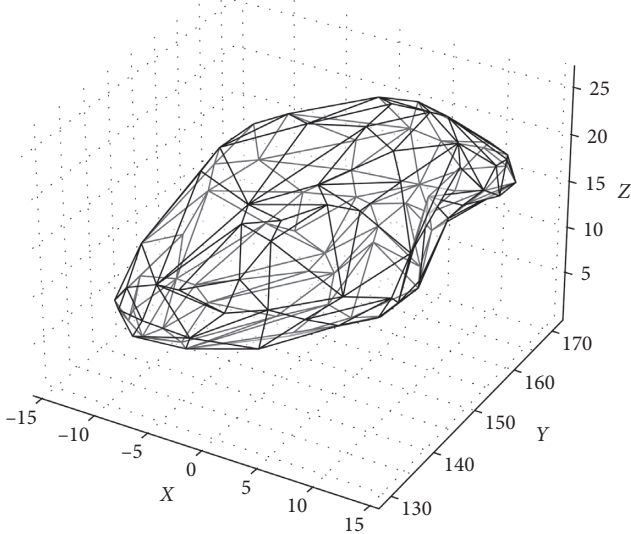
FIGURE 5: Simplified hematoma model.

Maximizing distance function:

$$F(P) = \max f(P) = \max \left\{ \min_{x,y,z \in p} \{w(x, y, z)\} \right\}. \quad (2)$$

MAX-AVG points' dispersion (MAPD): there are subsets $P = \{v_{i1}, v_{i2}, \ldots, v_{ip}\}(P \subset V)$ and integers $p(2 \leq p \leq n)$ which make $|P| = p$ and get the average distance function:

$$g(P) = \frac{2}{p(p-1)} \sum_{x,y,z \in P} w(x, y, z). \quad (3)$$

Maximizing average distance function:

$$G(P) = \max g(P) = \max \left\{ \frac{2}{p(p-1)} \sum_{x,y,z \in P} w(x, y, z) \right\}. \quad (4)$$

Number of point pairs in the point cloud:

$$\frac{p(p-1)}{2}. \quad (5)$$

Therefore, the maximized average distance is equal to the sum of the maximized distances.

The distance specified in MMPD or MAPD satisfies the triangle inequality, that is, any three different points $v_i, v_j,$ and v_k satisfy

$$w(v_i, v_j) + w(v_j, v_k) \geq w(v_i, v_k). \quad (6)$$

Existence distance functions and average distance functions: there are distance functions and average distance functions:

$$f(P) = \min_{x,y,z \in p} \{w(x, y, z)\},$$

$$g(P) = \frac{2}{p(p-1)} \sum_{x,y,z \in P} w(x, y, z). \quad (7)$$

The distance between pairs of points in space is Euclidean distance:

$$\text{dist}(X, Y, Z) = w(x, y, z) = \sqrt{(x_1 - x_2)^2 + (y_1 - y_2)^2 + (z_1 - z_2)^2}. \quad (8)$$

The above hematoma model was taken as an example to verify the algorithm, as shown in Figures 6 and 7.

From what has been discussed above, the long-axis extraction algorithm can be used to solve the farthest point pair problem in the point cloud model. The long axis of the model is the line segment with the longest Euclidean distance in the point cloud. The algorithm has the advantages of easy model iteration, low time consistency, convenient storage of calculation results, easy expansion, and more consistent with the geometry of the topology.

Preliminary results show that the main drainage tube can determine the direction of puncture and drainage according to the long axis of different hematomas so that the introduction of hemolytic agent and the extraction of hematoma fluid can be precise and avoid important brain functional areas. This design is far away from the dense area of the middle cerebral artery and the important branch of the external carotid artery in the scalp, which has little impact on the normal physiological structure, reduces the difficulty of surgery and reduces the risk of surgery.

2.3. Long-Axis Extraction Compared with the Horizontal Optimization of the Previous Method.
When using the long-axis extraction algorithm to extract the point cloud data, because there are many point cloud data in the initial geometry space, the method of simplifying the number of faces is adopted to simplify the hematoma geometry. In order to simplify the influence of different complexity degrees on the long-axis operation time and accuracy, the simplified point cloud data were used to conduct point cloud number statistics and time statistics, and the identification accuracy was compared. Point cloud data with different complexities were shown in Table 1.
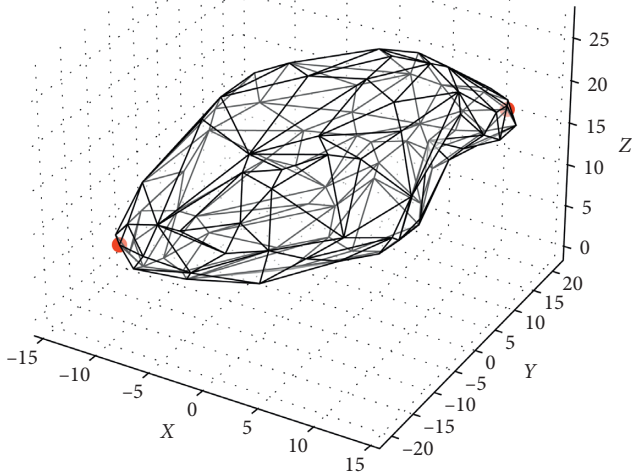
FIGURE 6: Schematic diagram of the farthest point pair of intracranial hematoma model.
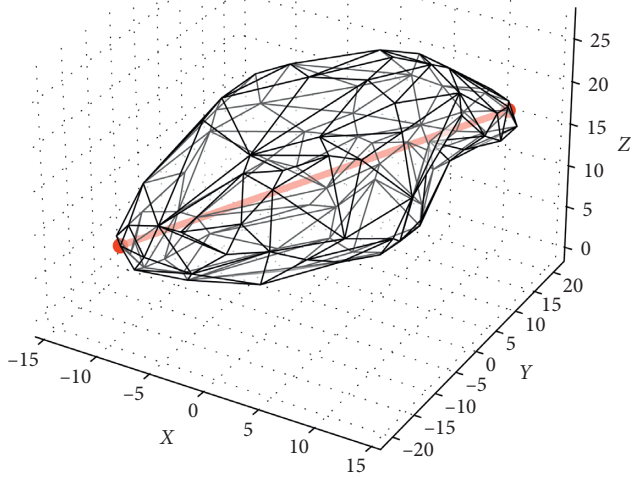
FIGURE 7: Schematic diagram of long-axis extraction of the intracranial hematoma model.

The transverse comparison (Table 1 and Figure 8) shows that the number of point clouds is positively correlated with the retrieval time, and the simplified data can meet the accuracy requirements within the allowable range of the calculation time, reduce the calculation time of the long axis of the hematoma as much as possible, and meet the requirements of the calculation of puncture hematoma surgery.

In tests of different levels of complexity, although the same number of iterations is used to find the long axis, it is obviously not enough for graphics with more point cloud data. For a graph with a complexity level of 7, a more accurate long axis can be obtained faster with the same number of iterations on the geometry, as shown in Figure 7.

TABLE 1: Number of hematoma point clouds and calculation time.

The complexity	Number of point clouds	Time (s)
1	131,820	60.877
2	52,440	25.4564
3	34,566	16.6662
4	17,460	8.17811
5	8082	3.86515
6	3834	1.80199
7	1872	0.8607
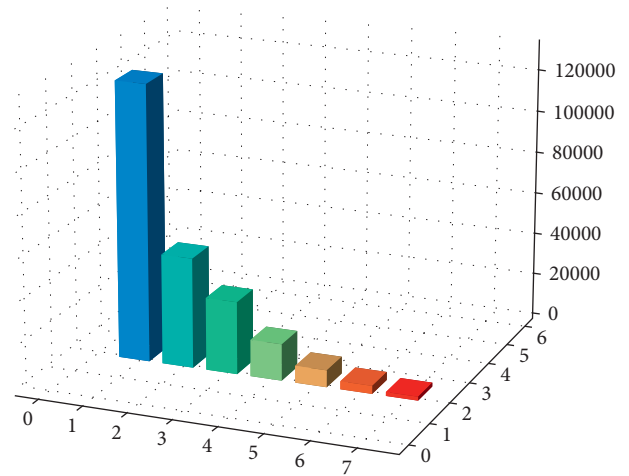
FIGURE 8: Different complexity of hematoma point cloud amount.

3. Optimal Design of Adaptive Drainage Branch Tube

3.1. Internal Points of Intracranial Hematoma Were Extracted Based on the Eight Diagrams Algorithm. The internal points of three-dimensional graphics are identified by using the Eight Diagrams algorithm. The points discussed in this paper are composed of contour data points and internal data points on the surface of geometry by graphic files for the 3D point cloud array [13]. The three-dimensional space is divided into the eight diagrams, as shown in Figure 9. When the target is close to the surface of the geometry, the tangent plane is generated. The target point and the geometry on the tangent plane are in the space rectangular coordinate system and at the side of the origin of the tangent plane. On the other side of the plane, there is at least one hexagram without a target and geometry, so the algorithm can be used for hematoma interior-point discriminant Eight Diagrams.

Eight Diagrams algorithm is used in this paper to discriminant of hematoma interior point, as shown in Figure 10. Take any target point a, vector representation of all surface points b_i with hematoma, remember to vector a_{b_i}, and divide the space where the target point a is; it is divided into eight hexagrams. If the vector exists in all eight hexagrams, it is the internal point of the hematoma. Similarly, if there is no vector a_{b_i} in at least one of the hexagrams, it is the surface point or external point of the hematoma.

For example, the target point is zero: $a(x_a, x_b, x_c)$.

The collection of surface points of hematoma is
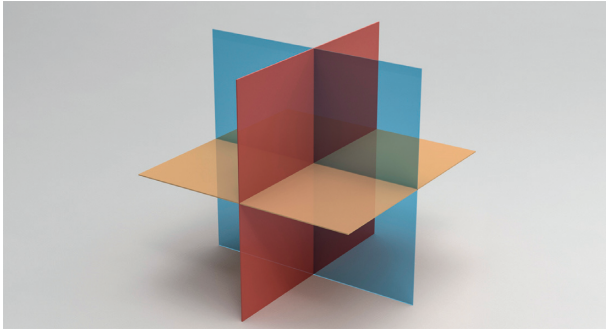
FIGURE 9: The space Eight Diagrams corresponds to the diagram of hexagrams.
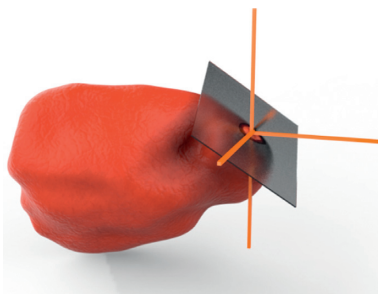
FIGURE 10: Schematic diagram of hematoma under the Eight Diagrams algorithm.

$$B = \left\{ (x_b, x_b, x_b) | x_b = x_{b_i}, y_b = y_{b_i}, z_b = z_{b_i}, i \in [1, n] \right\}. \tag{9}$$

The collection of internal points of the hematoma is

$$C = \left\{ (x_c, x_c, x_c) | x_c = x_{c_j}, y_c = y_{c_j}, z_c = z_{c_j}, j \in [1, m] \right\}. \tag{10}$$

The set of target point and hematoma surface point vector is

$$D = \{\mathbf{aB}\} = \left\{ \overrightarrow{\mathbf{ab}_i} \,|\, i \in [1, n] \right\}. \tag{11}$$

To judge the internal point of hematoma, if any hexagrams of the spatial Eight Diagrams contain vectors in set D and the symbols corresponding to each vector include the symbols corresponding to the above Eight Diagrams, then the target point is the internal point of hematoma. If there is at least one hexagram in the spatial Eight Diagrams that does not contain the vector in set D and there is at least one case in which the hexagram corresponding symbol does not contain the vector in set D, then the target point is the hematoma surface point or the external point.

Taking the above intracranial hematoma as an example, the Eight Diagrams algorithm was used to distinguish the internal points of hematoma and extract the data set of internal points and surface points of hematoma. The yellow points were internal data points of hematoma, and the red points were surface
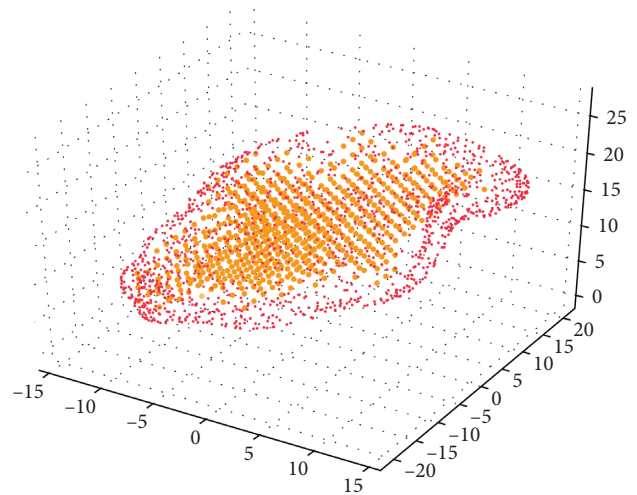
· The points on the surface of the training results
· The inner points

FIGURE 11: Schematic diagram of hematoma data points.
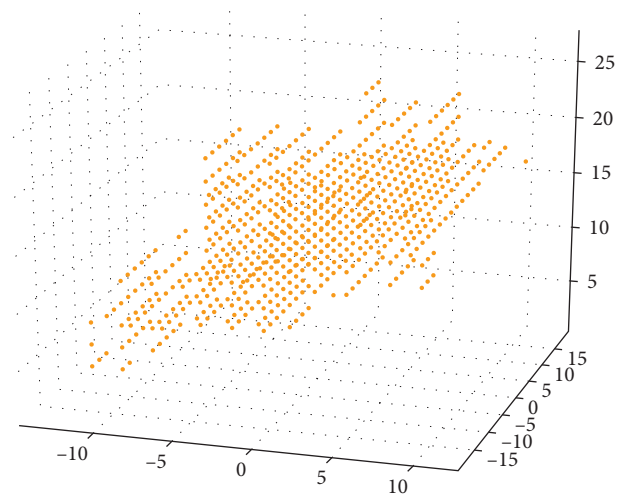
· The inner points

FIGURE 12: Schematic diagram of internal data points of hematoma.

data points of hematoma. The distribution of internal and surface data points of hematoma is shown in Figures 11–13 .

3.2. Extraction of Hematoma Absorption Points Based on K-Means Clustering Analysis Algorithm.

K-means clustering analysis algorithm clustered n data objects in the space with K points as the center and classified the target points closest to the center to get K clusters [14]. Through the iteration method, the coordinate values of each cluster center are updated successively so that the similarity of objects in the same cluster is high, while the similarity of objects in different clusters is low, and the optimal cluster center is obtained.

For example, we have n variables, $x_1, x_2, \ldots, x_n$, divided into k classes, $X_1, X_2, \ldots, X_k$, and N_i is the number of variables in class X_i, i, and m_i for the average:

· The points on the surface of the training results
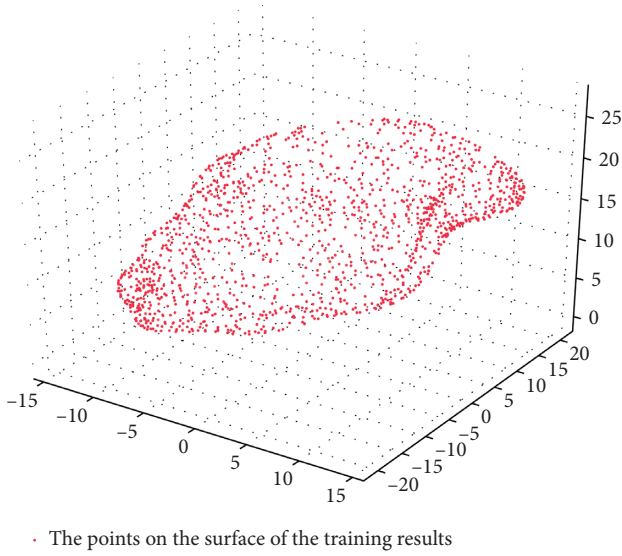
Figure 13: Schematic diagram of data points on the surface of hematoma.

(1) Select the initial center of k classes.

(2) Iterate for any sample, calculate the Euclidean distance to k center points, respectively, and group the sample to the class where the center with the shortest distance is located.

Euclidean distance:

$$d\left(x_j, m_i\right) = \sqrt{\sum_{i=1}^{k} \sum_{x_j \in K_j} \left(x_j - m_i\right)^2}. \qquad (12)$$

If $d\left(x_j, m_i\right) < d\left(x_i, m_i\right)$, among them, $1 \le p \le K$, $i = 1, \ldots, k$, so assign x_j to class p.

(3) Use the mean method to update the values of the center of the k classes.

(4) For all k clustering centers, the abovementioned (2) and (3) are repeated until each clustering center no longer changes. The iteration is finished and the classification is completed.

Combined with the above intracranial hematoma data set. K-means clustering analysis algorithm was adopted. The data objects of intracranial hematoma in space were clustered with 4 points as the center, and the target points nearest to the center were divided into 4 clusters. Through the iteration method, the coordinate values of each clustering center are updated successively so that the similarity of objects in the same clustering is higher, while the similarity of objects in different clustering is smaller. Finally, four optimal clustering centers are obtained. The data set is shown in Table 2.

K-means clustering analysis was performed on the internal data points of the hematoma, and the clustering results are shown in Figure 14. The four clusters were yellow, green, purple, and blue, and the four red dots were the

Table 2: Internal data set of hematoma.

Data set	Sample size	Number of categories
Hematoma	6380	4
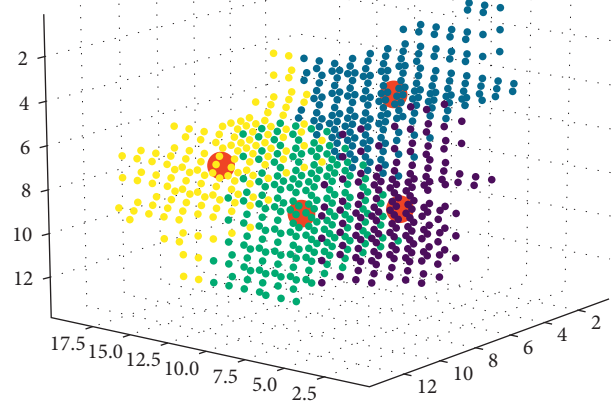
Figure 14: Cluster analysis of hematoma.

clustering centers, namely, the absorption points of the hematoma.

3.3. Determine the Point of Branching of the Hematoma on the Main Drainage Tube.

The origin is O at the end of the long axis, the major axis is the z-axis, and the outlet direction of the main outlet is the positive direction of the Z-axis. Thus, a three-dimensional coordinate system O-XYZ is established. Let the length of the long axis be L; divide the long axis into points n and take a point $a_i, i \in [1, n]$ at every interval L/n; vectors were made with four hematoma absorption sites $\overrightarrow{Z_{ij}}$; calculate the angle θ between each vector and the positive direction of the z-axis $\overrightarrow{z}$.

Let the supervisor start with $\mathbf{A_s} = (x_s, y_s, z_s)$.

The main end is $\mathbf{A_e} = (x_e, y_e, z_e)$.

Then, the leading vector is $\mathbf{a} = (x_s - x_e, y_s - y_e, z_s - z_e)$.

Supervisor above each point is $\mathbf{a_i} = (\mathbf{a}/n) \times i, i \in [1, n]$.

The set of vectors composed of each point on the main axis is $A = \{A_i \mid \mathbf{A_s} + \mathbf{a_i}, i \in [1, n]\}$.

Let the absorption point vector be $\mathbf{P_j} = (x_j, y_j, z_j), j \in [1, 4]$.

Then, the vector set from each point on the main to each absorption point is

$$\begin{cases} Z = \left\{\mathbf{Z_{ij}} \mid \mathbf{P_j} - \mathbf{A_i}, i \in [1, n], j \in [1, 4]\right\}, \\ \\ \cos\langle\mathbf{Z_{ij}}, \mathbf{z}\rangle = \dfrac{\mathbf{Z_{ij}} \cdot \mathbf{z}}{\left|\mathbf{Z_{ij}}\right| \cdot |\mathbf{z}|}, \qquad (13) \\ \\ \theta = \arccos\langle\mathbf{Z_{ij}}, \mathbf{z}\rangle. \end{cases}$$

In the error value calculation method, the measured value θ, E is the normal value 45°:

$$\delta = \frac{\theta - E}{E/100}. \tag{14}$$

The iterative calculation was carried out to make the error value $\varepsilon = 0.05$ satisfied $\delta < \varepsilon$ by giving the error value δ. The four points with the smallest error were taken as the branch bifurcation points of the main pipeline. By connecting the bifurcation point and absorption point, the telescopic length and direction of the subdrainage tube were obtained. Then, the overall structure of the bifurcation drainage tube was designed.

4. Result Analysis

In this paper, an adaptive bifurcation algorithm based on hematoma point cloud is proposed. To optimize the design of puncture drainage tube for clinical intracranial hematoma, the following steps are followed:

Step 1: based on the CT scan data of patients with intracranial hematoma, 3D reconstruction was performed to establish a 3D hematoma model. The point cloud data set was extracted to simplify the hematoma surface hierarchy and the surface point data set.

Step 2: use the long-axis extraction algorithm to select the farthest point pair of Euclidean distance as the two endpoints of the long axis to locate the location of the main drainage tube, and the coordinates of the two ends of the long axis are shown in Table 3;

Step 3: Eight Diagrams algorithm was used to extract internal point cloud of hematoma.

Step 4: the K-means clustering analysis algorithm is used to determine the position of absorption points. The coordinates of the absorption point are shown in Table 4;

Step 5: use numerical solution to calculate the branch point of the upper branch of the main pipe. The coordinates of the bifurcation point are shown in Table 5;

Step 6: the expansion direction and length of the adaptive bifurcation drainage tube were obtained by connecting the bifurcation point with the absorption point. Therefore, an adaptive bifurcation drainage tube model was designed, as shown in Figure 15.

Step 7: the three-dimensional reconstruction model of intracranial hematoma was imported into COMSOL. On this basis, the adaptive branching drainage tube model was introduced to obtain the visual simulation diagram of the influence of the adaptive branching drainage tube on hematoma, as shown in Figures 16 and 17.

In clinical medicine, the closed adaptive bifurcated drainage tube is delivered to the intracranial hematoma through a catheter, and the drainage tube is automatically stretched in the hematoma. Among them, the drainage pipe for special silicone material is soft in texture and small to tissue damage. When the hemolysis agent passes through the drainage tube into the hematoma, diffusion effect occurs

TABLE 3: The coordinates of the two endpoints of the long axis.

	X	Y	Z
Beginning of the long axis	−11.090294	−14.673927	7.278137
End of the long axis	11.579253	18.623718	16.95636

TABLE 4: The coordinates of absorption points.

	X	Y	Z
Absorption point 1	2.573604	−0.012183	17.796954
Absorption point 2	0.204969	−9.975155	16.968944
Absorption point 3	−6.164021	−2.222222	8.910053
Absorption point 4	3.172662	9.568345	14.748201

TABLE 5: Bifurcation point coordinates.

	X	Y	Z
Branch point 1	0.69787044	2.6408484	12.31081296
Branch point 2	5.68517078	9.9663303	14.44002202
Branch point 3	-2.0224752	-1.354869	11.1494262
Branch point 4	4.32499796	7.9684716	13.85932864

mainly in the export area around the four drainage tubes. Multicast delivery drainage achieves the purpose of uniform dosage and drainage, so as to speed up the blood clot dissolves and drainage. And, pressure is applied to quickly remove the main functional structure of the hematoma to reduce the damage that causes the disease of cerebral hemorrhage.

5. The Error Analysis

5.1. Error Analysis of Simplified Hematoma Surface. Hierarchy Structure Algorithm is used with the function approximation to perform error analysis on the simplified model and solve the geometric similarity measurement problem [15].

L_∞ and L_2 norms are two commonly used error measurement standards. Let the surface point function of the original hematoma be $f(t)$, The simplified surface point function of hematoma is $g(t)$, we give a closed interval [a, b]. The L_∞ norm is used to indicate the maximum deviation between two functions:

$$\|f - g\|_\infty = \max_{a \le t \le b} |f(t) - g(t)|. \tag{15}$$

The L_2 norm represents the average deviation between two functions:

$$\|f - g\|_2 = \sqrt{\int_a^b (f(t) - g(t))^2 \mathrm{d}t}. \tag{16}$$

After simplification, the surface point function of hematoma is $g(t)$, which is considered to be optimal; the similarity error measure of L_∞ norm and L_2 norm can be used to measure the error between two triangular mesh models. In the triangular mesh model, what is measured is

(a)   (b)
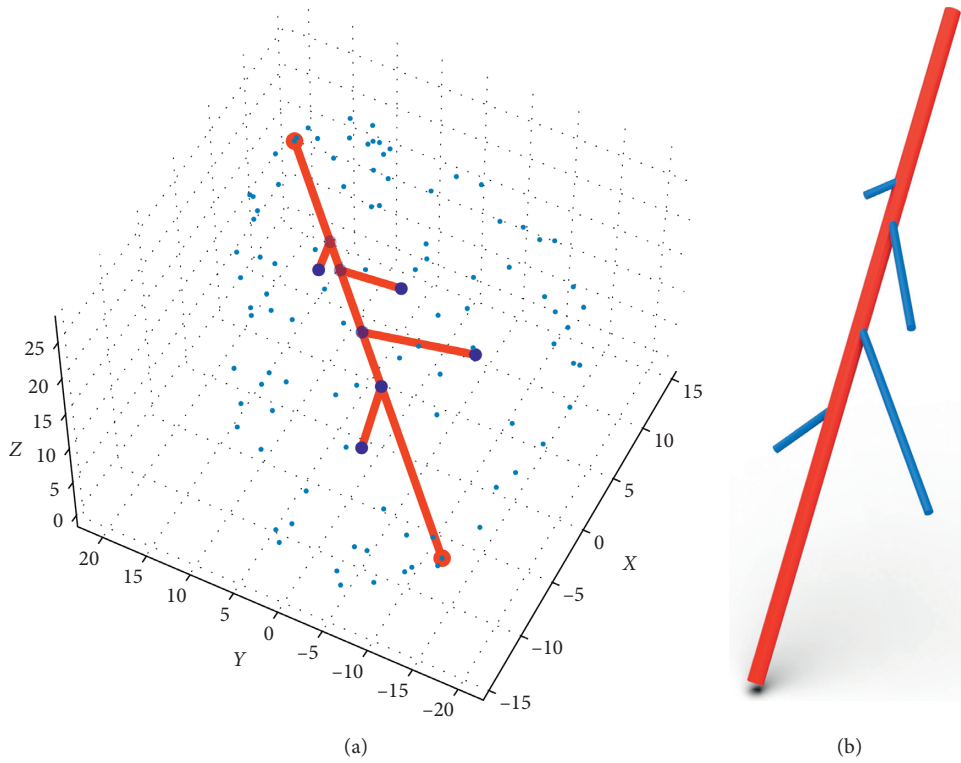
FIGURE 15: Adaptive bifurcation drainage tube.
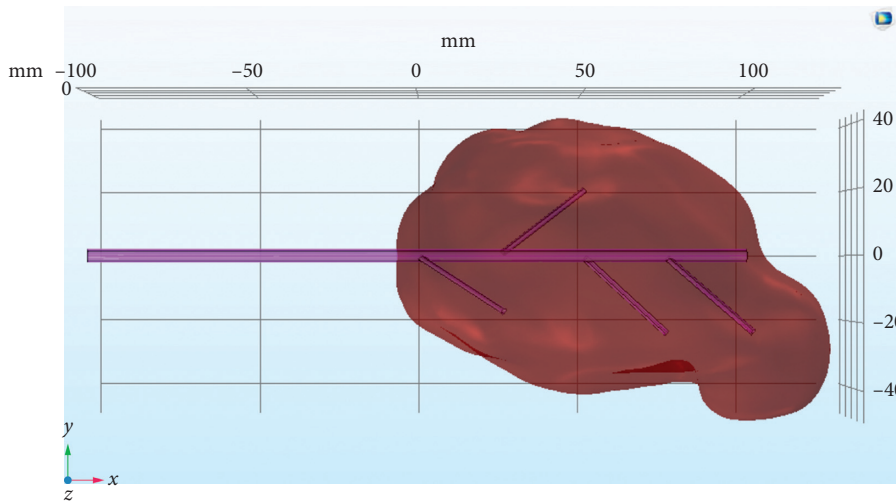
FIGURE 16: Side view of hematoma simulation.

the distance between the nearest point pairs, and the distance from point V to model M is defined as the distance between point V and the nearest point W on model M; among them, the $\|\cdot\|$ Euclidean distance between two vectors:

$$d_v(M) = \min_{w \in M} \|v - w\|. \tag{17}$$

After testing, the original hematoma model was simplified by 60% in this paper, and the geometric

similarity of the hematoma was within the error range. The simplified results could better simulate the original hematoma model.

5.2. Error Analysis of Optimized Long-Axis Extraction Algorithm.
The beginning end of the long axis A_{s1} and the end A_{e1} are obtained by the initial long-axis algorithm; the beginning end A_{s2} and the end A_{e2} of the long axis are obtained by optimizing the long-axis algorithm.
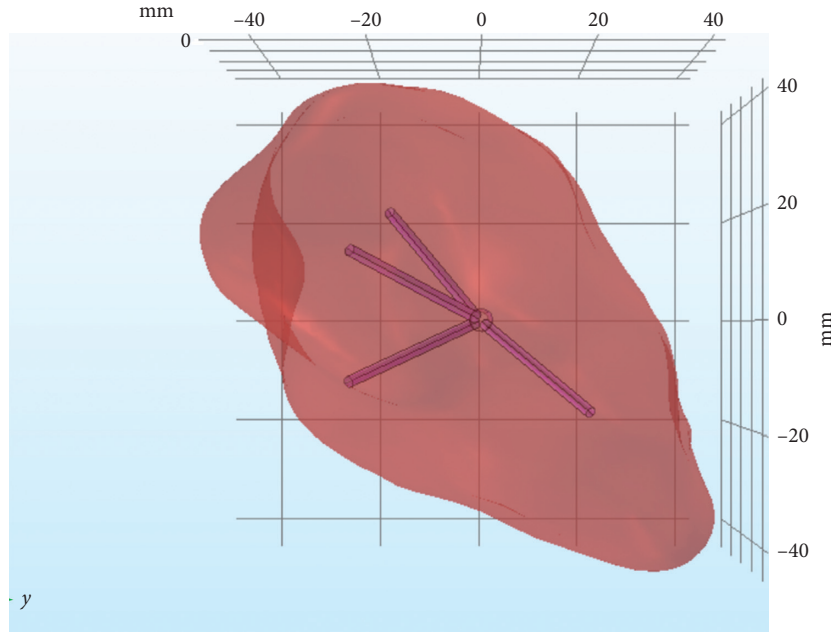
FIGURE 17: Front view of hematoma simulation.

The long-axis vector obtained by the initial long-axis algorithm $\mathbf{t}_1 = A_{s1} - A_{e1}$.

The long-axis vector obtained by optimizing the long-axis algorithm $\mathbf{t}_2 = A_{s2} - A_{e2}$.

Let $\varepsilon = 0.05$, and there are

$$
\begin{cases}
A_{s1} - A_{s2} < \varepsilon, \\
\\
A_{e1} - A_{e2} < \varepsilon, \\
\\
\arccos\left(\dfrac{\mathbf{t}_1 \cdot \mathbf{t}_2}{|\mathbf{t}_1| \cdot |\mathbf{t}_2|}\right) < \varepsilon.
\end{cases}
\tag{18}
$$

Through testing, the positions and directions of the two endpoints of the long axis before and after optimization in this paper are within the error range, and the optimized long-axis extraction algorithm has high computational efficiency, which reduces the preoperative planning time.

6. Conclusion

In this paper, the traditional drainage tube was optimized into an adaptive bifurcation drainage tube that could be customized according to different hematoma conditions. It makes the introduction of the hemolytic agent and the derivation of hematoma fluid precise. CT data are obtained from patients with intracranial hematoma to establish a three-dimensional hematoma model and simplify the hematoma surface hierarchy; then, the surface point cloud of hematoma was extracted; using long-axis extraction algorithm, locate the location of the main drainage tube. Accurately determine the entrance and direction of the puncture of the main drainage tube, using the Eight Diagrams algorithm and discriminating the internal data sets of hematomas and the visual processing.

The absorption points are determined by K-means clustering analysis algorithm; among them, the number of absorption points can be calculated according to the shape of hematoma. The telescopic direction and length of the subtube were obtained by connecting the absorption point and the bifurcation point. Based on this, the self-adaptive bifurcation drainage tube model was designed and finally applied to the puncture and drainage of intracranial hematoma. The algorithm can accurately determine the puncture point, the puncture path, and the location and number of subdrainage tubes according to the geometric characteristics of hematoma, achieve a uniform and accurate drug administration and drainage of intracranial hematoma, and accelerate the dissolution and drainage speed of hematoma. The adaptive bifurcation algorithm proposed in this paper is based on the idealized state, and it is necessary to consider the distribution of peripheral nerves and other important parts of intracranial hematoma in the application.

The application of adaptive bifurcated drainage tubes can effectively shorten the operative time of patients, reduce intraoperative blood loss, improve the hematoma clearance rate, and improve the neurological function and prognosis of patients, with accurate, minimally invasive, and safe effects [16]. It has clinical significance and application value for the medical treatment of intracranial hematoma and provides preoperative simulation. It can promote the subsequent hematoma deformation research and visualization analysis and provide important guidance and value for the formulation of a puncture surgery plan and the reduction of surgical risk.

Data Availability

The data used to support the findings of this study are restricted by the Tangshan Gongren Hospital in order to

protect patient privacy. The data are available from the Tangshan Gongren Hospital for researchers who meet the criteria for access to confidential data.

Conflicts of Interest

The authors declare that they have no conflicts of interest.

Acknowledgments

References

[1] Y. B. Li, X. Qu, S. W. Wang et al., "Analysis of the short-term effects of neuroendoscopy and minimally invasive puncture in the treatment of hypertensive cerebral hemorrhage" China," *Journal of Cerebrovascular Diseases*, vol. 17, no. 3, pp. 135–141, 2020.

[2] X. Y. Yang and J. D. Jing, "Observation on the efficacy of minimally invasive hematoma puncture removal in the treatment of hypertensive intracerebral hemorrhage and its effect on patients," *Quality of Life Medicine and Clinic in China*, vol. 20, no. 19, pp. 3262–3264, 2020.

[3] Y. Yu, X. C. Yi, T. Dong et al., "Efficacy and safety of neuronavigation-guided puncture and drainage of hematoma and conservative treatment for supratentorial hypertensive intracerebral hemorrhage with small hematoma," *Guizhou Medicine*, vol. 44, no. 9, pp. 1377–1379, 2020.

[4] Y. Zhu, M. Bao, M. Jiang, J. Chang, and J. Cui, "Visual analysis of flow and diffusion of hemolytic agents and hematomas," *Visual Computing for Industry, Biomedicine, and Art*, vol. 4, no. 1, p. 3, 2021.

[5] J. Z. Cui and Y. Cui, "The multifunctional drainage tube with multi-tube for intracranial hematoma," Springer, Berlin, Germany, CN Patent CN208405725U, 2019.

[6] Q. Pan, W. Zhu, X. Zhang, J. Chang, and J. Cui, "Research on a bifurcation location algorithm of a drainage tube based on 3D medical images," *Visual Computing for Industry, Biomedicine, and Art*, vol. 3, no. 1, p. 2, 2020.

[7] X. L. Zhang, K. X. Zhang, Q. L. Pan, and J. C. Chang, "Three-dimensional reconstruction of medical images based on 3D slicer," *Complexity Health Science*, vol. 2, no. 1, pp. 1–12, 2019.

[8] S. Pszczolkowski, Z. K. Law, R. G. Gallagher et al., "Automated segmentation of haematoma and perihaematomal oedema in MRI of acute spontaneous intracerebral haemorrhage," *Computers in Biology and Medicine*, vol. 106, pp. 126–139, 2019.

[9] J. Zhang, C.-H. Yan, C.-K. Chui, and S.-H. Ong, "Fast segmentation of bone in CT images using 3D adaptive thresholding," *Computers in Biology and Medicine*, vol. 40, no. 2, pp. 231–236, 2010.

[10] L. M. Chen and A. H. Qin, "A new algorithm for simplification of 3D graphics," *Chinese Journal of Image and Graphics*, vol. 32, no. 1, pp. 77–80, 1997.

[11] M. Fort, J. A. Sellarès, and N. Valladares, "Nearest and farthest spatial skyline queries under multiplicative weighted euclidean distances," *Knowledge Based Systems*, vol. 104, Article ID 105299, 2019.

[12] S. S. Ravi, D. J. Rosenkrantz, and G. K. Tayi, "Heuristic and special case algorithms for dispersion problems," *Operations Research*, vol. 42, no. 2, 1994.

[13] Q. Q. Cheng, P. Y. Sun, C. S. Yang et al., "A morphing-based 3D point cloud reconstruction framework for medical image processing," *Computer Methods and Programs in Biomedicine*, vol. 70, 2020.

[14] S. Chakraborty and S. Das, "K-means clustering with a new divergence-based distance metric: convergence and performance analysis," *Pattern Recognition Letters*, vol. 100, pp. 67–73, 2017.

[15] R. Zhang, *Research on Triangular Mesh Model Simplification Algorithm Based on Quadratic Error Measurement*, Xihua University, Chengdu, China, 2018.

[16] M. Lu, H. Li, B. Wu, J. Wu et al., "Chinese multidisciplinary expert consensus on the diagnosis and treatment of spontaneous cerebral hemorrhage," *Chinese Journal of Neurosurgery*, vol. 31, no. 12, pp. 1189–1194, 2015.

Research Article

An Efficient Modified AZPRP Conjugate Gradient Method for Large-Scale Unconstrained Optimization Problem

Ahmad Alhawarat ⬤,[1,2] **Thoi Trung Nguyen,**[1,3] **Ramadan Sabra,**[4] **and Zabidin Salleh** ⬤[5]

[1]*Division of Computational Mathematics and Engineering, Institute for Computational Science, Ton Duc Thang University, Ho Chi Minh City, Vietnam*
[2]*Faculty of Mathematics and Statistics, Ton Duc Thang University, Ho Chi Minh City, Vietnam*
[3]*Faculty of Civil Engineering, Ton Duc Thang University, Ho Chi Minh City, Vietnam*
[4]*Department of Mathematics, Faculty of Science, Jazan University, Jazan, Saudi Arabia*
[5]*Department of Mathematics, Faculty of Ocean Engineering Technology and Informatics, Universiti Malaysia Terengganu, Kuala Nerus 21030, Terengganu, Malaysia*

Correspondence should be addressed to Zabidin Salleh; zabidin@umt.edu.my

To find a solution of unconstrained optimization problems, we normally use a conjugate gradient (CG) method since it does not cost memory or storage of second derivative like Newton's method or Broyden–Fletcher–Goldfarb–Shanno (BFGS) method. Recently, a new modification of Polak and Ribiere method was proposed with new restart condition to give a so-call AZPRP method. In this paper, we propose a new modification of AZPRP CG method to solve large-scale unconstrained optimization problems based on a modification of restart condition. The new parameter satisfies the descent property and the global convergence analysis with the strong Wolfe-Powell line search. The numerical results prove that the new CG method is strongly aggressive compared with CG_Descent method. The comparisons are made under a set of more than 140 standard functions from the CUTEst library. The comparison includes number of iterations and CPU time.

1. Introduction

The conjugate gradient (CG) method aims to find a solution of optimization problems without constraint. Suppose that the following optimization problem is considered:

$$\min f(x), \quad x \in \mathbb{R}^n, \tag{1}$$

where $f: \mathbb{R}^n \longrightarrow \mathbb{R}$ is continuous, the function is differentiable, and the gradient $\nabla f(x)$ is available. The iterative method is given by the following sequence:

$$x_{k+1} = x_k + \alpha_k d_k, \quad k = 1, 2, \ldots, \tag{2}$$

where x_k is the starting point and $\alpha_k > 0$ is a step length. The search direction d_k of the CG method is defined as follows:

$$d_k = \begin{cases} -\nabla f(x), & \text{if } k = 1, \\ -\nabla f(x) + \beta_k d_{k-1}, & \text{if } k \geq 2, \end{cases} \tag{3}$$

where $\nabla f(x) = g(x_k)$ and β_k is a parameter.

To obtain the step length, we normally use the inexact line search, since the exact line search which is defined as follows,

$$f(x_k + \alpha_k d_k) = \min f(x_k + \alpha d_k), \quad \alpha > 0, \tag{4}$$

requires many iterations to obtain the step length. Normally, we use the strong version of Wolfe-Powell (SWP) [1, 2] line search which is given by

$$f(x_k + \alpha_k d_k) \leq f(x_k) + \delta \alpha_k g_k^T d_k, \tag{5}$$

$$\left| \nabla f(x_k + \alpha_k d_k)^T d_k \right| \leq \sigma \left| g_k^T d_k \right|, \tag{6}$$

where $0 < \delta < \sigma < 1$.

The weak Wolfe-Powell (WWP) line search is defined by (5) and

$$\nabla f(x_k + \alpha_k d_k)^T d_k \geq \sigma g_k^T d_k, \tag{7}$$

where $\nabla f = g_k = g(x_k)$. The famous parameters of β_k are the Hestenes–Stiefel (HS) [3], Fletcher–Reeves (FR) [4], and Polak–Ribière–Polyak (PRP) [5] formulas, which are given by

$$\beta_k^{HS} = \frac{g_k^T y_k}{d_{k-1}^T y_k},$$

$$\beta_k^{FR} = \frac{g_k^T g_k}{\|g_{k-1}\|^2}, \tag{8}$$

$$\beta_k^{PRP} = \frac{g_k^T y_k}{\|g_{k-1}\|^2},$$

where $y_k = g_k - g_{k-1}$.

Powell [6] shows that there exists a nonconvex function such that the PRP method does not globally converge. Gilbert and Nocedal [7] show that if $\beta_k^{PRP+} = \max\{0, \beta_k^{PRP}\}$ with the WWP and the descent property is satisfied, then it is globally convergent.

Al-Baali [8] proved that the CG method with FR coefficient is convergent with SWP line search when $\sigma \leq 1/2$. Hager and Zhang [9, 10] presented a new CG parameter with descent property, i.e., $g_k^T d_k \leq -(7/8)\|g_k\|^2$. This formula is given as follows:

$$\beta_k^{HZ} = \max\{\beta_k^N, \eta_k\}, \tag{9}$$

where $\beta_k^N = (1/d_k^T y_k)(y_k - 2d_k(\|y_k\|^2/d_k^T y_k))^T g_k$; $\eta_k = -(1/\|d_k\|\min\{\eta, \|g_k\|\})$; and $\eta > 0$ is a constant. In the numerical experiments, they set $\eta = 0.01$ in (9). Al-Baali et al. [11] compared β_k^{HZ} with a new three-term CG method (G3TCG).

Regarding the speed, memory requirements, number of iterations, function evaluations, gradient evaluations, and robustness to solve unconstrained optimization problems which have prompted the development of the CG method, the readers are advised to refer references [10–15] for more information on these new formulas.

2. The New Formula and the Algorithm

Alhawarat et al. [15] presented the following simple formula:

$$\beta_k^{AZPRP} = \begin{cases} \dfrac{\|g_k\|^2 - \mu_k |g_k^T g_{k-1}|}{\|g_{k-1}\|^2}, & \text{if } \|g_k\|^2 > \mu_k |g_k^T g_{k-1}|, \\ \\ 0, & \text{otherwise.} \end{cases} \tag{10}$$

Dai and Laio [12] presented the following formula:

$$\beta_k^{DL+} = \max\{\beta_k^{HS}, 0\} - t\frac{g_k^T s_{k-1}}{d_{k-1}^T y_{k-1}}, \tag{11}$$

where $s_{k-1} = x_k - x_{k-1}$ and $t \geq 0$.

The new formula is a modification of β_k^{AZPRP} and β_k^{DL+} is defined as follows:

$$\beta_k^A = \begin{cases} \dfrac{\|g_k\|^2 - \mu_k |g_k^T s_{k-1}|}{\|g_{k-1}\|^2}, & \text{if } \|g_k\|^2 > \mu_k |g_k^T s_{k-1}|, \\ \\ -t\dfrac{g_k^T s_{k-1}}{d_{k-1}^T y_{k-1}}, & \text{otherwise,} \end{cases} \tag{12}$$

where $\mu_k = (\|s_{k-1}\|/\|y_{k-1}\|)$ and $t > 0$.

We obtain the following relations (Algorithm 1):

$$\beta_k^A \geq 0,$$

$$\beta_k^A \leq \frac{\|g_k\|^2 - \mu_k |g_k^T s_{k-1}|}{\|g_{k-1}\|^2} \leq \frac{\|g_k\|^2}{\|g_{k-1}\|^2} = \beta_k^{FR}. \tag{13}$$

3. Convergence Analysis of Coefficient β_k^A with CG Method

Assumption 1

(A) The level set $\Psi = \{x | f(x) \leq f(x_1)\}$ is bounded, that is, a positive constant T exists such that

$$\|x\| \leq T, \quad \forall x \in \Psi. \tag{14}$$

(B) In some neighbourhoods N of Ψ, f is continuous and the gradient is available and its gradient is Lipschitz continuous; that is, for all $x, y \in N$, there exists a constant $L > 0$ such that

$$\|g(x) - g(y)\| \leq L\|x - y\|. \tag{15}$$

This assumption shows that there exists a positive constant B such that

$$\|g(u)\| \leq B, \quad \forall u \in N. \tag{16}$$

The descent condition

$$g_k^T d_k \leq -\|g_k\|^2, \quad \forall k \geq 1. \tag{17}$$

(17) plays an important role in the CG method. The sufficient descent condition proposed by Al-Baali [8] is a modification of (17) as follows:

$$g_k^T d_k \leq -c\|g_k\|^2, \quad \forall k \geq 1, \tag{18}$$

where $c \in (0, 1)$. Note that the general form of the sufficient descent condition is (18) with $c > 0$.
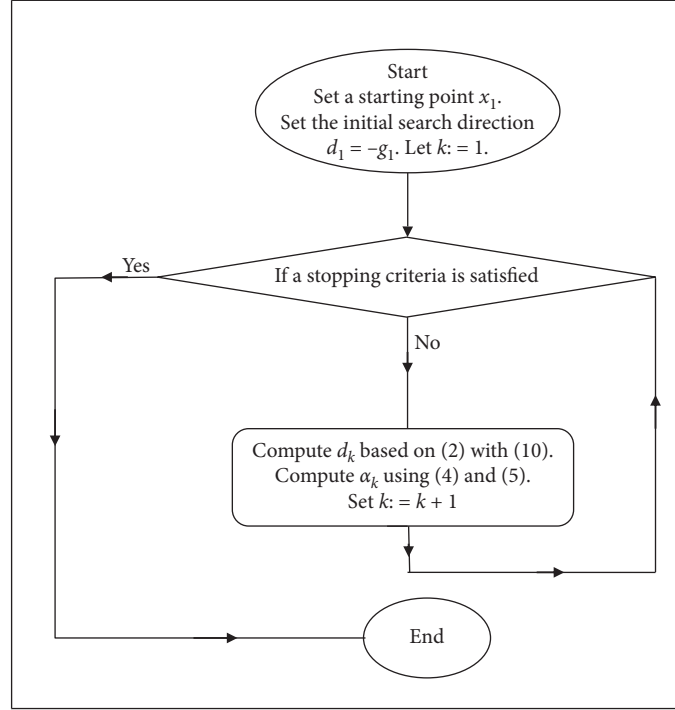
ALGORITHM 1: Steps of CG method with new modification to obtain the stationary point of functions.

3.1. Global Convergence for β_k^A with the SWP Line Search.
The following theorem demonstrates that β_k^A ensures that the sufficient descent condition (21) is satisfied with the SWP line search.

The following theorem shows that β_k^A satisfies the descent condition. The proof is similar to that presented in [8].

Theorem 1. *Let $\{g_k\}$ and $\{d_k\}$ be generated using (2), (3), and $\beta_k^A = (\|g_k\|^2 - \mu_k |g_k^T s_{k-1}| / \|g_{k-1}\|^2)$, where α_k is computed by the SWP line search (5) and (6). If $\sigma \in (0, 1/2]$, then the sufficient descent condition (18) holds.*

Algorithm 1 shows the steps to obtain the solution of optimization problem using strong Wolfe-Powell line search.

Descent condition is (18) with c > 0.

Proof. By multiplying () by g_k^T, we obtain

$$g_k^T d_k = g_k^T \left(-g_k^T + \beta_k d_{k-1} \right) = -\|g_k\|^2 + \beta_k g_k^T d_{k-1}. \quad (19)$$

Divide (19) by $\|g_k\|^2$; using

$$\left| \nabla f \left(x_k + \alpha_k d_k \right)^T d_k \right| \le \sigma \left| g_k^T d_k \right|, \quad (20)$$

and (12), we obtain

$$-1 + \sigma \frac{g_{k-1}^T d_{k-1}}{\|g_{k-1}\|^2} \le \frac{g_k^T d_k}{\|g_k\|^2} \le -1 - \sigma \frac{g_{k-1}^T d_{k-1}}{\|g_{k-1}\|^2}. \quad (21)$$

From (3), we obtain $g_1^T d_1 = -\|g_1\|^2$. Assume that it is true until $k - 1$, i.e., $g_i^T d_i < 0$, for $i = 1, 2, \ldots, k - 1$. Repeating the process for (21), we obtain

$$-\sum_{j=0}^{k-1} \sigma^j \le \frac{g_k^T d_k}{\|g_k\|^2} \le -2 + \sum_{j=0}^{k-1} \sigma^j. \quad (22)$$

As

$$\sum_{j=0}^{k-1} (\sigma)^j < \frac{1 - (\sigma)^k}{1 - \sigma}, \quad (23)$$

hence,

$$-\frac{1 - (\sigma)^k}{1 - \sigma} \le \frac{g_k^T d_k}{\|g_k\|^2} \le -2 + \frac{1 - (\sigma)^k}{1 - \sigma}, \quad (24)$$

and when $\sigma \le (1/2)$, we obtain $(1 - (\sigma)^k / 1 - \sigma) < 2$. Let $c = 2 - (1 - (\sigma)^k / 1 - \sigma)$, then

$$c - 2 \le \frac{g_k^T d_k}{\|g_k\|^2} \le -c. \quad (25)$$

The proof is complete. □

Theorem 2. *Let $\{g_k\}$ and $\{d_k\}$ be obtained by using (2), (3), and $\beta_k^A = -t \left(g_k^T s_{k-1} / d_{k-1}^T y_{k-1} \right)$ where α_k is computed by SWP line search (5) and (6), then the descent condition holds.*

Proof

$$\beta_k^{\text{DL-HS}} = -\mu_k \frac{g_k^T s_{k-1}}{d_{k-1}^T y_{k-1}}. \quad (26)$$

By multiplying (3) by g_k^T, and substituting β_k^A, we obtain

$$g_k^T d_k = -\|g_k\|^2 - \mu_k \frac{\alpha_{k-1} g_k^T d_{k-1}}{d_{k-1}^T y_{k-1}} g_k^T d_{k-1}$$

$$= -\|g_k\|^2 - \mu_k \frac{\alpha_{k-1} \|g_k^T d_{k-1}\|^2}{d_{k-1}^T y_{k-1}} < 0, \tag{27}$$

which completes the proof.

Zoutendijk [16] presented a useful lemma for global convergence property of the CG method. The condition is given as follows. □

Lemma 1. *Let Assumption 1 hold and consider any method in the form of (2) and (3), where α_k is obtained by the WWP line search (6) and (7), in which the search direction is descent. Then, the following condition holds:*

$$\sum_{k=0}^{\infty} \frac{\left(g_k^T d_k\right)^2}{\|d_k\|^2} < \infty. \tag{28}$$

Theorem 3. *Suppose Assumption 1 holds. Consider any form of equations (2) and (3), with the new formula (12), in which α_k is obtained from the SWP line search (5) and (6) with $\sigma \le 1/2$. Then,*

$$\liminf_{k \to \infty} \|g_k\| = 0. \tag{29}$$

The proof is similar to that presented in [8].

Proof. We will prove the theorem by contradiction. Assume that the conclusion is not true, then a constant $\varepsilon > 0$ exists such that

$$\|g_k\| \ge \varepsilon, \quad \forall k \ge 1. \tag{30}$$

Squaring both sides of equation (3), we obtain

$$\|d_k\|^2 = \|g_k\|^2 - 2\beta_k g_k^T d_{k-1} + \beta_k^2 \|d_{k-1}\|^2. \tag{31}$$

Divide (31) by $\|g_k\|^4$, we get

$$\frac{\|d_k\|^2}{\|g_k\|^4} = \frac{1}{\|g_k\|^2} - \frac{2\beta_k g_k^T d_{k-1}}{\|g_k\|^4} + \frac{\beta_k^2 \|d_{k-1}\|^2}{\|g_k\|^4}. \tag{32}$$

Using (6), (12), and (32), we obtain

$$\frac{\|d_k\|^2}{\|g_k\|^4} \le \frac{\|d_{k-1}\|^2}{\|g_{k-1}\|^4} + \frac{1}{\|g_k\|^2} + \frac{2\sigma|g_{k-1}^T d_{k-1}|}{\|g_{k-1}\|^2 \|g_k\|^2} \le \frac{\|d_{k-1}\|^2}{\|g_{k-1}\|^4} + \frac{1 + 2\sigma(2-c)}{\|g_k\|^2}. \tag{33}$$

Repeating the process for (33) and using the relationship $(1/\|g_1\|) = (1/\|d_1\|)$ yields

$$\frac{\|d_k\|^2}{\|g_k\|^4} \le (1 + 2\sigma(2-c)) \sum_{i=1}^{k} \frac{1}{\|g_i\|^2}. \tag{34}$$

From (33), we obtain

$$\frac{\|g_k\|^4}{\|d_k\|^2} \ge \frac{\varepsilon^2}{k(1 + 2\sigma(2-c))}. \tag{35}$$

Therefore,

$$\sum_{k=0}^{\infty} \frac{\|g_k\|^4}{\|d_k\|^2} = \infty. \tag{36}$$

This result contradicts (32), thus $\liminf_{k \to \infty} \|g_k\| = 0$. The proof is complete. □

4. Numerical Results

To investigate the effectiveness of the new parameter, several test problems in Table 1 from CUTEst [17] are chosen. We performed a comparison with the CG_Descent 5.3 based on the CPU time and the number of iterations. We employed the SWP line search with the line as mentioned in [1, 2] with $\delta = 0.01$ and $\sigma = 0.1$. The modified CG_Descent 6.8 where the memory (mem) equals zero is employed to obtain all results. The code can be downloaded from Hager web pagehttp://users.clas.ufl.edu/hager/papers/Software/.

The CG_Descent 5.3 results are obtained by run CG_Descent 6.8 with memory which equals zero. The host computer is an AMD A4-7210 with RAM 4 GB. The results are shown in Figures 1 and 2 in which a performance measure introduced by Dolan and More [18] was employed. As shown in Figure 1, formula A strongly outperforms over CG_Descent in number of iterations. In Figure 2, we notice that the new CG formula A is strongly competitive with CG_Descent.

4.1. Multimodal Function with Its Graph. In this section, we present six-hump camel back function, which is a multimodal function to test the efficiency of the optimization algorithm. The function is defined as follows:

$$\text{functions} :\cdot f(x) = \left(4 - 2.1x_1^2 + \frac{x_1^4}{3}\right)x_1^2 + x_1 x_2 + \left(-4 + 4x_2^2\right)x_2^2. \tag{37}$$

The number of variables (n) equals 2. This function has six local minima, with two of them being global. Thus, this function is a multimodal function usually used to test global minima. Global minima are $x_1^* = (-0.0898, 0.7126)$ and $x_2^* = (0.0898, -0.7126)$. The function value is $f(x^*) = -1.0316$. As its name describes, this function looks like the back of an upside down camel with six humps (see Figure 3 for a three-dimensional graph); for more information about two-dimensional functions, the reader can refer to [19].

Finally, note that CG method can be applied in image restoration problems and neural network and others. For more information, the reader can refer to [20, 21].

TABLE 1: The test functions.

Function	Dimension	CG_Descent 5.3		β_k^A	
		Number of iterations	CPU time	Number of iterations	CPU time
AKIVA	2	10	0.02	8	0.02
ALLINITU	4	12	0.02	9	0.02
ARGLINA	200	1	0.02	1	0.02
ARGLINB	200	5	0.02	6	0.11
ARWHEAD	5000	7	0.02	6	0.03
BARD	3	16	0.02	12	0.02
BDQRTIC	5000	136	0.58	161	0.75
BEALE	2	15	0.02	11	0.02
BIGGS6	6	27	0.02	24	0.02
BOX3	3	11	0.02	10	0.02
BOX	1000	8	0.08	7	0.08
BRKMCC	2	5	0.02	5	0.02
BROWNAL	200	9	0.02	9	0.02
BROWNBS	2	13	0.02	10	0.02
BROWNDEN	4	16	0.02	16	0.02
BROYDN7D	5000	1411	5.47	64	0.37
BRYBND	5000	85	0.38	39	0.22
CHAINWOO	4000	318	0.866	379	1.08
CHNROSNB	50	287	0.02	340	0.02
CLIFF	2	18	0.02	10	0.02
COSINE	10000	11	0.19	14	0.26
CRAGGLVY	5000	103	0.45	104	0.48
CUBE	2	32	0.02	17	0.02
CURLY10	10000	47808	173.7	42454	145.16
CURLY20	10000	66587	383.94	67279	366.03
CURLY30	10000	79030	639.63	74375	509.59
DECONVU	63	400	$2.00E-02$	227	0.02
DENSCHNA	2	9	0.02	6	0.02
DENSCHNB	2	7	0.02	6	0.02
DENSCHNC	2	12	0.02	11	0.02
DENSCHND	3	47	0.02	14	0.02
DENSCHNE	3	18	0.02	12	0.02
DENSCHNF	2	8	0.02	9	0.02
DIXMAANA	3000	7	0.02	6	0.02
DIXMAANB	3000	6	0.02	6	0.02
DIXMAANC	3000	6	0.02	6	0.02
DIXMAAND	3000	7	0.02	8	0.02
DIXMAANE	3000	222	0.33	218	0.33
DIXMAANF	3000	161	0.13	116	0.09
DIXMAANG	3000	157	0.12	173	0.14
DIXMAANH	3000	173	0.22	190	0.2
DIXMAANI	3000	3856	4.25	3160	3.34
DIXMAANJ	3000	327	0.36	360	0.39
DIXMAANK	3000	283	0.28	416	0.36
DIXMAANL	3000	237	0.2	399	0.36
DIXON3DQ	10000	10000	19.12	10000	19.12
DJTL	2	82	0.02	75	0.02
DQDRTIC	5000	5	0.02	5	0.02
DQRTIC	5000	17	0.03	15	0.03
EDENSCH	2000	26	0.03	32	0.05
EG2	1000	5	0.02	3	0.02
EIGENALS	2550	10083	178.36	7247	133.4
EIGENBLS	2550	15301	237	18846	290.3
EIGENCLS	2652	10136	174.19	11152	186.86
ENGVAL1	5000	27	0.06	23	0.12
ENGVAL2	3	26	0.02	26	0.02
ERRINROS	50	380	0.02	95504	2.36

TABLE 1: Continued.

Function	Dimension	CG_Descent 5.3		β_k^A	
		Number of iterations	CPU time	Number of iterations	CPU time
EXPFIT	2	13	0.02	9	0.02
EXTROSNB	1000	3808	1.25	2370	0.87
FLETCBV2	5000	1	0.02	1	0.02
FLETCHCR	1000	152	0.05	84	0.05
FMINSRF2	5625	346	$1.09E + 00$	485	1.4
FMINSURF	5625	473	1.51	542	1.64
FREUROTH	5000	25	0.11	29	0.19
GENROSE	500	1078	0.17	2098	0.45
GROWTHLS	3	156	0.02	109	0.02
GULF	3	37	0.02	33	0.02
HAIRY	2	36	0.02	17	0.02
HATFLDD	3	20	0.02	17	0.02
HATFLDE	3	30	0.02	13	0.02
HATFLDFL	3	39	0.02	21	0.02
HEART6LS	6	684	0.02	375	0.02
HEART8LS	8	249	0.02	253	0.02
HELIX	3	23	0.02	23	0.02
HIELOW	3	14	0.02	13	0.05
HILBERTA	2	2	0.02	2	0.02
HILBERTB	10	4	0.02	4	0.02
HIMMELBB	2	10	0.02	4	0.02
HIMMELBF	4	26	0.02	23	0.02
HIMMELBG	2	8	0.02	7	0.02
HIMMELBH	2	7	0.02	5	0.02
HUMPS	2	52	0.02	45	0.02
JENSMP	2	15	0.02	12	0.02
JIMACK	35449	8314	1182.25	7297	1030.3
KOWOSB	4	17	0.02	16	0
LIARWHD	5000	21	0.03	15	0.05
LOGHAIRY	2	27	0.02	26	0.02
MANCINO	100	11	0.08	11	0.08
MARATOSB	2	1145	0.02	589	0.02
MEXHAT	2	20	0.02	14	0.02
MOREBV	5000	161	0.41	161	0.38
MSQRTALS	1024	2905	8.64	2788	9.08
MSQRTBLS	1024	2280	6.91	2181	6.84
NCB20B	500	2035	46.36	4181	70.16
NCB20	5010	879	11.83	959	13
NONCVXU2	5000	6610	15.89	6379	15.92
NONDIA	5000	7	0.03	7	0.03
NONDQUAR	5000	1942	2.45	3058	3.88
OSBORNEA	5	94	0.02	82	0.02
OSBORNEB	11	62	0.02	57	0.02
PALMER1C	8	11	0.02	12	0.02
PALMER1D	7	11	0.02	10	0.02
PALMER2C	8	11	0.02	11	0.02
PALMER3C	8	11	0.02	11	0.02
PALMER4C	8	11	0.02	11	0.02
PALMER5C	6	6	0.02	6	0.02
PALMER6C	8	11	0.02	11	0.02
PALMER7C	8	11	0.02	11	0.02
PALMER8C	8	11	0.02	11	0.02
PARKCH	15	672	29.45	823	39.39
PENALTY1	1000	28	0.02	41	0.02
PENALTY2	200	191	0.05	200	0.03
PENALTY3	200	99	1.78	88	1.98

TABLE 1: Continued.

		CG_Descent 5.3		β_k^A	
Function	Dimension	Number of iterations	CPU time	Number of iterations	CPU time
POWELLSG	5000	26	0.02	27	0.05
POWER	10000	372	0.76	543	1.2
QUARTC	5000	17	0.03	15	0.02
ROSENBR	2	34	0.02	28	0.02
S308	2	8	0.02	7	0.02
SCHMVETT	5000	43	0.23	40	0.27
SENSORS	100	21	0.25	50	0.8
SINEVAL	2	64	0.02	46	0.02
SINQUAD	5000	14	0.09	15	0.08
SISSER	2	6	0.02	5	0.02
SNAIL	2	100	0.02	61	0.02
SPARSINE	5000	18358	73	21328	83
SPARSQUR	10000	28	0.31	35	0.98
SPMSRTLS	4999	203	0.59	219	0.61
SROSENBR	5000	11	0.02	9	0.03
STRATEC	10	462	19.98	170	6.23
TESTQUAD	5000	1577	1.52E + 00	1573	1.42
TOINTGOR	50	135	0.02	120	0.02
TOINTGSS	5000	4	0.02	5	0.02
TOINTPSP	50	143	0.02	157	0.02
TOINTQOR	50	29	0.02	29	0.02
TQUARTIC	5000	14	0.03	11	0.03
TRIDIA	5000	782	0.84	783	1.11
VAREIGVL		23	0.02	24	0.02
VIBRBEAM	50	138	0.02	98	0.02
WATSON	8	49	0.02	61	0.02
WOODS	12	22	0.06	22	0.03
YFITU	4000	84	0.02	68	0.02
ZANGWIL2	3	1	0.02	1	0.02
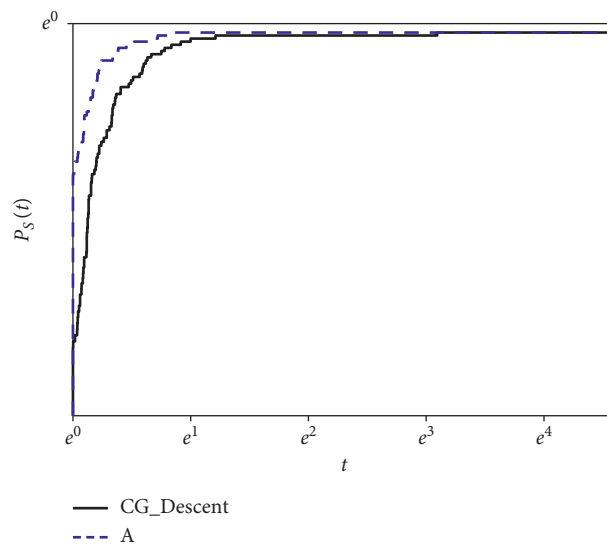
FIGURE 1: Performance measure based on the number of iterations.
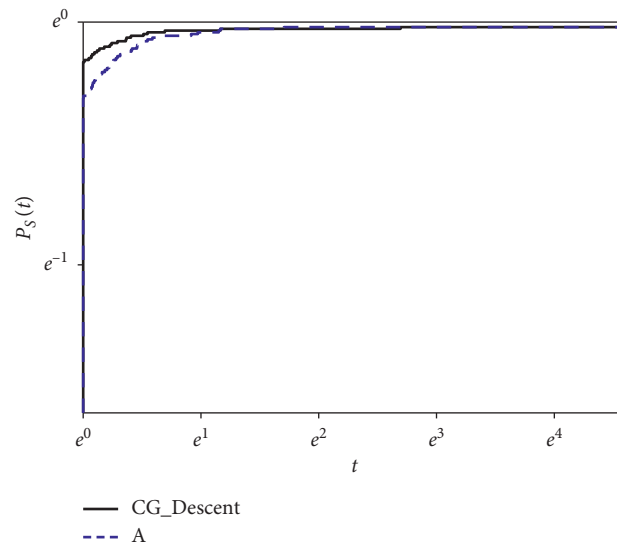
Figure 2: Performance measure based on the CPU time.
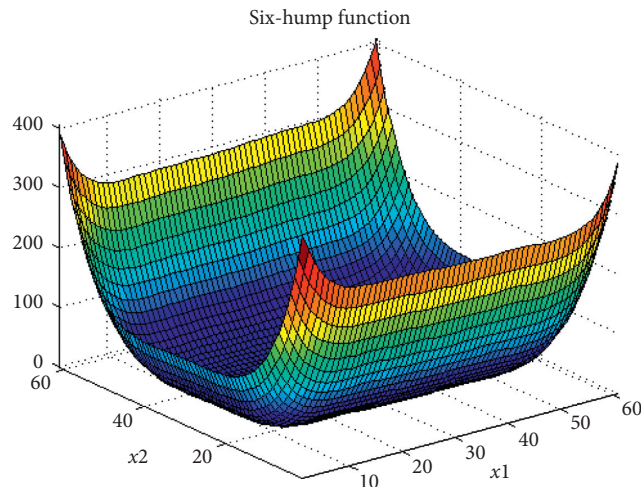
Figure 3: Six-hump camel back function in 3D.

5. Conclusions

In this study, a modified version of the CG algorithm (A) is suggested and its performance is investigated. The modified formula is restarted based on the value of the Lipchitz constant. The global convergence is established by using SWP line search. Our numerical results show that the new coefficient produces efficient and competitive results compared with other methods, such as CG_Descent 5.3. In the future, an application of the new version of CG method will be combined with feed-forward neural network (back-propagation (BP) algorithm) to improve the training process and produce fast training multilayer algorithm. This will help in reducing time needed to train neural network when the training samples are massive.

Data Availability

The data used to support the findings of this study are included within the article.

Conflicts of Interest

The authors declare that they have no conflicts of interest regarding the publication of this paper.

Acknowledgments

References

[1] P. Wolfe, "Convergence conditions for ascent methods," *SIAM Review*, vol. 11, no. 2, pp. 226–235, 1969.

[2] P. Wolfe, "Convergence conditions for ascent methods. II: some corrections," *SIAM Review*, vol. 13, no. 2, pp. 185–188, 1971.

[3] E. Stiefel, "Methods of conjugate gradients for solving linear systems," *Journal of Research of the National Bureau of Standards*, vol. 49, pp. 409–435, 1952.

[4] R. Fletcher and C. M. Reeves, "Function minimization by conjugate gradients," *The Computer Journal*, vol. 7, no. 2, pp. 149–154, 1964.

[5] E. Polak and G. Ribiere, "Note sur la convergence de méthodes de directions conjuguées," *ESAIM: Mathematical Modelling and Numerical Analysis-Modélisation Mathématique et Analyse Numérique*, vol. 3, no. R1, pp. 35–43, 1969.

[6] M. J. Powell, "Nonconvex minimization calculations and the conjugate gradient method," in *Numerical Analysis*, pp. 122–141, Springer, Berlin, Heidelberg, 1984.

[7] J. C. Gilbert and J. Nocedal, "Global convergence properties of conjugate gradient methods for optimization," *SIAM Journal on Optimization*, vol. 2, no. 1, pp. 21–42, 1992.

[8] M. Al-Baali, "Descent property and global convergence of the fletcher-reeves method with inexact line search," *IMA Journal of Numerical Analysis*, vol. 5, no. 1, pp. 121–124, 1985.

[9] W. W. Hager and H. Zhang, "A new conjugate gradient method with guaranteed descent and an efficient line search," *SIAM Journal on Optimization*, vol. 16, no. 1, pp. 170–192, 2005.

[10] W. W. Hager and H. Zhang, "The limited memory conjugate gradient method," *SIAM Journal on Optimization*, vol. 23, no. 4, pp. 2150–2168, 2013.

[11] M. Al-Baali, Y. Narushima, and H. Yabe, "A family of three-term conjugate gradient methods with sufficient descent property for unconstrained optimization," *Computational Optimization and Applications*, vol. 60, no. 1, pp. 89–110, 2015.

[12] Y.-H. Dai and L. Z. Liao, "New conjugacy conditions and related nonlinear conjugate gradient methods," *Applied Mathematics and Optimization*, vol. 43, no. 1, pp. 87–101, 2001.

[13] M. Al-Baali, E. Spedicato, and F. Maggioni, "Broyden's quasi-Newton methods for a nonlinear system of equations and unconstrained optimization: a review and open problems," *Optimization Methods and Software*, vol. 29, no. 5, pp. 937–954, 2014.

[14] S. Babaie-Kafaki and R. Ghanbari, "A descent family of Dai-Liao conjugate gradient methods," *Optimization Methods and Software*, vol. 29, no. 3, pp. 583–591, 2014.

[15] A. Alhawarat, Z. Salleh, M. Mamat, and M. Rivaie, "An efficient modified Polak-Ribière-Polyak conjugate gradient method with global convergence properties," *Optimization Methods and Software*, vol. 32, no. 6, pp. 1299–1312, 2017.

[16] G. Zoutendijk, *Nonlinear Programming, Computational Methods*, pp. 37–86, Integer and Nonlinear Programming, North Holland, Amsterdam, 1970.

[17] I. Bongartz, A. R. Conn, N. Gould, and P. L. Toint, "CUTE," *ACM Transactions on Mathematical Software*, vol. 21, no. 1, pp. 123–160, 1995.

[18] E. D. Dolan and J. J. Moré, "Benchmarking optimization software with performance profiles," *Mathematical Programming*, vol. 91, no. 2, pp. 201–213, 2002.

[19] A. Alhawarat and Z. Salleh, "Modification of nonlinear conjugate gradient method with weak Wolfe-Powell line search," *Abstract and Applied Analysis*, vol. 2017, Article ID 7238134, 6 pages, 2017.

[20] G. Yuan, T. Li, and W. Hu, "A conjugate gradient algorithm and its application in large-scale optimization problems and image restoration," *Journal of Inequalities and Applications*, vol. 2019, no. 1, pp. 1–25, 2019.

[21] G. Yuan, J. Lu, and Z. Wang, "The modified PRP conjugate gradient algorithm under a non-descent line search and its application in the Muskingum model and image restoration problems," *Soft Computing*, vol. 25, no. 8, pp. 5867–5879, 2021.

Research Article

Linear Barycentric Rational Method for Two-Point Boundary Value Equations

Qian Ge [ID] [1,2] **and Xiaoping Zhang** [ID] [2]

[1]*School of Mathematics and Statistics, Shandong Normal University, Jinan 250358, China*
[2]*School of Science, Shandong Jianzhu University, Jinan 250101, China*

Correspondence should be addressed to Xiaoping Zhang; geqian@sdjzu.edu.cn

Linear barycentric rational method for solving two-point boundary value equations is presented. The matrix form of the collocation method is also obtained. With the help of the convergence rate of the interpolation, the convergence rate of linear barycentric rational collocation method for solving two-point boundary value problems is proved. Several numerical examples are provided to validate the theoretical analysis.

1. Introduction

The analysis of many physical phenomena and engineering problems can be reduced to solving the boundary value problem of differential equation, most of which need to be solved by the numerical method. The barycentric interpolation method is a high precision calculation method, and a strong form of collocation that relies on differential equation, which has been studied extensively by many scholars. The linear barycentric rational method (LBRM) [1–3] has been used to solve certain problems such as delay Volterra integro-differential equations [4], Volterra integral equations [5–7], biharmonic equation [8], beam force vibration equation [9], boundary value problems [10], heat conduction problems [11], plane elastic problems [12], incompressible plane elastic problems [13], nonlinear problems [14], and so on [1, 15].

In this article, we pay our attention to the numerical solution of two-point boundary value problems:

$$(\mathrm{Tu})(x) \coloneqq u''(x) + \mathrm{qu}(x) = f(x), \quad x \in (a,b), \quad (1)$$

$$u(a) = u_\ell, u(b) = u_r. \quad (2)$$

Let the interval $[a,b]$ be partitioned into n uniform part with $h = (b-a)/n$ and $x_0, x_1, \ldots, x_n$ with its related function $f(x_i)$, $i = 0, 1, \ldots, n$. For any $0 \le d \le n$, with

$P(x_i)$, $i = 0, 1, \ldots, n - d$, to be the interpolation function at the point $x_i, x_{i+1}, \ldots, x_{i+d}$, then we have $P_i(x_k) = f(x_k)$, $k = i, i+1, \ldots, i+d$, and

$$r(x) = \frac{\sum_{i=0}^{n-d} \lambda_i(x) P_i(x)}{\sum_{i=0}^{n-d} \lambda_i(x)}, \quad (3)$$

where

$$\lambda_i(x) = \frac{(-1)^i}{(x - x_i) \cdots (x - x_{i+d})}. \quad (4)$$

Change the polynomial $P_i(x)$ into the Lagrange interpolation form as

$$P_i(x) = \sum_{k=i}^{i+d} \prod_{j=i, j \ne k}^{i+d} \frac{x - x_j}{x_k - x_j} f_k. \quad (5)$$

Combining (7) and (5) together, we get

$$\sum_{i=0}^{n-d} \lambda_i(x) P_i(x) = \sum_{i=0}^{n-d} (-1)^i \sum_{k=i}^{i+d} \frac{1}{x - x_k} \prod_{i,j \ne k}^{i+d} \frac{1}{x_k - x_j} f_k = \sum_{k=0}^{n} \frac{w_k}{x - x_k} f_k, \quad (6)$$

where $w_k = \sum_{i \in J_k} (-1)^i \prod_{j=i, j \ne k}^{i+d} 1/(x_k - x_j)$ and $J_k = \{i \in I; k - d \le i \le k\}$.

Then we get

$$r(x) = \frac{\sum_{j=0}^{n}\left[w_j/(x-x_j)\right]f_j}{\sum_{j=0}^{n}w_j/(x-x_j)}, \tag{7}$$

where its basis function is

$$L_j(x) = \frac{w_j/(x-x_j)}{\sum_{k=0}^{n}w_k/(x-x_k)}. \tag{8}$$

For the equidistant point, its weight function is

$$w_j = (-1)^{n-j}C_n^j. \tag{9}$$

The Chebyshev point of the second kind is

$$x_j = \cos\frac{j\pi}{n}, j = 0, 1, \ldots, n, \tag{10}$$

and its weight function is

$$w_j = (-1)^j\delta_j, \delta_j = \begin{cases} \dfrac{1}{2}, & j = 0, n, \\[2mm] 1, & \text{ortherwise.} \end{cases} \tag{11}$$

Consider the barycentric interpolation function as

$$u_n(x) = \sum_{j=0}^{n}L_j(x)u_j, \tag{12}$$

and the numerical scheme is given as

$$\sum_{j=0}^{n}u_jL_j''(x) + q\sum_{j=0}^{n}u_jL_j(x) = f(x). \tag{13}$$

By using the notation of the differential matrix, equation (13) is denoted as matrices in the form of

$$\sum_{j=0}^{n}D_{ij}^{(2)}u_j + q\sum_{j=0}^{n}\delta_{ij}u_j = f(x_i), \tag{14}$$

where $i = 1, 2, \ldots, n$.

Equation (13) is written as matrices in the form of

$$\left[\mathbf{D}^{(2)} + \mathbf{qI}\right]\mathbf{u} = \mathbf{f}, \tag{15}$$

where $\mathbf{L} := \mathbf{D}^{(2)} + \mathbf{qI}, \mathbf{u} = [u_0, u_1, u_2, \ldots, u_n]^{\mathrm{T}}, \mathbf{D}^{(k)} = [D_{ij}^{(k)}]_{(n+1)\times(n+1)}$,

$$D_{ij}^{(1)} = \begin{cases} \dfrac{\omega_j/\omega_i}{x_i - x_j}, & i \neq j, \\[4mm] -\sum_{k\neq i}D_{ik}^{(1)}, & i = j, \end{cases} \tag{16}$$

$$D_{ij}^{(2)} = \begin{cases} 2D_{ij}^{(1)}\left(D_{ii}^{(1)} - \dfrac{1}{x_i - x_j}\right), & i \neq j, \\[4mm] -\sum_{k\neq i}D_{ik}^{(2)}, & i = j, \end{cases}$$

and $\mathbf{q} = \operatorname{diag}[q], f = [f(x_0), f(x_1), f(x_2), \ldots, f(x_n)]^{\mathrm{T}}$. Using interpolation formulas, boundary conditions can be discretized into

$$\sum_{j=0}^{n}D_{1j}^{(1)}u_j = a, \sum_{j=0}^{n}D_{nj}^{(1)}u_j = b. \tag{17}$$

2. Convergence and Error Analysis

With the error function of difference formula

$$e(x) := u(x) - r(x) = (x - x_i)\cdots(x - x_{i+d})[x_i, x_{i+1}, \ldots, x_{i+d}, x]f, \tag{18}$$

and

$$e(x) = \frac{\sum_{i=0}^{n-d}\lambda_i(x)(u(x) - P_i(x))}{\sum_{i=0}^{n-d}\lambda_i(x)} = \frac{A(x)}{B(x)} = O(h^{d+1}), \tag{19}$$

where $A(x) := \sum_{i=0}^{n-d}(-1)^i[x_i, \ldots, x_{i+d}, x]f, B(x) := \sum_{i=0}^{n-d}\lambda_i(x)$. Taking the numerical scheme

$$\sum_{j=0}^{n}y_jL_j''(x) + q\sum_{j=0}^{n}y_jL_j(x) = f(x). \tag{20}$$

Combining (20) and (1), we have

$$Te(x) := e''(x) + qe(x) = R_f(x), \tag{21}$$

where $R_f(x) = f(x) - f(x_k), k = 0, 1, 2, \ldots, n$.

The following Lemma has been proved by Jean-Paul Berrut in [13].

Lemma 1 (see [13]). *For $e(x)$ defined in (18), we have*

$$\begin{cases} |e(x)| \le Ch^{d+1}, & u \in C^{d+2}[a, b], \\ |e'(x)| \le Ch^d, & u \in C^{d+3}[a, b], \\ |e''(x)| \le Ch^{d-1}, & u \in C^{d+4}[a, b], d \ge 1. \end{cases} \tag{22}$$

Let $u(x)$ be the solution of (1) and $u_n(x)$ is the numerical solution, then we have

$$Tu_n(x_k) = f(x_k), \quad k = 0, 1, 2, \ldots, n, \tag{23}$$

and

$$\lim_{n\to\infty}u_n(x) = u(x). \tag{24}$$

The results can be obtained in the reference of [14].

Based on the above lemma, we derive the following theorem.

Theorem 1. *Let $u_n(x): Tu_n(x) = f(x), u_n^*(x): Tu_n^*(x) = f^*(x)$, and $f(x) \in C[a, b]$, we have*

$$|u_n(x) - u_n^*(x)| \le Ch^{d-1}. \tag{25}$$

Proof. As $\mathbf{L} := \mathbf{D}^{(2)} + \mathbf{QI}$, where

$$\mathbf{D}^2 = \begin{bmatrix} D_{00}^{(2)} & D_{01}^{(2)} & D_{02}^{(2)} & D_{03}^{(2)} & \cdots & D_{0n}^{(2)} \\ D_{10}^{(2)} & D_{11}^{(2)} & D_{12}^{(2)} & D_{13}^{(2)} & \cdots & D_{1n}^{(2)} \\ D_{20}^{(2)} & D_{21}^{(2)} & D_{22}^{(2)} & D_{23}^{(2)} & \cdots & D_{2n}^{(2)} \\ D_{30}^{(2)} & D_{31}^{(2)} & D_{32}^{(2)} & D_{33}^{(2)} & \cdots & D_{3n}^{(2)} \\ \cdots & \cdots & \cdots & \cdots & \cdots & \cdots \\ D_{n-1,0}^{(2)} & D_{n-1,1}^{(2)} & D_{n-1,2}^{(2)} & D_{n-2,3}^{(2)} & \cdots & D_{n-1,n}^{(2)} \\ D_{n0}^{(2)} & D_{n1}^{(2)} & D_{n2}^{(2)} & D_{n3}^{(2)} & \cdots & D_{nn}^{(2)} \end{bmatrix}, \quad (26)$$

and

$$\mathbf{L} := \mathbf{D}^2 + \mathbf{QI} = \begin{bmatrix} q + D_{00}^{(2)} & D_{01}^{(2)} & D_{02}^{(2)} & D_{03}^{(2)} & \cdots & D_{0n}^{(2)} \\ D_{10}^{(2)} & q + D_{11}^{(2)} & D_{12}^{(2)} & D_{13}^{(2)} & \cdots & D_{1n}^{(2)} \\ D_{20}^{(2)} & D_{21}^{(2)} & q + D_{22}^{(2)} & D_{23}^{(2)} & \cdots & D_{2n}^{(2)} \\ D_{30}^{(2)} & D_{31}^{(2)} & D_{32}^{(2)} & D_{33}^{(2)} & \cdots & D_{3n}^{(2)} \\ \cdots & \cdots & \cdots & \cdots & \cdots & \cdots \\ D_{n-1,0}^{(2)} & D_{n-1,1}^{(2)} & D_{n-1,2}^{(2)} & D_{n-2,3}^{(2)} & \cdots & D_{n-1,n}^{(2)} \\ D_{n0}^{(2)} & D_{n1}^{(2)} & D_{n2}^{(2)} & D_{n3}^{(2)} & \cdots & q + D_{nn}^{(2)} \end{bmatrix}.$$
$$(27)$$

Putting column 2, column 3, column n added to column 1, we have

$$\mathbf{D}^2 = \begin{bmatrix} 0 & D_{01}^{(2)} & D_{02}^{(2)} & D_{03}^{(2)} & \cdots & D_{0n}^{(2)} \\ 0 & D_{11}^{(2)} & D_{12}^{(2)} & D_{13}^{(2)} & \cdots & D_{1n}^{(2)} \\ 0 & D_{21}^{(2)} & D_{22}^{(2)} & D_{23}^{(2)} & \cdots & D_{2n}^{(2)} \\ 0 & D_{31}^{(2)} & D_{32}^{(2)} & D_{33}^{(2)} & \cdots & D_{3n}^{(2)} \\ 0 & \cdots & \cdots & \cdots & \cdots & \cdots \\ 0 & D_{n-1,1}^{(2)} & D_{n-1,2}^{(2)} & D_{n-2,3}^{(2)} & \cdots & D_{n-1,n}^{(2)} \\ 0 & D_{n1}^{(2)} & D_{n2}^{(2)} & D_{n3}^{(2)} & \cdots & D_{nn}^{(2)} \end{bmatrix}, \quad (28)$$

which means the matrix $\mathbf{D}^{(2)}$ is the singular matrix.
Similarly we have

$$\mathbf{L} = \begin{bmatrix} q & D_{01}^{(2)} & D_{02}^{(2)} & D_{03}^{(2)} & \cdots & D_{0n}^{(2)} \\ q & q + D_{11}^{(2)} & D_{12}^{(2)} & D_{13}^{(2)} & \cdots & D_{1n}^{(2)} \\ q & D_{21}^{(2)} & q + D_{22}^{(2)} & D_{23}^{(2)} & \cdots & D_{2n}^{(2)} \\ q & D_{31}^{(2)} & D_{32}^{(2)} & q + D_{33}^{(2)} & \cdots & D_{3n}^{(2)} \\ q & \cdots & \cdots & \cdots & \cdots & \cdots \\ q & D_{n-1,1}^{(2)} & D_{n-1,2}^{(2)} & D_{n-2,3}^{(2)} & \cdots & D_{n-1,n}^{(2)} \\ q & D_{n1}^{(2)} & D_{n2}^{(2)} & D_{n3}^{(2)} & \cdots & q + D_{nn}^{(2)} \end{bmatrix}, \quad (29)$$

and then we assume $|\mathbf{L}| \neq 0$ with $q \neq 0$, $u_n(x) = \sum_{j=0}^{n} L_j(x) f_j, u_n^*(x) = \sum_{j=0}^{n} L_j(x) f_j^*,$ where. $U_n = (f(x_0), f(x_1), \ldots, f(x_n))^T$ and $U_n^* = (f^*(x_0), f^*(x_1), \ldots, f^*(x_n))^T$.

By

$$U_n - U_n^* = \mathbf{L}^{-1}(\mathbf{L}U_n - F_n^*), \quad (30)$$

which means

$$u_n(x) - u_n^*(x) = \sum_{j=0}^{n} M_j(x) Te(x), \quad (31)$$

where $M_j(x)$ is the element of matrix $\mathbf{L}^{-1}$.
Then we have

$$\left| u_n(x) - u_n^*(x) \right| \leq \left| \sum_{j=0}^{n} M_j(x) \right| |Te(x)| \leq Ch^{d-1}. \quad (32)$$

The proof is completed.
We know that the central difference method can achieve quadratic convergence and the convergence order is the same as that of $d = 3$. When $d > 3$, the convergence of the barycentric rational method is better than that of the central difference method. □

3. Numerical Example

Example 1. Consider the two-point boundary value:

$$-y'' + 400y = -400 \cos^2 \pi x - 2\pi^2 \cos 2\pi x, \quad (33)$$

$$y(0) = y(1) = 0, \quad (34)$$

and its analysis solution is

$$y(x) = \frac{e^{-20}}{1 + e^{-20}} e^{20x} + \frac{1}{1 + e^{-20}} e^{-20x} - \cos^2 \pi x. \quad (35)$$

In this example, we consider the two-point boundary value equations with the boundary condition $y(0) = y(1) = 0$. In Table 1, the convergence rate of equidistant nodes with different d is $O(h^d)$; in Table 2, the convergence rate of the Chebyshev point of the second kind with different d is $O(h^{d+2})$, $d \geq 2$. From Theorem 1, the convergence rate is $O(h^{d-1})$, and there are no convergence rates as $d = 1$. Here the convergence rate is $O(h)$ and $O(h^2)$ in Tables 1 and 2 for $d = 1$, respectively, and we will give exact analysis in other paper.

Example 2. Consider the two-point boundary value.

$$y'' + y' \sin x + ye^x = -16\pi^2 \sin 4\pi x + 4\pi \sin x \cos 4\pi x$$
$$+ e^x(2 + \sin 4\pi x), \quad -1 < x < 1, \quad (36)$$

with the boundary condition

$$y(-1) + y'(-1) = 2 + 4\pi, y(1) + y'(1) = 2 + 4\pi, \quad (37)$$

and its analysis solution is

$$y(x) = 2 + \sin 4\pi x. \quad (38)$$

In this example, we consider the variable coefficient of two-point boundary value equations with the boundary

Table 1: Errors of the equidistant nodes with different d.

n	$d = 1$	$d = 2$	$d = 3$	$d = 4$	$d = 5$
10	$5.6796e-02$	$4.7174e-02$	$3.6770e-02$	$2.9692e-02$	$2.5240e-02$
20	$3.1866e-02$	$2.0707e-02$	$1.2295e-02$	$7.5473e-03$	$4.6949e-03$
40	$1.1899e-02$	$4.8530e-03$	$1.8024e-03$	$6.8958e-04$	$2.6519e-04$
80	$4.0465e-03$	$8.2037e-04$	$1.7027e-04$	$3.6416e-05$	$7.8060e-06$
160	$1.4721e-03$	$1.1821e-04$	$1.2993e-05$	$1.4706e-06$	$1.6657e-07$
320	$4.9182e-04$	$1.5796e-05$	$8.9500e-07$	$5.2131e-08$	$3.0430e-09$
640	$1.5719e-04$	$2.0375e-06$	$5.8674e-08$	$1.7409e-09$	$5.1202e-11$

Table 2: Errors of the Chebyshev point with different d.

n	$d = 1$	$d = 2$	$d = 3$	$d = 4$	$d = 5$
10	$4.7235e-02$	$3.4143e-02$	$2.3198e-02$	$1.0658e-02$	$4.2299e-03$
20	$2.0966e-02$	$4.9675e-03$	$2.3057e-03$	$1.5490e-03$	$1.0185e-03$
40	$5.0812e-03$	$3.3376e-04$	$7.5530e-05$	$3.1018e-05$	$1.2517e-05$
80	$1.2482e-03$	$2.0099e-05$	$2.1222e-06$	$4.5138e-07$	$9.5181e-08$
160	$2.9995e-04$	$1.2091e-06$	$6.1512e-08$	$6.5988e-09$	$6.9630e-10$
320	$7.3360e-05$	$7.3634e-08$	$1.8414e-09$	$1.0610e-10$	$2.8788e-10$
640	$1.8092e-05$	$4.5328e-09$	$5.7970e-11$	$1.5463e-10$	$6.0430e-09$

Table 3: Errors of the equidistant nodes with different d.

n	$d = 1$	$d = 2$	$d = 3$	$d = 4$	$d = 5$
10	$3.1903e+00$	$5.8183e+00$	$4.2584e+00$	$3.3515e+00$	$3.8150e+00$
20	$9.0854e-01$	$1.8487e-01$	$4.7472e-02$	$5.6182e-02$	$2.1227e-02$
40	$1.9690e-01$	$3.8711e-02$	$5.9273e-04$	$1.9234e-04$	$4.9300e-05$
80	$4.4235e-02$	$3.9481e-03$	$4.9399e-06$	$2.3577e-06$	$2.4228e-07$
160	$9.6887e-03$	$3.4240e-04$	$1.9523e-07$	$1.9939e-08$	$2.8181e-09$
320	$2.0060e-03$	$2.7549e-05$	$5.5624e-09$	$1.6331e-09$	$7.9052e-08$
640	$3.7877e-04$	$2.1177e-06$	$1.0976e-09$	$2.1374e-08$	$1.2137e-06$

Table 4: Errors of the Chebyshev point with different d.

n	$d = 1$	$d = 2$	$d = 3$	$d = 4$	$d = 5$
10	$1.3687e+01$	$1.0866e+02$	$2.9315e+02$	$6.7980e+02$	$1.4700e+03$
20	$2.9375e+00$	$2.2412e+01$	$2.0846e+01$	$2.2744e+00$	$3.1001e+01$
40	$1.0678e+00$	$4.9833e+00$	$9.5860e-01$	$1.3524e+00$	$7.5788e-01$
80	$4.4216e-01$	$1.1571e+00$	$2.6706e-02$	$9.3346e-02$	$8.5273e-03$
160	$1.9821e-01$	$2.7788e-01$	$1.7104e-03$	$5.6811e-03$	$2.5039e-05$
320	$9.3181e-02$	$6.8032e-02$	$4.9655e-04$	$3.4460e-04$	$2.6914e-06$
640	$4.5032e-02$	$1.6827e-02$	$7.8365e-05$	$2.1132e-05$	$1.3480e-07$

condition $y(-1) + y'(-1) = 2 + 4\pi$, $y(1) + y'(1) = 2 + 4\pi$. In Table 3, the convergence rate of equidistant nodes with different d is $O(h^d)$; in Table 4, the convergence rate of the Chebyshev point of second kind with different d is $O(h^{d+2})$, $d \geq 2$.

4. Concluding Remarks

In this paper, the numerical approximation of linear barycentric rational collocation method for solving two-point boundary value equations is presented. The matrix form of the algorithm is given for the simple calculation; with the help of Newton formula, the error function of the convergence rate $O(h^{d-1})$ is also obtained. For the constant coefficient and variable coefficient of two-point boundary value equations, numerical results show that the convergence rate can reach $O(h^d)$ for the equidistant nodes and $O(h^{d+2})$ for the Chebyshev point of the second kind with $d \geq 2$. For the special case of $d = 1$, there are still convergence rates with $O(h)$, and the analysis of this phenomenon will be presented in other papers.

Data Availability

The data that support the findings of this study are available from the corresponding author upon reasonable request.

Conflicts of Interest

The authors declare that they have no conflicts of interest.

Acknowledgments

References

[1] M. S. Floater and K. Hormann, "Barycentric rational interpolation with no poles and high rates of approximation," *Numerische Mathematik*, vol. 107, no. 2, pp. 315–331, 2007.

[2] G. Klein and J.-P. Berrut, "Linear rational finite differences from derivatives of barycentric rational interpolants," *SIAM Journal on Numerical Analysis*, vol. 50, no. 2, pp. 643–656, 2012.

[3] G. Klein and J.-P. Berrut, "Linear barycentric rational quadrature," *BIT Numerical Mathematics*, vol. 52, no. 2, pp. 407–424, 2012.

[4] A. Abdi and J.-P. Berrut, A. H. Seyyed, "The linear barycentric rational method for a class of delay volterra integro-differential equations," *Journal of Scientific Computing*, vol. 75, no. 3, pp. 1757–1775, 2018.

[5] J. P. Berrut, S. A. Hosseini, and G. Klein, "The linear barycentric rational quadrature method for Volterra integral equations," *SIAM Journal on Scientific Computing*, vol. 36, no. 1, pp. 105–123, 2014.

[6] J. Li and Y. L. Cheng, "Linear barycentric rational collocation method for solving second-order Volterra integro-differential equation," *Computational and Applied Mathematics*, vol. 92, 2020.

[7] M. Li and C. Huang, "The linear barycentric rational quadrature method for auto-convolution Volterra integral equations," *Journal of Scientific Computing*, vol. 78, no. 1, pp. 549–564, 2019.

[8] J.-Y. Greengard and L. Greengardz, "A fast adaptive numerical method for stiff two-point boundary value problems," *SIAM Journal on Scientific Computing*, vol. 18, no. 2, pp. 403–429, 1997.

[9] J. Li and Y. L. Cheng, "Linear barycentric rational collocation method for solving heat conduction equation," *Numerical Methods for Partial Differential Equations*, vol. 37, no. 1, pp. 533–545, 2020.

[10] Z. Wang, L. Zhang, Z. Xu, and J. Li, "Barycentric interpolation collocation method based on mixed displacement-stress formulation for solving plane elastic problems," *Chinese Journal of Applied Mechanics*, vol. 35, no. 2, pp. 304–309, 2018.

[11] Z. Wang, Z. Xu, and J. Li, "Mixed barycentric interpolation collocation method of displacement-pressure for incompressible plane elastic problems," *Chinese Journal of Applied Mechanics*, vol. 35, no. 3, pp. 195–201, 2018.

[12] Z. Wang and S. Li, *Barycentric Interpolation Collocation Method for Nonlinear Problems*, National Defense Industry Press, Beijing, China, 2015.

[13] E. Cirillo and K. Hormann, "On the Lebesgue constant of barycentric rational Hermite interpolants at equidistant nodes," *Journal of Computational and Applied Mathematics*, vol. 349, pp. 292–301, 2019.

[14] J.-P. Berrut, M. S. Floater, and G. Klein, "Convergence rates of derivatives of a family of barycentric rational interpolants," *Applied Numerical Mathematics*, vol. 61, no. 9, pp. 989–1000, 2011.

[15] L. Greengard, "Spectral integration and two-point boundary value problems," *SIAM Journal on Numerical Analysis*, vol. 28, no. 4, pp. 1071–1080, 1991.

Research Article

Extended Error Expansion of Classical Midpoint Rectangle Rule for Cauchy Principal Value Integrals on an Interval

Chunxiao Yu [ID] and Lingling Wei

School of Science, Yanshan University, No. 438 West Hebei Avenue, Qinhuangdao City, Hebei 066004, China

Correspondence should be addressed to Chunxiao Yu; chxy@ysu.edu.cn

The classical composite midpoint rectangle rule for computing Cauchy principal value integrals on an interval is studied. By using a piecewise constant interpolant to approximate the density function, an extended error expansion and its corresponding superconvergence results are obtained. The superconvergence phenomenon shows that the convergence rate of the midpoint rectangle rule is higher than that of the general Riemann integral when the singular point coincides with some priori known points. Finally, several numerical examples are presented to demonstrate the accuracy and effectiveness of the theoretical analysis. This research is meaningful to improve the accuracy of the collocation method for singular integrals.

1. Introduction

Singular integrals, especially Cauchy principal value integrals, are usually encountered in the fields of Boundary Element Method (BEM) [1–3], for example, the fluid mechanics, the elasticity and fracture mechanics, the acoustics, and the electromagnetics. In these fields (including their related physical problems), much attention has been paid to the Cauchy principal value integrals [4–8]. We now consider the following integral:

$$I(f;s) = c.p \int_a^b \frac{f(x)}{x-s} dx = g(s), \quad s \in (a,b), \quad (1)$$

where $f(x)$ is Holder continuous on the interval $[a,b]$, $(f(x)/(x-s))$ is the density function, $c.p \int_a^b$ denotes a Cauchy principal value integral, and s is the singular point. There are many ways to define equation (1). However, these definitions can be proved to be mathematically equivalent. In this paper, we adopt the following definition:

$$c.p \int_a^b \frac{f(x)}{x-s} dx = \lim_{\varepsilon \longrightarrow 0} \left\{ \int_a^{s-\varepsilon} \frac{f(x)}{x-s} dx + \int_{s+\varepsilon}^b \frac{f(x)}{x-s} dx \right\}, \quad s \in (a,b). \quad (2)$$

For this level of regularity of integrand, some methods based on the Chebyshev series expansion are much effective. They are easy to include the adaptive feature and can be applied to much difficult integrands [9–11]. At the same time, there are numerous works that have been devoted to developing efficient quadrature formulas, such as the Gaussian method [12,13], the Newton–Cotes method [14–16], the spline method [17, 18], and some other methods [19–25]. Usually, Gaussian rules have good accuracy if the integrand is smooth, while Newton–Cotes rules are attractive due to their ease of implementation and flexibility of mesh. To improve the accuracy of boundary element analysis, an efficient method called general (composite) Newton–Cotes rule has been studied and used to compute Cauchy principal value integrals and Hadamard finite-part integrals [26, 27]. When the singular point s coincides with some priori known points, Newton–Cotes rules can reach a high-order convergence rate [28, 29]. This is the so-called pointwise superconvergence phenomenon of the Newton–Cotes rules.

In this paper, we will focus on the superconvergence phenomenon of midpoint rectangle rules for Cauchy principal integrals with the density function $(f(x)/(x-s))$ being replaced by the approximation function

$(f(\widehat{x}_i)/(\widehat{x}_i - s))$, $i = 0, 1, \ldots, n-1$, where $\widehat{x}_i$ is the middle point of each subinterval of $[a, b]$. Different from the idea provided by Linz in [30] to calculate the hypersingular integral on an interval, we will present a direct method to compute the Cauchy principal integral. Based on the error estimate [31–33], the error function is determined by a certain special function $S_0(\tau)$. We will also give the necessary and sufficient conditions to be satisfied by the super-convergence points. In addition, we will not only try to obtain the error estimate of the superconvergence phenomenon but also make some investigation about the superconvergence points.

The rest of this paper is organized as follows. In Section 2, some basic formulas of the midpoint rectangle rule are introduced, and our main results are presented. In Section 3, some lemmas are given and the proof of the main results is completed. In Section 4, several numerical examples are provided to validate our analysis. At last, the concluding remarks are presented.

2. The Superconvergence of the Composite Midpoint Rectangle Rule

Let $a = x_0 < x_1 < \cdots < x_{n-1} < x_n = b$ be a uniform partition of the interval $[a, b]$ with a mesh size $h = ((b-a)/n)$. We first define the piecewise constant interpolant for $f(x)$:

$$f_C(x) = f(\widehat{x}_i), \widehat{x}_i = x_i + \frac{h}{2}, \quad x \in (x_i, x_{i+1}), \quad (3)$$

and then, we define a linear transformation:

$$x = \widehat{x}_i(\tau) := \frac{(\tau + 1)(x_{i+1} - x_i)}{2} + x_i, \quad \tau \in [-1, 1], \quad (4)$$

which maps the reference element $[-1, 1]$ onto the subinterval $[x_i, x_{i+1}]$. By replacing $(f(x)/(x-s))$ in equation (1) with $(f_C(x)/(\widehat{x}_i - s))$, we can obtain the following composite midpoint rectangle rule:

$$I_n(f; s) = c.p \int_a^b \frac{f_C(x)}{\widehat{x}_i - s} dx = \sum_{i=0}^{n-1} w_i(s) f(\widehat{x}_i)$$

$$= c.p \int_a^b \frac{f(x)}{x - s} dx - E_n(f; s), \quad (5)$$

where $w_i(s)$ denotes the Cotes coefficient given by $w_i(s) = (h/\widehat{x}_i - s)$ and $E_n(f; s)$ is the error function.

Theorem 1 (see [5]). *Assume that $f(x) \in C^\alpha[a, b]$, $\alpha \in (0, 1]$. For the midpoint rectangle rule $I_n(f; s)$ defined in equation (5), assume that $s \in [x_m, x_{m+1}]$, $s \neq \widehat{x}_m$, $m = 0, 1, 2, \ldots, n-1$, and there exists a positive constant C that is independent of h and s, such that*

$$|E_n(f; s)| \leq C(|\ln h| + |\ln \gamma(\tau)|) h^\alpha, \quad (6)$$

where

$$\gamma(\tau) = \min_{0 \leq i \leq n} \frac{|s - x_i|}{h} = \frac{1 - |\tau|}{2}. \quad (7)$$

Before presenting the main results, we first define

$$\varphi_0(x) = \begin{cases} -\dfrac{1}{2x} c.p \displaystyle\int_{-1}^1 \frac{\tau}{\tau - x} d\tau, & |x| < 1, \\[4mm] -\dfrac{1}{2x} \displaystyle\int_{-1}^1 \frac{\tau}{\tau - x} d\tau, & |x| > 1, \end{cases}$$

$$S_0(\tau) := \varphi_0(\tau) + \sum_{i=1}^\infty [\varphi_0(2i + \tau) + \varphi_0(-2i + \tau)], \quad \tau \in (-1, 1). \quad (8)$$

Theorem 2. *Assume that $f(x) \in C^l[a, b]$, $l \geq 2$. For the midpoint rectangle rule $I_n(f; s)$ defined in equation (5), assume that $s = x_m + (1 + \tau)h/2$, $s \neq \widehat{x}_m$, $m = 0, 1, 2, \ldots, n-1$, and there exists a positive constant C that is independent of h and s, such that*

$$E_n(f; s) = -f(s) S_0(\tau) + R_n(s), \quad (9)$$

where

$$|R_n(s)| \leq C \left(|\ln h| + \gamma^{-1}(\tau) + \frac{\eta(s)}{h^{l-1}}\right) h^l, \quad (10)$$

where $\gamma(\tau)$ is defined by equation (7) and

$$\eta(s) = \max \left\{ \frac{1}{s - a}, \frac{1}{b - s} \right\}. \quad (11)$$

Remark 1. Under the same assumptions of Theorem 2, when τ^* is the zero of $S_0(\tau^*)$, we have

$$|E_n(f; s)| \leq C \left(|\ln h| + \gamma^{-1}(\tau^*) + \eta(s) h^{1-l}\right) h^l. \quad (12)$$

3. The Proof of the Main Results

In this section, we mainly complete the proof of Theorem 2.

3.1. Some Necessary Lemmas

Lemma 1. *Under the same assumptions of Theorem 2, there holds that*

$$(\widehat{x}_i - s) f(x) - (x - s) f(\widehat{x}_i) = f(s)(\widehat{x}_i - x)$$

$$+ \sum_{k=1}^{l-1} \frac{f^{(k)}(s)}{k!} (x - s)^k (\widehat{x}_i - x)$$

$$- \sum_{k=1}^{l-1} \sum_{j=k}^{l-1} \frac{f^{(j)}(s)}{k!(j-k)!} (x - s)^{j-k+1} (\widehat{x}_i - x)^k + R_f(x), \quad (13)$$

where

$$R_f(x) = R_f^1(x) + R_f^2(x) + R_f^3(x), \qquad (14)$$

with

$$R_f^1(x) = -\frac{f^{(l)}(\theta_1)}{l!}(x-s)(\widehat{x}_i - x)^l,$$

$$R_f^2(x) = \frac{f^{(l)}(\theta_2)}{l!}(x-s)^l(\widehat{x}_i - x), \qquad (15)$$

$$R_f^3(x) = -\sum_{k=1}^{l-1}\frac{f^{(l)}(\theta_3)}{k!(l-k)!}(x-s)^{l-k+1}(\widehat{x}_i - x),$$

and $\theta_1, \theta_2 \in (x_i, x_{i+1}), \theta_3 \in (x, s)$ or (s, x).

Proof. Note that $f(x) \in C^l[a, b]$. By applying the following Taylor expansion to $f(\widehat{x}_i)$ at the point x, we obtain

$$f(\widehat{x}_i) = f(x) + \sum_{k=1}^{l-1}\frac{f^{(k)}(x)}{k!}(\widehat{x}_i - x)^k$$

$$+ \frac{f^{(l)}(\theta_1)}{l!}(\widehat{x}_i - x)^l, \quad \theta_1 \in (x_i, x_{i+1}). \qquad (16)$$

Similarly, we have

$$f(x) = f(s) + \sum_{k=1}^{l-1}\frac{f^{(k)}(s)}{k!}(x-s)^k$$

$$+ \frac{f^{(l)}(\theta_2)}{l!}(x-s)^l, \quad \theta_2 \in (x_i, x_{i+1}). \qquad (17)$$

Thus,

$$(\widehat{x}_i - s)f(x) - (x-s)f(\widehat{x}_i) = f(s)(\widehat{x}_i - x)$$

$$+ \sum_{k=1}^{l-1}\frac{f^{(k)}(s)}{k!}(x-s)^k(\widehat{x}_i - x)$$

$$- \sum_{k=1}^{l-1}\frac{f^{(k)}(x)}{k!}(x-s)(\widehat{x}_i - x)^k - \frac{f^{(l)}(\theta_1)}{l!}(\widehat{x}_i - x)^l(x-s)$$

$$+ \frac{f^{(l)}(\theta_2)}{l!}(x-s)^l(\widehat{x}_i - x). \qquad (18)$$

On the contrary, for $k = 1, 2, \ldots, l-1$, we have

$$f^{(k)}(x) = f^{(k)}(s) + f^{(k+1)}(s)(x-s) + \cdots + \frac{f^{(l)}(\theta_3)}{(l-k)!}(x-s)^{l-k}$$

$$= \sum_{j=k}^{l-1}\frac{f^{(j)}(s)}{(j-k)!}(x-s)^{j-k} + \frac{f^{(l)}(\theta_3)}{(l-k)!}(x-s)^{l-k}, \qquad (19)$$

where $\theta_3 \in (x, s)$ or (s, x). According to equations (18) and (19), we can obtain equation (13). The proof is completed.

Define the error function:

$$E_m(x) = f(x) - \frac{f(\widehat{x}_m)(x-s)}{(\widehat{x}_m - s)} - \frac{f(s)(\widehat{x}_m - x)}{(\widehat{x}_m - s)}$$

$$- \sum_{k=1}^{l-1}\frac{f^{(k)}(s)(x-s)^k(\widehat{x}_m - x)}{k!(\widehat{x}_m - s)} \qquad (20)$$

$$+ \sum_{k=1}^{l-1}\sum_{j=k}^{l-1}\frac{f^{(j)}(s)(x-s)^{j-k+1}(\widehat{x}_m - x)^k}{k!(j-k)!(\widehat{x}_m - s)}. \qquad \square$$

Lemma 2. *Assume that $s \in (x_i, x_{i+1})$ for the integer m and let $c_i = (2(s - x_i)/h - 1), \quad 0 \le i \le n - 1$. Then, we have*

$$\varphi_0(c_i) = \begin{cases} -\dfrac{1}{2}c.p\displaystyle\int_{x_m}^{x_{m+1}}\dfrac{\widehat{x}_m - x}{(x-s)(\widehat{x}_m - s)}dx, & i = m, \\[3mm] -\dfrac{1}{2}\displaystyle\int_{x_i}^{x_{i+1}}\dfrac{\widehat{x}_i - x}{(x-s)(\widehat{x}_i - s)}dx, & i \neq m. \end{cases} \qquad (21)$$

Proof. If $i = m$, by using the definition of equation (2) and the linear transformation of equation (4), we have

$$c.p\int_{x_m}^{x_{m+1}}\frac{\widehat{x}_m - x}{(x-s)(\widehat{x}_m - s)}dx$$

$$= \lim_{\varepsilon \to 0}\left\{\int_{x_m}^{s-\varepsilon}\frac{\widehat{x}_m - x}{(x-s)(\widehat{x}_m - s)}dx + \int_{s+\varepsilon}^{x_{m+1}}\frac{\widehat{x}_m - x}{(x-s)(\widehat{x}_m - s)}dx\right\}$$

$$= c.p\int_{x_m}^{x_{m+1}}\frac{\tau}{c_m(\tau - c_m)}d\tau$$

$$= -2\varphi_0(c_m). \qquad (22)$$

If $i \neq m$, it can be proved by applying the same approach to the corresponding Riemann integral. The proof is completed. $\square$

Lemma 3. *Under the same assumptions of Theorem 2, for the function $E_m(x)$ in equation (20), there holds that*

$$\left|c.p\int_{x_m}^{x_{m+1}}\frac{E_m(x)}{x-s}dx\right| \le Ch^l|\ln\gamma(\tau)|, \qquad (23)$$

where $\gamma(\tau)$ is defined in equation (7).

Proof. Since $f(x) \in C^l[a, b]$, by using Taylor expansion, we have

$$\left|E_m^{(i)}(x)\right| \le Ch^{l-i}, \quad i = 0, 1. \qquad (24)$$

From the following defined relationship,

$$c.p\int_a^b\frac{f(x)}{x-s}dx = \int_a^b\frac{f(x) - f(s)}{x-s}dx + f(s)\ln\left|\frac{b-s}{s-a}\right|, \qquad (25)$$

we have

$$c.p \int_{x_m}^{x_{m+1}} \frac{E_m(x)}{x-s} dx = \int_{x_m}^{x_{m+1}} \frac{E_m(x) - E_m(s)}{x-s} dx$$
$$+ E_m(s)\ln\left|\frac{x_{m+1}-s}{s-x_m}\right|. \tag{26}$$

Nowm we estimate equation (26) term by term:

$$\left|\int_{x_m}^{x_{m+1}} \frac{E_m(x) - E_m(s)}{x-s} dx\right| = \left|\int_{x_m}^{x_{m+1}} E_m'(\xi_m) dx\right|$$
$$\leq Ch^l, \quad \xi_m \in (x_m, s) \text{ or } (s, x_{m+1}), \tag{27}$$

$$\left|E_m(s)\ln\left|\frac{x_{m+1}-s}{s-x_m}\right|\right| \leq Ch^l|\ln \gamma(\tau)|. \tag{28}$$

From equations (26)–(28), we can obtain equation (23). The proof is completed. □

Lemma 4 (see [5]).   *For $\tau \in (-1,1)$ and $m \geq 1$, we have*

$$\left|\sum_{i=m}^{\infty} \varphi_0(2i+\tau) + \sum_{i=n-m+1}^{\infty} \varphi_0(-2i+\tau)\right| \leq Ch\eta(s). \tag{29}$$

3.2. Proof of Theorem 2

Proof.   By Lemma 1, we have

$$\left(\int_a^{x_m} + \int_{x_{m+1}}^b\right) \frac{f(x)}{x-s} dx - \sum_{\substack{i=0, i \neq m}}^{n-1} \frac{f(\widehat{x}_i)h}{\widehat{x}_i - s}$$

$$= \sum_{\substack{i=0, i \neq m}}^{n-1} \int_{x_i}^{x_{i+1}} \left[\frac{f(x)}{x-s} - \frac{f(\widehat{x}_i)}{\widehat{x}_i - s}\right] dx$$

$$= \sum_{\substack{i=0, i \neq m}}^{n-1} \int_{x_i}^{x_{i+1}} \frac{(\widehat{x}_i - s)f(x) - (x-s)f(\widehat{x}_i)}{(x-s)(\widehat{x}_i - s)} dx$$

$$= f(s) \sum_{\substack{i=0, i \neq m}}^{n-1} \int_{x_i}^{x_{i+1}} \frac{(\widehat{x}_i - x)}{(x-s)(\widehat{x}_i - s)} dx + \sum_{k=1}^{l-1} \frac{f^{(k)}(s)}{k!} \sum_{\substack{i=0, i \neq m}}^{n-1} \int_{x_i}^{x_{i+1}} \frac{(x-s)^{k-1}(\widehat{x}_i - x)}{(\widehat{x}_i - s)} dx$$

$$- \sum_{k=1}^{l-1}\sum_{j=k}^{l-1} \frac{f^{(j)}(s)}{k!(j-k)!} \sum_{\substack{i=0, i \neq m}}^{n-1} \int_{x_i}^{x_{i+1}} \frac{(x-s)^{j-k}(\widehat{x}_i - x)^k}{(\widehat{x}_i - s)} dx - \sum_{\substack{i=0, i \neq m}}^{n-1} \int_{x_i}^{x_{i+1}} \frac{f^{(l)}(\theta_1)(\widehat{x}_i - x)^l}{l!(\widehat{x}_i - s)} dx$$

$$+ \sum_{\substack{i=0, i \neq m}}^{n-1} \int_{x_i}^{x_{i+1}} \frac{f^{(l)}(\theta_2)(x-s)^{l-1}(\widehat{x}_i - x)}{l!(\widehat{x}_i - s)} dx - \sum_{k=1}^{l-1}\sum_{\substack{i=0, i \neq m}}^{n-1} \int_{x_i}^{x_{i+1}} \frac{f^{(l)}(\theta_3)(x-s)^{l-k}(\widehat{x}_i - x)^k}{k!(l-k)!(\widehat{x}_i - s)} dx. \tag{30}$$

From the definition of $E_m(x)$ in equation (20), we have

$$c.p \int_{x_m}^{x_{m+1}} \left[\frac{f(x)}{x-s} - \frac{f(\widehat{x}_m)}{\widehat{x}_m - s}\right] dx = c.p \int_{x_m}^{x_{m+1}} \frac{E_m(x)}{x-s} dx + f(s)c.p \int_{x_m}^{x_{m+1}} \frac{(\widehat{x}_m - x)}{(x-s)(\widehat{x}_m - s)} dx$$

$$+ \sum_{k=1}^{l-1} \frac{f^{(k)}(s)}{k!} c.p \int_{x_m}^{x_{m+1}} \frac{(x-s)^{k-1}(\widehat{x}_m - x)}{(\widehat{x}_m - s)} dx \tag{31}$$

$$- \sum_{k=1}^{l-1}\sum_{j=k}^{l-1} \frac{f^{(j)}(s)}{k!(j-k)!} c.p \int_{x_m}^{x_{m+1}} \frac{(x-s)^{j-k}(\widehat{x}_m - x)^k}{(\widehat{x}_m - s)} dx.$$

According to equations (30) and (31), we can obtain

$$c.p \int_a^b \frac{f(x)}{x-s}dx - \sum_{i=0}^{n-1} \frac{f(\widehat{x}_i)h}{\widehat{x}_i - s}$$

$$= \sum_{i=0}^{n-1} c.p \int_{x_i}^{x_{i+1}} \left[\frac{f(x)}{x-s} - \frac{f(\widehat{x}_i)}{\widehat{x}_i - s}\right] dx$$

$$= \sum_{i=0, i \neq m}^{n-1} \int_{x_i}^{x_{i+1}} \left[\frac{f(x)}{x-s} - \frac{f(\widehat{x}_i)}{\widehat{x}_i - s}\right] dx \qquad (32)$$

$$+ c.p \int_{x_m}^{x_{m+1}} \left[\frac{f(x)}{x-s} - \frac{f(\widehat{x}_m)}{\widehat{x}_m - s}\right] dx$$

$$= -f(s)S_0(\tau) + R_n(s),$$

where

$$R_n(s) = R_n^{(1)}(s) + R_n^{(2)}(s) + R_n^{(3)}(s) + R_n^{(4)}(s), \qquad (33)$$

with

$$R_n^{(1)}(s) = \sum_{k=1}^{l-1} \frac{f^{(k)}(s)}{k!} \left[\sum_{i=0, i \neq m}^{n-1} \int_{x_i}^{x_{i+1}} \frac{(x-s)^{k-1}(\widehat{x}_i - x)}{(\widehat{x}_i - s)}dx + c.p \int_{x_m}^{x_{m+1}} \frac{(x-s)^{k-1}(\widehat{x}_m - x)}{(\widehat{x}_m - s)}dx\right]$$

$$- \sum_{k=1}^{l-1} \sum_{j=k}^{l-1} \frac{f^{(j)}(s)}{k!(j-k)!} \left[\sum_{i=0, i \neq m}^{n-1} \int_{x_i}^{x_{i+1}} \frac{(x-s)^{j-k}(\widehat{x}_i - x)^k}{(\widehat{x}_i - s)}dx + c.p \int_{x_m}^{x_{m+1}} \frac{(x-s)^{j-k}(\widehat{x}_m - x)^k}{(\widehat{x}_m - s)}dx\right], \qquad (34)$$

$$R_n^{(2)}(s) = - \sum_{i=0, i \neq m}^{n-1} \int_{x_i}^{x_{i+1}} \frac{f^{(l)}(\theta_1)(\widehat{x}_i - x)^l}{l!(\widehat{x}_i - s)}dx + \sum_{i=0, i \neq m}^{n-1} \int_{x_i}^{x_{i+1}} \frac{f^{(l)}(\theta_2)(x-s)^{l-1}(\widehat{x}_i - x)}{l!(\widehat{x}_i - s)}dx$$

$$- \sum_{k=1}^{l-1} \sum_{i=0, i \neq m}^{n-1} \int_{x_i}^{x_{i+1}} \frac{f^{(l)}(\theta_3)(x-s)^{l-k}(\widehat{x}_i - x)^k}{k!(l-k)!(\widehat{x}_i - s)}dx, \qquad (35)$$

$$R_n^{(3)}(s) = c.p \int_{x_m}^{x_{m+1}} \frac{E_m(x)}{x-s}dx, \qquad (36)$$

$$R_n^{(4)}(s) = f(s)\left[\sum_{i=m}^{\infty} \varphi_0(2i + \tau) + \sum_{i=n-m+1}^{\infty} \varphi_0(-2i + \tau)\right]. \qquad (37)$$

Now, we estimate these four terms one by one. For $R_n^{(1)}(s)$, by the definition of equation (2) and the linear transformation of equation (4), we have

$$\left|\sum_{k=1}^{l-1} \sum_{j=k}^{l-1} \frac{f^{(j)}(s)}{k!(j-k)!} \left[\sum_{i=0, i \neq m}^{n-1} \int_{x_i}^{x_{i+1}} \frac{(x-s)^{j-k}(\widehat{x}_i - x)^k}{(\widehat{x}_i - s)}dx + c.p \int_{x_m}^{x_{m+1}} \frac{(x-s)^{j-k}(\widehat{x}_m - x)^k}{(\widehat{x}_m - s)}dx\right]\right|$$

$$\leq C \left|\sum_{k=1}^{l-1} \sum_{j=k}^{l-1} \frac{f^{(j)}(s)}{k!(j-k)!} \left(\frac{h}{2}\right)^j \sum_{i=0}^{n-1} \frac{1}{c_i}\right| \leq Ch^l \gamma^{-1}(\tau). \qquad (38)$$

Then, we obtain

$$\left|c.p \int_{x_m}^{x_{m+1}} \frac{(x-s)^{j-k}(\widehat{x}_m - x)^k}{(\widehat{x}_m - s)}dx\right| \leq C \frac{1}{c_m}\left(\frac{h}{2}\right)^j. \qquad (39)$$

Similarly, by applying the same approach to the corresponding Riemann integral, we obtain

$$\left| \int_{x_i}^{x_{i+1}} \frac{(x-s)^{j-k}(\widehat{x}_i - x)^k}{(\widehat{x}_i - s)} dx \right| \leq C \frac{1}{c_i} \left(\frac{h}{2} \right)^j. \qquad (40)$$

By substituting equations (39) and (40) into the second part of $R_n^{(1)}(s)$, we can obtain

$$\left| \sum_{k=1}^{l-1} \sum_{j=k}^{l-1} \frac{f^{(j)}(s)}{k!(j-k)!} \left[\sum_{i=0, i \neq m}^{n-1} \int_{x_i}^{x_{i+1}} \frac{(x-s)^{j-k}(\widehat{x}_i - x)^k}{(\widehat{x}_i - s)} dx + c.p \int_{x_m}^{x_{m+1}} \frac{(x-s)^{j-k}(\widehat{x}_m - x)^k}{(\widehat{x}_m - s)} dx \right] \right| \qquad (41)$$

$$\leq C \left| \sum_{k=1}^{l-1} \sum_{j=k}^{l-1} \frac{f^{(j)}(s)}{k!(j-k)!} \left(\frac{h}{2} \right)^j \sum_{i=0}^{n-1} \frac{1}{c_i} \right| \leq Ch^l \gamma^{-1}(\tau).$$

In the same way, we can obtain

$$\left| \sum_{k=1}^{l-1} \frac{f^{(k)}(s)}{k!} \left[\sum_{i=0, i \neq m}^{n-1} \int_{x_i}^{x_{i+1}} \frac{(x-s)^{k-1}(\widehat{x}_i - x)}{(\widehat{x}_i - s)} dx + c.p \int_{x_m}^{x_{m+1}} \frac{(x-s)^{k-1}(\widehat{x}_m - x)}{(\widehat{x}_m - s)} dx \right] \right| \qquad (42)$$

$$\leq C \left| \sum_{k=1}^{l-1} \frac{f^{(k)}(s)}{k!} \left(\frac{h}{2} \right)^k \sum_{i=0}^{n-1} \frac{1}{c_i} \right| \leq Ch^l \gamma^{-1}(\tau).$$

As for $R_n^{(2)}(s)$, we have

$$\left| \sum_{i=0, i \neq m}^{n-1} \int_{x_i}^{x_{i+1}} \frac{f^{(l)}(\theta_1)(\widehat{x}_i - x)^l}{l!(\widehat{x}_i - s)} dx \right| \leq Ch^l \sum_{i=0, i \neq m}^{n-1} \int_{x_i}^{x_{i+1}} \frac{1}{|\widehat{x}_i - s|} dx \leq Ch^l [|\ln h| + 1]. \qquad (43)$$

From equation (40), we can obtain

$$\left| \sum_{i=0, i \neq m}^{n-1} \int_{x_i}^{x_{i+1}} \frac{f^{(l)}(\theta_2)(x-s)^{l-1}(\widehat{x}_i - x)}{l!(\widehat{x}_i - s)} dx \right| \leq C \left(\frac{h}{2} \right)^l \sum_{i=0, i \neq m}^{n-1} \frac{1}{c_i} \leq Ch^l \gamma^{-1}(\tau), \qquad (44)$$

$$\left| \sum_{k=1}^{l-1} \sum_{i=0, i \neq m}^{n-1} \int_{x_i}^{x_{i+1}} \frac{f^{(l)}(\theta_3)(x-s)^{l-k}(\widehat{x}_i - x)^k}{k!(l-k)!(\widehat{x}_i - s)} dx \right| \leq C \left(\frac{h}{2} \right)^l \sum_{i=0, i \neq m}^{n-1} \frac{1}{c_i} \leq Ch^l \gamma^{-1}(\tau). \qquad (45)$$

According to Lemmas 3 and 4, we know

$$\left| R_n^{(3)}(s) \right| \leq Ch^l |\ln \gamma(\tau)|, \qquad (46)$$

$$\left| R_n^{(4)}(s) \right| \leq Ch\eta(s). \qquad (47)$$

From the above estimates, equation (10) can be obtained. The proof is completed.

In addition, from [5], we know $S_0(\varphi_0, \tau) = -(\pi/2)\tan(\pi(\tau+1)/2)$. □

4. Numerical Examples

Example 1. We first consider the Cauchy principal value integral with $f(x) = x^6$, $a = -1$, and $b = 1$. The exact value can be expressed as $2s^5 + 2/3s^3 + 2/5s + s^6 \log(1 - s/1 + s)$.

We adopt the uniform mesh method to examine the convergence rate of the midpoint rectangle rule $I_n(x^6, s)$ with the dynamic points $s = x_{[n/4]} + (1+\tau)h/2$ and $s = a + (1+\tau)h/2$, respectively. For different values of n, the error distributions are shown in Figure 1 and Figure 2, respectively.
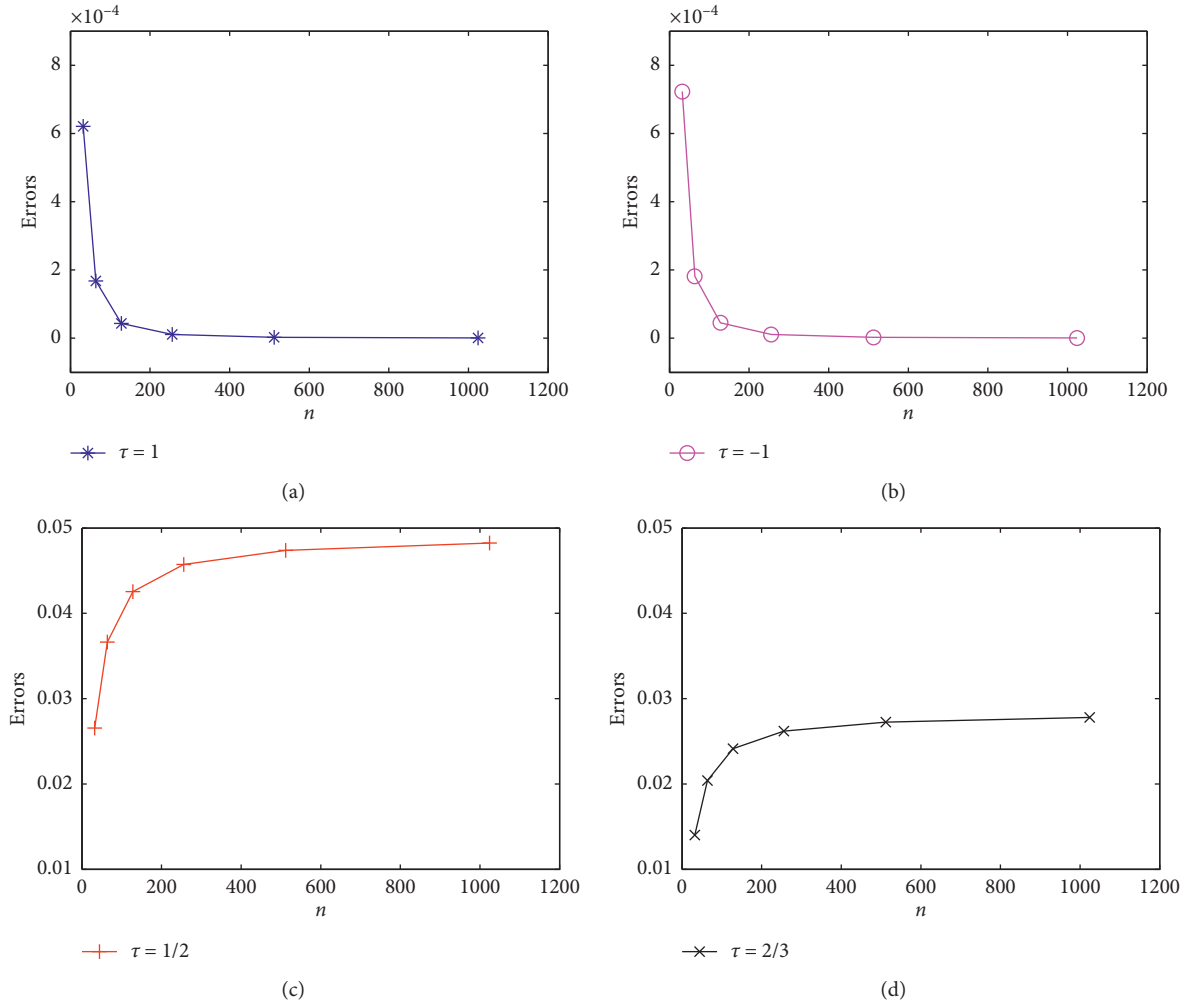
FIGURE 1: Error distributions for the midpoint rectangle rule with $s = x_{[n/4]} + (1 + \tau)h/2$.

When $s = x_{[n/4]} + (1 + \tau)h/2$, the convergence rate of the midpoint rectangle rule is $O(h^2)$ at the superconvergence points, and there is no convergence rate at the non-superconvergence points, as shown in Table 1. When $s = a + (1 + \tau)h/2$, because of the influence of $\eta(s)$, no superconvergence phenomenon occurs at both the super-convergence points and the non-superconvergence points, which coincides with the theoretical analysis, as shown in Table 2. For the case of $l = 2$, these numerical results agree quite well with the theoretical results in Theorem 2.

Example 2. In the second example, we further study the accuracy of the midpoint rectangle rule. We next consider the Cauchy principal value integral with $f(x) = x^2 - 1$, $a = -1, b = 1$. The exact value can be expressed as $2s + (1 - s^2)\log|1 + s/1 - s|$.

We adopt the uniform mesh method to examine the convergence rate of the midpoint rectangle rule $I_n(x^2 - 1, s)$ with the dynamic points $s = x_{[n/4]} + (1 + \tau)h/2$ and $s = a + (1 + \tau)h/2$, respectively. For different values of n, the error distributions are shown in Figure 3 and Figure 4, respectively.

For the case of $s = x_{[n/4]} + (1 + \tau)h/2$, when the local coordinate of singular point $\tau = \pm 1$, the convergence rate of the midpoint rectangle rule is $O(h^2)$ at the superconvergence points, and there is no convergence rate at the non-superconvergence points, as shown in Table 3. For the case of $s = a + (1 + \tau)h/2$ because of the limitation of the boundary condition $f(a) = f(b) = 0$, the convergence rate is $O(h)$ at both the superconvergence points and the non-super-convergence points, as shown in Table 4. These numerical results are consistent with the theoretical results of $l = 2$ in Theorem 2.

FIGURE 2: Error distributions for the midpoint rectangle rule with $s = a + (1 + \tau)h/2$.

TABLE 1: Errors and convergence for the midpoint rectangle rule with $s = x_{[n/4]} + (1 + \tau)h/2$.

n	$\tau = 1$	$\tau = -1$	$\tau = 1/2$	$\tau = 2/3$
32	$6.2074e - 004$	$7.2296e - 004$	$2.6547e - 002$	$1.4010e - 002$
64	$1.6800e - 004$	$1.8082e - 004$	$3.6631e - 002$	$2.0390e - 002$
128	$4.3607e - 005$	$4.5210e - 005$	$4.2533e - 002$	$2.4147e - 002$
256	$1.1102e - 005$	$1.1303e - 005$	$4.5724e - 002$	$2.6186e - 002$
512	$2.8007e - 006$	$2.8257e - 006$	$4.7384e - 002$	$2.7249e - 002$
1024	$7.0330e - 007$	$7.0643e - 007$	$4.8230e - 002$	$2.7791e - 002$
Convergence ratio	1.9571	1.9998	—	—

TABLE 2: Errors and convergence for the midpoint rectangle rule with $s = a + (1 + \tau)h/2$.

| n	$\tau = 1$	$\tau = -1$	$\tau = 1/2$	$\tau = 2/3$
32	$2.2989e - 002$	—	$2.3986e - 000$	$1.3505e - 000$
64	$2.9689e - 002$	—	$2.7767e - 000$	$1.5907e - 000$
128	$3.3079e - 002$	—	$2.9831e - 000$	$1.7230e - 000$
256	$3.4782e - 002$	—	$3.0909e - 000$	$1.7924e - 000$
512	$3.5635e - 002$	—	$3.1459e - 000$	$1.8280e - 000$
1024	$3.6062e - 002$	—	$3.1738e - 000$	$1.8460e - 000$
Convergence ratio	—	—	—	—

Figure 3: Error distributions for the midpoint rectangle rule with $s = x_{[n/4]} + (1 + \tau)h/2$.
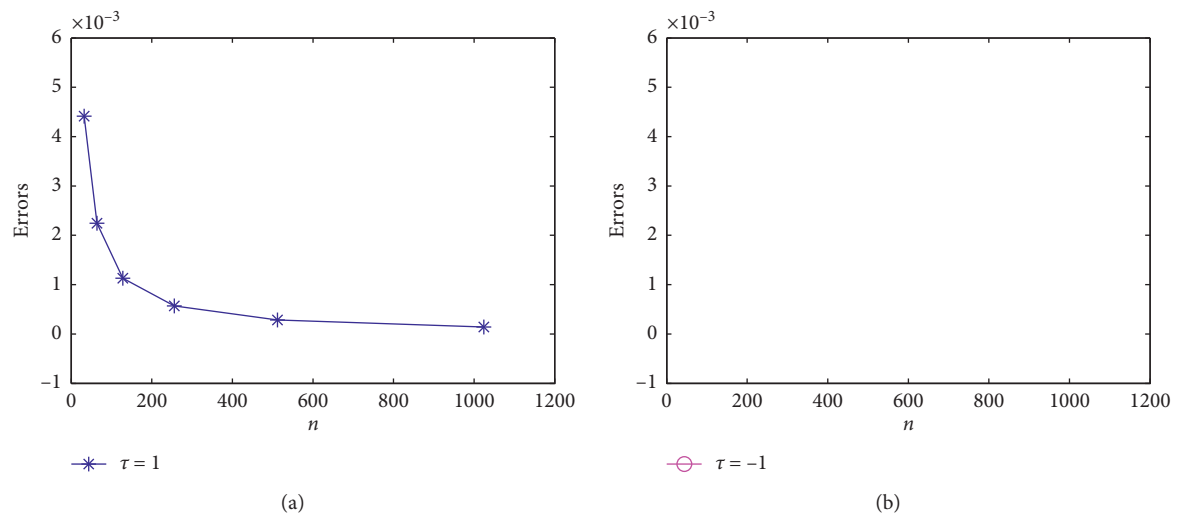
Figure 4: Continued.

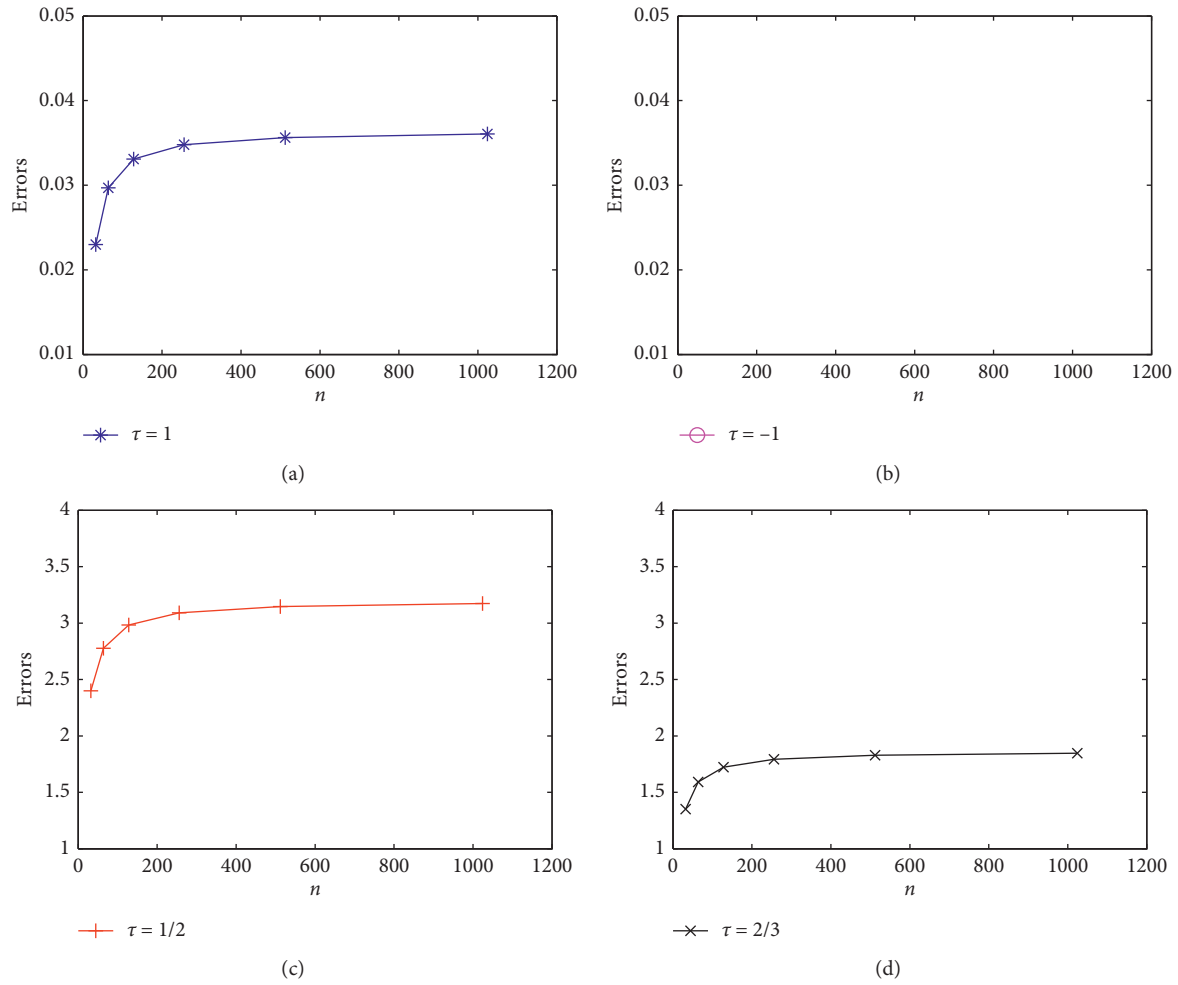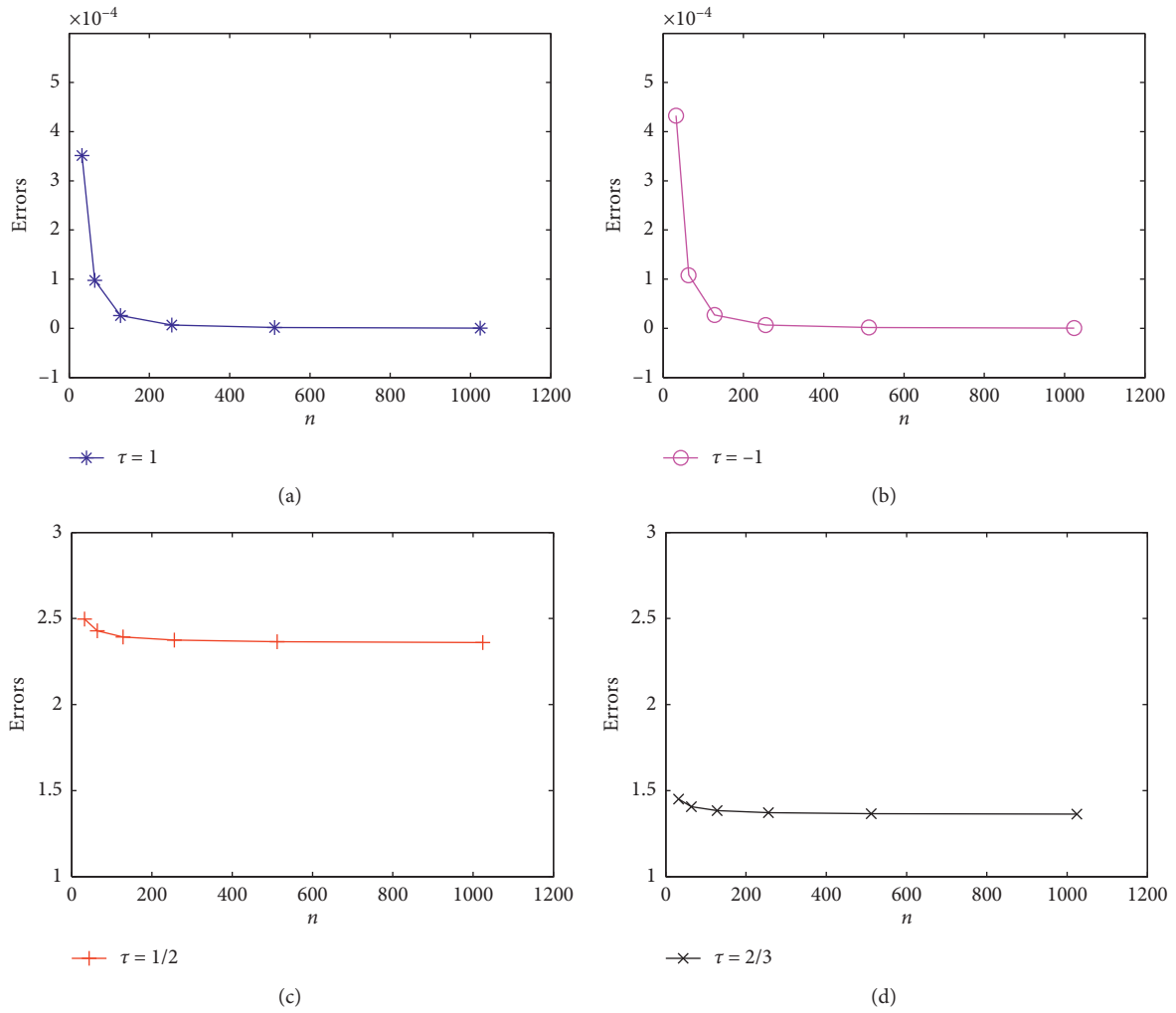(c)   (d)
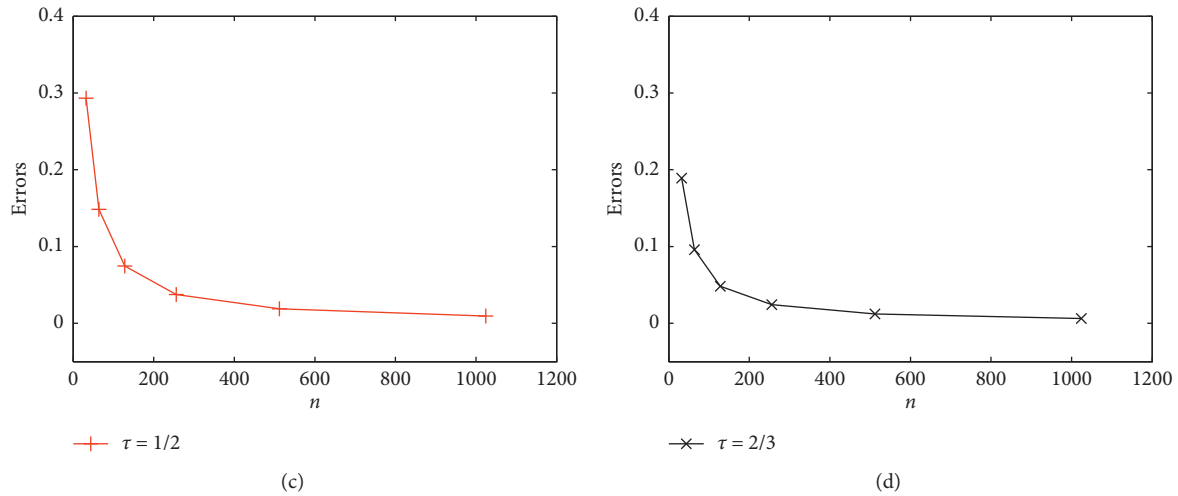
FIGURE 4: Error distributions for the midpoint rectangle rule with $s = a + (1 + \tau)h/2$.

TABLE 3: Errors and convergence for the midpoint rectangle rule with $s = x_{[n/4]} + (1 + \tau)h/2$.

n	$\tau = 1$	$\tau = -1$	$\tau = 1/2$	$\tau = 2/3$
32	$3.5138e - 004$	$4.3272e - 004$	$2.4969e + 000$	$1.4503e + 000$
64	$9.7712e - 005$	$1.0842e - 004$	$2.4282e + 000$	$1.4065e + 000$
128	$2.5746e - 005$	$2.7122e - 005$	$2.3926e + 000$	$1.3837e + 000$
256	$6.6071e - 006$	$6.7814e - e - 006$	$2.3745e + 000$	$1.3721e + 000$
512	$1.6735e - 006$	$1.6954e - 006$	$2.3654e + 000$	$1.3662e + 000$
1024	$4.2110e - 007$	$4.2385e - 007$	$2.3608e + 000$	$1.3633e + 000$
Convergence ratio	1.9409	1.9991	—	—

TABLE 4: Errors and convergence for the midpoint rectangle rule with $s = a + (1 + \tau)h/2$.

n	$\tau = 1$	$\tau = -1$	$\tau = 1/2$	$\tau = 2/3$
32	$4.4135e - 003$	—	$2.9313e - 001$	$1.8911e - 001$
64	$2.2443e - 003$	—	$1.4833e - 001$	$9.5823e - 002$
128	$1.1313e - 003$	—	$7.4603e - 002$	$4.8228e - 002$
256	$5.6792e - 004$	—	$3.7411e - 002$	$2.4193e - 002$
512	$2.8452e - 004$	—	$1.8733e - 002$	$1.2116e - 002$
1024	$1.4240e - 004$	—	$9.3735e - 003$	$6.0631e - 003$
Convergence ratio	0.9908	—	0.9934	0.9926

5. Conclusions

In this paper, the interpolation method and Taylor expansion method are used to obtain the extended error expansion of classical composite midpoint rectangle rule for the computation of Cauchy principal value integrals. For the case of $f(x) \in C^l[a, b], \quad l \geq 2$, the error expansion and its accuracy are analyzed by theoretical proofs and numerical experiments. Based on the expansion of the error function, some superconvergence results are obtained. It shows that the increased rate of convergence occurs at the singular points whose location changes are allowed. This kind of Cauchy principal value integral can be widely used in many engineering areas, and the positions of singular points are fixed in real applications. Moreover, it is very possible to extend the above presented results to improve the accuracy of the collocation method for singular integrals by choosing the superconvergence points to be the collocation points.

Data Availability

The data used to support the results of this study are included within the article.

Conflicts of Interest

The authors declare that they have no conflicts of interest.

Acknowledgments

References

[1] D. H. Yu, *Natural Boundary Integral Method and its Applications*, Science Press, Beijing, China, 2002.

[2] P. Junghanns and B. Silbermann, "Numerical analysis for one-dimensional Cauchy singular integral equations," *Journal of Computational and Applied Mathematics*, vol. 125, no. 1-2, pp. 395–421, 2000.

[3] Y. Liu and B. Song, "Numerical solution of Cauchy singular integral equations with Hilbert kernel on the circle," *Journal of Mathematics*, vol. 32, no. 4, pp. 582–588, 2012.

[4] J. Li and D. H. Yu, "Error expansion of classical trapezoidal rule for computing Cauchy principal value integral," *CMES-Computer Modeling in Engineering & Sciences*, vol. 93, no. 1, pp. 47–67, 2013.

[5] J. Li, J. E. Yang, and D. Yu, "Error expansion of classical midpoint rectangle rule for computing Cauchy principal value integrals on an interval," *International Journal of Computer Mathematics*, vol. 91, no. 10, pp. 2294–2306, 2014.

[6] T. Hasegawa and H. Sugiura, "Uniform approximation to Cauchy principal value integrals with logarithmic singularity," *Journal of Computational and Applied Mathematics*, vol. 327, pp. 1–11, 2018.

[7] M. H. Xia and J. Li, "Extrapolation method for Cauchy principal value integral with classical rectangle rule on interval," *CMES-computer Modeling in Engineering & Sciences*, vol. 115, no. 3, pp. 313–326, 2018.

[8] Y. Ma and J. Huang, "Asymptotic error expansions and splitting extrapolation algorithm for two classes of two-dimensional Cauchy principal-value integrals," *Applied Mathematics and Computation*, vol. 357, pp. 107–118, 2019.

[9] H. Wang and S. Xiang, "On the evaluation of Cauchy principal value integrals of oscillatory functions," *Journal of Computational and Applied Mathematics*, vol. 234, no. 1, pp. 95–100, 2010.

[10] P. Keller, "A practical algorithm for computing Cauchy principal value integrals of oscillatory functions," *Applied Mathematics and Computation*, vol. 218, no. 9, pp. 4988–5001, 2012.

[11] G. He and S. Xiang, "An improved algorithm for the evaluation of Cauchy principal value integrals of oscillatory functions and its application," *Journal of Computational and Applied Mathematics*, vol. 280, pp. 1–13, 2015.

[12] K. Diethelm, "Gaussian quadrature formulae of the third kind for Cauchy principal value integrals: basic properties and error estimates," *Journal of Computational and Applied Mathematics*, vol. 65, no. 1–3, pp. 97–114, 1995.

[13] G. Criscuolo and G. Mastroianni, "Formule gaussiane per il calcolo di integrali a valor principale secondo Cauchy e loro convergenza," *Calcolo*, vol. 22, no. 3, pp. 391–411, 1985.

[14] J. Wu and W. Sun, "The superconvergence of Newton-Cotes rules for the Hadamard finite-part integral on an interval," *Numerische Mathematik*, vol. 109, no. 1, pp. 143–165, 2008.

[15] X. Zhang, J. Wu, and D. Yu, "The superconvergence of composite Newton-Cotes rules for Hadamard finite-part integral on a circle," *Computing*, vol. 85, no. 3, pp. 219–244, 2009.

[16] J. Li, X. Zhang, and D. Yu, "Superconvergence and ultraconvergence of Newton-Cotes rules for supersingular integrals," *Journal of Computational and Applied Mathematics*, vol. 233, no. 11, pp. 2841–2854, 2010.

[17] A. P. Orsi, "Spline approximation for Cauchy principal value integrals," *Journal of Computational and Applied Mathematics*, vol. 30, no. 2, pp. 191–201, 1990.

[18] G. Behforooz, "Approximation of Cauchy principal value integrals by piecewise Hermite quartic polynomials by spline," *Applied Mathematics Letters*, vol. 5, no. 1, pp. 75–78, 1992.

[19] M. Branders and R. Piessens, "An extension of Clenshaw-Curtis quadrature," *Journal of Computational and Applied Mathematics*, vol. 1, no. 1, pp. 55–65, 1975.

[20] T. Hasegawa and T. Torii, "An automatic quadrature for indefinite integral of algebraic singular integrand," *Transactions of the Japan Society for Industrial and Applied Mathematics*, vol. 1, pp. 1–11, 1991.

[21] P. Kim and B. I. Yun, "On the convergence of interpolatory-type quadrature rules for evaluating Cauchy integrals," *Journal of Computational and Applied Mathematics*, vol. 149, no. 2, pp. 381–395, 2002.

[22] P. Keller and I. Wróbel, "Computing Cauchy principal value integrals using a standard adaptive quadrature," *Journal of Computational and Applied Mathematics*, vol. 294, pp. 323–341, 2016.

[23] G. Liu and S. Xiang, "Clenshaw-Curtis-type quadrature rule for hypersingular integrals with highly oscillatory kernels," *Applied Mathematics and Computation*, vol. 340, pp. 251–267, 2019.

[24] J. Li and Y. L. Cheng, "Linear barycentric rational collocation method for solving second-order Volterra integro-differential equation," *Computational and Applied Mathematics*, vol. 39, p. 92, 2020.

[25] J. Li and Y. Cheng, "Linear barycentric rational collocation method for solving heat conduction equation," *Numerical Methods for Partial Differential Equations*, vol. 37, no. 1, pp. 533–545, 2021.

[26] D. Liu, J. Wu, and X. Zhang, "The adaptive composite trapezoidal rule for Hadamard finite-part integrals on an interval," *Journal of Computational and Applied Mathematics*, vol. 325, pp. 165–174, 2017.

[27] J. Li and Y.-T. Chen, "Finite element methods for electromagnetics," *Computational Partial Differential Equations Using MATLAB*, vol. 37, no. 2, pp. 261–330, 2019.

[28] D. Liu, J. Wu, and D. Yu, "The superconvergence of the Newton-Cotes rule for Cauchy principal value integrals," *Journal of Computational and Applied Mathematics*, vol. 235, no. 3, pp. 696–707, 2010.

[29] J. Li, Y. L. Cheng, and Z. C. Li, "Superconvergence of the composite rectangle rule for computing hypersingular integral on interval," *Numerical Mathematics: Theory, Methods and Applications*, vol. 13, no. 3, pp. 770–787, 2020.

[30] P. Linz, "On the approximate computation of certain strongly singular integrals," *Computing*, vol. 35, no. 3-4, pp. 345–353, 1985.

[31] F. Lin, "On error for Cauchy principal integrals and Cauchy-type integrals under perturbation of integral curve and their applications," *Complex Variables and Elliptic Equations*, vol. 60, no. 11, pp. 1457–1474, 2015.

[32] J. Li, Q. Zhao, and H. Huang, "Error expansion of piecewise constant interpolation rule for certain two-dimensional Cauchy principal value integrals," *Computers & Mathematics with Applications*, vol. 72, no. 9, pp. 2119–2142, 2016.

[33] J. Li and H. Rui, "Error expansion of trapezoidal rule for certain two-dimensional Cauchy principal value integrals," *Computers & Mathematics with Applications*, vol. 74, no. 10, pp. 2608–2637, 2017.

Research Article

Numerical Solution for Third-Order Two-Point Boundary Value Problems with the Barycentric Rational Interpolation Collocation Method

Qian Ge [ID] **and Xiaoping Zhang** [ID]

School of Science, Shandong Jianzhu University, Jinan 250101, China

Correspondence should be addressed to Xiaoping Zhang; 15098931339@163.com

The numerical solution for a kind of third-order boundary value problems is discussed. With the barycentric rational interpolation collocation method, the matrix form of the third-order two-point boundary value problem is obtained, and the convergence and error analysis are obtained. In addition, some numerical examples are reported to confirm the theoretical analysis.

1. Introduction

Differential equations can give full play to their mathematical advantages in various disciplines. Combining the theory of differential equations with practical problems can build models of practical problems. Many engineering and physical problems can be transformed into the initial boundary value problems of differential equations. In these problems, only a few simple cases can be solved analytically, and most engineering problems need to be solved by numerical methods. Compared with polynomial interpolation, rational function interpolation has higher interpolation accuracy and can effectively overcome the instability of interpolation [1–4]. Barycentric rational interpolation not only has high interpolation accuracy on special distributed nodes but also has high interpolation accuracy for equidistant nodes [5–7]. This method has been used to solve certain problems such as Volterra integral equations [2, 8, 9], delay Volterra integrodifferential equations [10, 11], plane elastic problems [12], nonlinear problems [13], heat conduction equation [14], and so on [15–17].

The third-order differential equation has a wide range of applications and important theoretical values in many

scientific fields, such as applied mathematics and physics. Therefore, the third-order boundary value problem has been widely concerned by many scholars [18–20]. In this paper, we consider the numerical solution of the third-order two-point boundary value problem,

$$u'''(x) + pu''(x) + qu'(x) + ru(x) = f(x), \quad a < x < b, \tag{1}$$

$$u(a) = A, u'(a) = B, u'(b) = C, \text{ (or)}$$
$$u(a) = A, u'(a) = B, u''(a) = C, \tag{2}$$

by the barycentric rational interpolation collocation method.

Barycentric rational interpolation collocation method means using barycentric interpolation polynomials to find the differential matrix of a function at each discrete point; thus, the solution of the differential equation can be obtained by matrix operation. The barycentric rational interpolation has excellent numerical stability and high approximation accuracy, and the barycentric rational interpolation formula has a compact calculation formula of all order derivatives. Therefore, the barycentric rational interpolation collocation

method is an effective method for solving boundary value problems of differential equations.

2. Formula of the Barycentric Interpolation Collocation Method

Discretize the interval $[a, b]$ into n uniform parts with $h = ((b - a)/n)$, and suppose $u_1, u_2, \ldots, u_n$ is the function value of an unknown function u at discrete nodes $x_1, x_2, \ldots, x_n$.

For any $0 \leq d \leq n$, $P(x_i), i = 0, 1, \ldots, n - d$, is the interpolation function at the point $x_i, x_{i+1}, \ldots, x_{i+d}$; then, we have $P_i(x_k) = f(x_k), k = i, i + 1, \ldots, i + d$, and

$$r(x) = \frac{\sum_{i=0}^{n-d} \lambda_i(x) P_i(x)}{\sum_{i=0}^{n-d} \lambda_i(x)}, \tag{3}$$

where

$$\lambda_i(x) = \frac{(-1)^i}{(x - x_i) \cdots (x - x_{i+d})}. \tag{4}$$

By changing the polynomial $P_i(x)$ into the Lagrange interpolation form as

$$P_i(x) = \sum_{k=i}^{i+d} \prod_{j=i, j \neq k}^{i+d} \frac{x - x_j}{x_k - x_j} f_k \tag{5}$$

and combining (4) and (5) together, we get

$$\sum_{i=0}^{n-d} \lambda_i(x) P_i(x) = \sum_{i=0}^{n-d} (-1)^i \sum_{k=i}^{i+d} \frac{1}{x - x_k} \prod_{j=i, j \neq k}^{i+d} \frac{1}{x_k - x_j} f_k = \sum_{k=0}^{n} \frac{w_k}{x - x_k} f_k, \tag{6}$$

where $w_k = \sum_{i \in J_k} (-1)^i \prod_{j=i, j \neq k}^{i+d} (1 \ /x_k - x_j), J_k = \{i \in I; k - d \leq i \leq k\}$.

Then, we get

$$r(x) = \frac{\sum_{j=0}^{n} (w_j/x - x_j) f_j}{\sum_{j=0}^{n} (w_j/x - x_j)}, \tag{7}$$

where its basis function is

$$L_j(x) = \frac{(w_j/x - x_j)}{\sum_{k=0}^{n} (w_k/x - x_k)}. \tag{8}$$

For the equidistant point, the weight function is

$$w_j = (-1)^{n-j} C_n^j. \tag{9}$$

For the Chebyshev point of the second kind,

$$x_j = \cos \frac{j\pi}{n}, \quad j = 0, 1, \ldots, n, \tag{10}$$

the weight function is

$$w_j = (-1)^j \delta_j, \delta_j = \begin{cases} \dfrac{1}{2}, & j = 0, n, \\ \\ 1, & \text{otherwise.} \end{cases} \tag{11}$$

By formula (8), the m-th order derivative of $u(x)$ at the nodes $x_1, x_2, \ldots, x_n$ can be expressed as

$$u^{(m)}(x_j) := u_i^{(m)} = \frac{d^m u(x_j)}{dx^m} = \sum_{k=1}^{n} L_k^{(m)}(x_j) u_k$$

$$= \sum_{k=1}^{n} D_{ij}^{(m)} u_k, \quad m = 1, 2, \ldots, \tag{12}$$

and then (12) can be written in the matrix form as

$$u^{(m)} = D^{(m)} u, \tag{13}$$

where $u^{(m)} = [u_1^{(m)}, u_2^{(m)}, \ldots, u_n^{(m)}]^T$ and $u = [u_1, u_2, \ldots, u_n]^T$.

By using the barycentric interpolation function as

$$u_n(x) = \sum_{j=0}^{n} L_j(x) u_j, \tag{14}$$

equation (1) can be written in the numerical form as

$$\sum_{j=0}^{n} u_j L_j''(x) + p \sum_{j=0}^{n} u_j L_j''(x) + q \sum_{j=0}^{n} u_j L_j'(x) + r \sum_{j=0}^{n} u_j L_j(x) = f(x). \tag{15}$$

By using the notation of the differential matrix, (15) can also be denoted as

$$\sum_{j=0}^{n} D_{ij}^{(3)} u_j + p \sum_{j=0}^{n} D_{ij}^{(2)} u_j + q \sum_{j=0}^{n} D_{ij}^{(1)} u_j + r$$

$$\sum_{j=0}^{n} \delta_{ij} u_j = f(x_i), \quad i = 1, 2, \ldots, n, \tag{16}$$

or the simple matrix form

$$\left[D^{(3)} + p D^{(2)} + q D^{(1)} + r I \right] \mathbf{u} = \mathbf{f}. \tag{17}$$

Boundary conditions (2) can be divided into

$$u_1 = A, u'(x_1) = \sum_{j=0}^{n} D_{1j}^{(1)} u_j = B,$$

$$u'(x_n) = \sum_{j=0}^{n} D_{nj}^{(1)} u_j = C, \text{ (or)}$$

$$u_1 = A, u'(x_1) = \sum_{j=0}^{n} D_{1j}^{(1)} u_j = B,$$

$$u''(x_1) = \sum_{j=0}^{n} D_{1j}^{(2)} u_j = C, \tag{18}$$

where $D^{(k)} = [D_{ij}^{(k)}]_{(n+1) \times (n+1)}$,

$$D_{ij}^{(1)} = \begin{cases} \dfrac{w_i}{x_i - x_j}, & i \neq j, \\[3mm] -\sum_{k \neq i} D_{ik}^{(1)}, & i = j, \end{cases}$$

$$D_{ij}^{(2)} = \begin{cases} 2\left(D_{ii}^{(1)} D_{ij}^{(1)} - \dfrac{D_{ij}^{(1)}}{x_i - x_j} \right), & i \neq j, \\[3mm] -\sum_{k \neq i} D_{ik}^{(2)}, & i = j, \end{cases} \tag{19}$$

$$D_{ij}^{(3)} = \begin{cases} 3\left(D_{ii}^{(2)} D_{ij}^{(1)} - \dfrac{D_{ij}^{(2)}}{x_i - x_j} \right), & i \neq j, \\[3mm] -\sum_{k \neq i} D_{ik}^{(3)}, & i = j. \end{cases}$$

$$\mathbf{u} = [u_0, u_1, \ldots, u_n]^T,$$

$$\mathbf{f} = [f(x_0), f(x_1), \ldots, f(x_n)]^T.$$

3. Convergence and Error Analysis

In this section, we will consider the error problem of equidistant interpolation nodes:

$$x_i = a + \frac{(b-a)}{n} i, \quad i = 0, 1, \ldots, n. \tag{20}$$

Let $u(x)$ be the solution of (1); for any $0 \leq d \leq n$, suppose $P(x_i), i = 0, 1, \ldots, n - d$, to be the barycentric interpolation function at the point $x_i, x_{i+1}, \ldots, x_{i+d}$; then, we have $P_i(x_k) = f(x_k), k = i, \quad i + 1, \ldots, i + d$, and

$$r(x) = \frac{\sum_{i=0}^{n-d} \lambda_i(x) P_i(x)}{\sum_{i=0}^{n-d} \lambda_i(x)}, \tag{21}$$

where

$$\lambda_i(x) = \frac{(-1)^i}{(x - x_i) \cdots (x - x_{i+d})}. \tag{22}$$

Then, the error function is defined as

$$e(x) := u(x) - P(x) = (x - x_i) \cdots$$
$$(x - x_{i+d})[x_i, x_{i+1}, \ldots, x_{i+d}, x] f, \tag{23}$$

and

$$e(x) = \frac{\sum_{i=0}^{n-d} \lambda_i(x)(u(x) - P_i(x))}{\sum_{i=0}^{n-d} \lambda_i(x)} = \frac{A(x)}{B(x)} = O(h^{d+1}), \tag{24}$$

where $A(x) := \sum_{i=0}^{n-d} (-1)^i [x_i, \ldots, x_{i+d}, x] f$ and $B(x) := \sum_{i=0}^{n-d} \lambda_i(x)$.

Taking the numerical form,

$$\sum_{j=0}^{n} u_j L_j''(x) + p \sum_{j=0}^{n} u_j L_j''(x) + q \sum_{j=0}^{n} u_j L_j'(x) + r$$

$$\sum_{j=0}^{n} u_j L_j(x) = f(x), \tag{25}$$

and combining (24) and (1), we get

$$e'''(x) + p e''(x) + q e'(x) + r e(x) = R_f(x), \tag{26}$$

where $R_f(x) = f(x) - f(x_k), k = 0, 1, 2, \ldots, n$.

Lemma 1. *For $e(x)$ defined in (23), we have*

$$\begin{cases} |e(x)| \leq C h^{d+1}, & u \in C^{d+2}[a, b], \\ |e'(x)| \leq C h^d, & u \in C^{d+2}[a, b], \\ |e''(x)| \leq C h^{d-1}, & u \in C^{d+3}[a, b], \quad d \geq 1, \\ |e'''(x)| \leq C h^{d-2}, & u \in C^{d+4}[a, b], \quad d \geq 2. \end{cases} \tag{27}$$

Let $u(x)$ be the solution of (1) and $u_n(x)$ be the numerical solution; then, we have

$$u_n''(x_k) + p u_n''(x_k) + q u_n'(x_k) + r u_n(x_k)$$
$$= f(x_k), \quad k = 0, 1, 2, \ldots, \ldots n \ldots, \tag{28}$$

and

$$\lim_{n \to \infty} u_n(x) = u(x). \tag{29}$$

The results can be obtained in [1].

Based on Lemma 1, we can get the following theorem.

Theorem 1. *Let* $f(x) \in C[a, b]$, $Tu(x):= u'''(x) + pu''(x) + qu'(x) + ru(x)$, *and*

$$= \begin{bmatrix} D_{00}^{(3)} + pD_{00}^{(2)} + qD_{00}^{(1)} + r & D_{01}^{(3)} + pD_{01}^{(2)} + qD_{01}^{(1)} & \cdots & D_{0n}^{(3)} + pD_{0n}^{(2)} + qD_{0n}^{(1)} \\ D_{10}^{(3)} + pD_{10}^{(2)} + qD_{10}^{(1)} & D_{11}^{(3)} + pD_{11}^{(2)} + qD_{11}^{(1)} + r & \cdots & D_{1n}^{(3)} + pD_{1n}^{(2)} + qD_{1n}^{(1)} \\ \cdots & \cdots & \cdots & \cdots \\ D_{n0}^{(3)} + pD_{n0}^{(2)} + qD_{n0}^{(1)} & D_{n1}^{(3)} + pD_{n1}^{(2)} + qD_{n1}^{(1)} & \cdots & D_{nn}^{(3)} + pD_{nn}^{(2)} + qD_{nn}^{(1)} + r \end{bmatrix}. \tag{31}$$

Add column 2, column 3,..., column n to column 1, and we have

$$L = \begin{bmatrix} r & D_{01}^{(3)} + pD_{01}^{(2)} + qD_{01}^{(1)} & \cdots & D_{0n}^{(3)} + pD_{0n}^{(2)} + qD_{0n}^{(1)} \\ r & D_{11}^{(3)} + pD_{11}^{(2)} + qD_{11}^{(1)} + r & \cdots & D_{1n}^{(3)} + pD_{1n}^{(2)} + qD_{1n}^{(1)} \\ \cdots & \cdots & \cdots & \cdots \\ r & D_{n1}^{(3)} + pD_{n1}^{(2)} + qD_{n1}^{(1)} & \cdots & D_{nn}^{(3)} + pD_{nn}^{(2)} + qD_{nn}^{(1)} + r \end{bmatrix}. \tag{32}$$

Then, we have $|\mathbf{L}| \neq 0$ with $r \neq 0$, $u_n(x) = \sum_{j=0}^{n} L_j(x) f_j$, and $u_n^*(x) = \sum_{j=0}^{n} L_j(x) f_j^*$, where $U_n = (f(x_0), f(x_1), \ldots, f(x_n))^T$ and $U_n^* = (f^*(x_0), f^*(x_1), \ldots, f^*(x_n))^T$.

By

$$U_n - U_n^* = \mathbf{L}^{-1}(\mathbf{L}U_n - F_n^*), \tag{33}$$

which means

$$u_n(x) - u_n^*(x) = \sum M_j(x) Te(x), \tag{34}$$

where $M_j(x)$ is the element of matrix $\mathbf{L}^{-1}$, we have

$$|u_n(x) - u_n^*(x)| \leq \left|\sum M_j(x)\right| |Te(x)| \leq Ch^{d-2}. \tag{35}$$

The proof is completed. □

4. Numerical Example

As an example, we consider the two-point boundary value problem:

$$y''' + y = f(x), \quad -1 < x < 1, \tag{36}$$

$$y(-1) = 0, y(1) = 0, y'(-1) = 0. \tag{37}$$

$u_n(x): Tu_n(x) = f(x), u_n^*(x): Tu_n^*(x) = f^*(x);$ *then,   we have*

$$|u_n(x) - u_n^*(x)| \leq Ch^{d-2}. \tag{30}$$

Proof. Let L: $= D^{(3)} + pD^{(2)} + qD^{(1)} + rI$

For this problem, we can find a function $f(x)$ such that the analysis solution is

$$y = (1 - x^2)(1 + x)e^{\lambda x}, \tag{38}$$

where λ is a freely selected parameter.

Substituting (38) into (36), we get

$$f(x) = \left[-6 - 6\lambda(1 + 3x) + 3\lambda^2(1 - 2x - 3x^2)\right.$$
$$\left. + \lambda^3(1 + x - x^2 - x^3) + (1 - x^2)(1 + x)\right]e^{\lambda x}. \tag{39}$$

For different values of d and different number of nodes, we can calculate the corresponding relative error and convergence rate; some of the data are shown in Tables 1 and 2.

In Table 1, the convergence rate of equidistant nodes with different d is $O(h^{d-2})$; in Table 2, the convergence rate of the Chebyshev point of the second kind with different d is $O(h^{d+2}), d \geq 2$.

For different values of λ and different number of nodes, we can calculate the corresponding relative error; some of the data are shown in Tables 3 and 4.

From Tables 3 and 4, we can find that, for different values of λ, the convergence rate can reach $O(h^{d+2})(d \geq 2)$ both for equidistant and nonequidistant nodes.

TABLE 1: Errors and convergence rate of the equidistant nodes with different d.

| n | $d = 2$ | | $d = 3$ | | $d = 4$ | | $d = 5$ | |
	Error	h^α	Error	h^α	Error	h^α	Error	h^α
				($\lambda = 2$)				
10	$7.1976e + 00$		$4.6412e + 00$		$2.4217e + 00$		$1.1522e + 00$	
20	$3.5555e + 00$	1.0175	$1.2336e + 00$	1.9117	$3.6419e - 01$	2.7333	$9.9594e - 02$	3.5322
40	$1.4588e + 00$	1.2853	$2.6378e - 01$	2.2254	$4.1431e - 02$	3.1359	$6.0309e - 03$	4.0456
80	$5.5050e - 01$	1.4060	$5.1045e - 02$	2.3695	$4.1384e - 03$	3.3236	$3.1073e - 04$	4.2786
160	$2.0058e - 01$	1.4566	$9.4229e - 03$	2.4375	$3.8810e - 04$	3.4146	$1.4799e - 05$	4.3921
320	$7.1879e - 02$	1.4806	$1.7004e - 03$	2.4703	$3.5301e - 05$	3.4586	$6.7836e - 07$	4.4473
640	$2.5569e - 02$	1.4912	$3.0357e - 04$	2.4858	$3.1616e - 06$	3.4810	$3.1718e - 08$	4.4187
1280	$9.0650e - 03$	1.4960	$5.3912e - 05$	2.4933	$2.8666e - 07$	3.4632	$1.2685e - 08$	1.3222

TABLE 2: Errors and convergence rate of the Chebyshev point with different d.

| n | $d = 2$ | | $d = 3$ | | $d = 4$ | | $d = 5$ | |
	Error	h^α	Error	h^α	Error	h^α	Error	h^α
				($\lambda = 2$)				
10	$2.4329e + 00$		$1.3897e + 00$		$2.5216e - 01$		$1.1033e - 01$	
20	$8.8604e - 01$	1.4572	$1.3680e - 02$	6.6665	$4.5076e - 03$	5.8058	$1.5195e - 03$	6.1821
40	$1.8242e - 01$	2.2801	$2.8639e - 03$	2.2561	$1.4419e - 04$	4.9664	$7.2659e - 06$	7.7082
80	$3.2188e - 02$	2.5026	$1.7517e - 04$	4.0311	$3.0543e - 06$	5.5610	$1.0125e - 07$	6.1652
160	$5.2215e - 03$	2.6240	$8.5892e - 06$	4.3501	$5.9098e - 08$	5.6916	$1.0071e - 06$	—
320	$8.0770e - 04$	2.6926	$2.9760e - 07$	4.8511	$1.9760e - 06$	—	$2.2948e - 05$	—
640	$1.2077e - 04$	2.7416	$2.8632e - 06$	—	$6.856e - 05$	—	$1.0211e - 03$	—
1280	$1.7925e - 05$	2.7522	$7.4861e - 05$	—	$1.2910e - 02$	—	$9.6669e - 02$	—

TABLE 3: Errors and convergence rate of the equidistant nodes with different λ.

| n | $\lambda = -5$ | | $\lambda = 1$ | | $\lambda = 5$ | | $\lambda = 20$ | |
	Error	h^α	Error	h^α	Error	h^α	Error	h^α
				($d = 4$)				
10	$3.6809e + 01$		$2.2939e - 01$		$2.1508e + 02$		$3.0238e + 08$	
20	$1.3259e + 01$	1.4731	$2.6894e - 02$	3.0925	$6.1838e + 01$	1.7983	$8.0305e + 08$	—
40	$2.2319e + 00$	2.5707	$2.7208e - 03$	3.3052	$9.5448e + 00$	2.6957	$6.7632e + 08$	$2.4778e - 01$
80	$2.6875e - 01$	3.0539	$2.5675e - 04$	3.4056	$1.1054e + 00$	3.1101	$1.6623e + 08$	2.0246
160	$2.7599e - 02$	3.2835	$2.3416e - 05$	3.4548	$1.1147e - 01$	3.3098	$2.4028e + 07$	2.7904
320	$2.6249e - 03$	3.3943	$2.1009e - 06$	3.4784	$1.0509e - 02$	3.4070	$2.7001e + 06$	3.1536

TABLE 4: Errors and convergence rate of the Chebyshev point with different λ.

| n | $\lambda = -5$ | | $\lambda = 1$ | | $\lambda = 5$ | | $\lambda = 20$ | |
	Error	h^α	Error	h^α	Error	h^α	Error	h^α
				($d = 4$)				
10	$1.0975e + 01$		$1.8992e - 02$		$4.4245e + 01$		$1.3431e\_01$	
20	$1.5012e - 01$	6.1919	$2.6112e - 04$	6.1845	$1.3603e + 00$	5.0235	$2.5740e + 08$	2.3835
40	$5.5289e - 03$	4.7630	$8.0762e - 06$	5.0149	$4.7712e - 02$	4.8334	$1.4800e + 07$	4.1204
80	$1.1729e - 04$	5.5589	$1.6777e - 07$	5.5891	$1.0350e - 03$	5.5267	$3.5715e + 05$	5.3729
160	$2.2528e - 06$	5.7022	$1.8130e - 08$	3.2100	$2.3528e - 05$	5.4591	$8.3139e + 03$	5.4249
320	$1.3043e - 05$	—	$2.5236e - 06$	—	$2.4682e - 06$	3.2529	$2.1982e + 02$	5.2411

5. Conclusion

In this paper, the barycentric rational collocation method for solving third-order two-point boundary value equations is presented, and the error function of the convergence rate $O(h^{d-2})$ is also obtained. For the constant coefficient and variable coefficient of two-point boundary value equations, numerical results show that the convergence rate can reach $O(h^{d-2})$ for the equidistant nodes and Chebyshev point of the second kind with $d \geq 2$, so the barycentric rational collocation method is an effective method. Compared with other methods, the advantage of this method is that the matrix equation can be easily obtained, the program is simple, and high computational accuracy can be obtained by using a few points.

Data Availability

The data that support the findings of this study are available from the corresponding author upon reasonable request.

Conflicts of Interest

The authors declare that there are no conflicts of interest regarding the publication of this paper.

Acknowledgments

References

[1] J.-P. Berrut, M. S. Floater, and G. Klein, "Convergence rates of derivatives of a family of barycentric rational interpolants," *Applied Numerical Mathematics*, vol. 61, no. 9, pp. 989–1000, 2011.

[2] J.-P. Berrut, S. A. Hosseini, and G. Klein, "The linear barycentric rational quadrature method for Volterra integral equations," *SIAM Journal on Scientific Computing*, vol. 36, no. 1, pp. 105–123, 2014.

[3] J.-P. Berrut and G. Klein, "Recent advances in linear barycentric rational interpolation," *Journal of Computational and Applied Mathematics*, vol. 259, pp. 95–107, 2014.

[4] A. Gillette, A. Rand, and C. Bajaj, "Error estimates for generalized barycentric interpolation," *Advances in Computational Mathematics*, vol. 37, no. 3, pp. 417–439, 2012.

[5] G. Klein and J.-P. Berrut, "Linear rational finite differences from derivatives of barycentric rational interpolants," *SIAM Journal on Numerical Analysis*, vol. 50, no. 2, pp. 643–656, 2012.

[6] G. Klein and J.-P. Berrut, "Linear barycentric rational quadrature," *BIT Numerical Mathematics*, vol. 52, no. 2, pp. 407–424, 2012.

[7] M. S. Floater and K. Hormann, "Barycentric rational interpolation with no poles and high rates of approximation," *Numerische Mathematik*, vol. 107, no. 2, pp. 315–331, 2007.

[8] J. Li and Y. Cheng, "Linear barycentric rational collocation method for solving second-order Volterra integro-differential equation," *Computational and Applied Mathematics*, vol. 39, no. 2, pp. A1936–A1960, 2020.

[9] M. Li and C. Huang, "The linear barycentric rational quadrature method for auto-convolution Volterra integral equations," *Journal of Scientific Computing*, vol. 78, no. 1, pp. 549–564, 2019.

[10] A. Abdi, J.-P. Berrut, and S. A. Hosseini, "The linear barycentric rational method for a class of Delay Volterra integro-differential equations," *Journal of Scientific Computing*, vol. 75, no. 3, pp. 1757–1775, 2018.

[11] J. Li and Y. Cheng, "Numerical solution of Volterra integro-differential equations with linear barycentric rational method," *International Journal of Applied and Computational Mathematics*, vol. 6, p. 137, 2020.

[12] Z. Wang, L. Zhang, Z. Xu, and J. Li, "Barycentric interpolation collocation method based on mixed displacement-stress formulation for solving plane elastic problems," *Chinese Journal of Applied Mechanics*, vol. 35, no. 2, pp. 304–309, 2018.

[13] Z. Wang and S. Li, *Barycentric Interpolation Collocation Method for Nonlinear Problems*, National Defense Industry Press, Beijing, China, 2015.

[14] J. Li and Y. Cheng, "Linear barycentric rational collocation method for solving heat conduction equation," *Numerical Methods for Partial Differential Equations*, vol. 37, no. 1, pp. 533–545, 2021.

[15] E. Cirillo and K. Hormann, "On the Lebesgue constant of barycentric rational Hermite interpolants at equidistant nodes," *Journal of Computational and Applied Mathematics*, vol. 349, pp. 292–301, 2019.

[16] Z. Wang, Z. Xu, and J. Li, "Mixed barycentric interpolation collocation method of displacement-pressure for incompressible plane elastic problems," *Chinese Journal of Applied Mechanics*, vol. 35, no. 3, pp. 195–201, 2018.

[17] J. Li and Y. Cheng, "Barycentric rational method for solving biharmonic equation by depression of order," *Numerical Methods for Partial Differential Equations*, pp. 1–15, 2020.

[18] E. Ugurlu, "Some singular third-order boundary value problems," *Mathematical Methods in the Applied Sciences*, vol. 43, pp. 2202–2215, 2020.

[19] X. Feng, H. Feng, and H. Tan, "Existence and iteration of positive solutions for third-order Sturm-Liouville boundary value problems with p-Laplacian," *Applied Mathematics and Computation*, vol. 266, pp. 634–641, 2015.

[20] M. Abushammala, S. A. Khuri, and A. Sayfy, "A novel fixed point iteration method for the solution of third order boundary value problems," *Applied Mathematics and Computation*, vol. 271, pp. 131–141, 2015.

Research Article

Exact Solution for the Torsional Vibration of an Elastic Pile in a Radially Inhomogeneous Saturated Soil

Xibin Li [ID],[1] **Zhiqing Zhang** [ID],[1] **and Jianchao Sheng**[2]

[1]*School of Landscape Architecture, Zhejiang A & F University, Hangzhou, Zhejiang 311300, China*
[2]*School of Civil Engineering, Shaoxing University, Shaoxing, Zhejiang 312000, China*

Correspondence should be addressed to Zhiqing Zhang; zhangzhiqing2000@163.com

An exact solution is proposed to study the time-harmonic torsional vibration of an elastic pile embedded in a radially inhomogeneous saturated soil. The radially inhomogeneous saturated soil is composed of inner disturbed and outer semi-infinite undisturbed concentric annular regions, with the shear modulus of the inner region changing in an exponential form along the radial direction. The governing equation of each region of the saturated soil is solved through rigorous mathematical derivation and the soil torsional impedance is derived with an exact and explicit expression. Making use of the boundary and continuity conditions of the pile-soil system, the torsional complex stiffness at the pile top is obtained in an exact closed form in the frequency domain. Selected numerical results are presented to investigate the influence of the radial inhomogeneity of the surrounding soil on the vibration characteristics of the pile-soil system.

1. Introduction

Soil-structure dynamic interaction problem, including the interaction between a loaded rigid disc (footing) and the adjacent soil and the interaction between the pile and surrounding soil, has been the subject of extensive studies in civil engineering for many years. For these interaction problems, the establishment of a dynamic model of the soil medium and the corresponding solution is the key to study the vibration characteristics of the soil-structure system. For instance, Pan et al. [1] and Zhang and Pan [2] used fundamental solutions of the surface/buried annular patch torsional load on/in the soil medium and then solved the dynamic impedance of the rigid circular disc via integral least-square approach. Pak and Abedzadeh [3] used boundary integral technique to determine the reaction of the soil and finally proposed the solution for the rigid circular disc under time-harmonic torsional load. For the pile-soil dynamic interaction problem, the analytical method [4, 5] and numerical method [6] are developed to solve the torsional vibration of an elastic pile embedded in a homogeneous or layered soil medium.

It should be pointed out that when studying pile-soil torsional vibration problems, the surrounding soil was mostly regarded as a radially uniform medium. However, in actual engineering, no matter precast piles or cast-in-place piles, they are bound to disturb or squeeze the surrounding soil in a certain range during the construction process. Therefore, the properties of the soil around the pile body (e.g., shear modulus of the soil) inevitably have continuous variation, so the soil shows obvious radial inhomogeneity. In an early study, Novak and Sheta [7] proposed a radially inhomogeneous medium model based on the assumption of plane strain and analyzed the torsional and longitudinal impedance of the weakened soil in the inner region induced by the construction of the pile. Afterwards, researchers conducted detailed analyses on the torsional and longitudinal vibration characteristics of the radially inhomogeneous soils. However, these studies regarded the foundation soil as a single-phase medium [8–13].

It is worth noting that saturated soil is very common in engineering practice. Since Biot [14, 15] established the theory of wave propagation in fluid-saturated porous medium, this theory has been widely used in engineering. Li

et al. [16] studied the torsional vibration of an elastic pile embedded in an inhomogeneous saturated soil, but the solution is actually semianalytical due to the fact that the surrounding soil is subdivided into many sublayers to simulate the continuous change of soil properties. Considering the deficiencies of previous research, the objective of the present study is to propose an exact solution to study the time-harmonic torsional vibration of an elastic pile embedded in a radially inhomogeneous saturated soil with soil modulus changing in an exponential form along the radial direction. Based on the derived solution, the influence of the characteristic parameters of the radially inhomogeneous soil on the torsional impedance of the soil and the torsional complex stiffness at the pile top is analyzed in detail. The exact solution presented in this study can be served as benchmarks for future numerical simulations.

2. Statement of the Boundary-Value Problem

2.1. Geometric Model and Assumptions. The problem to be solved is illustrated in Figure 1, where an elastic circular pile of radius r_0 and length H is embedded in a radially inhomogeneous saturated soil. The elastic pile is subjected to a time-harmonic torsional load $T_0 e^{i\omega t}$, in which ω and t are the circular frequency of excitation and time variable, respectively. In view of the symmetry of the problem, the cylindrical coordinate system (r, θ, z) is attached to the saturated soil layer with its origin at the center of the pile top and on the surface of soil layer. Considering the influence of construction disturbance in pile driving process, the surrounding saturated soil can be modeled as two concentric annular regions: one is a disturbed soil region with a radial thickness t_m, and the other is a radially semi-infinite, undisturbed uniform soil region. The distance from the interface of the two regions to the center of the pile is R_0. In order to establish a mathematical model for this problem, it is assumed that the pile is well bonded with the surrounding soil, and the interface between two regions is also in perfect contact. Based on the study by Dotsos and Veletsos [10], the shear modulus of the soil in the inner disturbed region is assumed to change in an exponential form along the radial direction.

In order to simulate the exponential change of the shear modulus of the soil in the inner region along the radial

direction (see Figure 2), the complex shear modulus of the soil in the inner and outer regions can be expressed as

$$G_s^*(r) = \begin{cases} G_{sm}(1 + iD_{sm})(r/r_0)^m, & (r_0 \le r \le R_0), \\ G_{s0}(1 + iD_{s0}), & (r \ge R_0), \end{cases} \quad (1)$$

where G_{s0} and G_{sm} are, respectively, the shear moduli of the soil in the outer undisturbed region and at the pile-soil interface; D_{s0} and D_{sm} are the corresponding soil damping coefficients, respectively; $i = (-1)^{0.5}$; m is a real number with $m \ne 1$ representing the continuous change of shear modulus in an exponential form and $m = 1$ representing the continuous change of shear modulus in a reduced linear form.

Considering the continuous change of the soil shear modulus and according to equation (1), the following relationship exists at the interface between the inner and outer soil regions:

$$G_{sm}\left(\frac{R_0}{r_0}\right)^m = G_{s0}. \quad (2)$$

2.2. Governing Equation. According to the dynamic consolidation theory proposed by Biot [14, 15], the equation of motion of the soil under dynamic torsional load can be written as

$$\frac{\partial \sigma_{r\theta}}{\partial r} + \frac{\partial \sigma_{\theta z}}{\partial z} + 2\frac{\sigma_{r\theta}}{r} = \rho\frac{\partial^2 u_\theta(r, z, t)}{\partial t^2} + \rho_f\frac{\partial^2 w_\theta(r, z, t)}{\partial t^2}, \quad (3)$$

where $u_\theta(r, t)$ and $w_\theta(r, t)$ are, respectively, the circumferential displacement of the solid phase and that of the fluid phase relative to the solid phase; $\sigma_{ij}(i, j = r, \theta, z)$ represents the total stress components; ρ_s and ρ_f are the densities of soil phase and pore fluid, respectively; $\rho = (1 - n)\rho_s + n\rho_f$ is the density of the soil, with n being the porosity of the soil.

Militano and Rajapakse [17] pointed out that neglecting the gradient of the soil stress component along z direction has negligible influence on the dynamic response of the pile. Therefore, under the same assumptions and considering the continuous change of the shear modulus of the soil, the equation of motion of the soil can be further expressed as

$$G_s^*(r)\left(\frac{\partial^2 u_\theta(r, t)}{\partial r^2} + \frac{1}{r}\frac{\partial u_\theta(r, t)}{\partial r} - \frac{u_\theta(r, t)}{r^2}\right) + \frac{dG_s^*(r)}{dr}\left(\frac{\partial u_\theta(r, t)}{\partial r} - \frac{u_\theta(r, t)}{r}\right)$$

$$= \rho\frac{\partial^2 u_\theta(r, t)}{\partial t^2} + \rho_f\frac{\partial^2 w_\theta(r, t)}{\partial t^2}. \quad (4)$$
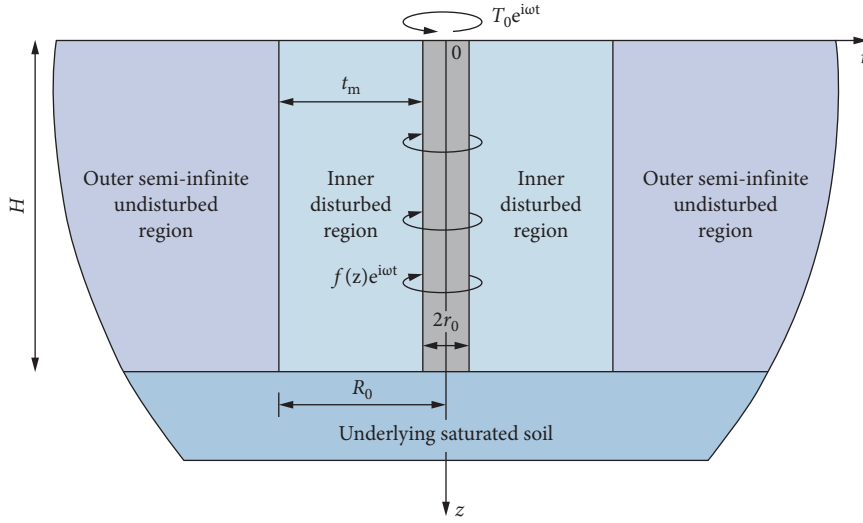
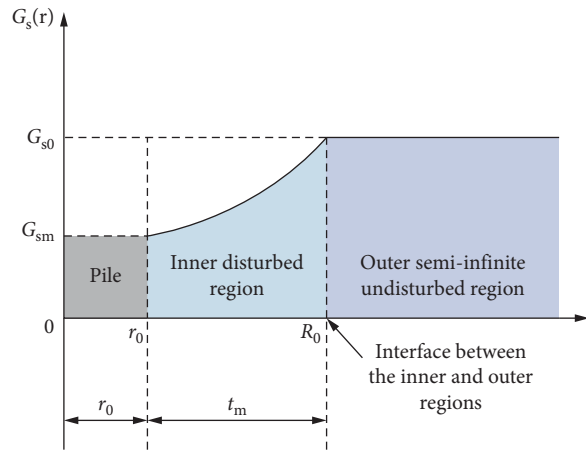FIGURE 1: Dynamic torsional interaction between an elastic pile and a radially inhomogeneous saturated soil.

FIGURE 2: Diagrammatic sketch of the radially inhomogeneous soil.

Substituting equation (1) into equation (4), we have

$$G_{sm}\left(1 + iD_{sm}\right)\left(\frac{r}{r_0}\right)^m\left(\frac{\partial^2 u_\theta(r,t)}{\partial r^2} + \frac{1}{r}\frac{\partial u_\theta(r,t)}{\partial r} - \frac{u_\theta(r,t)}{r^2}\right) + \frac{mG_{sm}\left(1 + iD_{sm}\right)}{r_0}\left(\frac{r}{r_0}\right)^{m-1}\left(\frac{\partial u_\theta(r,t)}{\partial r} - \frac{u_\theta(r,t)}{r}\right)$$

$$= \rho_m\frac{\partial^2 u_\theta(r,t)}{\partial t^2} + \rho_{fm}\frac{\partial^2 w_\theta(r,t)}{\partial t^2}, \quad \left(r_0 \leq r \leq R_0\right),$$

(5)

$$G_{s0}\left(1 + iD_{s0}\right)\left(\frac{\partial^2 u_\theta(r,t)}{\partial r^2} + \frac{1}{r}\frac{\partial u_\theta(r,t)}{\partial r} - \frac{u_\theta(r,t)}{r^2}\right) = \rho_0\frac{\partial^2 u_\theta(r,t)}{\partial t^2} + \rho_{f0}\frac{\partial^2 w_\theta(r,t)}{\partial t^2}, \quad \left(r \geq R_0\right),$$

(6)

where $\rho_m = (1 - n_m)\rho_{sm} + n_m\rho_{fm}$ and $\rho_0 = (1 - n_0)\rho_{s0} + n_0\rho_{f0}$ are the densities of soil in disturbed and undisturbed regions, respectively; ρ_{sm} (ρ_{s0}), ρ_{fm} (ρ_{f0}), and n_m (n_0) are the densities of solid phase and fluid phase and porosities in disturbed (and undisturbed) regions, respectively.

The fluid motion equation of the saturated soil medium can be expressed in the following simplified form [18, 19]:

$$\frac{\rho_{fm}g}{k_{dm}}\frac{\partial w_\theta(r,t)}{\partial t} + \rho_{fm}\frac{\partial^2 u_\theta(r,t)}{\partial t^2} + \frac{\rho_{fm}}{n_m}\frac{\partial^2 w_\theta(r,t)}{\partial t^2} = 0, \quad (r_0 \le r \le R_0),$$

$$\frac{\rho_{f0}g}{k_{d0}}\frac{\partial w_\theta(r,t)}{\partial t} + \rho_{f0}\frac{\partial^2 u_\theta(r,t)}{\partial t^2} + \frac{\rho_{f0}}{n_0}\frac{\partial^2 w_\theta(r,t)}{\partial t^2} = 0, \quad (r \ge R_0),$$

$$(7)$$

where k_{dm} and k_{d0} are the horizontal dynamic permeability coefficients of saturated soil in disturbed and undisturbed regions, respectively, and g is the acceleration of gravity.

Due to the time-harmonic vibration of the pile-soil system, $u_\theta(r, t)$ and $w_\theta(r, t)$ can be further expressed as

$$\begin{cases} u_\theta(r,t) &= u_\theta(r)e^{i\omega t} = u_\theta e^{i\omega t}, \\ w_\theta(r,t) &= w_\theta(r)e^{i\omega t} = w_\theta e^{i\omega t}, \end{cases} \quad (8)$$

where $u_\theta = u_\theta(r)$ and $w_\theta = w_\theta(r)$ are, respectively, the amplitude of circumferential displacement of the solid phase and that of the relative circumferential displacement of the fluid phase to the solid phase.

Combining equations (5)–(8) and introducing $\xi = r/r_0$, the governing equation for the radially inhomogeneous saturated soil can be expressed as

$$\xi^2\frac{d^2 u_\theta}{d\xi^2} + \xi(1+m)\frac{du_\theta}{d\xi} - \left(1 + m + \lambda_m^2\xi^{2-m}\right)u_\theta = 0, \quad (1 \le \xi \le \xi_0),$$

$$\xi^2\frac{d^2 u_\theta}{d\xi^2} + \xi\frac{du_\theta}{d\xi} - \left(1 + \lambda_0^2\xi^2\right)u_\theta = 0, \quad (\xi \ge \xi_0),$$

$$(9)$$

where

$$b_m = \frac{n_m\rho_{fm}g}{k_{dm}},$$

$$b_0 = \frac{n_0\rho_{f0}g}{k_{d0}},$$

$$\lambda_m = i\omega r_0\left[\frac{1}{G_{sm}(1+iD_{sm})}\left(\rho_m + \frac{n_m\rho_{fm}\omega}{(ib_m/\rho_{fm})-\omega}\right)\right]^{(1/2)},$$

$$\lambda_0 = i\omega r_0\left[\frac{1}{G_{s0}(1+iD_{s0})}\left(\rho_0 + \frac{n_0\rho_{f0}\omega}{(ib_0/\rho_{f0})-\omega}\right)\right]^{(1/2)},$$

$$\xi_0 = \frac{R_0}{r_0}.$$

$$(10)$$

Given that the elastic pile is forced to vibrate under the action of the time-harmonic torsional load at the pile top, the equation of motion of pile can be expressed as

$$G_p\frac{\partial^2}{\partial z^2}\left[\phi(z)e^{i\omega t}\right] + \frac{4f(z)e^{i\omega t}}{r_0^2} = \rho_p\frac{\partial^2}{\partial t^2}\left[\phi(z)e^{i\omega t}\right], \quad (11)$$

where ρ_p, G_p, and r_0 are the density, shear modulus, and radius of the pile, respectively, and $f(z)$ is the amplitude of the circumferential shear stress at the pile-soil interface.

2.3. Boundary and Continuity Conditions of Pile-Soil System. Given that the displacement of the soil at infinity tends to zero, the following relationship holds:

$$u_\theta(r \longrightarrow \infty) = 0. \quad (12)$$

It is assumed that the soil at the interface between inner and outer soil regions (i.e., $r = R_0$) is well bonded. Then, continuity conditions at $r = R_0$ can be written as

$$u_\theta(r = R_{0-}) = u_\theta(r = R_{0+}),$$
$$\tau_{r\theta}(r = R_{0-}) = \tau_{r\theta}(r = R_{0+}). \quad (13)$$

The boundary conditions of the pile can be expressed as

$$\frac{d\phi(z)}{dz}\Big|_{z=0} = -\frac{T_0}{G_pI_p},$$

$$\left[\frac{d\phi(z)}{dz} + \frac{\phi(z)k_{pb}}{G_pI_p}\right]\Big|_{z=H} = 0, \quad (14)$$

where $I_p = (\pi r_0^4/2)$ is the polar moment of inertia of the pile. It is noted that it is reasonable to use the static stiffness of the disc with the same radius on the surface of the elastic half-space to simulate the stiffness of the pile bottom [17]. That is to say, the supporting stiffness coefficient k_{pb} of the pile bottom is taken as $(16G_{sb}r_0^3/3)$ with G_{sb} being the shear modulus of the soil at the bottom of the pile.

The continuity conditions between pile and soil interface can be expressed as

$$u_\theta|_{r=r_0} = \phi(z)r_0,$$

$$\tau_{r\theta}|_{r=r_0} = G_{sm}(1+iD_{sm})\left(\frac{du_\theta}{dr} - \frac{u_\theta}{r}\right)\Big|_{r=r_0} = f(z). \quad (15)$$

3. Solution of the Pile-Soil System

When $m \ne 2$, the solutions of equation (9) can be expressed as

$$u_\theta = \xi^{(-m/2)}\left[A_1K_{2\kappa-1}\left(\kappa\lambda_m\xi^{(1/\kappa)}\right) + B_1I_{2\kappa-1}\left(\kappa\lambda_m\xi^{(1/\kappa)}\right)\right], \quad (1 \le \xi \le \xi_0),$$

$$u_\theta = C_1K_1(\lambda_0\xi) + D_1I_1(\lambda_0\xi), \quad (\xi \ge \xi_0),$$

$$(16)$$

where

$$\kappa = \left(\frac{2}{2-m}\right). \tag{17}$$

Substituting the boundary condition given in equation (12) into equation (16) and making use of the behavior of the modified Bessel function, we have

$$D_1 = 0. \tag{18}$$

Substituting the continuity condition given in equation (13) into equation (16) yields

$$A_1 K_{2\kappa-1}\left(\kappa\lambda_m\xi_0^{(1/\kappa)}\right) + B_1 I_{2\kappa-1}\left(\kappa\lambda_m\xi_0^{(1/\kappa)}\right) = C_1\xi_0^{(m/2)}K_1\left(\lambda_0\xi_0\right), \tag{19}$$

$$-A_1 K_{2\kappa}\left(\kappa\lambda_m\xi_0^{(1/\kappa)}\right) + B_1 I_{2\kappa}\left(\kappa\lambda_m\xi_0^{(1/\kappa)}\right) = -C_1\sqrt{\frac{1+iD_{s0}}{GR\left(1+iD_{sm}\right)}}K_2\left(\lambda_0\xi_0\right), \tag{20}$$

where A_1, B_1, and C_1 are undetermined constants; $GR = G_{sm}/G_{s0}$ reflects the softening or hardening degree of the soil. $GR = 1$ denotes the homogeneous soil, $GR > 1$ denotes the strengthened soil, and $GR < 1$ denotes the weakened soil. It is noted that, for the weakened soil,

smaller GR is associated with the larger softening degree, while for the strengthened soil, greater GR is corresponding to the larger hardening degree.

Combining equations (19) and (20), the following relationship between A_1 and B_1 can be determined:

$$Q_1 = \frac{A_1}{B_1} = \frac{\sqrt{\left(\left(1+iD_{s0}\right)/\left(GR\left(1+iD_{sm}\right)\right)\right)}K_2\left(\lambda_0\xi_0\right)I_{2\kappa-1}\left(\kappa\lambda_m\xi_0^{(1/\kappa)}\right) + \xi_0^{(m/2)}K_1\left(\lambda_0\xi_0\right)I_{2\kappa}\left(\kappa\lambda_m\xi_0^{(1/\kappa)}\right)}{-\sqrt{\left(\left(1+iD_{s0}\right)/\left(GR\left(1+iD_{sm}\right)\right)\right)}K_2\left(\lambda_0\xi_0\right)K_{2\kappa-1}\left(\kappa\lambda_m\xi_0^{(1/\kappa)}\right) + \xi_0^{(m/2)}K_1\left(\lambda_0\xi_0\right)K_{2\kappa}\left(\kappa\lambda_m\xi_0^{(1/\kappa)}\right)}. \tag{21}$$

The circumferential shear stress at the pile-soil interface (i.e., at $r = r_0$) can be further expressed as

$$\begin{aligned}\tau_{r\theta}\left(r = r_0\right) &= \frac{G_{sm}\left(1+iD_{sm}\right)}{r_0}\left(\frac{du_\theta}{d\xi} - \frac{u_\theta}{\xi}\right)\Big|_{\xi=1} \\ &= \frac{1}{r_0}G_{sm}\left(1+iD_{sm}\right)\lambda_m\xi^{-(m/2)+(1/\kappa)-1}B_1\left[-Q_1 K_{2\kappa}\left(\kappa\lambda_m\xi^{(1/\kappa)}\right) + I_{2\kappa}\left(\kappa\lambda_m\xi^{(1/\kappa)}\right)\right].\end{aligned} \tag{22}$$

The torsional impedance of the soil can be defined as

$$K_\theta = -\frac{2\pi r_0^3\tau_{r\theta}\left(r = r_0\right)}{u_\theta\left(r = r_0\right)} = 2\pi G_{sm}\left(1+iD_{sm}\right)\lambda_m r_0^2\frac{Q_1 K_{2\kappa}\left(\kappa\lambda_m\right) - I_{2\kappa}\left(\kappa\lambda_m\right)}{Q_1 K_{2\kappa-1}\left(\kappa\lambda_m\right) + I_{2\kappa-1}\left(\kappa\lambda_m\right)}, \tag{23}$$

where K_θ is the torsional impedance of the soil.

For the convenience of subsequent analysis, K_θ can be further expressed as follows:

$$K_\theta = G_{s0}r_0^2\left(S_{w1} + iS_{w2}\right), \tag{24}$$

where S_{w1} and S_{w2} are the stiffness and damping parts of the torsional impedance of the radially inhomogeneous soil, respectively.

Based on equations (16) and (21), the circumferential displacement of the solid phase at the pile-soil interface can be expressed as

$$u_\theta\left(r = r_0\right) = B_1\left[Q_1 K_{2\kappa-1}\left(\kappa\lambda_m\right) + I_{2\kappa-1}\left(\kappa\lambda_m\right)\right]. \tag{25}$$

Substituting the continuity condition given in equation (15) into equation (25) results in

$$B_1 = \frac{\phi(z)r_0}{Q_1 K_{2\kappa-1}(\kappa\lambda_m) + I_{2\kappa-1}(\kappa\lambda_m)}. \tag{26}$$

Then, the shear stress at the pile-soil interface can be further expressed as

$$\tau_{r\theta}(r = r_0) = G_{sm}(1 + iD_{sm})\lambda_m \frac{-Q_1 K_{2\kappa}(\kappa\lambda_m) + I_{2\kappa}(\kappa\lambda_m)}{Q_1 K_{2\kappa-1}(\kappa\lambda_m) + I_{2\kappa-1}(\kappa\lambda_m)}\phi(z). \tag{27}$$

Substituting equation (27) into equation (11), the governing equation of the pile under time-harmonic torsional load can be rewritten as

$$\frac{d^2\phi(z)}{dz^2} + \left[\frac{4G_{sm}(1 + iD_{sm})\lambda_m}{G_p r_0^2}\frac{-Q_1 K_{2\kappa}(\kappa\lambda_m) + I_{2\kappa}(\kappa\lambda_m)}{Q_1 K_{2\kappa-1}(\kappa\lambda_m) + I_{2\kappa-1}(\kappa\lambda_m)} + \frac{\rho_p\omega^2}{G_p}\right]\phi(z) = 0. \tag{28}$$

The general solution of ordinary differential equation (28) can be expressed as

$$\phi(z) = \alpha_1 \cos(\gamma_1 z) + \alpha_2 \sin(\gamma_1 z), \tag{29}$$

in which

$$\gamma_1 = \left[\frac{4G_{sm}(1 + iD_{sm})\lambda_m}{G_p r_0^2}\frac{-Q_1 K_{2\kappa}(\kappa\lambda_m) + I_{2\kappa}(\kappa\lambda_m)}{Q_1 K_{2\kappa-1}(\kappa\lambda_m) + I_{2\kappa-1}(\kappa\lambda_m)} + \frac{\rho_p\omega^2}{G_p}\right]^{(1/2)}, \tag{30}$$

where α_1 and α_2 are constants to be determined by the boundary conditions.

Substituting the boundary conditions of the pile given in equation (14) into equation (29), we have

$$\alpha_1 = -\frac{T_0}{G_p I_p \gamma_1 \tan(\gamma_1 H - \varphi_1)},$$
$$\alpha_2 = -\frac{T_0}{G_p I_p \gamma_1}, \tag{31}$$

where $\varphi_1 = \arctan[\bar{k}_{pb}/\gamma_1 H]$ is the phase angle and $\bar{k}_{pb} = (k_{pb}H/G_p I_p)$ is the dimensionless pile bottom supporting coefficient.

According to the definition of the torsional complex stiffness at the pile top proposed by Militano and Rajapakse [17], the dimensionless torsional complex stiffness k_T at the pile top can be expressed as

$$k_T = \frac{3T_0}{16G_{s0}r_0^3\phi(z = 0)} = \frac{3\pi r_0\bar{\mu}\gamma_1 \tan(\gamma_1 H - \varphi_1)}{32}, \tag{32}$$

where $\bar{\mu} = (G_p/G_{s0})$ is the pile-soil modulus ratio.

For the convenience in the subsequent analysis, the torsional complex stiffness at the pile top can be expressed in the following dimensionless form:

$$k_T = k_{T1} + ik_{T2}, \tag{33}$$

where k_{T1} is the real part of the complex stiffness at the pile top, which represents the real stiffness of the pile, and k_{T2} is the imaginary part of the complex stiffness at the pile top, which reflects the energy dissipation.

It is noted that the above solution is corresponding to the case where $m \neq 2$. When $m = 2$, the denominator in equation (17) is equal to zero, and the above solution does hold. Therefore, the solution corresponding to $m = 2$ is listed in Appendix A.

4. Results and Discussion

4.1. Torsional Impedance of the Soil. This section will mainly study the influence of soil radial heterogeneity caused by pile driving on the torsional impedance of the soil. It is worth noting that when the value of m is given (see equation (2)), there is a definite relationship between t_m/r_0 and $GR = G_{sm}/G_{s0}$, and these two values cannot be changed arbitrarily. The soil parameters used in the following calculation are listed in Table 1.

We first compare the reduced radially inhomogeneous single-phase medium solution (i.e., dry soil solution with setting $\rho_f = n = 0$) with the homogeneous single-phase solution of Novak et al. [20] to study the changing trend of soil torsional impedance corresponding to different softening and hardening degree of the soil. It can be seen from Figure 3 that, in the whole frequency range, the stiffness and damping parts of the torsional impedance (e.g., $GR = 0.25$) corresponding to the weakened soil case are lower than those of the homogeneous medium solution by Novak et al. [20]. It is indicated that the torsional impedance of the weakened soil is remarkably lower than that of the undisturbed soil. Meanwhile, it can also be observed from Figure 3 that the stiffness and damping parts (e.g., $GR = 2$) corresponding to the strengthened soil case are greater than those of the homogeneous medium solution by Novak et al. [20]. It means that the torsional impedance of the strengthened soil is remarkably greater than that of the undisturbed soil. Hence, it is important to consider the radial inhomogeneity of the soil when the surrounding soil is disturbed during the construction.

Figure 4 depicts the comparison of soil torsional impedance between the radially inhomogeneous saturated soil and the corresponding dry soil. It can be seen from Figure 4 that, in the entire frequency range, the torsional impedance of the saturated soil is significantly different from that of the

TABLE 1: Calculation parameters of the saturated soil.

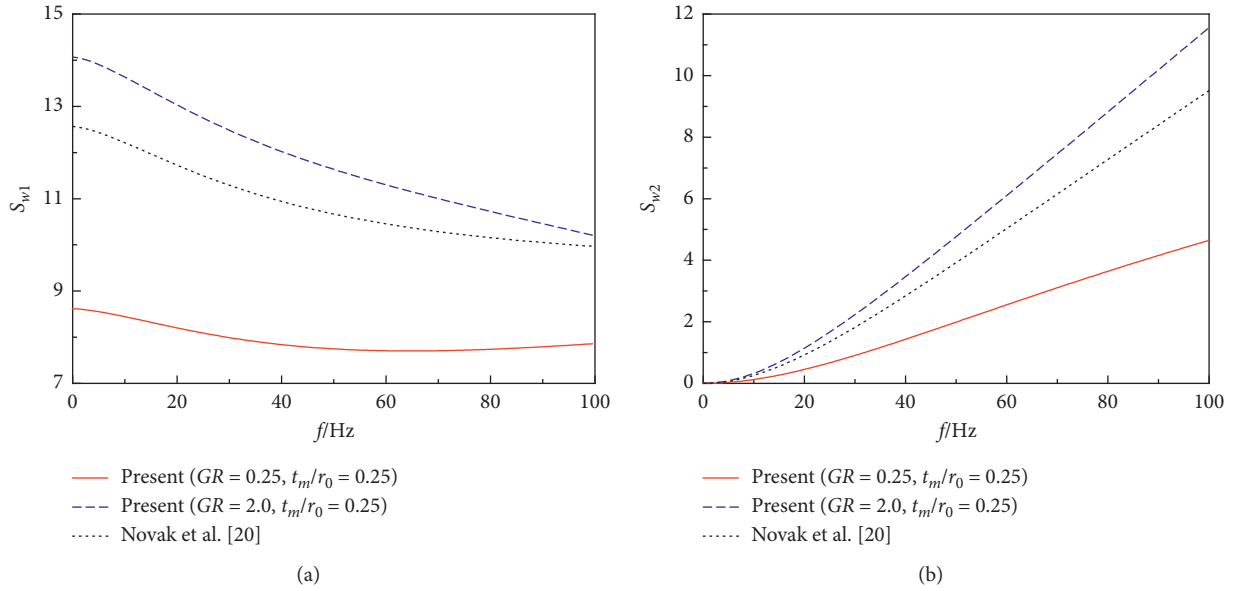| G_{s0} (MPa)	ρ_s (kg/m^3)	ρ_f (kg/m^3)	n	k_d (m/s)
20	2650	1000	0.4	10^{-7}

(a)

(b)

FIGURE 3: Comparison of the present reduced single-phase medium solution with the homogeneous medium solution ($D_{sm} = D_{s0} = 0$, $r_0 = 0.3$ m).
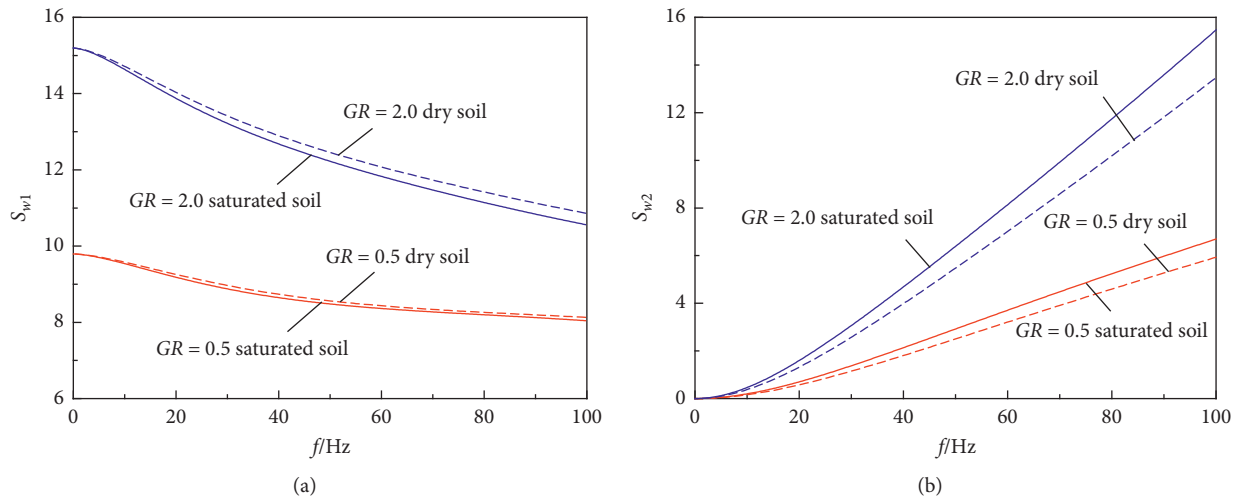

(a)

(b)

FIGURE 4: Comparison of torsional impedance of saturated soil solution with the reduced dry soil solution for a radially inhomogeneous soil ($D_{sm} = D_{s0} = 0$, $t_m/r_0 = 0.5$, $r_0 = 0.3$ m).

dry soil, no matter it is a weakened or strengthened soil. The stiffness part of the torsional impedance of the saturated soil is lower than that of the dry soil, and the damping part of the saturated soil is greater than that of the dry soil. This indicates that the pore fluid in the saturated soil can increase the damping during the vibration process. Therefore, it is important to consider the dynamic interaction between the

solid phase and the pore fluid when the voids of soil are filled with water.

4.2. Torsional Complex Stiffness at the Pile Top. This section mainly analyzes the influence of the characteristic parameters of soil radial heterogeneity on the torsional complex
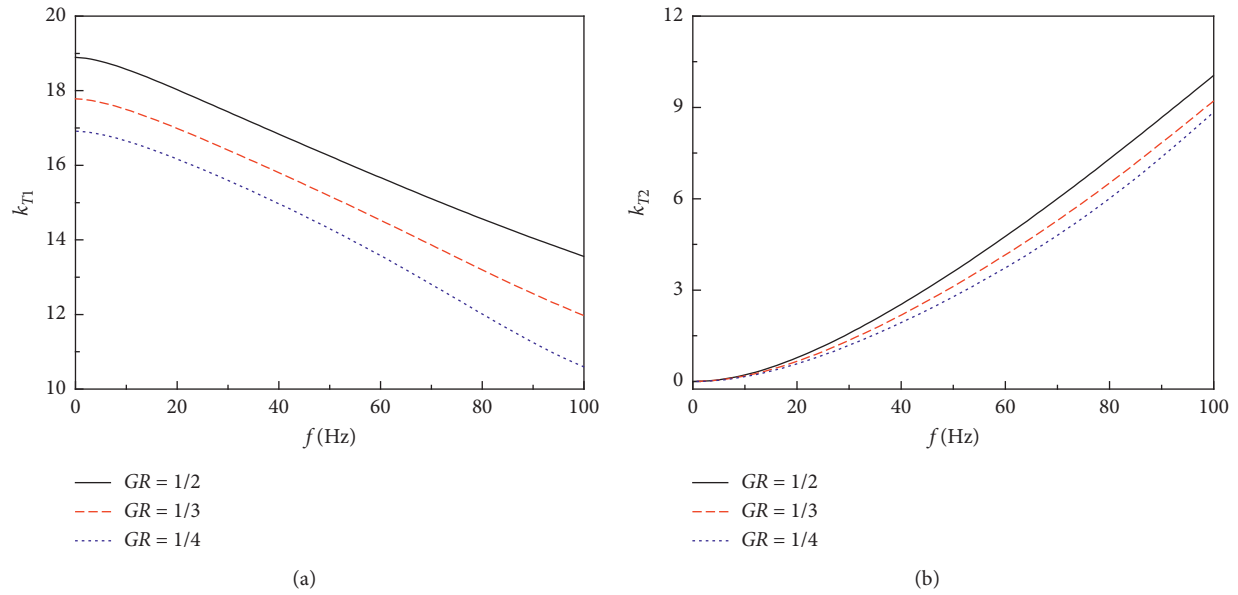
FIGURE 5: Influence of the shear modulus ratio $GR = G_{sm}/G_{s0}$ on the complex stiffness at the pile top when the inner soil is weakened ($D_{sm} = D_{s0} = 0$, $t_m/r_0 = 0.25$).
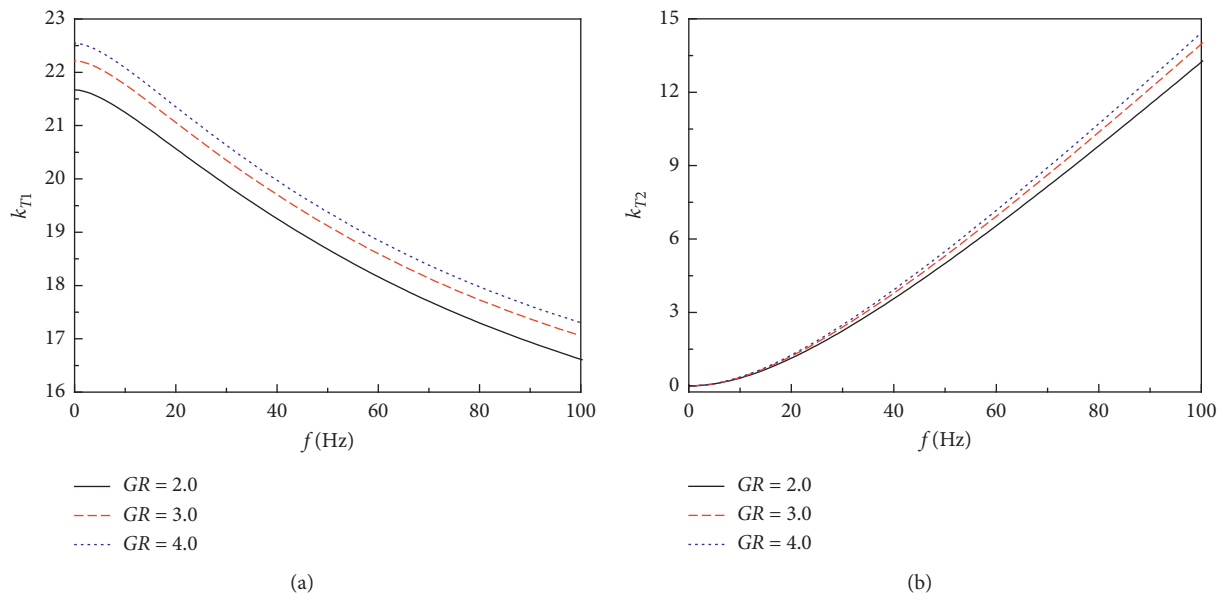

FIGURE 6: Influence of the shear modulus ratio $GR = G_{sm}/G_{s0}$ on the complex stiffness at the pile top when the inner soil is strengthened ($D_{sm} = D_{s0} = 0$, $t_m/r_0 = 0.25$).

stiffness at the pile top. The calculation parameters of the pile and pile bottom soil are taken as $\rho_p = 2500 \, \text{kg/m}^3$, $G_p = 12.1 \, \text{GPa}$, $H = 10 \, \text{m}$, $r_0 = 0.3 \, \text{m}$, and $G_{sb} = 20 \, \text{MPa}$. Figure 5 describes the influence of the ratio of the shear modulus of the outer soil to that at the pile-soil interface (i.e., GR) on the complex stiffness at the pile top when the inner soil is weakened. It can be seen from Figure 5 that, in the whole frequency range, the real stiffness and dynamic damping at the pile top decrease with the increase of softening degree of the inner soil.

Figure 6 shows the influence of GR on the complex stiffness at the pile top when the inner soil is strengthened. It can be seen from Figure 6 that, in the whole frequency range, the real stiffness and dynamic damping at the pile top increase with increasing GR. Compared with Figure 5, it can be observed that the real stiffness and dynamic damping corresponding to the strengthened soil are greater than those corresponding to the weakened soil, which indicates that the weakened soil can reduce the dynamic torsional resistance of the pile-soil system. Therefore, it is of great importance to
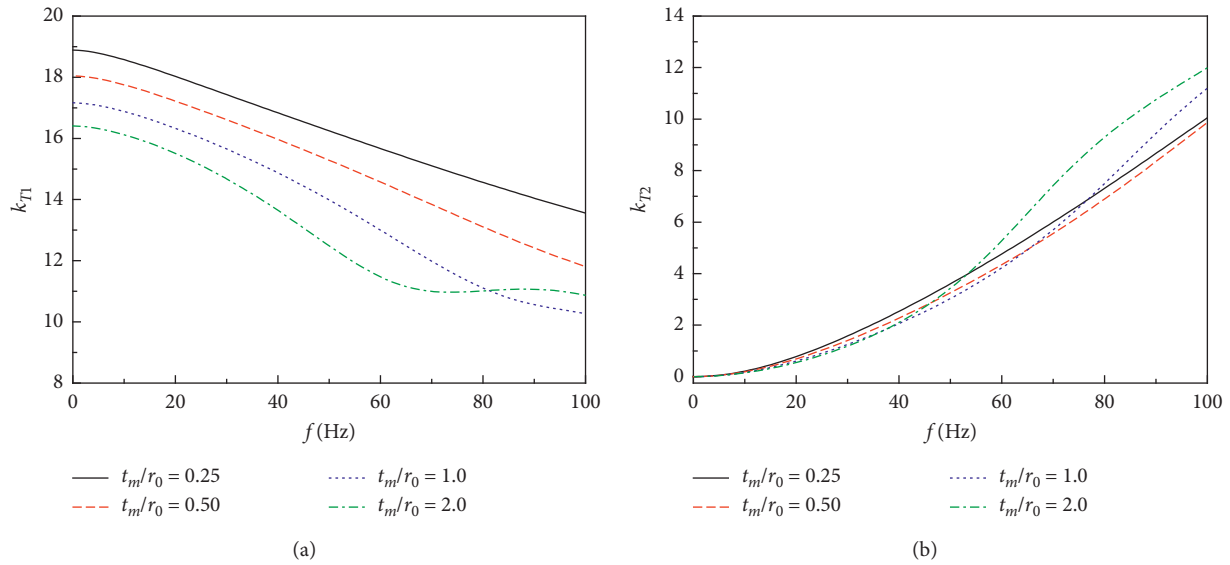
(a)

(b)

FIGURE 7: Influence of the disturbance range t_m/r_0 on the complex stiffness at the pile top when the inner soil is weakened ($D_{sm} = D_{s0} = 0$, $GR = 0.5$).
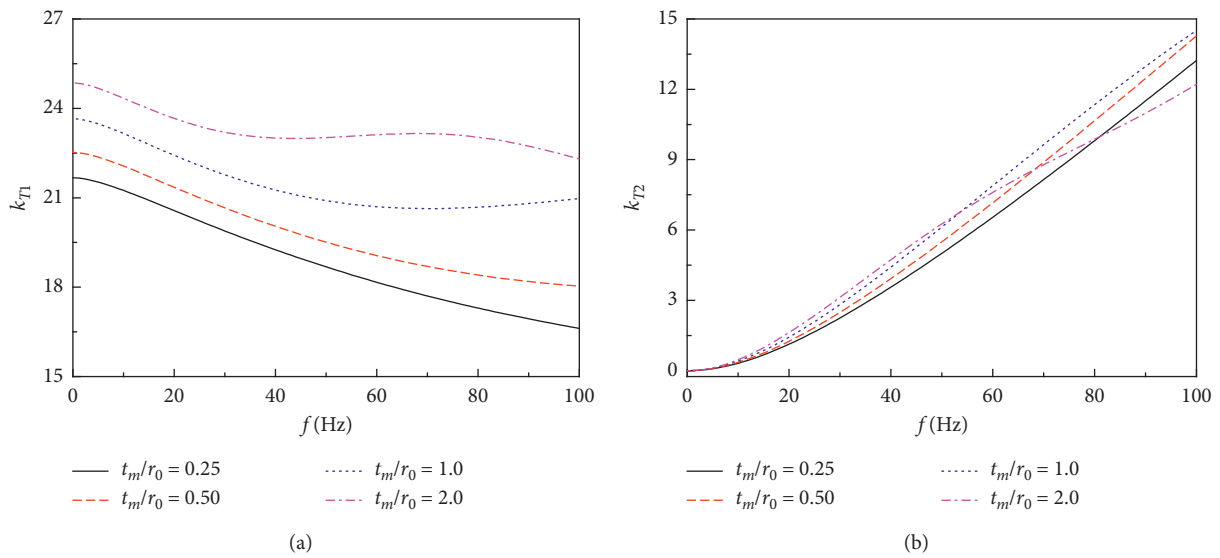

(a)

(b)

FIGURE 8: Influence of the disturbance range t_m/r_0 on the complex stiffness at the pile top when the inner soil is strengthened ($D_{sm} = D_{s0} = 0$, $GR = 2$).

consider the softening degree of the inner soil in the dynamic foundation design.

Figure 7 illustrates the influence of the disturbance range on the complex stiffness at the pile top when the inner soil is weakened. It can be seen that, in the low frequency range, the real stiffness and dynamic damping at the pile top decrease with the increase of t_m/r_0. However, as the frequency further increases, the real stiffness and dynamic damping show certain fluctuation when t_m/r_0 is large (e.g., $t_m/r_0 = 2$). It can be concluded from Figure 7 that, in the low frequency range concerned in the dynamic foundation design (0–50 Hz), greater disturbance range will reduce the resistance of the pile-soil system to the torsional deformation for the

weakened soil, which should be paid special attention in the related design.

Figure 8 shows the influence of the disturbance range on the complex stiffness at the pile top when the inner soil is strengthened. It can be seen from Figure 8 that, in the low frequency range, the real stiffness and dynamic damping at the pile top increase with the increase of t_m/r_0. However, when frequency is relatively high, the dynamic damping shows certain fluctuation with larger t_m/r_0.

Figures 9 and 10 reflect the influence of the material damping of the inner soil on the complex stiffness at the pile top corresponding to the weakened and strengthened soil cases. It can be seen that, for both weakened and
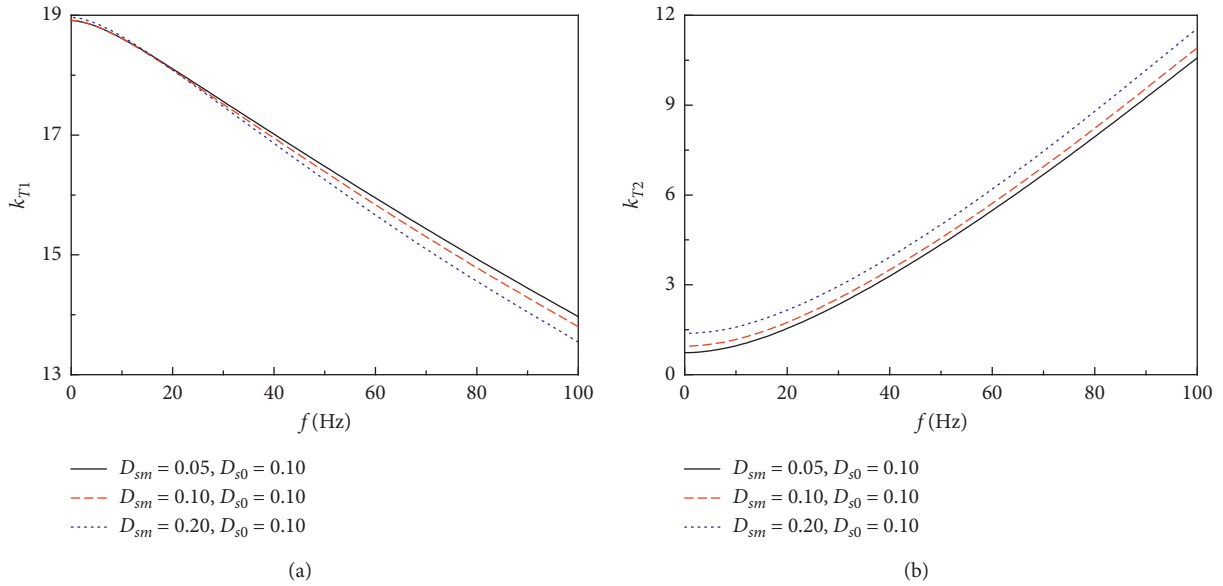
FIGURE 9: Influence of material damping of the inner disturbed soil on the complex stiffness at the pile top when the inner soil is weakened ($GR = 0.5$, $t_m/r_0 = 0.5$).
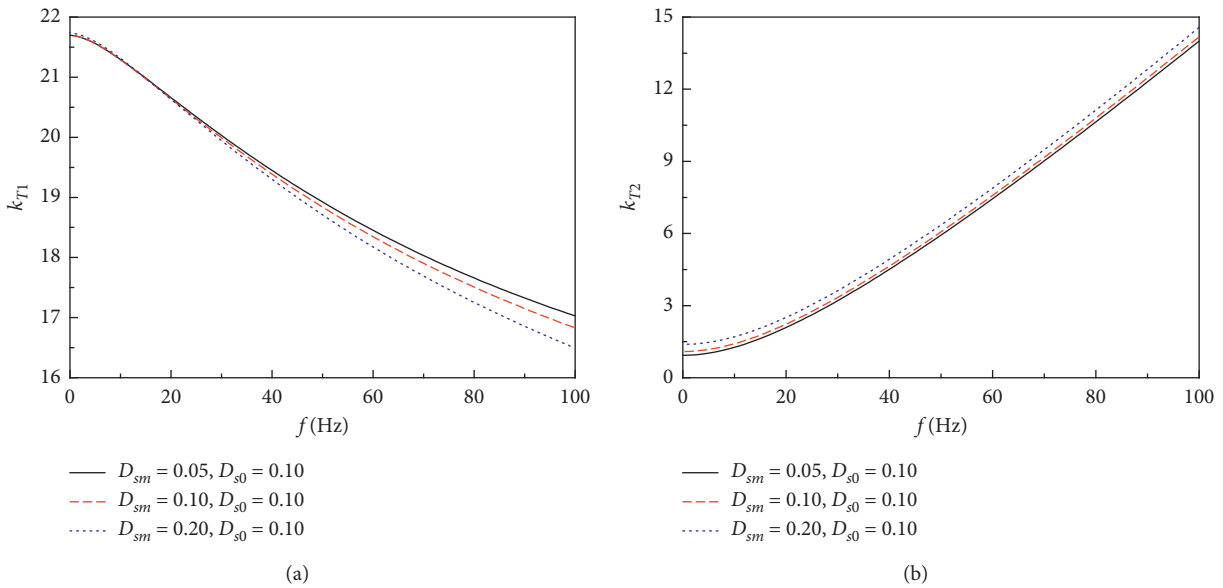

FIGURE 10: Influence of material damping of the inner disturbed soil on the complex stiffness at the pile top when the inner soil is strengthened ($GR = 2$, $t_m/r_0 = 0.5$).

strengthened soils, when the excitation frequency is small, the material damping of the soil in the inner region basically has negligible effect on the real stiffness. With the increase of the excitation frequency, the greater the material damping of the soil in the inner region is, the smaller the real stiffness is. Meanwhile, it can be also observed that, in the entire frequency range, the dynamic damping increases with the increase of the material damping of the inner soil. Therefore, in general, for dynamic foundation design, the damping of the soil has limited influence on the torsional complex stiffness at the pile top.

5. Conclusions

Based on the dynamic consolidation theory proposed by Biot, the exact solution for the torsional vibration of an elastic pile embedded in a radially inhomogeneous saturated soil with shear modulus changing in an exponential form along the radial direction is developed. This exact solution can be further served as benchmarks for future numerical methods. Through detailed calculation and analysis, it is found that when considering the dynamic interaction between the solid phase and pore fluid, the torsional

impedance of the saturated soil is different from that of the dry soil. In addition, the softening/hardening degree and the disturbance range of the saturated soil have marked influence on the torsional complex stiffness at the pile top. However, for dynamic foundation design (i.e., the low frequency range is concerned), the damping of the soil has limited influence on the torsional complex stiffness at the pile top.

Appendix

A. The Solution for the Pile-Soil System When $m = 2$

The solution of equation (9) can be expressed as

$$
\begin{aligned}
u_\theta &= A_2\xi^{\delta_1} + B_2\xi^{\delta_2}, \quad (1 \leq \xi \leq \xi_0), \\
u_\theta &= C_2 K_1(\lambda_0\xi) + D_2 I_1(\lambda_0\xi), \quad (\xi \geq \xi_0),
\end{aligned}
\tag{A.1}
$$

where

$$
\delta_1 = -1 + \sqrt{4 + \lambda_m^2}; \, \delta_2 = -1 - \sqrt{4 + \lambda_m^2}.
\tag{A.2}
$$

Substituting the boundary condition given in equation (12) into equation (A.1) and using the properties of the modified Bessel function, we have $D_2 = 0$. Substituting the continuity condition in equation (13) into equation (A.1), we have

$$
Q_2 = \frac{A_2}{B_2} = \frac{-\xi_0^{\delta_2}(\delta_2 - 1)K_1(\lambda_0\xi_0) - \lambda_0\xi_0^{\delta_2+1}K_2(\lambda_0\xi_0)}{\xi_0^{\delta_1}(\delta_1 - 1)K_1(\lambda_0\xi_0) + \lambda_0\xi_0^{\delta_1+1}K_2(\lambda_0\xi_0)}.
\tag{A.3}
$$

The circumferential shear stress amplitude at the pile-soil interface can then be derived, and the torsional impedance of the soil can be written as

$$
K_\theta = -\frac{2\pi r_0^3\tau_{r\theta}}{u_\theta}\Big|_{\xi=1} = -2\pi G_{sm}(1 + iD_{sm})r_0^2\frac{Q_2(\delta_1 - 1) + (\delta_2 - 1)}{Q_2 + 1}.
\tag{A.4}
$$

According to the continuity conditions at the pile-soil interface, the governing equation for an elastic pile under time-harmonic torsional load can be further expressed as

$$
\frac{d^2\phi(z)}{dz^2} + \left\{\frac{G_{sm}(1 + iD_{sm})}{Q_2\xi^{\delta_1} + \xi^{\delta_2}}[Q_2(\delta_1 - 1) + (\delta_2 - 1)] + \frac{\rho_p\omega^2}{G_p}\right\}\phi(z) = 0.
\tag{A.5}
$$

The solution of ordinary differential equation (A.5) can be expressed as

$$
\phi(z) = \alpha_3\cos(\gamma_2 z) + \alpha_4\sin(\gamma_2 z),
\tag{A.6}
$$

in which

$$
\gamma_2 = \left[\frac{G_{sm}(1 + iD_{sm})}{Q_2\xi^{\delta_1} + \xi^{\delta_2}}[Q_2(\delta_1 - 1) + (\delta_2 - 1)] + \frac{\rho_p\omega^2}{G_p}\right]^{(1/2)},
\tag{A.7}
$$

where α_3 and α_4 are the constants to be determined by the boundary conditions.

Substituting the boundary conditions of the pile into equation (A.6), we have

$$
\begin{aligned}
\alpha_1 &= -\frac{T_0}{G_p I_p \gamma_2 \tan(\gamma_2 H - \varphi_2)}, \\
\alpha_2 &= -\frac{T_0}{G_p I_p \gamma_2},
\end{aligned}
\tag{A.8}
$$

where

$$
\begin{aligned}
\varphi &= \arctan\left[\frac{\overline{k}_{pb}}{(\gamma_2 H)}\right], \\
\overline{k}_{pb} &= \frac{k_{pb}H}{G_p I_p}.
\end{aligned}
\tag{A.9}
$$

The dimensionless torsional complex stiffness k_T at the pile top can be finally expressed as

$$
k_T = \frac{3T_0}{16G_{s0}r_0^3\phi(z = 0)} = \frac{3\pi r_0\overline{\mu}\gamma_2\tan(\gamma_2 H - \varphi)}{32}.
\tag{A.10}
$$

Data Availability

The data of Figures 3–10 used to support the findings of this study are available from the corresponding author upon request.

Conflicts of Interest

The authors declare that they have no conflicts of interest.

Acknowledgments

References

[1] E. Pan, H. Liu, and Z. Zhang, "Vertical and torsional vibrations of a rigid circular disc on a transversely isotropic and layered half-space with imperfect interfaces," *Soil Dynamics and Earthquake Engineering*, vol. 113, pp. 442–453, 2018.

[2] Z. Zhang and E. Pan, "Vertical and torsional vibrations of an embedded rigid circular disc in a transversely isotropic multilayered half-space," *Engineering Analysis with Boundary Elements*, vol. 99, pp. 157–168, 2019.

[3] R. Y. S. Pak and F. Abedzadeh, "Forced torsional oscillation from the interior of a half-space," *Journal of Sound and Vibration*, vol. 160, no. 3, pp. 401–415, 1993.

[4] Y. Le, N. Wang, W. T. Hu, D. X. Geng, and Y. L. Jiang, "Torsional dynamic impedance of a stepped pile based on the wedged soil model," *Computers and Geotechnics*, vol. 128, Article ID 103854, 2020.

[5] W. Wu, H. Liu, M. H. El Naggar, G. Mei, and G. Jiang, "Torsional dynamic response of a pile embedded in layered soil based on the fictitious soil pile model," *Computers and Geotechnics*, vol. 80, pp. 190–198, 2016.

[6] L. G. Tham, Y. K. Cheung, and Z. X. Lei, "Torsional dynamic analysis of single piles by time-domain BEM," *Journal of Sound and Vibration*, vol. 174, no. 4, pp. 505–519, 1994.

[7] M. Novak and M. Sheta, *Approximate Approach to Contact Problems of Piles, Proceedings of the Geotechnical Engineering Division*, American Society of Civil Engineering National Convention, Florida, USA, 1980.

[8] A. S. Veletsos and K. W. Dotson, "Impedances of soil layer with disturbed boundary zone," *Journal of Geotechnical Engineering*, vol. 112, no. 3, pp. 363–368, 1986.

[9] A. S. Veletsos and K. W. Dotson, "Vertical and torsional vibration of foundations in inhomogeneous media," *Journal of Geotechnical Engineering*, vol. 114, no. 9, pp. 1002–1021, 1988.

[10] K. W. Dotsos and A. S. Veletsos, "Vertical and torsional impedances for radially inhomogeneous viscoelastic soil layer," *Soil Dynamics and Earthquake Engineering*, vol. 9, no. 3, pp. 110–119, 1990.

[11] Y. C. Han and G. C. Sabin, "Impedances for radially inhomogeneous viscoelastic soil media," *Journal of Engineering Mechanics*, vol. 121, no. 9, pp. 939–947, 1995.

[12] Z. Li and Y. F. Gao, "Torsional vibration of a large-diameter pipe pile embedded in inhomogeneous soil," *Ocean Engineering*, vol. 172, pp. 737–758, 2019.

[13] Z. Zhang and E. Pan, "Dynamic torsional response of an elastic pile in a radially inhomogeneous soil," *Soil Dynamics and Earthquake Engineering*, vol. 99, pp. 35–43, 2017.

[14] M. A. Biot, "Theory of propagation of elastic waves in a fluid-saturated porous solid. I. Low-Frequency range," *The Journal of the Acoustical Society of America*, vol. 28, no. 2, pp. 168–178, 1956.

[15] M. A. Biot, "Mechanics of deformation and acoustic propagation in porous media," *Journal of Applied Physics*, vol. 33, no. 4, pp. 1482–1498, 1962.

[16] Z. Li, Y. Gao, and K. Wang, "Torsional vibration of an end bearing pile embedded in radially inhomogeneous saturated soil," *Computers and Geotechnics*, vol. 108, pp. 117–130, 2019.

[17] G. Militano and R. K. N. D. Rajapakse, "Dynamic response of a pile in a multi-layered soil to transient torsional and axial loading," *Géotechnique*, vol. 49, no. 1, pp. 91–109, 1999.

[18] O. C. Zienkiewicz, C. T. Chang, and P. Bettess, "Drained, undrained, consolidating and dynamic behaviour assumptions in soils," *Géotechnique*, vol. 30, no. 4, pp. 385–395, 1980.

[19] Z. Zhang and E. Pan, "Time-harmonic response of transversely isotropic and layered poroelastic half-spaces under general buried loads," *Applied Mathematical Modelling*, vol. 80, pp. 426–453, 2020.

[20] M. Novak, T. Nogami, and A. E. Fakhry, "Dynamic soil reactions for plane strain case," *Journal of the Engineering Mechanics Division, ASCE*, EM4, vol. 104, pp. 953–959, 1978.

Research Article

A Kind of FM-BEM Penalty Function Method for a 3D Elastic Frictional Contact Nonlinear System

Chunxiao Yu [ID], Dinghui Jing, Chang Fu, and Yanfang Yang

School of Science, Yanshan University, No. 438 West Hebei Avenue, Qinhuangdao 066004, Hebei, China

Correspondence should be addressed to Chunxiao Yu; chxy@ysu.edu.cn

In this paper, a kind of node_face frictional contact FM-BEM penalty function method is presented for 3D elastic frictional contact nonlinear problems. According to the principle of minimum potential energy, nonpenetrating constraints are introduced into the elastic frictional contact system as a penalty term. By using the least square method and penalty function method, an optimization mathematical model and a mathematical programming model with a penalty factor are established for the node_face frictional contact nonlinear system. For the two models, a penalty optimization IGMRES (m) algorithm is proposed, and the influences of different penalty factors on the solution of the whole system are analyzed. Finally, a numerical simulation is carried out for two elastic frictional contact objects, and some important results including displacements, pressures, friction forces, and friction slips in the contact area are presented. Theoretical analysis and numerical experiment show that the newly presented FM-BEM penalty function method not only is efficient and practical but also has much superiority. It is easy to implement, and it is fast convergent with good stability.

1. Introduction

Elastic frictional contact is a multiple nonlinear problem [1, 2], and it is necessary to accurately track the motion of the object before contact and the interaction between objects after contact, which includes the correct simulation of friction and deformation behavior between contact surfaces and the analysis of the possible energy conversion problem. For the contact problems, only very few of them can be solved by analytical methods, and most of them need to be simulated by numerical methods such as the Finite Element Method (FEM) [3, 4] and the Boundary Element Method (BEM) [5, 6]. The FEM is relatively mature and widely used [7–10]. However, the BEM has the advantages of dimension reduction, singularity adaptation, high precision, and so on [11–14].

The penalty function method [15, 16] is a common method to solve optimization problems, and it is also one of the effective methods to solve an elastic contact problem [17–19]. Without increasing the system's Degree of Freedom (DOF), this method can be used to directly apply constraints to the two contact objects. Many scholars have used it to solve the frictional contact problems in different fields [20–23]. In engineering, gradient-based optimization algorithms, for example, the existing FEM such as the Lagrange multiplier method and penalty function method, are often used to solve the contact problems. For the case of non-frictional contact, sufficiently stable results can be obtained. For the case of frictional contact, severe numerical oscillation may occur with the change of loads or meshes, and it will be very difficult to obtain a stable result unless special treatments are made. In addition, the procedures of existing numerical algorithms are usually complicated and much memory space and computing time are required, so repeated checking and revision are needed to obtain suitable results. At present, various kinds of commercial computing software often fail to give accurate and reliable results for the analysis of frictional contact. Therefore, it is very urgent to develop some stable and efficient numerical algorithms [24–27].

In recent years, the Fast Multipole Boundary Element Method (FM-BEM) [28, 29] has attracted much attention as a kind of new and efficient numerical method [30–34]. Our

research group studied the mathematical and mechanical theories of the FM-BEM from the perspective of fundamental solution. By using the superiorities of FM-BEM such as high precision, high computational efficiency and being suitable for large-scale computing, we have successfully applied it to the numerical analysis of elastic frictional contact problems and have completed some simulations [35–38], for example, the interference fit between taper sleeve and roll neck of an oil film bearing and a surface force field of screw pair in a rolling mill.

For the study of elastic frictional contact problems, the penalty function method in the existing literature was used to solve some optimization problems with a node_node contact mode. The BEM and FM-BEM focused on the modeling and numerical analysis for the nonpenetrating contact mode and often failed to give numerical results for the penetrating contact mode. According to the above-mentioned analysis, we will present a kind of FM-BEM penalty function method to solve the elastic node_face frictional contact problems. As the same time, we will establish a mathematical programming model with a penalty factor and propose a penalty optimization algorithm. In this method, some important factors will be synthetically considered, which include the deformation and stress condition in a contact process, the nonlinearity of boundary condition for the contact surface, the size and mutual position of the contact area, the change of contact state, and so on. The research work will involve some mathematical, mechanical, and physical problems that are closely related to the frictional contact. The purpose is to provide new ideas and numerical methods for the solution of elastic frictional contact problems.

This paper is organized as follows. In Section 1, basic thought of the Penalty Function Method is introduced. In Section 2, fundamental formulas and frictional contact condition for the 3D elastic frictional contact FM-BEM are presented. In Section 3, interpolation constraints are analyzed for the node_face frictional contact nonlinear system. Then, an optimization mathematical model and a mathematical programming model with a penalty factor are established by using the least square method and penalty function method. In Section 4, a penalty optimization IGMRES (m) algorithm is proposed. In Section 5, a

simulation of two elastic objects' frictional contact process is provided and numerical analysis is completed. At last, the concluding remarks are presented.

2. Basic Idea of the Penalty Function Method

For the optimization problem

$$
\begin{cases}
\min & f(x) \\
s.t. & h_i(x) = 0, \quad i = 1, 2, \ldots, l,
\end{cases}
\tag{1}
$$

we introduce a parameter λ and define an augmented objective function as follows:

$$
F(x, \lambda) = f(x) + \lambda \sum_{i=1}^{l} \left[h_i(x) \right]^2,
\tag{2}
$$

where $F(x, \lambda)$ is called a penalty function and the parameter λ is called a penalty factor that is a very large positive number. When $h_i(x) = 0$, $(i = 1, 2, \ldots l)$, the penalty function $F(x, \lambda)$ is just equal to the objective function $f(x)$ in equation (1); otherwise, its value will be very large and equation (1) will be transformed into the following unconstrained problem:

$$
\min F(x, \lambda) = \min \left\{ f(x) + \lambda \sum_{i=1}^{l} \left[h_i(x) \right]^2 \right\}.
\tag{3}
$$

3. 3D Elastic Frictional Contact FM-BEM

3.1. Fundamental Formulas. For 3D elastic frictional contact problems, the boundary integral equation without consideration of body force is expressed as follows [6]:

$$
c_{ij} u_j(x) + \int_{\Gamma} T_{ij}(x, y) u_j(y) \mathrm{d}\Gamma = \int_{\Gamma} U_{ij}(x, y) t_j(y) \mathrm{d}\Gamma,
\tag{4}
$$

where x indicates a source node, y indicates an arbitrary node in boundary Γ, c_{ij} indicates a boundary shape coefficient, and $U_{ij}(x, y)$ and $T_{ij}(x, y)$ indicate the kernel functions of displacement and surface force fundamental solutions, respectively. By the FM-BEM, equation (4) can be discretized as follows [29]:

$$
c_{ij} u_j(x^q) + R_{ijm}(x^q) \sum_{k,l,s} \frac{1}{|x^q - y_c|} \left\{ u_j^{kl} \phi^l(\xi^s) n_m[y(\xi^s)] J[y(\xi^s)] \omega^s \right\} +
$$

$$
S_{im}(x^q) \sum_{k,l,s} \frac{1}{|x^q - y_c|} \left\{ u_j^{kl} \phi^l(\xi^s) n_m[y(\xi^s)] y_j(\xi^s) J[y(\xi^s)] \omega^s \right\} -
$$

$$
P_{ij}(x^q) \sum_{k,l,s} \frac{1}{|x^q - y_c|} \left\{ t_j^{kl} \phi^l(\xi^s) J[y(\xi^s)] \omega^s \right\} -
$$

$$
Q_i(x^q) \sum_{k,l,s} \frac{1}{|x^q - y_c|} \left\{ t_j^{kl} \phi^l(\xi^s) y_j(\xi^s) J[y(\xi^s)] \omega^s \right\} = 0,
$$

$$
\tag{5}
$$

where x^q indicates a source node, y_c indicates a multiple central node, s indicates an element integral node, ω^s indicates the integral weight function of ξ^s, and $J[y(\xi^s)]$ indicates a Jacobian determinant.

With the given boundary conditions, equation (5) can be transformed into the following system of equation:

$$Ax = b, \tag{6}$$

where x indicates an unknown column vector for displacements and surface force.

3.2. Frictional Contact Condition.

When two objects contact each other, in order to ensure the balance and stability, the contact system must be satisfied with nonpenetrating constraints, as is shown in Figure 1.

Namely, the following expression is satisfied:

$$\Delta u_A \cdot n \le \tau, \tag{7}$$

where Δu_A indicates the displacement vector increment of the node A, n indicates the unit normal vector, and τ indicates the tolerance of contact distance. Otherwise, once penetration occurs in the contact area, the system solution will not be carried out normally.

4. Modeling and Optimization for the Node_Face Frictional Contact System Using the FM-BEM Penalty Function Method

4.1. Analysis of Node_Face Frictional Contact.

We consider two objects A and B in contact with each other. We suppose that object A (with fixed displacement constraints) is passive and object B is active. The numbers of discrete nodes are represented as N_A and N_B, respectively. Also, the numbers of contact nodes are represented as N_A^c and N_B^c, respectively. For the traditional BEM, the DOF of the final system of equations is $3(N_A + N_B)$ and the displacements and surface force for each contact node are unknown. As a result, for each contact node, three supplement equations must be established.

For each contact node of object B, it contacts with some element of object A, and its displacement can be obtained by the interpolation of its contact element nodes' displacements. Then, displacement constraints are established. According to Coulomb's Law of Friction, if relative slip occurs between the contact node and its contact surface, tangential displacement constraints can be replaced by tangential friction ones. The node_face frictional contact constraints are shown in the following expressions:

Stick state:

$$U_k^B = \sum_{l=1}^{M} \varphi^l(\xi_1, \xi_2) U_{kl}^A, \quad (k = 1, 2, 3). \tag{8}$$

Slip state:

$$T_1^B = -T_t \cos\theta,$$
$$T_2^B = -T_t \sin\theta,$$
$$U_3^B = \sum_{l=1}^{M} \varphi^l(\xi_1, \xi_2) U_{3l}^A. \tag{9}$$

For each contact node of object A, it contacts with some element of object B, and its surface force can be obtained by the interpolation of its contact element nodes' force. Then, surface force constraints are established. Similarly, if relative slip occurs between the contact node and its contact surface, tangential surface force constraints can be replaced by tangential friction ones. The node_face frictional contact constraints are shown in the following expressions:

Stick state:

$$T_k^A = -\sum_{l=1}^{M} \varphi^l(\xi_1, \xi_2) T_{kl}^B, \quad (k = 1, 2, 3). \tag{10}$$

Slip state:

$$T_1^A = T_t \cos\theta,$$
$$T_2^A = T_t \sin\theta,$$
$$T_3^A = -\sum_{l=1}^{M} \varphi^l(\xi_1, \xi_2) T_{3l}^B. \tag{11}$$

In equations (8)–(11), U_k^B indicates k-direction displacement of each node in object B, U_{kl}^A indicates k-direction displacement of node l in object A, T_k^A indicates k-direction surface force of each node in object A, M indicates the node number of a contact element, φ^l indicates the interpolation function, T_t indicates the friction at t moment, (ξ_1, ξ_2) indicates the local coordinate, and θ indicates a slip angle. Here, ξ_1, ξ_2, θ can be predetermined by the least square method. According to equations (8)–(11), three supplement equations can be established for each contact node. Then, the total DOF of the contact system becomes $3(N_A + N_B + N_A^c + N_B^c)$. For convenience, it can be written as NF.

4.2. Optimization Mathematical Model for Node_Face Frictional Contact.

Node_face frictional contact constraints show high nonlinearity, which results in a very difficult and time-consuming solution procedure. To accelerate the iterative convergence, nonlinear contact constraints will be linearized. At first, the least square method is applied to equations (8)–(11) to obtain ξ_1, ξ_2, θ while the contact behavior is precisely simulated. Then, mathematical programming is conducted on the frictional contact system and an optimization mathematical model is established. The detailed process is as follows:

For the object B, the system of equations formed by the traditional BEM can be expressed as $A'x = b'$, where $A' = (a'_{ij}), b' = (b'_i)$. Let
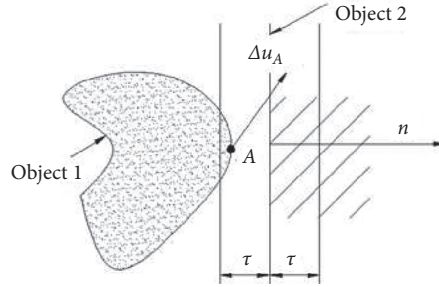
FIGURE 1: A sketch of nonpenetrating constraints.

$$f_i^B(x_j) = b_i' - \sum_{j=1}^{NF} a_{ij}' x_j, \quad (i = 1, 2, \ldots, 3N_B; \ j = 1, 2, \ldots, NF). \tag{12}$$

After equations (8) and (9) have been linearized, according to equation (12), they can be rewritten as

$$f_{ik}^B(x_j) = U_{ik}^B - \sum_{l=1}^{M} \varphi^l(\xi_1, \xi_2) U_{ikl}^A, \quad (i = 1, 2, \ldots, 3N_B^c; \ j = 1, 2, \ldots, NF; \ k = 1, 2, 3), \tag{13}$$

$$f_{i1}^B(x_j) = T_{i1}^B + T_{it} \cos\theta, \ f_{i2}^B(x_j) = T_{i2}^B + T_{it} \sin\theta, \ f_{i3}^B(x_j) = U_{i3}^B - \sum_{l=1}^{M} \varphi^l(\xi_1, \xi_2) U_{i3l}^A, \quad (i = 1, 2, \ldots, 3N_B^c; \ j = 1, 2, \ldots, NF). \tag{14}$$

For the object A, the system of equations formed by the traditional BEM can be expressed as $A'' x = b''$, where $A'' = (a_{ij}''), b'' = (b_i'')$. Let

$$f_i^A(x_j) = b_i'' - \sum_{j=1}^{NF} a_{ij}'' x_j, \quad (i = 1, 2, \ldots, 3N_A; \ j = 1, 2, \ldots, NF). \tag{15}$$

After equations (10) and (11) have been linearized, according to equation (15), they can be rewritten as

$$f_{ik}^A(x_j) = T_{ik}^A + \sum_{l=1}^{M} \varphi^l(\xi_1, \xi_2) T_{ikl}^B, \quad (i = 1, 2, \ldots, 3N_A^c; \ j = 1, 2, \ldots, NF; \ k = 1, 2, 3), \tag{16}$$

$$f_{i1}^A(x_j) = T_{i1}^A - T_{it} \cos\theta,$$
$$f_{i2}^A(x_j) = T_{i2}^A - T_{it} \sin\theta,$$
$$f_{i3}^A(x_j) = T_{i3}^A + \sum_{l=1}^{M} \varphi^l(\xi_1, \xi_2) T_{i3l}^B, \quad (i = 1, 2, \ldots, 3N_A^c; \ j = 1, 2, \ldots, NF). \tag{17}$$

According to equations (12)–(17), let $x = (x_j)$ $(j = 1, 2, \ldots, NF)$, and we define an objective function for the nonlinear analysis of node_face frictional contact as follows:

$$\|f(x)\| = \sqrt{\sum_{i=1}^{3N_B} \left[f_i^B(x)\right]^2 + \sum_{i=1}^{3N_B^c} \sum_{k=1}^{3} \left[f_{ik}^B(x)\right]^2 + \sum_{i=1}^{3N_A} \left[f_i^A(x)\right]^2 + \sum_{i=1}^{3N_A^c} \sum_{k=1}^{3} \left[f_{ik}^A(x)\right]^2}. \tag{18}$$

According to equations (12)–(18), an optimization mathematical model for the node_face frictional contact system can be established as follows:

$$\begin{cases} \min & \|f(x)\|, \\ f_i^B(x) = 0, & (i = 1, 2, \ldots, 3N_B), \\ f_i^B(x) = 0, & (i = 1, 2, \ldots, 3N_B^c), \\ f_i^A(x) = 0, & (i = 1, 2, \ldots, 3N_A), \\ f_i^A(x) = 0, & (i = 1, 2, \ldots, 3N_A^c). \end{cases} \tag{19}$$

4.3. Penalty Factor Programming Model for Node_Face Frictional Contact. From the abovementioned analysis, when the contact system is stable, the involved objects satisfy nonpenetrating constraints shown in equation (7); otherwise, the penalty function method can be used to apply contact constraints. We suppose that there is a "spring" between a possible contact node and its contact surface and its compressive stiffness is very large while the tensile stiffness is zero. The stiffness is taken as a penalty factor and written as α. According to the principle of minimum potential energy, when two objects contact each other, if equation (7) is satisfied, the work performed by the spring will be zero, namely, the penalty factor $\alpha = 0$, and the contact system will be stable with minimum potential energy (written as E_0). Otherwise, the spring will prevent the objects from contacting and do work, so the potential energy (written as E_c) will sharply increase. For the node_face frictional contact system, let

$$f(x) = b - Ax, \ x = \left(x_j\right), \quad (j = 1, 2, \ldots, NF). \tag{20}$$

We construct an energy objective function as follows:

$$E = E_0 + E_c, \tag{21}$$

where

$$E_0 = \|f(x)\|_2^2 = \sum_{i=1}^{3N_B} \left[f_i^B(x)\right]^2 + \sum_{i=1}^{3N_B^c} \left[f_i^B(x)\right]^2 + \sum_{i=1}^{3N_A} \left[f_i^A(x)\right]^2 + \sum_{i=1}^{3N_A^c} \left[f_i^A(x)\right]^2,$$

$$E_c = \frac{1}{2}\alpha \sum_{i=1}^{NF} \delta_i \left(d_i - \pi\right)^2, \quad \delta_i = \begin{cases} 1, d_i - \tau > 0, \\ 0, d_i - \tau \le 0, \end{cases} \tag{22}$$

where d_i indicates the distance between a contact node and its contact surface.

For the node_face frictional contact system, we suppose the contact surface is smooth and the deformation is very small. According to equations (3) and (19)–(21), a penalty factor programming model can be established as follows:

$$\min E = \min \left(E_0 + E_c\right). \tag{23}$$

So, the solution of node_face frictional contact is transformed into an unconstrained optimization problem.

4.4. Selection of Penalty Factor. From equations (3) and (23), we know the optimization of penalty factor α is very important. For each factor α, a corresponding objective function value can be obtained, and it will increase with the increase of α. When $\alpha = 0$, equation (23) has the same solution as equation (6). While $\alpha \longrightarrow \infty$, the solution of equation (23) will converge to the analytical solution, and abnormalities may occur for a too large factor α. So, the penalty factor α should not be taken as a too large value. From energetics point of view, the penalty factor α is equivalent to spring stiffness. When an object is subjected to fixed loads, the factor α will be inversely proportional to the deformation increments within the elastic range. For example, if two elastic objects contact each other, the relationship of the factor α and the objective function value can be as shown in Figure 2.

According to Figure 2, when the penalty factor α varies within the range between 10 and 10^8, the objective function value will be close to zero, namely, the nonpenetrating constraints expressed in equation (7) can be satisfied and the system will be stable. So, the penalty factor α can be taken as 10^8. While penalty factor α is larger than 10^8, the objective function value will increase sharply, namely, equation (7) cannot be satisfied, and the "spring" will carry out punishments on the contact. Then, the system cannot be solved properly.

5. Penalty Optimization IGMRES (m) Algorithm

To solve equation (23), a penalty optimization IGMRES (m) algorithm is presented. The detailed process is as follows:

$$r^{(0)} = b - Ax^{(0)}, \beta = \left\| r^{(0)} \right\|, v_1 = \frac{r^{(0)}}{\beta}, V_1 = \{v_1\}, E^{(0)} = \left\| E(x^{(0)}) \right\|. \tag{24}$$

(2) Iteration: for $j = 1, 2, \ldots, m$, we have

$$h_{ij} = (Av_j, v_i) \ (i = j_0, \ldots, j), \widehat{v}_{j+1} = Av_j - \sum_{i=j_0}^{j} h_{ij}v_i, \ j_0 = \max\{1, j - q - 1\}. \tag{25}$$

(2) Standardization:

$$h_{j+1,j} = \left\| \widehat{v}_{j+1} \right\|, v_{j+1} = \frac{\widehat{v}_{j+1}}{h_{j+1,j}}. \tag{26}$$

(3) Updation of V_{j+1} and $\overline{H}_j$:

$$V_{j+1} = (V_j, v_{j+1}),$$

$$\overline{H}_j = \begin{pmatrix} \overline{H}_{j-1} & h_{ij} \\ 0 & h_{j+1,j} \end{pmatrix}_{(j+1)\times j}, \tag{27}$$

where $\overline{H}_j$ indicates an upper Hessenberg matrix. Then, we have

$$AV_m = V_{m+1}\overline{H}_m. \tag{28}$$

When $j = 1$, the first column will be omitted.

(3) We solve the following least square problem to obtain y_m:

$$\left\| r^{(m)} \right\| = \min_{y_m \in C^m} \left\| \beta e_1 - \overline{H}_m y_m \right\|. \tag{29}$$

(4) We construct the approximate solution:

$$x^{(m)} = x^{(0)} + V_m y_m. \tag{30}$$

(5) The modules of residual vectors and the value of energy objective function are computed.

$$\left\| r^{(m)} \right\| = \left\| f - Ax^{(m)} \right\|, E^{(m)} = \left\| E(x^{(m)}) \right\|. \tag{31}$$

(6) Restart judgment: if $\left\| r^{(m)} \right\| \leq \varepsilon$ and $E^{(m)} < E^{(0)}$, then let $x = x^{(m)}$ and stop. Otherwise, reset $x^{(0)} = x^{(m)}$ and return to the initialization step.

(1) Initialization: for a fixed parameter m, we set an appropriate precision ε and a parameter q ($2 \leq q \leq m$). We take an initial value $x^{(0)}$ and compute

(1) Incomplete orthogonalization:

6. Numerical Example

We consider two elastic objects A and B in contact with each other. A is a support with a width $W = 50$ mm, a height $H = 30$ mm, and a length $L1 = 50$ mm. B is a half cylinder with a radius $R = 15$ mm and a length $L2 = 60$ mm. The two objects are isotropic with Young's modulus $E = 210$ Gpa, Poisson's ratio $\nu = 0.3$, and a frictional coefficient $f = 0.1$. The object B is subjected to a uniform load. The total load is divided into six steps, and the contact distance tolerance is $\tau = 0.0001$ mm. The computation model and discrete mesh are shown in Figure 3, and the discrete data are shown in Table 1.

When the object B is subjected to a uniform load P that is not more than 1 GPa, the penalty factor is taken as a value that ranges from 10 to 10^8, and the obtained results agree well with the theoretical analysis. The solution process is very stable. When $P = 100$ MPa, the distributions of contact displacement, pressure and friction force, and the friction slip field are presented, as is shown in Figures 4–7. These results agree well with the experimental analysis. In addition, the contact displacements and pressures under different loads are compared, as is shown in Figures 8, and 9, which shows that the edge effect is becoming more and more obvious with the load increase.

When $P = 1$ GPa and the penalty factor α is taken as 10^9, the solution procedure is abnormal and the friction directions of some contact nodes change, as is shown in Figure 10(a). When $P = 10$ GPa and the penalty factor α is taken as 10^{10}, the solution procedure is more abnormal, as is shown in Figure 10(b). When $P \geq 100$ GPa and the penalty factor α is taken as a value ranging from 1.0×10^{11} to 2.1×10^{11}, the solution will be impossible. The reason why the solution is impossible or abnormal is that penetration occurs when two objects contact each other, namely, equation (7) is not satisfied.
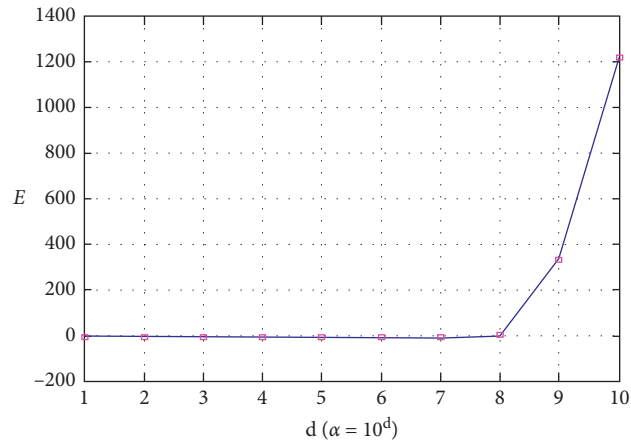
FIGURE 2: Influence of a penalty factor α on objective function values.
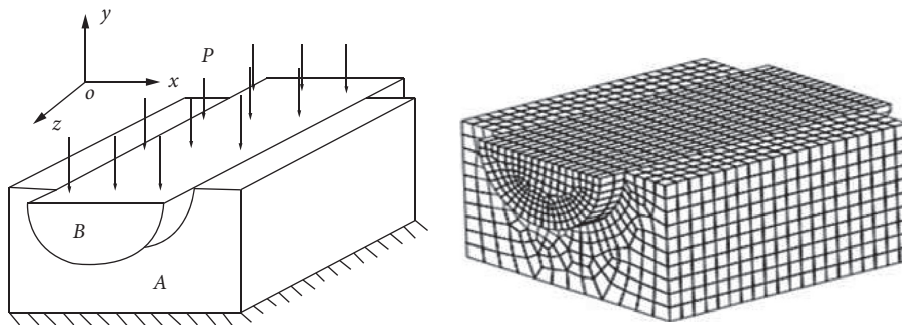
FIGURE 3: Computation model and discrete mesh.

TABLE 1: Discrete data.

Objects	Totality		Contact area		DOF
	Node number	Element number	Node number	Element number	
A	1650	1648	567	520	6651
B	1198	1196	459	468	4971
Total	2848	2844	1026	988	11622
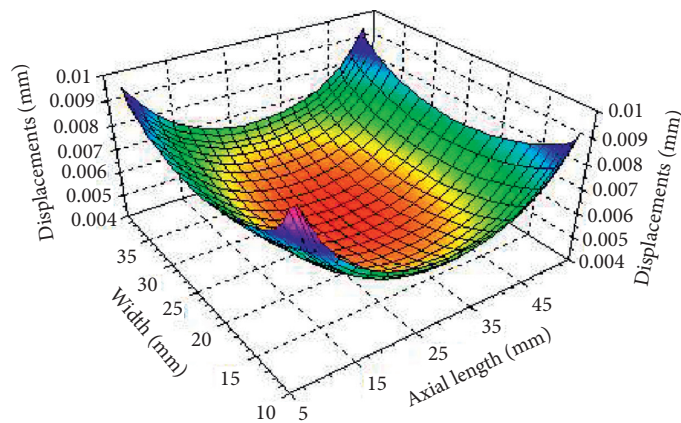
FIGURE 4: Displacement distributions in the contact area.

Figure 5: Pressure distributions in the contact area.

Figure 6: Friction distributions in the contact area.

Figure 7: Friction slip field in the contact area.

FIGURE 8: Comparison of contact displacements under different loads.

FIGURE 9: Comparison of contact pressures under different loads.
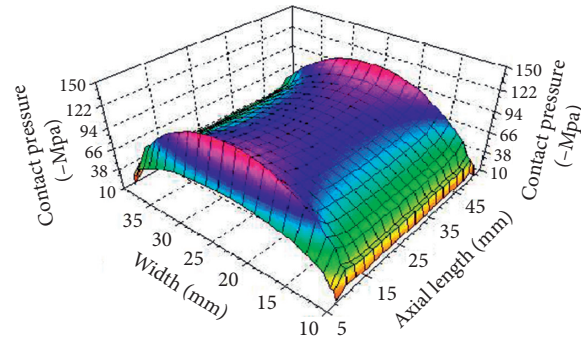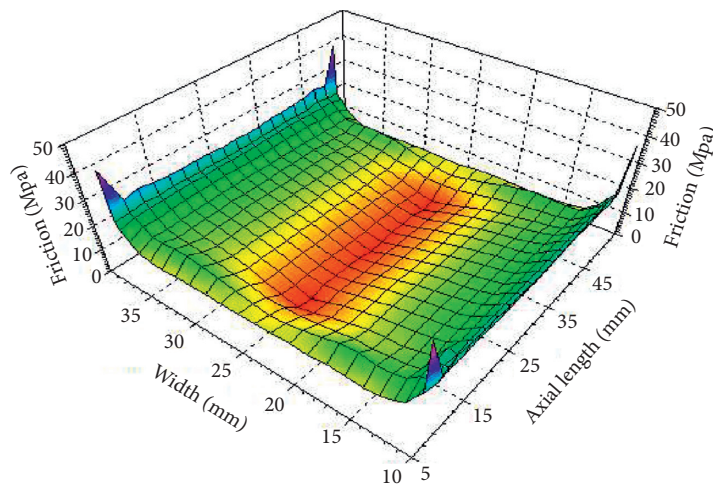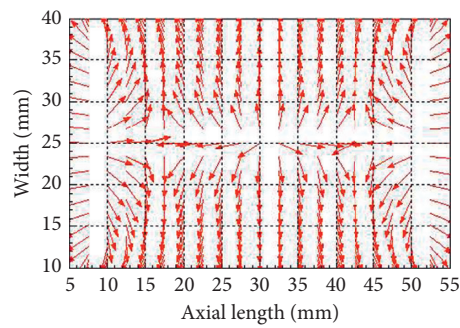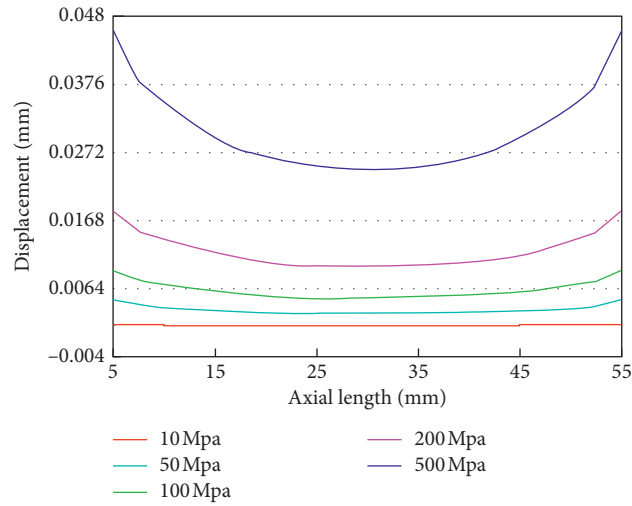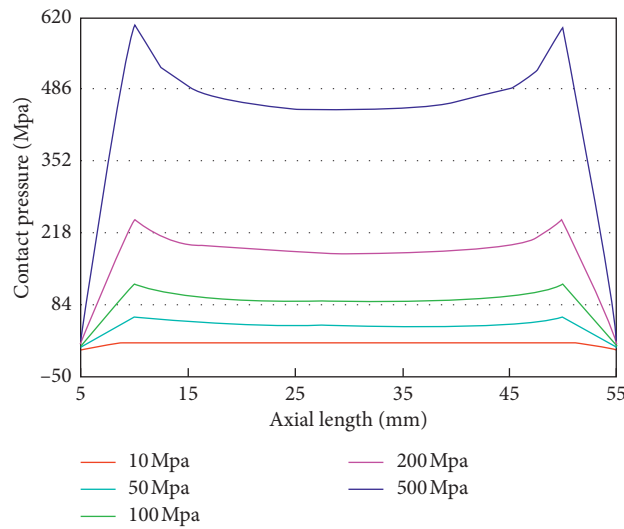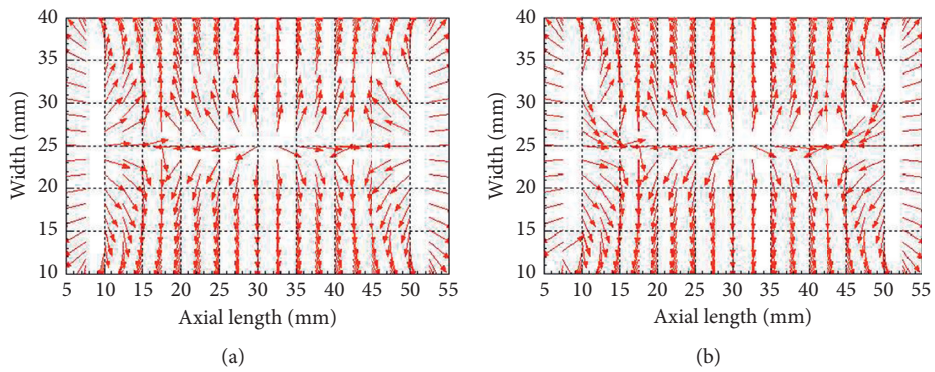

(a)

(b)

FIGURE 10: Friction slip field in the contact area. (a) Friction slip ($P = 1$ GPa). (b) Friction slip ($P = 10$ GPa).
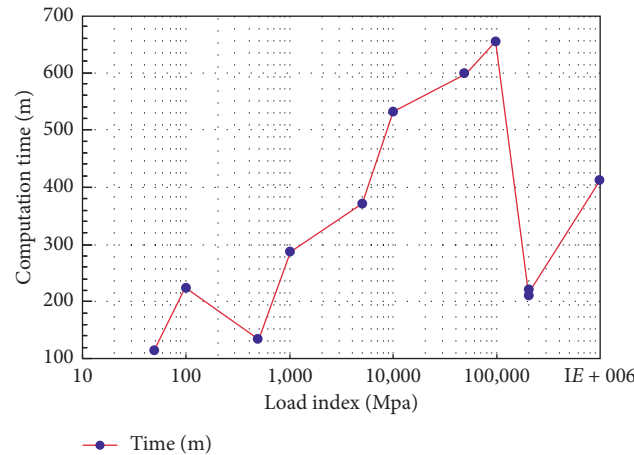
FIGURE 11: Influence of a penalty factor on the computational efficiency.

In addition, numerical experiments show that when the loads increase gradually, if the penalty factor α is taken as an inappropriate value, the computation time will sharply increase, as is shown in Figure 11.

7. Conclusions

Based on the FM-BEM, a node_face frictional contact mode was analyzed and nonpenetrating constraints were presented for 3D elastic frictional contact problems. For the case of frictional contact without penetration, nonlinear contact constraints were linearized by use of the least square method and an optimization mathematical model with node_face frictional contact mode was established. For the case of frictional contact with penetration, according to the principle of minimum potential energy, a penalty function method was used to apply the contact constraints and an energy objective function was constructed; then, a node_face frictional contact analysis was transformed into an unconstrained optimization problem. For the elastic frictional contact FM-BEM problem, nonpenetrating constraints were introduced into the system as a penalty term. Without increasing the system variables, a penalty factor mathematical programming model was established by the penalty function method. The influence of penalty factor on the solution process was analyzed, and a penalty optimization IGMRES (m) algorithm was presented. The frictional contact of two elastic objects under different loads was numerically simulated, and the results of displacements, pressures, friction forces and friction slips in the contact area were obtained. Theoretical analysis and numerical experiment showed that the new method had much superiority in efficiency, applicability, easy numerical implementation, fast convergence, stability, etc. The proposed FM-BEM penalty functional method could provide new ideas and methods for the solution of frictional contact problems and related mathematical, mechanical, and physical problems.

Data Availability

The data used to support the results of this study are included within the article.

Conflicts of Interest

The authors declare that they have no conflicts of interest.

Acknowledgments

References

[1] S. Zhang, X. Li, and R. Ran, "Self-adaptive projection and boundary element methods for contact problems with Tresca friction," *Communications in Nonlinear Science and Numerical Simulation*, vol. 68, pp. 72–85, 2019.

[2] J. Han and H. Zeng, "Variational analysis and optimal control of dynamic unilateral contact models with friction," *Journal of Mathematical Analysis and Applications*, vol. 473, no. 2, pp. 712–748, 2019.

[3] K. Feng and Z. C. Shi, *Mathematical Theory of Elastic Structure*, Science Press, Beijing, China, 1981.

[4] D. Z. Meng and W. Liu, *Modern Science and Engineering Computing*, Higher Education Press, Beijing, China, 2009.

[5] Z. H. Yao and H. T. Wang, *Boundary Element Method*, Higher Education Press, Beijing, China, 2010.

[6] G. X. Shen, H. Xiao, and Y. M. Chen, *Boundary Element Method*, Mechanical Industry Press, Beijing, China, 1998.

[7] Y. Li and G. R. Liu, "A novel node-based smoothed finite element method with linear strain fields for static, free and forced vibration analyses of solids," *Applied Mathematics and Computation*, vol. 352, pp. 30–58, 2019.

[8] J. Zhou, D. Xu, and X. Dai, "Weak Galerkin finite element method for the parabolic integro-differential equation with weakly singular kernel," *Computational and Applied Mathematics*, vol. 38, no. 2, 2019.

[9] Z. W. Qian, D. J. Shang, Q. H. Sun et al., "Acoustic radiation from a cylinder in shallow water by finite element-parabolic equation method," *Acta Physica Sinica*, vol. 68, no. 2, pp. 139–152, 2019.

[10] Z. L. Chen, Z. C. Yang, Y. Y. Wang et al., "A high-frequency shock response analysis method based on energy finite

element method and virtual mode synthesis and simulation," *Acta Aeronautica ET Astronautica Sinica*, vol. 39, no. 8, pp. 177–186, 2018.

[11] F. Kosior and N. Guyot, "Analysis of frictional contact problem using boundary element method and domain decomposition method," *International Journal for Numerical Methods in Engineering*, vol. 46, no. 1, pp. 65–82, 2015.

[12] B.-D. Zhong, F. Yan, and J.-H. Lv, "Continuous-discontinuous hybrid boundary node method for frictional contact problems," *Engineering Analysis with Boundary Elements*, vol. 87, pp. 19–26, 2018.

[13] G. Q. Li, "A conjugate boundary element method for complex analysis of analytic functions," *Applied Mathematics and Mechanics*, vol. 38, no. 8, pp. 863–876, 2017.

[14] Z. M. He and B. S. Wang, "Research on added mass of cavitating vehicles by boundary element method," *Journal of Ship Mechanics*, vol. 22, no. 2, pp. 127–134, 2018.

[15] Z. Q. Meng, R. Shen, C. Y. Dang et al., "A barrier objective penalty function algorithm for mathematical programming," *Journal of Systems Science and Mathematical Sciences*, vol. 36, no. 1, pp. 75–92, 2016.

[16] Y. Zheng and Z. Q. Meng, "An algorithm of new objective penalty function," *Journal of Systems Science and Mathematical Sciences*, vol. 36, no. 10, pp. 1697–1709, 2016.

[17] I. Dione, "Optimal convergence analysis of the unilateral contact problem with and without Tresca friction conditions by the penalty method," *Journal of Mathematical Analysis and Applications*, vol. 472, no. 1, pp. 266–284, 2019.

[18] C. Fu, "Three dimensional elastic frictional contact system modeling and optimization of penalty function method based on the boundary element method," Master's degree thesis, Yanshan University, Qinhuangdao, China, 2017.

[19] F. Chen, "Research of DDA contact theory and application of higher order displacement mode theory based on penalty function method and double potential energy theory," Master's degree thesis, Southwest Jiaotong University, Chengdu, China, 2017.

[20] M. Zang, W. Gao, and Z. Lei, "A contact algorithm for 3D discrete and finite element contact problems based on penalty function method," *Computational Mechanics*, vol. 48, no. 5, pp. 541–550, 2011.

[21] F. Hamad, S. Giridharan, and C. Moormann, "A penalty function method for modelling frictional contact in MPM," *Procedia Engineering*, vol. 175, pp. 116–123, 2017.

[22] R. Ortega, J. C. García Orden, M. Cruchaga, and C. García, "Energy-consistent simulation of frictional contact in rigid multibody systems using implicit surfaces and penalty method," *Multibody System Dynamics*, vol. 41, no. 3, pp. 275–295, 2017.

[23] H. Baek and K. Park, "Cohesive frictional-contact model for dynamic fracture simulations under compression," *International Journal of Solids and Structures*, vol. 144-145, pp. 86–99, 2018.

[24] J. Li, Y. L. Cheng, and Z. C. Li, "Superconvergence of the composite rectangle rule for computing hypersingular integral on interval," *Numreical Mathematics: Theory, Methods and Applications*, vol. 13, no. 3, pp. 770–787, 2020.

[25] J. Li and Y. L. Cheng, "Linear barycentric rational collocation method for solving second-order Volterra integro-differential equation," *Computational and Applied Mathematics*, vol. 39, p. 92, 2020.

[26] J. Li and Y. Cheng, "Linear barycentric rational collocation method for solving heat conduction equation," *Numerical Methods for Partial Differential Equations*, vol. 37, no. 1, pp. 533–545, 2021.

[27] J. Li and Y. Cheng, "Barycentric rational method for solving biharmonic equation by depression of order," *Numerical Methods for Partial Differential Equations*, 2020.

[28] Y. J. Liu, *Fast Multipole Boundary Element Method: Theory and Applications in Engineering*, Cambridge University Press, Cambridge, UK, 2009.

[29] G. X. Shen, D. Y. Liu, and C. X. Yu, *Fast Multipole Boundary Element Method and Engineering of Rolling Mill*, Science Press, Beijing, China, 2005.

[30] A. T. Htet, G. B. Saturnino, E. H. Burnham, G. M. Noetscher, A. Nummenmaa, and S. N. Makarov, "Comparative performance of the finite element method and the boundary element fast multipole method for problems mimicking transcranial magnetic stimulation (TMS)," *Journal of Neural Engineering*, vol. 16, no. 2, Article ID 024001, 2019.

[31] Q. Wang, W. Zhou, Y. Cheng, G. Ma, X. Chang, and B. Liu, "A NURBS-enhanced improved interpolating boundary element-free method for 2D potential problems and accelerated by fast multipole method," *Engineering Analysis with Boundary Elements*, vol. 98, pp. 126–136, 2019.

[32] J. Li, W. Chen, and Q. Qin, "A modified dual-level fast multipole boundary element method based on the Burton-Miller formulation for large-scale three-dimensional sound field analysis," *Computer Methods in Applied Mechanics and Engineering*, vol. 340, pp. 121–146, 2018.

[33] J. J. Rong, J. Y. Xiao, and L. H. Wen, "A high order kernel independent fast multipole boundary element method for elasto dynamics," *Chinese Journal of Theoretical and Applied Mechanics*, vol. 46, no. 5, pp. 776–785, 2014.

[34] Y. G. Wang, G. L. Wen, Z. F. Chen et al., "A multipole Galerkin BEM for acoustic problems," *China Mechanical Engineering*, vol. 24, no. 8, pp. 1033–1037, 2013.

[35] C. X. Yu and Y. F. Mu, "Nonlinear mathematical programming FM-BEM for the elastic frictional contact system," *International Journal of Innovative Computing Information and Control*, vol. 4, no. 2, pp. 403–412, 2008.

[36] C. X. Yu, H. Y. Yu, and Y. M. Chen, "Fast multipole boundary element method for 2-D Helmholtz equation problems and its error analysis," *Journal of Information & Computational Science*, vol. 9, no. 18, pp. 5571–5578, 2012.

[37] C. Yu, C. Ren, and X. Bai, "VRP-GMRES (m) iteration algorithm for fast multipole boundary element method," *Mathematical and Computational Applications*, vol. 21, no. 4, p. 49, 2016.

[38] C. Yu, D. Liu, Y. Zheng, and G. Shen, "3-D rolling processing analysis by fast multipole boundary element method," *Engineering Analysis with Boundary Elements*, vol. 70, pp. 72–79, 2016.

Research Article

SVR Prediction Algorithm for Crack Propagation of Aviation Aluminum Alloy

Jincai Chang (ID),[1] **Zhihang Wang** (ID),[1] **Qingyu Zhu,**[2] and **Zhao Wang**[1]

[1]*College of Science, North China University of Science and Technology, Tangshan, Hebei 063210, China*
[2]*Avic China Aero-Polytechnology Establishment, Beijing 100028, China*

Correspondence should be addressed to Zhihang Wang; wzh8240@126.com

Aluminum alloy material is an important component material in the safe flight of aircraft. It is very important and necessary to predict the fatigue crack growth between holes of aviation aluminum alloy materials. At present, the investigation on the prediction of the cracks between two holes and multiholes is a key problem to be solved. Due to the fact that the fatigue crack growth test of aluminum alloy plate with two or three holes was carried out by the MTS fatigue testing machine, the crack length growth data under different test conditions were obtained. In this paper, support vector regression (SVR) was used to fit the crack data, and the parameters of SVR are optimized by the grid search algorithm at the same time. And then the model of SVR to predict the crack length was established. Discussion on the results shows that the prediction model is effective. Furthermore, the crack growth between three holes was predicted accurately through the model of the crack law between two holes under the same load form.

1. Introduction

As we all know, the aluminum alloy material studied in this paper, as an important component material in the aviation field, is widely used in the aviation industry [1] and plays an important role in ensuring the safety of the aviation aircraft flight. Therefore, we should attach great importance to carry out relevant research work on it.

The investigation on fatigue crack growth prediction has a history of several decades. The study of fatigue originated from the embryonic period of the European industrial revolution in the first half of the 19th century. As early as the middle of the 19th century, Wohler, a German railway engineer, put forward the concept of stress-life (*S-N*) curve and fatigue limit and pointed out the influence degree of factors affecting materials fatigue. After that, some researchers developed Wohler's investigation [2–5] from 1870 to 1890. After decades of development, there are much research on fatigue crack propagation, which is microinvestigation on materials and mechanism analysis by the finite element method. As we all know, fatigue failure of materials needs to

go through three stages: crack initiation, crack stable propagation, and crack instability propagation. The total fatigue life is also composed of these three parts. Generally, the $(da/dN) - \Delta K$ curve in the double logarithmic coordinate system is used to describe the fatigue crack growth rate.

In Figure 1, zone 1 is a low rate region, zone 2 is a medium rate region, and zone 3 is a high rate region. In the medium rate region (i.e., zone 2), $(da/dN) - \Delta K$ has a good logarithmic linear relationship, which is the focus of fatigue crack growth research in this paper.

The rapid development of fracture mechanics in the early 20th century provides a theoretical basis for the study of fatigue crack growth. In 1961, Paris et al. [6] put forward the Paris formula suitable for the medium rate region on the basis of the fracture mechanics method to express the law of crack propagation, which is the most widely used method in engineering. Besides, Alshamma and Jassim [7] confirmed all parameters of the Paris Law in the experiment and found the crack growth speed through the experiment and analysis. On the basis of the previous studies, the investigation on
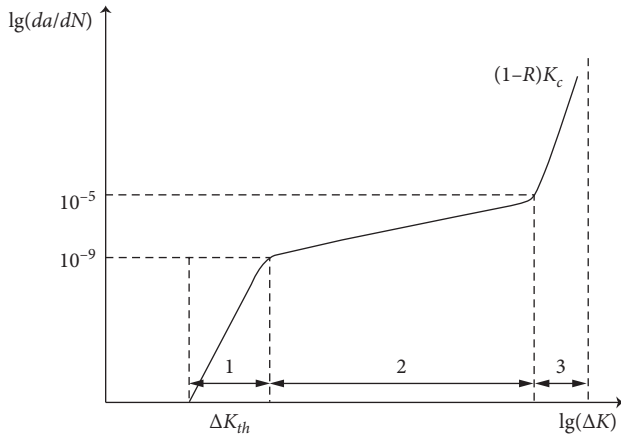
Figure 1: $(da/dN) - \Delta K$ curve.

crack growth and fracture is in the ascendant in recent years [8–12], and the main progress is described as follows: Lei [13] takes 2024-T4 aluminum alloy as the investigation object and uses the finite element method to investigate the influence rule and mechanism of overload condition on the change trend of subsequent fatigue crack growth rate (da/dN). For the problem of crack propagation in a plate with a single hole central crack, Zhang and Wang [14] introduced a new Z fracture criterion which can well predict the crack propagating direction of mode I crack in carbon-fiber reinforced composite laminates and proposed new concepts of in-plane average strain, in-plane dilatational strain energy density factor, and reciprocal characteristic function. Furthermore, Hajimohamadi and Ghajar [15] investigated the analytical solution of the stress field and stress intensity in an infinite plane with elliptical holes with an unequal length of prefabricated cracks. For the crack growth problem of two holes plate, Bhargava and Jangid [16] proposed a mathematical model of two unequal-collinear crack growth. Additionally, Singh et al. [17] proposed an improved strip saturation model based on the combination of two internal electric saturation bands and studied two-dimensional (2D) arbitrarily polarized semipermeable dielectric analytically. For the crack growth problem of the porous plate. Zhao et al. [18] applied the basic principle of the complex stress function method and its approximate superposition method to the solution of stress intensity factor of collinear multiple cracks in infinite plates and made a preliminary exploration on the solution of porous cracks. Moreover, Li et al. [19] used the Eshelby inclusion theory and weight function method to give the approximate analytical solution of stress intensity factor of the typical porous multicrack problem and combined with Paris crack growth formula to predict the fatigue crack growth life. Zhu et al. [20–22] conducted an in-depth study on the stress intensity factor and crack opening displacement of interpore crack by using the complex variable function and relevant integral method and then obtained the relevant laws of stress intensity factor and crack opening displacement. Li et al. [23–25] carried out theoretical innovation on the numerical calculation methods used in the fatigue crack growth problem, providing the possibility of

solving such problems more accurately in theory. These investigations on the prediction of fatigue crack growth are based on the empirical formula, analytical method and the finite element method. Based on the existing mechanism investigation and crack growth performance, the analytical expression of crack growth law is obtained. In view of the fact that dealing with the actual aviation crack data which is an urgent proposition to find as way to find a way to get the crack growth law by data-driven method [26], the intelligent algorithm model of aviation fatigue crack growth based on the data-driven method will be built in the focus of this paper.

On the other hand, the support vector regression (SVR) algorithm is an extension of the support vector machine algorithm in regression problem, which was first proposed by Drucker et al. [27]. After years of development, the SVR algorithm is widely used in all aspects of scientific investigation. The application of the SVR algorithm in crack growth and life prediction is as follows: based on grey theory and support vector regression method, Yang et al. [28] proposed GMSVR model and parameter optimization method of the artificial bee colony and applied it to FCG prediction of 7075 aluminum alloy. Furthermore, Song et al. [29] used XFEM and SVR to predict the fatigue life of plate cracks. SVR algorithm has a large number of kernel functions to use, so it can be very flexible to solve various nonlinear regression problems. In addition, the SVR algorithm is based on the principle of structural risk minimization, which avoids overlearning problem and has strong generalization ability. Moreover, it is a convex optimization problem, so the local optimal solution must be the global optimal solution. The SVR algorithm is used to study the crack growth of the aluminum alloy plate. We just use the SVR model established from the data to get the prediction result of crack growth, which avoids the discussion of crack growth mechanism based on the empirical formula. Therefore, it is feasible to apply the SVR algorithm to the crack growth prediction of aluminum alloy plate, which has the advantage of solving such problems.

In order to predict the interhole crack growth length of the aeronautical aluminum alloy plate by data-driven method, it is necessary to collect the crack growth length and the corresponding cycle number under different load spectrum and initial crack conditions. The support vector regression (SVR) [30, 31] algorithm, especially, is a data-driven based method, which is used to fit the crack growth data obtained from the fatigue load test in this paper. Under the same load form, a model which can predict the crack rule between three circular holes by the crack rule between two holes is established, and its fitting effect is tested. The aviation aluminum alloy plate with two or three holes is the test materials of the fatigue load test. First of all, the data of crack length and cycle number of plate crack growth under constant amplitude load and variable amplitude load are collected in this experiment. After that, to get the general rule of crack growth, data exploration, data preprocessing, and so on are carried out. Finally, the applicable support vector regression algorithm is used to fit the crack growth data to get the prediction results of the model and evaluate

the effect of the model. This model can be used in the field of fatigue crack growth prediction of the porous edge of aluminum alloy materials for aircraft. It can predict the crack growth length by the number of cycles and can also predict the number of cycles by the crack growth length through the model. The establishment of the crack prediction model for the aviation aluminum alloy plate can predict three-hole crack rule from two-hole crack and solve the prediction problem of unknown crack growth rule between holes. It is a breakthrough in crack prediction between holes based on a data-driven method. This model not only provides the basis for the prediction of the crack law of aviation aluminum alloy materials but also can be applied to the prediction of safe flight and life of aviation aircraft and guide the prediction of the crack growth law between holes of actual aviation aluminum alloy plate.

2. Test Content

2.1. Test Introduction. In this section, to investigate the crack growth law of aviation aluminum alloy plate with two holes and three holes under constant amplitude load and variable amplitude load, respectively, is one purpose of this experimental investigation. And, on the other hand, to use the suitable support vector regression algorithm to fit and analyze the experimental data is another purpose of this experimental investigation. Besides, MTS fatigue testing machine system is used in this test, which is used in fatigue test and crack growth test of typical aviation connection structure with multiple cracks. Moreover, the crack growth behavior was measured by a high power optical microscope. Figures 2 and 3 show the MTS fatigue testing machine system.

In addition, the most commonly used aluminum-lithium alloy on the active advanced aircraft is the experimental materials used in this test. In order to explore the propagation law of cracks between holes in the aviation aluminum alloy plate, the aviation aluminum alloy plate is divided into two holes and three holes. Besides, the schematic diagram of the two types of aviation aluminum alloy plates used is shown in Figures 4 and 5.

Besides, the diameters of the small circular holes in the aluminum alloy plate specimens are 4 mm, while the distance between points B and C in the figure and the distance between points D and E are 12 mm, which is shown in Figures 4 and 5. The parameters of the fatigue load test are shown in Table 1.

Points A, B, C, D, E, and F in Figures 4 and 5 preset the initial crack length, respectively, so as to obtain the crack growth in the test.

The aircraft aluminum alloy plate we use has two holes and three holes. For the load, there are two categories of constant amplitude load and variable amplitude load. For the statistics of the initial crack prefabrication of aviation aluminum alloy plates, we divided the constant amplitude and variable amplitude into two categories, respectively, and then distinguished the configuration of two-hole and three-hole cracks in each category; then, there is the following statistical table of crack prefabrication. Among them, there are 11 constant amplitude plate specimens and 9 variable

FIGURE 2: MTS fatigue testing machine system.

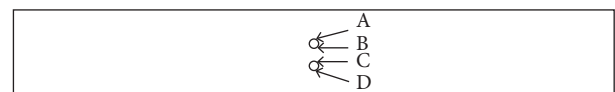FIGURE 3: Test diagram of two-hole plate specimen.

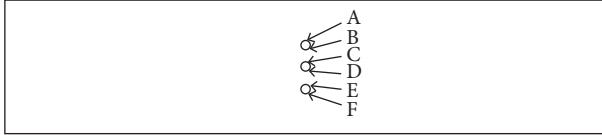FIGURE 4: Schematic diagram of two-hole plate specimen.

Figure 5: Schematic diagram of three-hole plate specimen.

Table 1: Table of fatigue load test parameters.

	Load range (kN)	Load median (kN)	Load amplitude (kN)	Median of variable amplitude load (kN)	Amplitude of variable amplitude load (kN)
Constant amplitude load	1.3–13	7.15	5.85	—	—
Variable amplitude load	1.3–13	7.15	5.85	14.3	11.7

Table 2: Initial preset cracks of two-hole specimen with constant amplitude.

Serial number	A	B	C	D
01	1	1	0	0
02	1	1.5	0	0
03	1	1	1	1
04	1	1.5	1	1
05	1	1.5	1.5	1
06	0.5	1.5	0.5	0.5
07	0.5	1.5	1.5	0.5
08	0.5	0.5	0.5	0.5
09	0.5	1.5	0	0
10	0.5	1.5	1.5	0.5
11	0.5	0.5	0	0

Table 3: Initial preset cracks of three-hole specimen with constant amplitude.

A	B	C	D	E	F
0.5	0.5	1.5	1.5	0.5	0.5

amplitude plate specimens. As shown in Tables 2 and 3, the statistics of crack preset of plate specimen under constant amplitude load (the crack length refers to the length of crack propagation with the initial crack tip as the origin, unit: mm):

It can be seen that Tables 4 and 5 (unit: mm) show the statistics of the preset cracks of the plate specimen under variable amplitude load.

The vertical line of points B and C is taken as the axis of symmetry for two-hole aluminum alloy plate in this paper. It can be seen that point A corresponds to point D and point B corresponds to point C. If the initial crack length of the four points is the same, it is regarded as the case of initial crack

Table 4: Initial preset cracks of two-hole specimen with variable amplitude.

Serial number	A	B	C	D
01	0.5	0.5	0	0
02	0.5	1.5	0	0
03	0.5	0.5	0.5	0.5
04	0.5	1.5	0.5	0.5
05	0.5	1.5	1.5	0.5

Table 5: Initial preset cracks of three-hole specimen with variable amplitude.

A	B	C	D	E	F
0.5	0.5	1.5	0.5	0.5	0.5

symmetry. Similarly, the vertical line of point C and point D is taken as the axis of symmetry for three-hole aluminum alloy plate. It can be seen that point A corresponds to point F, point B corresponds to point E, and point C corresponds to point D. Whether the initial crack is symmetrical or not will have different results in the study of crack propagation mechanism. In the data exploration stage, the symmetry of the initial crack will directly affect the speed of the subsequent crack growth. Therefore, it is necessary to discuss whether the crack is symmetrical or not, whether it is in the relevant mechanical mechanism or the collected data exploration images. In the case of the above initial crack configuration, the type of the initial crack length at each hole edge of the two-hole aluminum alloy plate is involved in this paper. In this way, the random configuration of the initial crack can be considered. In this paper, the initial crack random configuration here means that the subsequent crack length adopts the cumulative crack length between holes. The initial crack configuration has certain randomness, which weakens the influence of the initial crack length configuration between holes on the crack growth law, so more attention is paid to the growth law of the crack accumulation length. With such a random initial crack configuration, a general prediction model of interpore crack length under the same load spectrum (considering only the cumulative crack length) can be established. It can provide the basis for the follow-up investigation work through the above analysis.

2.2. Test Process. Firstly, the abovementioned constant amplitude fatigue load spectrum and variable amplitude fatigue load spectrum (see Table 1) which are suitable for laboratory use are adopted. Secondly, the fatigue crack growth test of porous plate specimen under constant amplitude load spectrum is carried out. The fatigue crack growth data of multiple cracks are collected, and the growth rule is analyzed. Finally, the fatigue crack growth test of plate specimen with porous edge cracks under variable amplitude load is carried out. Therefore, the data of crack length and number of cycles are collected to provide test data for the

prediction of crack length. According to the previous solution, it also can even establish the life of fatigue multicrack propagation law.

2.3. Experimental Data. In this section, the test data of crack growth length and cycle times of 20 groups of aluminum alloy specimens are obtained, which are saved in 20 Excel files, respectively, through the above fatigue loading test. Some original data of crack growth for the abovementioned aluminum alloy specimens are presented in this paper. The initial cracks at points A, B, C, and D in the constant amplitude two-hole test specimen 03 are all 1.0 mm test data, some of which are shown in Table 6 (the data in the first column of the table is the number of cycles, and the rest is in mm).

The initial crack configuration of the constant amplitude three-hole specimen is as follows: the initial crack at points A, B, E, and F is 0.5 mm and the initial crack at point C and point D is 1.5 mm. Some of the data are shown in Table 7 (the data in the first column of the table is the number of cycles, and the rest is in mm).

For the sample with variable amplitude, it should be clear that the effect of retardation after the application of overload will occur. The intuitionistic crack growth image of variable amplitude specimen is obviously different from that under constant amplitude load, which will experience a long slow growth period, thus prolonging the life of the component, while the crack growth rate under constant amplitude load will continue to increase, and its life is shorter than that under variable amplitude load. These features are visually shown in Figures 6–9.

However, the initial cracks at points A, B, C, and D in the two-hole variable amplitude test specimen 03 (complement) are all 0.5 mm test data, some of which are shown in Table 8 (the data in the first column of the table is the number of cycles, and the rest is in mm).

The initial crack configuration of the variable amplitude three-hole specimen is as follows: the initial crack at points A, B, D, E, and F is 0.5 mm and the initial crack at point C is 1.5 mm. Some of the data are shown in Table 9 (the data in the first column of the table is the number of cycles, and the rest is in mm).

3. The Theory of Support Vector Regression

As we know, support vector regression (SVR) is a development of the support vector machine algorithm, which was first extended to support vector regression by Drucker et al. [27]. Support vector regression is a small specimen learning method with a solid theoretical basis. And the traditional process from induction to deduction can be avoided by it. By this means, SVR simplified greatly the usual regression problem. The support vector regression algorithm avoids "dimension disaster" in a sense and has good robustness. The main principles of SVR are as follows.

Given training samples $T = \{(\mathbf{x}_1, y_1), (\mathbf{x}_2, y_2), \ldots, (\mathbf{x}_m, y_m)\}$, $y_i \in \mathbb{R}$. The regression model shaped as ($f(\mathbf{x}) =$

TABLE 6: Partial test data of constant amplitude two-hole test specimen 03.

	A	B	C	D
13000	0.6	0.9	0.9	0.9
13200	0.6	0.9	0.9	1
13400	0.7	1	1.1	1
13600	0.8	1	1.1	1.05
13800	0.8	1.2	1.2	1.05
. . .				
18900	5	4.7	5	5.6
18925	5.2	4.7	5	5.9
18950	5.5	4.7	5	6.2
18975	5.7	4.7	5	6.6
19000	6	4.7	5	7

TABLE 7: Partial test data of constant amplitude three-hole test specimen.

	A	B	C	D	E	F
5000	0	0	0	0	0	0
28000	0	0	0	0	0	0
28500	0	0	0	0.1	0	0
29000	0	0	0	0.2	0	0
29500	0	0	0	0.3	0	0
. . .						
64250	3.4	2	8	7.2	2.8	6.6
64500	3.7	2	8	7.2	2.8	7.5
64750	4	2	8	7.2	2.8	7.6
64973	6.2	2	8	7.2	2.8	10.2
64976	17.2	2	8	7.2	2.8	16.8

— Normalized data of two holes with constant amplitude
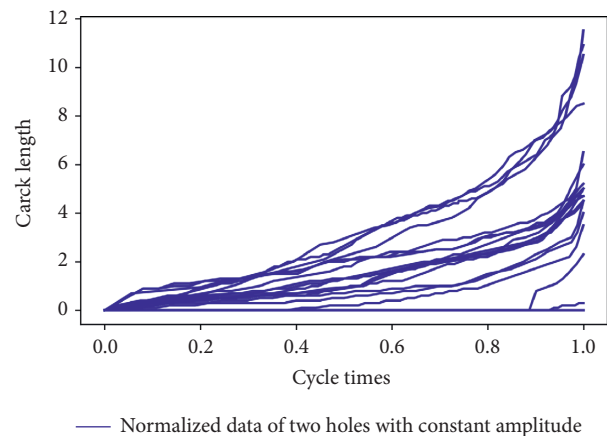
FIGURE 6: Normalized data of two holes with constant amplitude.

$\mathbf{w}^T \mathbf{x} + b$) is the learning objective function. Moreover, the model parameters which make $f(\mathbf{x})$ as close as possible to y, $\mathbf{w}$, and b are to be determined.

Next, support vector regression [30] assumes that we can tolerate the maximum deviation of ε between $f(\mathbf{x})$ and y. That is to say, the loss is only calculated when the absolute value of the difference between $f(\mathbf{x})$ and y is greater than (ε). As shown in Figure 10, this is equivalent to building a spacing band (i.e., the part sandwiched between the two

FIGURE 7: Normalized data of three holes with constant amplitude.

— Normalized data of three holes with constant amplitude
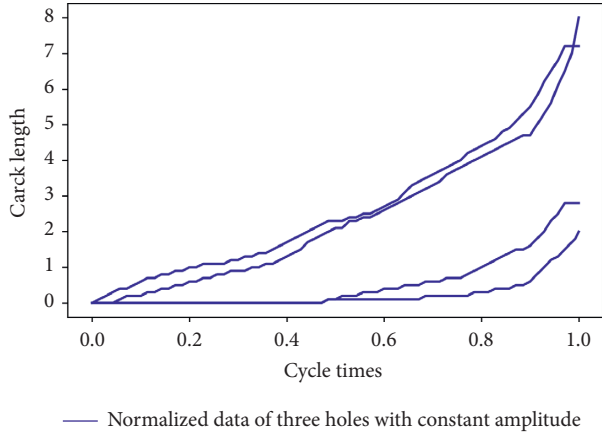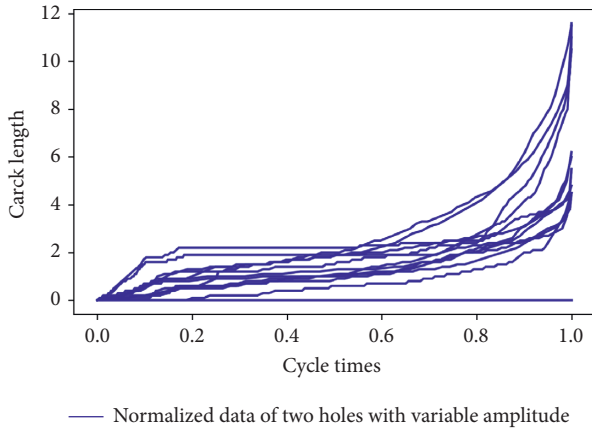

FIGURE 8: Normalized data of two holes with variable amplitude.

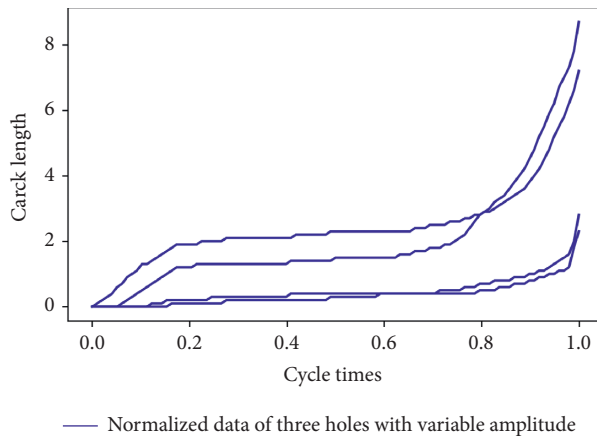— Normalized data of two holes with variable amplitude

FIGURE 9: Normalized data of three holes with variable amplitude.

— Normalized data of three holes with variable amplitude

TABLE 8: Partial test data of variable amplitude two-hole test specimen 03 (complement).

	A	B	C	D	
11000	0	0.1	0.1	0.1	
11500	0	0.1	0.1	0.1	
12000	0.1	0.1	0.1	0.1	
12500	0.1	0.1	0.1	0.1	
13000	0.1	0.2	0.2	0.1	
		...			
15750	0.5	0.5	0.6	0.6	
16000	0.6	0.5	0.6	0.6	Added a variant
16500	0.6	0.5	0.6	0.6	
		.....			
42100	6.3	4.8	6.2	7.2	
42200	6.5	4.8	6.2	7.5	
42300	7	4.8	6.2	7.8	
42400	8	4.8	6.2	9	
42448	17.1	4.8	6.2	18.2	

TABLE 9: Partial test data of variable amplitude three-hole test specimen.

	A	B	C	D	E	F	
5000	0	0	0	0	0	0	
10000	0	0	0	0	0	0	
15000	0	0	0	0	0	0	
20000	0	0	0	0	0	0	
25000	0	0	0	0	0	0	
			...				
46000	0	0.1	1.8	1.1	0.2	0	
47000	0	0.1	1.9	1.2	0.2	0	Added a variant
48000	0	0.1	1.9	1.2	0.2	0	
			...				
132500	6.3	2.8	7.2	8.7	2.3	5.3	
133000	8	2.8	7.2	8.7	2.3	5.9	
133250	9.1	2.8	7.2	8.7	2.3	6.7	
133500	10.5	2.8	7.2	8.7	2.3	7.7	
133532	17.3	2.8	7.2	8.7	2.3	18	

$$\min_{\mathbf{w},b} \frac{1}{2}\|\mathbf{w}\|^2 + b, \tag{1}$$

where $b = C \sum_{i=1}^{m} l_\varepsilon (f(\mathbf{x}_i) - y_i)$ and C is the regularization constant. It can be seen from Figure 11 that l_ε is the ε-insensitive loss function:

$$l_\varepsilon (z) = \begin{cases} 0, & \text{if } |z| \le \varepsilon, \\ |z| - \varepsilon, & \text{otherwise.} \end{cases} \tag{2}$$

By introducing relaxation variables ξ_i and $\widehat{\xi}_i$, (1) can be rewritten as

$$\min_{\mathbf{w},b,\xi_i,\widehat{\xi}_i} \frac{1}{2}\|\mathbf{w}\|^2 + C \sum_{i=1}^{m} \left(\xi_i + \widehat{\xi}_i \right),$$

$$f(\mathbf{x}_i) - y_i \le \varepsilon + \xi_i, \tag{3}$$

$$\text{s.t.} \quad y_i - f(\mathbf{x}_i) \le \varepsilon + \widehat{\xi}_i,$$

$$\xi_i \ge 0, \widehat{\xi}_i \ge 0, \quad i = 1, 2, \ldots, m.$$

dashed lines in the figure) with a width of (ε) centered on $f(\mathbf{x})$ (i.e., the solid line in the figure). On the contrary, if the training samples fall into this interval, they are considered to be correctly predicted.
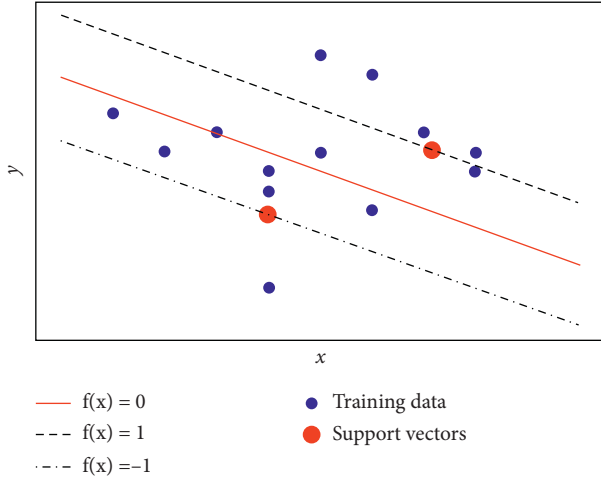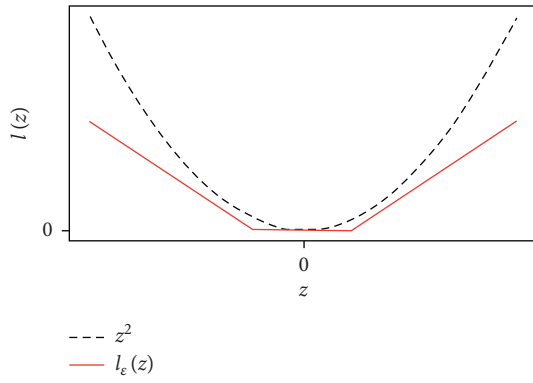
Therefore, the SVR problem can be formalized as

FIGURE 10: Schematic diagram of support vector regression.

FIGURE 11: (ε)-insensitive loss function.

Therefore, the solution of SVR can be obtained by the Lagrange multiplier method as follows:

$$f(\mathbf{x}) = \sum_{i=1}^{m} (\widehat{\alpha}_i - \alpha_i)\mathbf{x}_i^T \mathbf{x} + b. \qquad (4)$$

Furthermore, the samples of $(\widehat{\alpha}_i - \alpha_i) \neq 0$ in equation (4) are the support vectors of SVR, which must fall outside the ε-interval. Obviously, support vectors in SVR are only a part of the training samples; that is, its solution is still sparse.

If the feature mapping form $f(\mathbf{x}) = \mathbf{w}^T \phi(\mathbf{x}) + b$ is considered, then the corresponding solution can be obtained by the Lagrange multiplier method:

$$\mathbf{w} = \sum_{i=1}^{m} (\widehat{\alpha}_i - \alpha_i)\phi(\mathbf{x}_i). \qquad (5)$$

Substituting equation (5) into $f(\mathbf{x}) = \mathbf{w}^T \phi(\mathbf{x}) + b$, SVR can be expressed as

$$f(\mathbf{x}) = \sum_{i=1}^{m} (\widehat{\alpha}_i - \alpha_i)\kappa(\mathbf{x}, \mathbf{x}_i) + b, \qquad (6)$$

where $\kappa(\mathbf{x}_i, \mathbf{x}_j) = \phi(\mathbf{x}_i)^T \phi(\mathbf{x}_j)$ represent the kernel function. The kernel function used in this paper is Gauss kernel function, whose expression is $\kappa(\mathbf{x}_i, \mathbf{x}_j) = \exp(-(\|\mathbf{x}_i - \mathbf{x}_j\|^2/2\sigma^2))$. Where $\sigma > 0$ stand for the width of the Gaussian kernel.

4. Prediction of Crack Length by SVR

4.1. Data Standardization. As we all know, the input data to be normalized is required in the SVR algorithm. Therefore, it is necessary to normalize the data to be processed. The data to be used needs to be determined before normalization. According to the data exploration in the early stage, we can know from the visual graph that the crack length data is in the state of nonexpansion when the number of cycles is small. That is, a large number of zero values in the original data have no impact on the prediction results, so it can be discarded. After a certain length that the crack length reaches, the crack length remains unchanged when the number of cycles in the later period is large. Therefore, this part of the data can be discarded and only part of the data with changing rules can be retained. The influence of point A and point D of the two-hole plate and point A and point F of three-hole plate on interpore crack propagation is ignored in this test. Therefore, the following investigating contents only consider the crack growth between holes. We also add the initial crack length of each crack to each row of crack data, so that the crack data has a certain physical significance.

For convenience, standardization methods in data standardization are as follows:

Transform sequence $(x_1, x_2, \ldots, x_n)$ $x_i^* = ((x_i - \min_{1 \leq j \leq n} x_j)/(\max_{1 \leq j \leq n} x_j - \min_{1 \leq j \leq n} x_j))$, the new sequence $(x_1^*, x_2^*, \ldots, x_n^* \in [0,1])$ is dimensionless. The data can be standardized first for data preprocessing.

Using the Matplotlib Library in Python to draw the image and get the relevant statistics for each test specimen. Data preprocessing images between holes cracks of the above specimen are presented in this paper. Each image drawn below does not consider the zero-value data in the front part of the data file, and the number of cycles is processed by the above normalization method. The abscissa is the number of cycles after normalization and the ordinate is the crack length in mm, as expected in Figures 6–9 for the specific image.

After the above-standardized treatment, the crack length is treated as follows: the crack data of point B and point C are added to get the cumulative crack length, which is recorded as I_{BC}, and the cumulative crack length is about 12 mm for the two-hole crack specimen. Meanwhile, the crack data of points B, C, D, and E are added and record as I_{BCDE} to get the cumulative crack length, which is about 25 mm for the three-hole crack specimen.
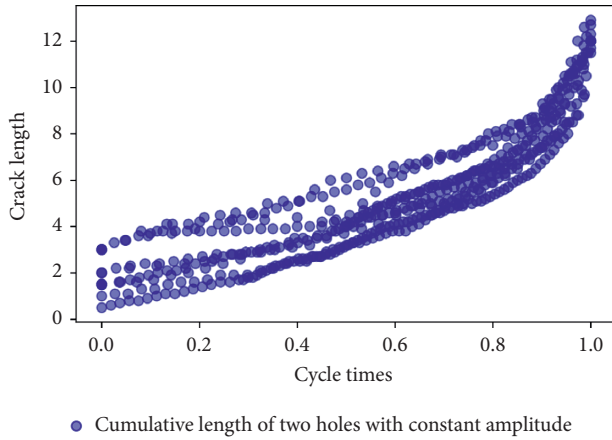
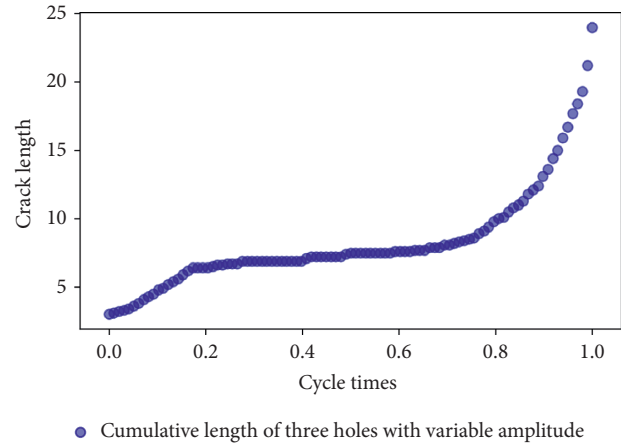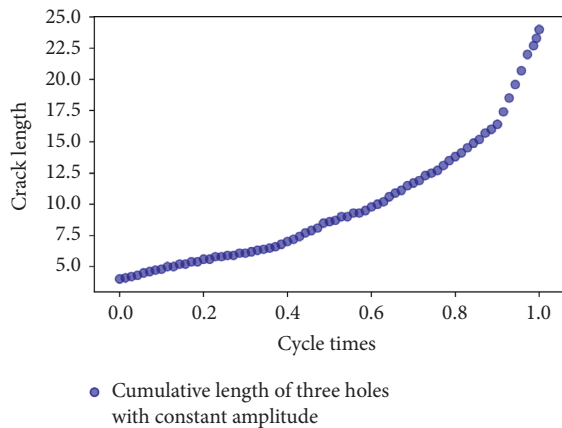FIGURE 12: Cumulative length of two holes with constant amplitude.

FIGURE 13: Cumulative length of three holes with constant amplitude.
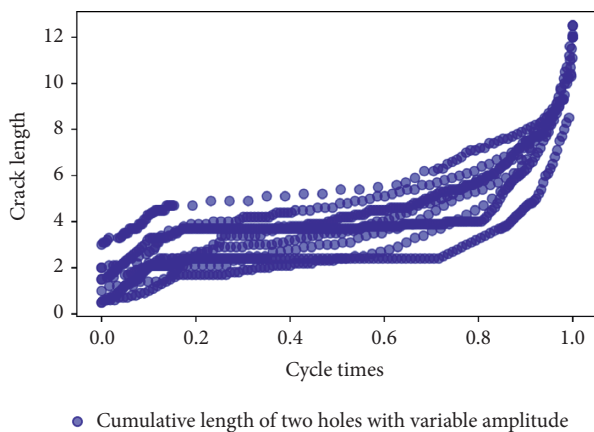

FIGURE 14: Cumulative length of two holes with variable amplitude.

After the abovementioned processing, the preprocessing image of crack growth data of each test piece is obtained. The abscissa is the number of cycles, and the ordinate is the sum of crack length between holes I_{BC} or I_{BCDE} data whose unit

FIGURE 15: Cumulative length of three holes with variable amplitude.

is mm in all the following figures. See Figures 12–15 for the specific image.

4.2. Prediction Steps of SVR. Obviously, the steps of using support vector regression to predict the crack length are as follows: first, establish the support vector regression model for the normalized I_{BC} crack data of the constant amplitude two-hole specimen, obtain the training and testing errors, and then test the effect of the model on the constant amplitude two-hole specimen. Then, the support vector regression model was established and predicted for I_{BCDE} crack data of normalized constant amplitude three-hole specimen, observe the error and deviation, and verify the prediction effect of the model. Finally, the prediction model is established for the variable amplitude specimen similar to the above prediction steps.

The SVR algorithm in scikit-learn is used to build the SVR model for crack prediction of aviation aluminum alloy plate by adjusting the parameters such as kernel (i.e., specify the kernel type to be used in the algorithm), gamma (i.e., for kernel coefficient), and C (i.e., for penalty parameter C of error term) in this paper.

Furthermore, this paper adopts the grid search optimization algorithm when adjusting the parameters. Grid search optimization algorithm is a kind of exhaustive search algorithm which optimizes the parameters by cross-validation and then obtains the optimal learning algorithm, that is to say, to traverse and search the corresponding permutation and combination values of each parameter in a given range, and each group of combination results constitutes a "grid." Then, each combination is applied to the training learning algorithm, and the evaluation results are obtained by cross-validation. After traversing and training all the parameter combinations, the grid search algorithm will automatically return the best parameter combination with the highest score, and its corresponding learning model is the optimal regression model.

It is known that the kernel, gamma, and C parameters need to be adjusted in SVR. For the kernel, that is, the type of

the kernel function, we specify using the radial basis kernel function. For gamma and C parameters, we use the Grid-SearchCV method in scikit-learn to optimize the grid search parameters and get the optimal parameters in this paper, where the value range of gamma is set as $\{0.01, 0.1, 1, 10, 100\}$, that is, (gamma $\in \{0.01, 0.1, 1, 10, 100\}$), and the value range of C is set as $\{1, 10, 100, 1000\}$, that is $C \in \{1, 10, 100, 1000\}$. According to the range of gamma and C from the above, there are 20 grid points in this method.

4.3. Evaluating Indicator.
Data set partition standard: for the division of data sets under different load spectra, this paper uses two-hole data under the corresponding load spectrum as training data and three-hole data as test data.

The commonly used cross-validation method in machine learning is used for the aspect of model evaluation in data set partition. In view of the fact that the half-fold cross-validation method [32] is specifically used in this paper, the reliable evaluation of the model effect is obtained by making full use of the data set, so as to verify the performance of the established SVR model for crack prediction of aviation aluminum alloy plate.

Additionally, error analysis indicators, mean square error [33], root mean square error, [34] and other error analysis indicators, are commonly used in regression problems. Variance, standard deviation, mean square error, and root mean square error are the error evaluation indicators used in this paper. The calculation formulas of each indicator are as follows:

Variance (S^2):

$$S^2 = \frac{1}{m} \sum_{i=1}^{m} (y_i - \overline{y})^2. \tag{7}$$

Standard deviation (S):

$$S = \sqrt{\frac{1}{m} \sum_{i=1}^{m} (y_i - \overline{y})^2}. \tag{8}$$

Mean square error (MSE):

$$\text{MSE} = \frac{1}{m} \sum_{i=1}^{m} (y_i - \widehat{y}_i)^2. \tag{9}$$

Root mean square error (RMSE):

$$\text{RMSE} = \sqrt{\frac{1}{m} \sum_{i=1}^{m} (y_i - \widehat{y}_i)^2}, \tag{10}$$

where m, y_i, $\widehat{y}_i$, and $\overline{y}$ are the total number of samples, the predicted value of the model, the real value, and the sample mean value, respectively.

It is significant to compare variance and standard deviation with MSE and RMSE. For example, if the MSE of prediction error is almost equal to the variance of the target (or RMSE is almost equal to the standard deviation of the target), this indicates that the prediction algorithm is not effective. By simply averaging the target value to replace the prediction algorithm, almost the same effect can be achieved. If the prediction error RMSE is about half of the actual target standard deviation, this is already pretty good performance. Because the variance and MSE comparison and the standard deviation and RMSE comparison have a certain correlation, thus, the comparison between standard deviation and RMSE is the main error indicator used in this paper.

4.4. Result Analysis.
According to the previous solution, this paper presents a visual image of the results of predicting the crack length of three-hole aluminum alloy plate specimens under the same load spectrum. In the visualization image, Figures 16 and 17 are the images of test data and prediction data. Besides, Figures 18 and 19 are the learning curve images. In the images in Figures 16 and 17, the red lines are the line graph of test data, and the blue lines are the line graph of support vector regression prediction data.

However, through the optimization of SVR parameters by the grid search algorithm, we get the optimal SVR model for aluminum alloy plate under constant amplitude. The parameters of it are as follows: SVR ($C = 100.0$, cache_size = 200, coef0 = 0.0, degree = 3, epsilon = 0.1, gamma = 10.0, kernel = "RBF," max_iter = −1, shrinking = true, tol = 0.001, verbose = false). Among them, kernel = "RBF" is the setting parameter, $C = 100.0$ and gamma = 10.0 are the optimization parameters of the grid search algorithm. And other parameters are the default values. A simple interpretation can be given as follows.

Figures 16 and 18 show the results of constant amplitude three-hole specimen.

The standard deviation is about 10.11 and the RMSE of this model is about 0.64 which is far less than the standard deviation. It is easily found that the effect of this model is very well. The results of half-fold cross-validation are 0.99942329, 0.99940067, 0.9994369, 0.9991129, 0.9994331, and the mean value is 0.9993613737263342, which also shows that the prediction effect of the model is good. In this way, the model can be used for this problem.

Moreover, through the optimization of SVR parameters by the grid search algorithm, we get the optimal SVR model for aluminum alloy plate under variable amplitude. The parameters of it are as follows: SVR ($C = 1000.0$, cache_size = 200, coef0 = 0.0, degree = 3, epsilon = 0.1, gamma = 1.0, kernel = "RBF," max_iter = −1, shrinking = true, tol = 0.001, verbose = false). Among them, kernel = "RBF" is the setting parameter, and $C = 1000.0$ and gamma = 1.0 are the optimization parameters of the grid search algorithm. And other parameters are the default values. A simple interpretation can be given as follows.

Figures 17 and 19 show the results of variable amplitude three-hole specimen:

The standard deviation is about 9.56, and the RMSE of this model is about 0.86 which is far less than the standard deviation. It is easily found that the effect of this model is very well. The results of half-fold cross-validation are 0.99930434, 0.99930836, 0.99873057, 0.999125, and 0.9991911, with the mean value of
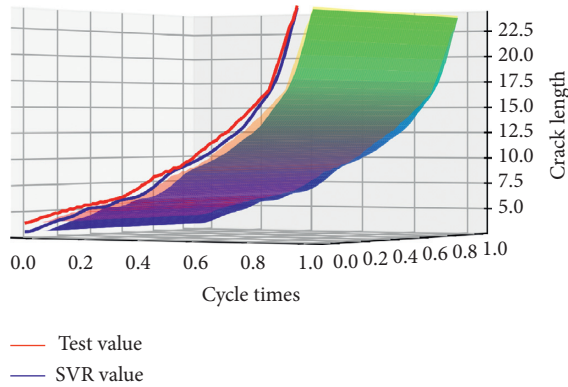
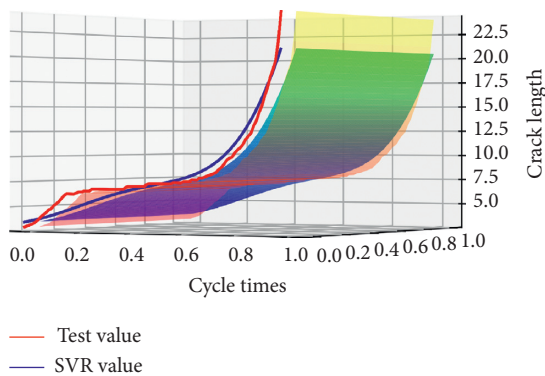FIGURE 16: Prediction of crack length with constant amplitude by SVR.

FIGURE 17: Prediction of crack length with variable amplitude by SVR.
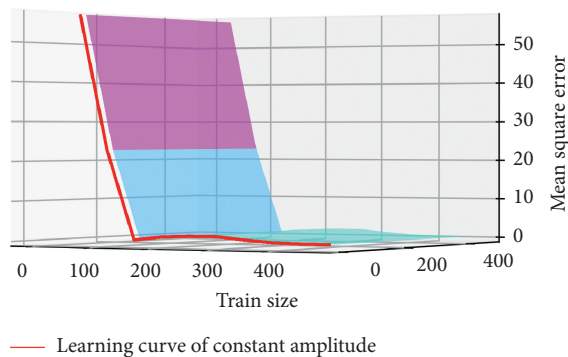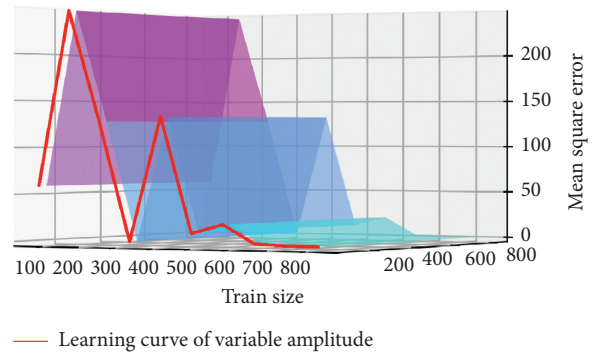

FIGURE 18: Learning curve of constant amplitude.

FIGURE 19: Learning curve of variable amplitude.

in each type of model. Therefore, three-hole crack data can be predicted by two-hole crack data under the same load form. In practical application, we can refer to the crack configuration form of the specimen in this paper and find a crack configuration form model similar to the actual situation. In addition, we can get the crack growth prediction results through the model. In addition, in the actual aviation aluminum alloy interhole crack prediction problem, under the same load spectrum situation, only two-hole plate test is needed to predict the corresponding three-hole plate crack propagation through the established SVR model. And the prediction accuracy of this model is high so that it can effectively improve the efficiency of solving such problems and reduce various costs.

5. Conclusion

The SVR model can be used to predict the crack between holes in similar aluminum alloy plates. Using different models under different conditions can make the prediction more accurate: use the model with a higher score in constant amplitude model under constant amplitude condition and use the model with a higher score in variable amplitude model under variable amplitude condition. According to the results, we can know that two-hole and three-hole aluminum alloy plate have roughly the same crack propagation law under the same load spectrum. It leads us to predict the crack law between three holes with constant amplitude by the crack law between two holes with constant amplitude. And at the same time, we also can predict the crack law between three holes with variable amplitude by the crack law between two holes with variable amplitude. Alternatively, the data-driven SVR algorithm model for crack growth prediction is a useful supplement to the existing methods for crack growth prediction in this paper. In the practical prediction of interpore crack growth, the results of the method in this paper and the existing methods can be considered comprehensively, and the more reliable prediction results can be obtained through mutual verification. The accuracy of the model can meet the accuracy requirements of the aviation crack growth problem. In view of this, the established model can be modified into the aviation crack growth prediction method to a certain extent and can

0.9991318738985194, which also shows that the prediction effect of the model is good. In this way, the model can be used for this problem.

Additionally, through the establishment, implementation, and evaluation of the above models, it can be seen that the constant amplitude data and the variable amplitude data are two different types of models. The crack propagation law between the holes of the two-hole aluminum alloy plate and three-hole aluminum alloy plate has roughly the same trend

guide the actual prediction of the law of the aviation cracks between holes.

Data Availability

The data that support the findings of this study are available from the corresponding author upon reasonable request.

Conflicts of Interest

The authors declare that they have no conflicts of interest.

Acknowledgments

References

[1] M. Yang, Y. Bi, J. Ren, H. Wang, and W. Jiang, "Study on propagation life of fretting fatigue crack of aerial aluminum alloy," *Equipment Environmental Engineering*, vol. 9, no. 5, pp. 1–5, 2012.

[2] Z. Zheng and Z. Wang, "Historical review of fatigue study," *Journal Materials Science and Engineering*, vol. 2, pp. 1–6, 1993.

[3] P. C. Paris, M. P. Gomez, and W. P. Anderson, "A rational analytic theory of fatigue," *The Trend in Engineering*, vol. 13, pp. 9–14, 1961.

[4] N. Thompson, N. Wadsworth, and N. Louat, "The origin of fatigue fracture in copper," *Philosophical Magazine*, vol. 1, no. 2, pp. 113–126, 1956.

[5] X. Yang and C. Chen, *Fatigue and Fracture,* pp. 152–182, Huazhong University of Science and Technology Press, Wuhan, China, 2nd edition, 2018.

[6] X. Ni, X. Li, and X. Wang, "General modification and application of the Paris law for fatigue crack propagation," *Pressure Vessel Technology*, vol. 23, no. 12, pp. 8–15, 2006.

[7] F. A. Alshamma and O. A. Jassim, "Dynamic crack propagation in nano-composite thin plates under multi-axial cyclic loading," *Journal of Materials Research and Technology*, vol. 8, no. 5, pp. 4672–4681, 2019.

[8] H. Liu and Z. Zhou, "Dynamic behavior of rectangular crack in three-dimensional orthotropic elastic medium by means of non-local theory," *Applied Mathematics and Mechanics*, vol. 38, no. 2, pp. 173–190, 2017.

[9] Z. Zhuravlova, "Stress analysis near the tips of a transverse crack in an elastic semi-strip," *Applied Mathematics and Mechanics*, vol. 38, no. 7, pp. 935–956, 2017.

[10] M. Karimi, A. Ghassemi, A. Atrian, and M. Vahabi, "Compensation of stress intensity factors in hollow cylinders containing several cracks under torsion by electro-elastic coating," *Applied Mathematics and Mechanics*, vol. 40, no. 9, pp. 1335–1360, 2019.

[11] X. Zhao, Z. Qian, J. Liu, and C. Gao, "Effects of electric/magnetic impact on the transient fracture of interface crack in piezoelectric-piezomagnetic sandwich structure: anti-plane case," *Applied Mathematics and Mechanics*, vol. 41, no. 1, pp. 139–156, 2020.

[12] Xu Wang and P. Schiavone, "Elastic field near the tip of an anticrack in a decagonal quasicrystalline material," *Applied Mathematics and Mechanics*, vol. 41, no. 3, pp. 401–408, 2020.

[13] B. Lei, "Study on fatigue crack growth behavior and fracture mechanism of al-alloy subjected to tensile overloads", M.S. thesis, Chang'an University, Xi'an, China, 2018.

[14] S. Zhang and W. Yang, "Prediction of mode .crack propagation direction in crabon-fiber reinforced composite plate," *Applied Mathematics and Mechanics (English Edition)*, vol. 25, no. 6, pp. 714–722, 2004.

[15] M. Hajimohamadi and R. Ghajar, "An analytical solution for the stress field and stress intensity factor in an infinite plane containing an elliptical hole with two unequal aligned cracks," *Applied Mathematics and Mechanics*, vol. 39, no. 8, pp. 1103–1118, 2018.

[16] R. R. Bhargava and K. Jangid, "Strip-coalesced interior zone model for two unequal collinear cracks weakening piezoelectric media," *Applied Mathematics and Mechanics*, vol. 35, no. 10, pp. 1249–1260, 2014.

[17] S. Singh, K. Sharma, and R. R. Bhargava, "Modified strip saturated models for two equal collinear cracks with coalesced zones in piezoelectric media," *Applied Mathematics and Mechanics*, vol. 40, no. 8, pp. 1097–1118, 2019.

[18] J. Zhao, L. Xie, and J. Liu, "Calculation of stress intensity factor for plate containing a number of symmetrical collinear holes," *Machinery Design and Manufacture*, vol. 12, pp. 12–14, 2010.

[19] Z. Li, Wu Xu, X. Zhang et al., "Experimental and analytical analyses of fatigue crack growth in sheets with multiple holes and cracks," *Acta Aeronautica et Astronautica Sinica*, vol. 39, no. 7, pp. 154–162, 2018.

[20] Q. Zhu, Bo Song, and Z. Zeng, "Research of opening displacements for two cracks emanating from a circular hole in an infinite plate under pressure on part of crack surface," *Journal of Mechanical Strength*, vol. 41, no. 3, pp. 713–717, 2019.

[21] Q. Zhu and R. Zhou, "Complex variable function solutions of mixed-mode stress intensity factors for two cracks of arbitrary length emanating from an elliptical hole," *Journal of Mechanical Strength*, vol. 41, no. 4, pp. 983–987, 2019.

[22] Q. Zhu and J. Jiang, "Complex variable function solutions of stress intensity factors for multiple hole-edge cracks," *Journal of Mechanical Strength*, vol. 42, no. 2, pp. 437–442, 2020.

[23] J. Li, Y. Cheng, and Z. Li, "Superconvergence of the composite rectangle rule for computing hypersingular integral on interval," *Numreical Mathematics: Theory, Methods and Applications*, vol. 13, no. 3, pp. 770–787, 2020.

[24] Li Jin and Y. Cheng, "Linear barycentric rational collocation method for solving second-order Volterra integro-differential equation," *Journal of Computational and Applied Mathematics*, vol. 39, pp. 1–9, 2020.

[25] Li Jin and Y. Cheng, "Linear barycentric rational collocation method for solving heat conduction equation," *Numerical Methods for Partial Differential Equations*, pp. 1–13, 2020.

[26] J. Chang, Q. Pan, Z. Shen, and H. Qin, "Intelligent prediction of refrigerant amounts based on internet of things," *Complexity*, vol. 2020, Article ID 1743973, 12 pages, 2020.

[27] H. Drucker, C. J. C. Burges, L. Kaufman et al., "Support vector regression machines," *Advances in Neural Information Processing Systems*, Vol. 9, MIT Press, Cambridge, MA, USA, 1996.

[28] D. Yang, Y. Liu, S. Li, J. Tao, C. Liu, and J. Yi, "Fatigue crack growth prediction of 7075 aluminum alloy based on the GMSVR model optimized by the artificial bee colony

algorithm," *Engineering Computations*, vol. 34, no. 4, pp. 1034–1053, 2017.

[29] W. Song, Z. Jiang, and H. Jiang, "Predict the fatigue life of crack based on extended finite element method and SVR," in *Proceedings of the 6th International Conference on Computer-Aided Design, Manufacturing, Modeling and Simulation (CDMMS 2018)*, American Institute of Physics, Busan, South Korea, April 2018.

[30] Z. Zhou, *Machine Learning,* pp. 121–140, Tsinghua University Press, Beijing, China, 1nd edition, 2016.

[31] H. Li, *Statistical Learning Methods,* pp. 111–154, Tsinghua University Press, Beijing, China, 2nd edition, 2019.

[32] T. Braun, S. Spiliopoulos, C. Veltman et al., "Detection of myocardial ischemia due to clinically asymptomatic coronary artery stenosis at rest using supervised artificial intelligence-enabled vectorcardiography-a five-fold cross validation of accuracy," *Journal of Electrocardiology*, vol. 59, pp. 100–105, 2020.

[33] H. Yao, J. Zhou, L. Lin et al., "Solar radiation prediction method using bat algorithm optimized SVR," *Renewable Energy Resources*, vol. 36, no. 11, pp. 1612–1617, 2018.

[34] Z. Shang, "Research on the boarding passengers prediction algorithm of subway trains based on SVR," *Modern Computer (Professional)*, vol. 7, pp. 42–44, 2019.

Review Article

Nontrivial Solutions for the $2n^{\text{th}}$ Lidstone Boundary Value Problem

Yaohong Li,[1] Jiafa Xu [ID],[2] and Yongli Zan[3]

[1]*School of Mathematics and Statistics, Suzhou University, Suzhou 234000, Anhui, China*
[2]*School of Mathematical Sciences, Chongqing Normal University, Chongqing 401331, China*
[3]*School of Mathematics and Statistics, Qilu University of Technology (Shandong Academy of Sciences), Jinan 250353, Shandong, China*

Correspondence should be addressed to Jiafa Xu; xujiafa292@sina.com

In this paper, we study the existence of nontrivial solutions for the $2n^{\text{th}}$ Lidstone boundary value problem with a sign-changing nonlinearity. Under some conditions involving the eigenvalues of a linear operator, we use the topological degree theory to obtain our main results.

1. Introduction

In this paper, we investigate the existence of nontrivial solutions for the following $2n^{\text{th}}$ Lidstone boundary value problem with a sign-changing nonlinearity:

$$
\begin{cases}
(-1)^n u^{(2n)}(t) = f\left(t, u(t), -u''(t), \ldots, (-1)^{n-1} u^{(2n-2)}(t)\right), & 0 < t < 1, \\
u^{(2i)}(0) = u^{(2i)}(1) = 0, & i = 0, 1, \ldots, n-1,
\end{cases}
\tag{1}
$$

where the nonlinearity f satisfies the following condition:

(i) (C0) $f \in C([0,1] \times \mathbb{R}^n, \mathbb{R})$ and there exist three nonnegative functions $a(t), b(t),$ and $K(x_1, x_2, \ldots, x_n)(\not\equiv 0)$ such that

$$
f(t, x_1, x_2, \ldots, x_n) \geq -a(t) - b(t) K(x_1, x_2, \ldots, x_n),
$$

$$
\text{for } t \in [0,1], x_i \in \mathbb{R}, i = 1, 2, \ldots, n.
\tag{2}
$$

The Lidstone boundary value problem arises in many different areas of applied mathematics and physics. When $n = 2$, problem (1) describes the deformation of an elastic beam in which both ends are simply supported. Recently, this problem has been extensively studied, and the authors refer the reader to [1–11] and references cited therein. For example, in [1], the authors used a cone-theoretic fixed point theorem to study the existence of nontrivial solutions for the nonlinear Lidstone boundary value problem:

$$\begin{cases} y^{(2m)}(t) = \lambda a(t) f\Big(y(t), \ldots, y^{(2j)}(t), \ldots y^{(2(m-1))}(t)\Big), & 0 < t < 1, \\ y^{(2i)}(0) = 0 = y^{(2i)}(1), & i = 0, \ldots m-1, \end{cases} \tag{3}$$

where $(-1)^m f > 0$ is continuous and a is nonnegative. In [2], the authors investigated the existence and uniqueness of positive solutions for the following generalized Lidstone boundary value problem:

$$\begin{cases} (-1)^n u^{(2n)} = f\Big(t, u, -u'', \ldots, (-1)^{n-1} u^{(2n-2)}\Big), \\ \alpha_0 u^{(2i)}(0) - \beta_0 u^{(2i+1)}(0) = 0 \, (i = 0, 1, 2, \ldots, n-1), \\ \alpha_1 u^{(2i)}(1) - \beta_1 u^{(2i+1)}(1) = 0 \, (i = 0, 1, 2, \ldots, n-1), \end{cases} \tag{4}$$

where $\alpha_j \geq 0, \beta_j \geq 0 \, (j = 0, 1)$ and $\alpha_0 \alpha_1 + \alpha_0 \beta_1 + \alpha_1 \beta_0 > 0$. In view of symmetry, these results demonstrate that problem (4) is essentially identical with Dirichlet boundary condition (1).

Meanwhile, we also note that there are a large number of papers in the literature devoted to sign-changing nonlinearities, and some results can be found in a series of papers [12–32] and the references cited therein. For example, in [12], the authors studied the following higher-order non-linear fractional boundary value problem involving Riemann–Liouville fractional derivatives:

$$\begin{cases} D_{0^+}^\alpha u(t) = -f\Big(t, u(t), D_{0^+}^{\beta_1} u(t), D_{0^+}^{\beta_2} u(t), \ldots, D_{0^+}^{\beta_{n-1}} u(t)\Big), & 0 < t < 1, \\ u(0) = u'(0) = \cdots = u^{(n-2)}(0) = D_{0^+}^\beta u(1) = 0, \end{cases} \tag{5}$$

where f is a sign-changing nonlinearity. Under some appropriate conditions involving the eigenvalues of the relevant linear operators, they utilized the topological degree to obtain a nontrivial solution for (5). In [13], the authors adopted the similar method in [12] to study the existence of nontrivial solutions for the following system of fractional q-difference equations with q-integral boundary conditions:

$$\begin{cases} D_q^\alpha x(t) + f_1(t, y(t)) = 0, & t \in (0, 1), \\ D_q^\alpha y(t) + f_2(t, x(t)) = 0, & t \in (0, 1), \\ x(0) = 0, D_q x(0) = 0, D_q^\nu x(1) = \int_0^1 h(t) D_q^\nu x(t)) d_q t, \\ y(0) = 0, D_q y(0) = 0, D_q^\nu y(1) = \int_0^1 h(t) D_q^\nu y(t) d_q t, \end{cases} \tag{6}$$

where $\alpha \in (2, 3), \nu \in (1, 2)$, and D_q^α is the α-order Riemann–Liouville's fractional q-derivative.

Inspired by the aforementioned works, in this paper, we study the existence of nontrivial solutions for (1) where the nonlinearity f is sign-changing. Under some conditions involving the eigenvalues of the revelent linear operators, we use the topological degree to obtain our results.

2. Preliminaries

Let $E := C([0, 1], \mathbb{R}), \|v\| := \max_{t \in [0,1]} |v(t)|, P := \{v \in E: v(t) \geq 0, \forall t \in [0, 1]\}, B_r = \{v \in E: \|v\| < r\}$ for $r > 0$. Clearly, $(E, \|\cdot\|)$ is a real Banach space and P is a solid cone in E. In (1), let $(-1)^{n-1} u^{(2n-2)}(t) = v(t)$ and from [2, P224], we can obtain that (1) is equivalent to the following integral equation:

$$\begin{aligned} v(t) = \int_0^1 G_1(t, s) f\bigg(& s, \int_0^1 G_{n-1}(s, \tau) v(\tau) d\tau, \ldots, \\ & \int_0^1 G_1(s, \tau) v(\tau) d\tau, v(s) \bigg) ds, \end{aligned} \tag{7}$$

where

$$\begin{aligned} G_1(t, s) &= \begin{cases} t(1-s), & 0 \leq t \leq s \leq 1, \\ s(1-t), & 0 \leq s \leq t \leq 1, \end{cases} \\ G_i(t, s) &= \int_0^1 G_1(t, \tau) G_{i-1}(\tau, s) d\tau, \quad i = 2, 3, \ldots. \end{aligned} \tag{8}$$

Next, we provide a lemma, which expresses some vital properties of the functions $G_i \, (i = 1, 2, \ldots)$.

Lemma 1 *(i) G_i are nonnegative continuous functions on $[0, 1]^2$, and $G_i(t, s) > 0, (t, s) \in (0, 1)^2$*

(ii) G_1 has the inequalities $t(1-t)G_1(s, s) \leq G_1(t, s) \leq G_1(s, s), \forall t, s \in [0, 1]$

(iii) $G_i(t, s) = G_i(s, t), \forall t, s \in [0, 1]$

(iv) $\int_0^1 G_i(t, s) \sin \pi s \, ds = (1/\pi^2)^i \sin \pi t, t \in [0, 1]$, and $\int_0^1 G_i(t, s) \sin \pi t \, dt = (1/\pi^2)^i \sin \pi s, s \in [0, 1]$

Proof. We only prove (iii) and (iv). For (iii), $i = 1$ holds obviously. From the definition of G_i, we have

$$G_i(s,t) = \int_0^1 G_1(s,\tau_1)G_{i-1}(\tau_1,t)d\tau_1$$
$$= \int_0^1\int_0^1 G_1(s,\tau_1)G_1(\tau_1,\tau_2)G_{i-2}(\tau_2,t)d\tau_2d\tau_1$$
$$= \cdots$$
$$= \underbrace{\int_0^1\cdots\int_0^1}_{i-1} G_1(s,\tau_1)G_1(\tau_1,\tau_2)G_1(\tau_2,\tau_3)\cdots G_1(\tau_{i-1},t)d\tau_{i-1}\cdots d\tau_2d\tau_1$$
$$= \underbrace{\int_0^1\cdots\int_0^1}_{i-1} G_1(t,\tau_{i-1})\cdots G_1(\tau_3,\tau_2)G_1(\tau_2,\tau_1)G_1(\tau_1,s)d\tau_{i-1}\cdots d\tau_2d\tau_1$$
$$= G_i(t,s), \quad for\, t,s \in [0,1].$$
(9)

For (iv), when $i = 1$, we have

$$\int_0^1 G_1(t,s)\sin\pi s\,ds = \int_0^t s(1-t)\sin\pi s\,ds + \int_t^1 t(1-s)\sin\pi s\,ds$$
$$= \frac{1}{\pi^2}\sin\pi t.$$
(10)

Noting that $G_1(s,t) = G_1(t,s)$, we have

$$\int_0^1 G_1(t,s)\sin\pi t\,dt = \int_0^1 G_1(s,t)\sin\pi t\,dt = \frac{1}{\pi^2}\sin\pi s.$$
(11)

When $i \geq 1$, we have

$$\int_0^1 G_i(t,s)\sin\pi s\,ds = \underbrace{\int_0^1\cdots\int_0^1}_{i} G_1(t,\tau_{i-1})\cdots G_1(\tau_3,\tau_2)G_1(\tau_2,\tau_1)G_1(\tau_1,s)\sin\pi s\,ds d\tau_{i-1}\cdots d\tau_2 d\tau_1$$
$$= \frac{1}{\pi^2}\underbrace{\int_0^1\cdots\int_0^1}_{i-1} G_1(t,\tau_{i-1})\cdots G_1(\tau_3,\tau_2)G_1(\tau_2,\tau_1)\sin\pi\tau_1 d\tau_{i-1}\cdots d\tau_2 d\tau_1$$
$$= \cdots$$
$$= \left(\frac{1}{\pi^2}\right)^i\sin\pi t.$$
(12)

Using the symmetry of G_i, we easily have

$$\int_0^1 G_i(t,s)\sin\pi t\,dt = \left(\frac{1}{\pi^2}\right)^i\sin\pi s.$$
(13)

This completes the proof.

Let $\alpha_i \geq 0$ with $\sum_{i=1}^n \alpha_i^2 \neq 0$. Then, we have the following equations:

$$\int_0^1 G_{\alpha_1,\ldots,\alpha_n}(t,s)\sin\pi s\,ds = \left[\alpha_1\left(\frac{1}{\pi^2}\right)^n + \cdots + \alpha_n\left(\frac{1}{\pi^2}\right)^1\right]\sin\pi t,$$
$$t \in [0,1],$$
(14)

$$\int_0^1 G_{\alpha_1,\ldots,\alpha_n}(t,s)\sin\pi t\,dt = \left[\alpha_1\left(\frac{1}{\pi^2}\right)^n + \cdots + \alpha_n\left(\frac{1}{\pi^2}\right)^1\right]\sin\pi s,$$
$$s \in [0,1],$$
(15)

where

$$G_{\alpha_1,\ldots,\alpha_n}(t,s) = \alpha_1 G_n(t,s) + \cdots + \alpha_n G_1(t,s), \quad for\, t,s \in [0,1].$$
(16)

Lemma 2. Let $(Lv)(t) = \int_0^1 G_1(t,s)v(s)ds$, for $t \in [0,1]$. Then, if $v \in P$, we have $Lv \in P_0$, where

$$P_0 = \{v \in P: v(t) \geq t(1-t)\|v\|, \quad \forall t \in [0,1]\}.$$
(17)

This is a direct result from Lemma 1 (ii), so we omit its proof.

Remark 1. $\sin\pi t \in P_0$, for $t \in [0,1]$.

Lemma 3 (see [33], Theorem 1 [3]). *Let Ω be a bounded open set in a Banach space E and $T: \Omega \longrightarrow E$ be a continuous compact operator. If there exists $x_0 \in E\backslash\{0\}$ such that*

$$x - Tx \neq \mu x_0, \quad \forall x \in \partial\Omega, \ \mu \geq 0, \tag{18}$$

then the topological degree $\deg(I - T, \Omega, 0) = 0$.

Lemma 4 (see [33], Lemma 4 [1]). *Let Ω be a bounded open set in a Banach space E with $0 \in \Omega$ and $T: \overline{\Omega} \longrightarrow E$ be a continuous compact operator. If*

$$Tx \neq \mu x, \quad \forall x \in \partial\Omega, \ \mu \geq 1, \tag{19}$$

then the topological degree $\deg(I - T, \Omega, 0) = 1$.

3. Main Results

Define the operator $A: E \longrightarrow E$ by

$$(Av)(t) = \int_0^1 G_1(t, s) f\left(s, \int_0^1 G_{n-1}(s, \tau)v(\tau)d\tau, \ldots, \right.$$
$$\left. \int_0^1 G_1(s, \tau)v(\tau)d\tau, v(s)\right)ds. \tag{20}$$

Moreover, the continuity of f implies that A is completely continuous and the existence of solutions for (1) is equivalent to that of fixed points of A.

Now, we list some assumptions for the functions f and K:

(C1) There exist $\beta_i \geq 0 \, (i = 1, 2, \ldots, n)$ with $\sum_{i=1}^n \beta_i^2 \neq 0$ such that

$$\lim_{\beta_1|x_1|+\beta_2|x_2|+\cdots+\beta_n|x_n| \longrightarrow +\infty} \frac{K(x_1, x_2, \ldots, x_n)}{\beta_1|x_1| + \beta_2|x_2| + \cdots + \beta_n|x_n|} = 0. \tag{21}$$

(C2) $\liminf_{\beta_1|x_1|+\beta_2||x_2|+\cdots+\beta_n \ |x_n| \longrightarrow +\infty} (f(t, x_1, x_2, \ldots, x_n)/ (\beta_1|x_1| + \beta_2|x_2| + \cdots + \beta_n|x_n|)) > \lambda_{\beta_1, \beta_2, \ldots, \beta_n}$, uniformly for $t \in [0, 1]$.

(C3) There exist $\gamma_i \geq 0 \, (i = 1, 2, \ldots, n)$ with $\sum_{i=1}^n \gamma_i^2 \neq 0$ such that

$$\limsup_{\gamma_1|x_1|+\gamma_2|x_2|+\cdots+\gamma_n|x_n| \longrightarrow 0} \frac{|f(t, x_1, x_2, \ldots, x_n)|}{\gamma_1|x_1| + \gamma_2|x_2| + \cdots + \gamma_n|x_n|} < \lambda_{\gamma_1, \gamma_2, \ldots, \gamma_n}, \tag{22}$$

where

$$\lambda_{\beta_1, \beta_2, \ldots, \beta_n}^{-1} = \beta_1\left(\frac{1}{\pi^2}\right)^n + \cdots + \beta_n\left(\frac{1}{\pi^2}\right)^1,$$
$$\lambda_{\gamma_1, \gamma_2, \ldots, \gamma_n}^{-1} = \gamma_1\left(\frac{1}{\pi^2}\right)^n + \cdots + \gamma_n\left(\frac{1}{\pi^2}\right)^1. \tag{23}$$

Theorem 1. *Suppose that (C0)–(C3) hold. Then, (1) has at least one nontrivial solution.*

Proof. We divide the following two steps:

(i) *Step 1.* By (C3), there exist $\varepsilon_1 \in (0, \lambda_{\gamma_1, \gamma_2, \ldots, \gamma_n})$ and $r > 0$ such that

$$|f(t, x_1, x_2, \ldots, x_n)| \leq (\lambda_{\gamma_1, \gamma_2, \ldots, \gamma_n} - \varepsilon_1)(\gamma_1|x_1| + \gamma_2|x_2| + \cdots + \gamma_n|x_n|), \tag{24}$$

for all $t \in [0, 1]$, $x_i \in \mathbb{R} \, (i = 1, 2, \ldots, n)$ with $0 \leq \gamma_1|x_1| + \gamma_2|x_2| + \cdots + \gamma_n|x_n| \leq r$. Substituting this inequality into (20), we have

$$|(Av)(t)| \leq \int_0^1 G_1(t, s) \left|f\left(s, \int_0^1 G_{n-1}(s, \tau)v(\tau)d\tau, \ldots, \int_0^1 G_1(s, \tau)v(\tau)d\tau, v(s)\right)\right| ds$$

$$\leq (\lambda_{\gamma_1, \gamma_2, \ldots, \gamma_n} - \varepsilon_1) \int_0^1 G_1(t, s) \left(\gamma_1 \left|\int_0^1 G_{n-1}(s, \tau)v(\tau)d\tau\right| + \cdots + \gamma_{n-1}\left|\int_0^1 G_1(s, \tau)v(\tau)d\tau\right| + \gamma_n v(s)\right) ds$$

$$\leq (\lambda_{\gamma_1, \gamma_2, \ldots, \gamma_n} - \varepsilon_1) \int_0^1 (\gamma_1 G_n(t, s) + \cdots + \gamma_{n-1} G_2(t, s) + \gamma_n G_1(t, s))|v(s)| ds$$

$$= (\lambda_{\gamma_1, \gamma_2, \ldots, \gamma_n} - \varepsilon_1) \int_0^1 G_{\gamma_1, \ldots, \gamma_n}(t, s)|v(s)| ds. \tag{25}$$

Now for this r, we claim

$$Av \neq \lambda v, \quad \forall v \in \partial B_r, \lambda \geq 1. \tag{26}$$

Suppose the contrary. Then, there exist $v_0 \in \partial B_r$ and $\lambda_0 \geq 1$ such that $Av_0 = \lambda_0 v_0$ Therefore, we obtain

$$|v_0(t)| \leq \lambda_0 |v_0(t)| = |(Av_0)(t)| \leq (\lambda_{\gamma_1, \gamma_2, \ldots, \gamma_n} - \varepsilon_1)$$
$$\int_0^1 G_{\gamma_1, \ldots, \gamma_n}(t, s)|v_0(s)| ds. \tag{27}$$

Multiply by $\sin \pi t$ on both sides and integrate over $[0, 1]$ and use (15) to obtain

$$\int_0^1 |v_0(t)|\sin \pi t \, dt \le \left(\lambda_{\gamma_1,\gamma_2,\ldots,\gamma_n} - \varepsilon_1\right)\int_0^1 \int_0^1 G_{\gamma_1,\ldots,\gamma_n}(t,s)|v_0(s)|\sin \pi t \, dt \, ds$$

$$= \left(\lambda_{\gamma_1,\gamma_2,\ldots,\gamma_n} - \varepsilon_1\right)\lambda_{\gamma_1,\gamma_2,\ldots,\gamma_n}^{-1}\int_0^1 |v_0(s)|\sin \pi s \, ds. \tag{28}$$

This indicates that $\int_0^1 |v_0(t)|\sin \pi t \, dt = 0$, and thus, $|v_0(t)| \equiv 0$, $t \in [0,1]$. This contradicts to $v_0 \in \partial B_r$. Consequently, (26) holds and Lemma 4 yields that

$$\deg(I - A, B_r, 0) = 1. \tag{29}$$

Step 2. By virtue of (C2), there exist $\varepsilon_2 > 0$ and $X_0 > 0$ such that

$$f(t, x_1, x_2, \ldots, x_n) \ge \left(\lambda_{\beta_1,\beta_2,\ldots,\beta_n} + \varepsilon_2\right)$$
$$\cdot \left(\beta_1|x_1| + \beta_2|x_2| + \cdots + \beta_n|x_n|\right), \tag{30}$$

for all $t \in [0,1]$ and $\beta_1|x_1| + \beta_2|x_2| + \cdots + \beta_n|x_n| > X_0$. For any given ε with $\varepsilon_2 - \|b\|\varepsilon > 0$, and using (C1), there exists $X_1 > X_0$ such that

$$K(x_1, x_2, \ldots, x_n) \le \varepsilon\left(\beta_1|x_1| + \beta_2|x_2| + \cdots + \beta_n|x_n|\right),$$
$$\text{for all } \beta_1|x_1| + \beta_2|x_2| + \cdots + \beta_n|x_n| > X_1. \tag{31}$$

Consequently, when $t \in [0,1], \beta_1|x_1| + \beta_2|x_2| + \cdots + \beta_n|x_n| > X_1$, we have

$$f(t, x_1, x_2, \ldots, x_n) \ge \left(\lambda_{\beta_1,\beta_2,\ldots,\beta_n} + \varepsilon_2\right)\left(\beta_1|x_1| + \beta_2|x_2| + \cdots + \beta_n|x_n|\right) - a(t) - b(t)K(x_1, x_2, \ldots, x_n)$$

$$\ge \left(\lambda_{\beta_1,\beta_2,\ldots,\beta_n} + \varepsilon_2\right)\left(\beta_1|x_1| + \beta_2|x_2| + \cdots + \beta_n|x_n|\right) - a(t) - b(t)\varepsilon\left(\beta_1|x_1| + \beta_2|x_2| + \cdots + \beta_n|x_n|\right) \tag{32}$$

$$\ge \left(\lambda_{\beta_1,\beta_2,\ldots,\beta_n} + \varepsilon_2 - \|b\|\varepsilon\right)\left(\beta_1|x_1| + \beta_2|x_2| + \cdots + \beta_n|x_n|\right) - a(t).$$

Noting that when $t \in [0,1]$, $\beta_1|x_1| + \beta_2|x_2| + \cdots + \beta_n|x_n| \le X_1$, $f(t, x_1, \ldots, x_n)$, and $K(x_1, \ldots, x_n)$ are bounded, we can let

$$C_{X_1} = \max_{0 \le t \le 1, \beta_1|x_1| + \beta_2|x_2| + \cdots + \beta_n|x_n| \le X_1} |f(t, x_1, \ldots, x_n)|$$
$$+ \left(\lambda_{\beta_1,\beta_2,\ldots,\beta_n} + \varepsilon_2 - \|b\|\varepsilon\right)X_1,$$

$$K^* = \max_{\beta_1|x_1| + \beta_2|x_2| + \cdots + \beta_n|x_n| \le X_1} K(x_1, \ldots, x_n). \tag{33}$$

Then, we can obtain

$$f(t, x_1, x_2, \ldots, x_n) \ge \left(\lambda_{\beta_1,\beta_2,\ldots,\beta_n} + \varepsilon_2 - \|b\|\varepsilon\right)$$
$$\cdot \left(\beta_1|x_1| + \beta_2|x_2| + \cdots + \beta_n|x_n|\right)$$
$$- a(t) - C_{X_1}, \tag{34}$$

for all $t \in [0,1], x_i \in \mathbb{R}, i = 1, 2, \ldots, n$. Note that ε can be chosen arbitrarily small, and let

$$R > \max\left\{\frac{\int_0^1 G_1(s,s)\left(a(s) + K^*b(s) + C_{X_1}\right)ds}{1 - \|b\|\varepsilon\max_{t \in [0,1]}\int_0^1 G_{\beta_1,\ldots,\beta_n}(t,\tau)d\tau}, S_1\right\}, \tag{35}$$

where

$$S_1 = \frac{\int_0^1 \left[\left(\lambda_{\beta_1,\beta_2,\ldots,\beta_n} + \varepsilon_2 - \|b\|\varepsilon\right) + (\varepsilon_2 - \|b\|\varepsilon)G_1(y,y)\right]\left(a(y) + K^*b(y) + C_{X_1}\right)dy}{(\varepsilon_2 - \|b\|\varepsilon)\left(1 - \|b\|\varepsilon\max_{t \in [0,1]}\int_0^1 G_{\beta_1,\ldots,\beta_n}(t,\tau)d\tau\right) - \varepsilon\left(\lambda_{\beta_1,\beta_2,\ldots,\beta_n} + \varepsilon_2 - \|b\|\varepsilon\right)\int_0^1 b(y)\sum_{i=1}^n \int_0^1 \beta_i G_{n-i}(y,\tau)d\tau dy}, \tag{36}$$

and $G_0(y,\tau) \equiv 1$. Now, we claim

$$v - Av \ne \mu\varphi, \quad \forall v \in \partial B_R, \mu \ge 0, \tag{37}$$

where $\varphi(t) = \sin \pi t, t \in [0,1]$. Suppose that (37) is not satisfied. Then, there exist $v_1 \in \partial B_R$ and $\mu_1 > 0$ such that

$$v_1 - Av_1 = \mu_1\varphi. \tag{38}$$

Let

$$\tilde{v}(t) = \int_0^1 G_1(t,s)\left(a(s) + b(s)K\left(\int_0^1 G_{n-1}(s,\tau)v_1(\tau)d\tau, \dots, \int_0^1 G_1(s,\tau)v_1(\tau)d\tau, v_1(s) \right) + C_{X_1} \right)ds. \tag{39}$$

Then, from Lemma 2, we have $\tilde{v} \in P_0$. Now, we estimate the norm of $\tilde{v}$. Noting that $v_1 \in \partial B_R (\|v_1\| = R)$, we obtain

$$\begin{aligned}
\tilde{v}(t) &\le \int_0^1 G_1(t,s)\left(a(s) + b(s)\left[\varepsilon\left(\beta_1\left|\int_0^1 G_{n-1}(s,\tau)v_1(\tau)d\tau\right| + \cdots + \beta_{n-1}\left|\int_0^1 G_1(s,\tau)v_1(\tau)d\tau\right| + \beta_n\|v_1(s)\| \right) + K^* \right] + C_{X_1} \right)ds \\
&\le \int_0^1 G_1(s,s)\left(a(s) + K^*b(s) + C_{X_1} \right)ds + \|b\|\varepsilon \int_0^1 G_{\beta_1,\dots,\beta_n}(t,\tau)|v_1(\tau)|d\tau \\
&\le \int_0^1 G_1(s,s)\left(a(s) + K^*b(s) + C_{X_1} \right)ds + \|b\|\|v_1\|\varepsilon \max_{t\in[0,1]} \int_0^1 G_{\beta_1,\dots,\beta_n}(t,\tau)d\tau \\
&< R.
\end{aligned} \tag{40}$$

We calculate $v_1 + \tilde{v}$. By (38) we have

$$\begin{aligned}
v_1(t) + \tilde{v}(t) &= (Av_1)(t) + \mu_1\varphi(t) + \tilde{v}(t) \\
&= \int_0^1 G_1(t,s)\left[f\left(s, \int_0^1 G_{n-1}(s,\tau)v_1(\tau)d\tau, \dots, \int_0^1 G_1(s,\tau)v_1(\tau)d\tau, v_1(s) \right) \right. \\
&\quad \left. + a(s) + b(s)K\left(\int_0^1 G_{n-1}(s,\tau)v_1(\tau)d\tau, \dots, \int_0^1 G_1(s,\tau)v_1(\tau)d\tau, v_1(s) \right) + C_{X_1} \right]ds + \mu_1\varphi(t).
\end{aligned} \tag{41}$$

Using (C0), Lemma 2 and Remark 1, we find

$$v_1 + \tilde{v} \in P_0. \tag{42}$$

Therefore, (34) enables us to calculate

$$\begin{aligned}
(Av_1)(t) + \tilde{v}(t) &\ge \left(\lambda_{\beta_1,\beta_2,\dots,\beta_n} + \varepsilon_2 - \|b\|\varepsilon \right)\int_0^1 G_1(t,s)\left(\beta_1\left|\int_0^1 G_{n-1}(s,\tau)v_1(\tau)d\tau\right| + \cdots + \beta_{n-1}\left|\int_0^1 G_1(s,\tau)v_1(\tau)d\tau\right| + \beta_n|v_1(s)| \right)ds \\
&\quad - \int_0^1 G_1(t,s)\left(a(s) + C_{X_1} \right)ds \\
&\quad + \int_0^1 G_1(t,s)\left[a(s) + b(s)K\left(\int_0^1 G_{n-1}(s,\tau)v_1(\tau)d\tau, \dots, \int_0^1 G_1(s,\tau)v_1(\tau)d\tau, v_1(s) \right) + C_{X_1} \right]ds \\
&\ge \left(\lambda_{\beta_1,\beta_2,\dots,\beta_n} + \varepsilon_2 - \|b\|\varepsilon \right)\int_0^1 G_1(t,s)\left(\beta_1\left|\int_0^1 G_{n-1}(s,\tau)v_1(\tau)d\tau\right| + \cdots + \beta_{n-1}\left|\int_0^1 G_1(s,\tau)v_1(\tau)d\tau\right| + \beta_n|v_1(s)| \right)ds \\
&= \left(\lambda_{\beta_1,\beta_2,\dots,\beta_n} + \varepsilon_2 - \|b\|\varepsilon \right)\left|\int_0^1 G_{\beta_1,\dots,\beta_n}(t,s)v_1(s)ds\right| \\
&\ge \left(\lambda_{\beta_1,\beta_2,\dots,\beta_n} + \varepsilon_2 - \|b\|\varepsilon \right)\int_0^1 G_{\beta_1,\dots,\beta_n}(t,s)v_1(s)ds.
\end{aligned} \tag{43}$$

Consequently, we have

$$
\begin{aligned}
\left(\lambda_{\beta_1,\beta_2,\ldots,\beta_n} + \varepsilon_2 - \|b\|\varepsilon\right) \int_0^1 G_{\beta_1,\ldots,\beta_n}(t,s)\left(v_1(s) + \widetilde{v}(s)\right)\mathrm{d}s &= \left(\lambda_{\beta_1,\beta_2,\ldots,\beta_n} + \varepsilon_2 - \|b\|\varepsilon\right) \int_0^1 G_{\beta_1,\ldots,\beta_n}(t,s)\left(v_1(s) + \widetilde{v}(s)\right)\mathrm{d}s \\
&\quad - \left(\lambda_{\beta_1,\beta_2,\ldots,\beta_n} + \varepsilon_2 - \|b\|\varepsilon\right) \int_0^1 G_{\beta_1,\ldots,\beta_n}(t,s)\widetilde{v}(s)\mathrm{d}s \\
&= \lambda_{\beta_1,\beta_2,\ldots,\beta_n} \int_0^1 G_{\beta_1,\ldots,\beta_n}(t,s)\left(v_1(s) + \widetilde{v}(s)\right)\mathrm{d}s + \left(\varepsilon_2 - \|b\|\varepsilon\right) \\
&\quad \int_0^1 G_{\beta_1,\ldots,\beta_n}(t,s)\left(v_1(s) + \widetilde{v}(s)\right)\mathrm{d}s \\
&\quad - \left(\lambda_{\beta_1,\beta_2,\ldots,\beta_n} + \varepsilon_2 - \|b\|\varepsilon\right) \int_0^1 G_{\beta_1,\ldots,\beta_n}(t,s)\widetilde{v}(s)\mathrm{d}s.
\end{aligned}
\tag{44}
$$

Now, we estimate $\left(\varepsilon_2 - \|b\|\varepsilon\right) \int_0^1 G_{\beta_1,\ldots,\beta_n}(t,s)\left(v_1(s) + \widetilde{v}(s)\right)\mathrm{d}s - \left(\lambda_{\beta_1,\beta_2,\ldots,\beta_n} + \varepsilon_2 - \|b\|\varepsilon\right) \int_0^1 G_{\beta_1,\ldots,\beta_n}(t,s)\widetilde{v}(s)\mathrm{d}s$. From (42), we have $v_1(t) + \widetilde{v}(t) \geq t(1-t)\|v_1 +$ $\widetilde{v}\| \geq t(1-t)\left(\|v_1\| - \|\widetilde{v}\|\right), t \in [0,1]$, and using $G_1(t,s) \leq t(1-t), t,s \in [0,1]$, we have

$$
\begin{aligned}
&\left(\varepsilon_2 - \|b\|\varepsilon\right) \int_0^1 G_{\beta_1,\ldots,\beta_n}(t,s)\left(v_1(s) + \widetilde{v}(s)\right)\mathrm{d}s - \left(\lambda_{\beta_1,\beta_2,\ldots,\beta_n} + \varepsilon_2 - \|b\|\varepsilon\right) \int_0^1 G_{\beta_1,\ldots,\beta_n}(t,s)\widetilde{v}(s)\mathrm{d}s \\
&\geq \left(\varepsilon_2 - \|b\|\varepsilon\right) \int_0^1 G_{\beta_1,\ldots,\beta_n}(t,s)s(1-s)\left(\|v_1\| - \|\widetilde{v}\|\right)\mathrm{d}s \\
&\quad - \left(\lambda_{\beta_1,\beta_2,\ldots,\beta_n} + \varepsilon_2 - \|b\|\varepsilon\right) \int_0^1 G_{\beta_1,\ldots,\beta_n}(t,s) \\
&\quad \cdot \int_0^1 s(1-s)\left(a(y) + b(y)\left[\varepsilon\left(\beta_1\left|\int_0^1 G_{n-1}(y,\tau)v_1(\tau)\mathrm{d}\tau\right| + \cdots + \beta_{n-1}\left|\int_0^1 G_1(y,\tau)v_1(\tau)\mathrm{d}\tau\right| + \beta_n|v_1(y)|\right) + K^*\right] + C_{X_1}\right)\mathrm{d}y\mathrm{d}s \\
&\geq \int_0^1 G_{\beta_1,\ldots,\beta_n}(t,s)s(1-s)\mathrm{d}s \\
&\quad \cdot \left[\left(\varepsilon_2 - \|b\|\varepsilon\right)\left(\|v_1\| - \|\widetilde{v}\|\right) - \left(\lambda_{\beta_1,\beta_2,\ldots,\beta_n} + \varepsilon_2 - \|b\|\varepsilon\right) \int_0^1 \left(a(y) + b(y)\left(\varepsilon\|v_1\|\sum_{i=1}^n \int_0^1 \beta_i G_{n-i}(y,\tau)\mathrm{d}\tau + K^*\right) + C_{X_1}\right)\mathrm{d}y\right] \\
&\geq 0.
\end{aligned}
\tag{45}
$$

As a result, by means of (43) and (44), we obtain

$$
\left(Av_1\right)(t) + \widetilde{v}(t) \geq \lambda_{\beta_1,\beta_2,\ldots,\beta_n} \int_0^1 G_{\beta_1,\ldots,\beta_n}(t,s)\left(v_1(s) + \widetilde{v}(s)\right)\mathrm{d}s.
\tag{46}
$$

Combining this with (38), we have

$$
\begin{aligned}
v_1(t) + \widetilde{v}(t) &= \left(Av_1\right)(t) + \mu_1\varphi(t) + \widetilde{v}(t) \\
&\geq \lambda_{\beta_1,\beta_2,\ldots,\beta_n} \int_0^1 G_{\beta_1,\ldots,\beta_n}(t,s)\left(v_1(s) + \widetilde{v}(s)\right)\mathrm{d}s + \mu_1\varphi(t) \\
&\geq \mu_1\varphi(t).
\end{aligned}
\tag{47}
$$

Define $\mu^* = \sup S = \sup\{\mu > 0 : v_1 + \widetilde{v} \geq \mu\varphi\}$. Then, $S \neq \varnothing (\mu_1 \in S)$ and $\mu^* \geq \mu_1$. Hence, from (14), we have

$$
\begin{aligned}
v_1(t) + \widetilde{v}(t) &\geq \lambda_{\beta_1,\beta_2,\ldots,\beta_n} \int_0^1 G_{\beta_1,\ldots,\beta_n}(t,s)\left(v_1(s) + \widetilde{v}(s)\right)\mathrm{d}s + \mu_1\varphi(t) \\
&\geq \lambda_{\beta_1,\beta_2,\ldots,\beta_n} \int_0^1 G_{\beta_1,\ldots,\beta_n}(t,s)\mu^*\varphi(s)\mathrm{d}s + \mu_1\varphi(t) \\
&= \lambda_{\beta_1,\beta_2,\ldots,\beta_n}\lambda_{\beta_1,\beta_2,\ldots,\beta_n}^{-1}\mu^*\varphi(t) + \mu_1\varphi(t) \\
&= \left(\mu^* + \mu_1\right)\varphi(t),
\end{aligned}
\tag{48}
$$

which contradicts the definition of μ^*. Therefore, (37) holds, and from Lemma 3, we obtain

$$
\deg\left(I - A, B_R, 0\right) = 0.
\tag{49}
$$

Now, (29) and (49) together imply that

$$
\deg\left(I - A, \frac{B_R}{B_r}, 0\right) = \deg\left(I - A, B_R, 0\right) - \deg\left(I - A, B_r, 0\right) = -1.
\tag{50}
$$

Therefore, the operator A has at least one fixed point in $B_R/\overline{B}_r$. Equivalently, (1) has at least one nontrivial solution. This completes the proof.

4. Conclusion

In this paper, we use the topological degree to study the nontrivial solutions for the $2n^{\text{th}}$ Lidstone boundary value problem (1). To the best of our knowledge, there are few works that deal with the problem where the nonlinear terms may be unbounded and sign-changing. Moreover, it is remarked that the main result is discussed under some conditions concerning the first eigenvalues corresponding to the relevant linear operators. These mean that our main result is an improvement in some related works.

Data Availability

No data were used to support this study.

Conflicts of Interest

The authors declare that there are no conflicts of interest regarding the publication of this paper.

Authors' Contributions

The study was carried out in collaboration among all authors. All authors read and approved the final manuscript.

Acknowledgments

References

[1] P. Eloe, "Nonlinear eigenvalue problems for higher order lidstone boundary value problems," *Electronic Journal of Qualitative Theory of Differential Equations*, vol. 2, no. 2, 8 pages, 2000.

[2] Z. Yang, "Existence and uniqueness of positive solutions for a higher order boundary value problem," *Computers & Mathematics with Applications*, vol. 54, no. 2, pp. 220–228, 2007.

[3] R. P. Agarwal and P. J. Y. Wong, "Lidstone polynomials and boundary value problems," *Computers & Mathematics with Applications*, vol. 17, no. 10, pp. 1397–1421, 1989.

[4] R. P. Agarwal, D. O'Regan, and S. Staněk, "Singular lidstone boundary value problem with given maximal values for solutions," *Nonlinear Analysis: Theory, Methods & Applications*, vol. 55, no. 7-8, pp. 859–881, 2003.

[5] Z. Bai and W. Ge, "Solutions of $2n^{\text{th}}$ Lidstone boundary value problems and dependence on higher order derivatives," *Journal of Mathematical Analysis and Applications*, vol. 279, no. 2, pp. 442–450, 2003.

[6] J. M. Davis, P. W. Eloe, and J. Henderson, "Triple positive solutions and dependence on higher order derivatives," *Journal of Mathematical Analysis and Applications*, vol. 237, no. 2, pp. 710–720, 1999.

[7] J. Ehme and J. Henderson, "Existence and local uniqueness for nonlinear lidstone boundary value problems," *Journal of Inequalities in Pure and Applied Mathematics (JIPAM)*, vol. 1, p. 8, 2000.

[8] Y. Ma, "Existence of positive solutions of lidstone boundary value problems," *Journal of Mathematical Analysis and Applications*, vol. 314, no. 1, pp. 97–108, 2006.

[9] Y.-M. Wang, "On $2n^{\text{th}}$-order lidstone boundary value problems," *Journal of Mathematical Analysis and Applications*, vol. 312, no. 2, pp. 383–400, 2005.

[10] Z. Yang, "Existence of positive solutions for a system of generalized lidstone problems," *Computers & Mathematics with Applications*, vol. 60, no. 3, pp. 501–510, 2010.

[11] X. Hao, D. O'Regan, and J. Xu, "Positive solutions for a system of $2n^{\text{th}}$-order boundary value problems involving semipositone nonlinearities," *Journal of Inequalities and Applications*, vol. 2020, p. 20, 2020.

[12] K. Zhang, D. O'Regan, J. Xu, and Z. Fu, "Nontrivial solutions for a higher order nonlinear fractional boundary value problem involving riemann-liouville fractional derivatives," *Journal of Function Spaces*, vol. 2019, Article ID 2381530, 11 pages, 2019.

[13] Y. Li, J. Liu, D. O'Regan, and J. Xu, "Nontrivial solutions for a system of fractional q-difference equations involving q-integral boundary conditions," *Mathematics*, vol. 8, no. 5, p. 828, 2020.

[14] Z. Fu, S. Bai, D. O'Regan, and J. Xu, "Nontrivial solutions for an integral boundary value problem involving riemann-liouville fractional derivatives," *Journal of Inequalities and Applications*, vol. 2019, p. 104, 2019.

[15] B. Liu, J. Li, and L. Liu, "Nontrivial solutions for a boundary value problem with integral boundary conditions," *Boundary Value Problems*, vol. 2014, p. 15, 2014.

[16] K. Zhang, D. O'Regan, and Z. Fu, "Nontrivial solutions for boundary value problems of a fourth order difference equation with sign-changing nonlinearity," *Advances in Difference Equations*, vol. 2018, p. 370, 2018.

[17] W. Fan, X. Hao, L. Liu, and Y. Wu, "Nontrivial solutions of singular fourth-order Sturm-Liouville boundary value problems with a sign-changing nonlinear term," *Applied Mathematics and Computation*, vol. 217, no. 15, pp. 6700–6708, 2011.

[18] J. Xu, J. Jiang, and D. O'Regan, "Positive solutions for a class of p-laplacian hadamard fractional-order three-point boundary value problems," *Mathematics*, vol. 8, no. 3, p. 308, 2020.

[19] H. Zhang, Y. Li, and J. Xu, "Positive solutions for a system of fractional integral boundary value problems involving hadamard-type fractional derivatives," *Complexity*, vol. 2019, p. 11, Article ID 2671539, 2019.

[20] B. Liu and Y. Liu, "Positive solutions of a two-point boundary value problem for singular fractional differential equations in Banach space," *Journal of Function Spaces*, vol. 2013, p. 9, Article ID 585639, 2013.

[21] Y. Liu and H. Yu, "Bifurcation of positive solutions for a class of boundary value problems of fractional differential inclusions," *Abstract and Applied Analysis*, vol. 2013, p. 8, Article ID 942831, 2013.

[22] Y. Liu, "Positive solutions using bifurcation techniques for boundary value problems of fractional differential equations," *Abstract and Applied Analysis*, vol. 2013, p. 7, Article ID 162418, 2013.

[23] T. Qi, Y. Liu, and Y. Cui, "Existence of solutions for a class of coupled fractional differential systems with nonlocal boundary conditions," *Journal of Function Spaces*, vol. 2017, p. 9, Article ID 6703860, 2017.

[24] T. Qi, Y. Liu, and Y. Zou, "Existence result for a class of coupled fractional differential systems with integral boundary value conditions," *The Journal of Nonlinear Sciences and Applications*, vol. 10, no. 07, pp. 4034–4045, 2017.

[25] Y. Wang, Y. Liu, and Y. Cui, "Multiple solutions for a nonlinear fractional boundary value problem via critical point theory," *Journal of Function Spaces*, vol. 2017, Article ID 8548975, 8 pages, 2017.

[26] Y. Wang, Y. Liu, and Y. Cui, "Multiple sign-changing solutions for nonlinear fractional kirchhoff equations," *Boundary Value Problems*, vol. 2018, p. 193, 2018.

[27] Y. Liu and D. O'Regan, "Controllability of impulsive functional differential systems with nonlocal conditions," *Electronic Journal of Differential Equations*, vol. 19410 pages, 2013.

[28] Y. Liu, "Bifurcation techniques for a class of boundary value problems of fractional impulsive differential equations," *Journal of Nonlinear Sciences and Applications*, vol. 09, no. 04, pp. 340–353, 2015.

[29] Y. Wang, Y. Liu, and Y. Cui, "Infinitely many solutions for impulsive fractional boundary value problem with p-laplacian," *Boundary Value Problems*, vol. 2018, p. 94, 2018.

[30] J. Li, Y. Cheng, and Z. Li, "Superconvergence of the composite rectangle rule for computing hypersingular integral on interval," *Numerical Mathematics: Theory, Methods and Applications*, vol. 13, no. 3, pp. 770–787, 2020.

[31] J. Li and Y. Cheng, "Linear barycentric rational collocation method for solving second-order volterra integro-differential equation," *Computational and Applied Mathematics*, vol. 39, no. 2, p. 92, 2020.

[32] J. Li and Y. Cheng, "Linear barycentric rational collocation method for solving heat conduction equation," *Numerical Methods for Partial Differential Equations*, in press, 2020.

[33] D. Guo and V. Lakshmikantham, *Nonlinear Problems in Abstract Cones*, Academic Press, Orlando, FL, USA, 1988.